FERMILAB-Pub-00/108-E June 2000

A Feasibility Study of a Neutrino Source Based on a Muon Storage Ring

edited by:

Norbert Holtkamp
David Finley

List of Authors

Fermilab: T.Anderson[2], N.Andreev[2], C.M.Ankenbrandt[1], S.Assadi[2], M.Atac[1], C.Bhat[2], V.I.Balbekov[1], R.Bernstein[1], C.Bohn[2], D.Boehnlein[1], E.Buckley-Geer[1], M.Carena[1], D.Carey[1], M.Champion[2], S.Childress[2], W.Chou[1], D.Cossairt[2], F.deJongh[1], H.T.Diehl[1], A.Drozhdin[1], V.Dudnikov[2], D.Elvira[1], H.Edwards[2], S.Fang[2], D.A.Finley[1], B.Flora[2], M.Foley[2], S.H.Geer[1], K.Gounder[1], J.Griffin[2], M.Harding[2], D.A.Harris[1], N.Holtkamp[1], C.Jach[2], C.Jensen[2],D.Johnson[2], C.Johnstone[1], J.Johnstone[2], T.Jurgens[2], T.Kobilarcik[2], I.Kourbanis[2], G.Krafczyk[2], O.Krivoshev [2], T.Lackowski[2], C.Laughton[2], P.Lebrun[1], J.Leibfritz[2], J.D.Lykken[1],E.Malone[2], J.Marriner[2],M.Mcashan[2], D.Mcginnis[2], J.Mclachlan[2], E.Mcrory[2], F.E.Mills[1], N.V.Mokhov[1], J.Monroe[1], A.Moretti[1], D.V.Neuffer[1], K.-Y.Ng[1], J.Ostiguy[2], S.Ohnuma[2], T.Peterson[2], H.Pfeffer[2], M.Popovic[1], Z.Qian[1], R.Raja[1], T.Raymond[2], J.Reid[2], A.Rowe[2], C.Schmidt[2], J.Sims[2], D.Snee[2], P.Spentzouris[1], R.Stefanski[1], J.Steimel[2], S.Striganov[1], D.Sun [2], I.Terechkine[2], J.Theilacker[2], A.V.Tollestrup[1], A. van Ginneken[1], S.Vejic[1], W.Wan[1], D.Wolff[2], V.Wu[1], D.Wildman[2], J.Yu[1]

Argonne National Laboratory: D.Ayres[1], M.Goodman[1], A.Hassanein[1], T.Joffe-Minor[1], D.Krakauer[1], J.H.Norem[1], C.B.Reed[1], P.Schoessow[1], D.Smith[1], R.Talaga[1], J.Thron[1], L.C.Teng[1], C.Wagner[1], C.-X.Wang[1]

Brookhaven National Laboratory: S.Berg[1], E.B.Blum[1], M.Blaskiewicz[1], R.C.Fernow[1], W.Fischer[1], J.C.Gallardo[1], W.S.Graves[1], R.Hackenburg[1], H.Huang[1], S.A.Kahn[1], J.Keane[1], B.J.King[1], H.G.Kirk[1], D.Lissauer[1], L.S.Littenberg[1], V.Lodestro[1], D.Lowenstein[1], W.Morse[1], R.B.Palmer[1], Z.Parsa[1], F.Pilat[1], P.Pile[1], S.Protopopescu[1], P.Rehak[1], J.Rose[1], T.Roser[1], A.Ruggiero[1], N.P.Samios[1], R.Samulyak[2], Y.Semertzidis[1], I.Stumer[1], M.J.Tannenbaum[1], V.Tcherniatine[1], M.Todosow[2], D.Trbojevic[1], H.Wang[1], R.Weggel[1], J.Wei[1], W.-T.Weng[1], E.H.Willen[1], S.Y.Zhang[1], Y.Zhao[1]

Budker Inst.Nuclear Physics (Russia): G.I.Silvestrov[1], A.N.Skrinsky[1], T.A.Vsevolozhskaya[1]

UC Berkeley: E.-S.Kim[1], G.Penn[1], J.Wurtele[1]

UC Davis: J.F.Gunion[1], Vilchez[1]

Univ. of California Los Angeles: D.B.Cline[1], Y.Fukui[1], A.A.Garren[1], K.Lee[1], Y.Pischalnikov[1]

CERN, (Switzerland): B.Autin[2], A.Blondel[2], R.Garoby[2], H.Haseroth[2], C.Johnson[2], E.Keil[2], F.Zimmermann[2], L.J.Tavian[2], R.Losito[2], A.Lombardi[2], R.Scrivens[2]

Univ. of Chicago: K.-J.Kim[1], Oreglia[1], R.Winston[1]

Columbia Univ.: A.Caldwell[1], J.Conrad[1], M.Shaevitz[1], F.Sciulli[1], W.J.Willis[1],

Cornell Univ.: D.Hartill[2], H.Padamsee[2], M.Tigner[1]

ETH Zurich, (Switzerland): A.Badertscher[1], A.Bueno[1], M.Campanelli[1], C.Carpanese[1], J.Rico[1], A.Rubbia[1], N.Sinanis[1]

Fairfield Univ.: D.R.Winn[1]

Indiana Univ.: M.S.Berger[1], G.G.Hanson[1], P.Schwandt[1]

Illinois Inst. of Technology: E.L.Black[1], D.M.Kaplan[1]

Univ. Iowa: Y.Onel[1]

Joint Inst. of Nuclear Research, Dubna, (Russia): V. Kazacha, A. Sidorov

Kansas State Univ.: T.Bolton[1]

Research Center Karlsruhe[1], Germany: R.Rossmanith[1]

KEK[1], Japan: Y.Kuno[1], Y.Mori[1], T.Yokoi[1]

Lawrence Berkeley National Laboratory: S.Caspi[1], S.Chattopadhyay[1], J.Corlett[1], S.Eylon[2], J.Fockler[2], M.A.Furman[1], M.A.Green[1], R.Gupta[1], C.H.Kim[#] [1], D.Li[1], A.D.McInturff[1], R.M.Scanlan[1], A.M.Sessler[1], W.C.Turner[1], R.M.Yamamoto[1],S.Yu[2], M.Zisman[1], M.S.Zolorotorev[1]

Inst.of Math. in Novosibirsk, Russia: I.F.Ginzburg[1],

Michigan State Univ.: M.Berz[1], R.York[1], A.Zeller[1], K. Makino

Univ. Minnesota: J.K.Nelson[1], E.Peterson[1],

Univ. Mississippi: L.Cremaldi[1], D.Summers[1],

Nat.High Magnetic Field Laboratory: J.H.Miller[1], S.Prestemon[1], S.Van Sciver[1], Y.Eyssa[1]

Northern Illinois Univ.: G.Blazey[1], M.A.Cummings[1], D.Hedin[1]

SUNY Stony Brook: C.K.Jung[1], R.Shrock[1], Y.Torun[1]

Northwestern Univ.: H.Schellman[1]

Oak Ridge National Laboratory: J.Chesser[2], T.Gabriel[1], F.C. Gallmeier[2], J.Haines[1], R.A. Lillie[2], T.McManamy[2], P.Spampinato[2], R.Taleyarkhan[1]

Oxford Univ.: J.Cobb[1]

Princeton Univ.: A.Bazarko[1], C.Lu[1], K.T.McDonald[1], P.D.Meyers[1], E.J.Prebys[1],

Institute of High Energy Physics, Protvino, Russia: I. Bogdanov[2], S.Kozub[2], V. Pleskach, P. Shcherbakov, V. Sytnik, L.Tkachenko[2], V. Zubko [2]

RAL, United Kingdom: R.Bennett[1], R.Edgecock[1], D.Petyt[1]

Univ. Rochester: A.Bodek[1], K.S.McFarland[1]

Rockefeller Univ.: G.Apollinari[1], E.J.N.Wilson[1]

Stanford Linear Accelerator Center: A.Sery[1], D.Sprehn[2], D.Ritson[2]

Tel-Aviv Univ (Israel).: O.Benary[1]

Thomas Jefferson National Accelerator Facility : S.A.Bogacz[1], J.Delayen[2], D.Douglas[2], L.Harwood[2], G. Krafft[2], V.Lebedev[2], C. Leemann[2], L.Merminga[2]

Univ. Texas Pan American: W.R.Leeson[1], A.Mahmood[1]

Tufts Univ.: T.Patzak[1]

Univ. Victoria (Canada): R.V.Kowalewski[1]

Univ. Wisconsin: V.D.Barger[1], T.Han[1]

1: Participant of study group and Member of the Neutrino Factory and Muon Collider Collaboration.
2: Participant of study group and non Collaboration Member.

[#] Charles Kim most recently passed away in a tragic accident.

Table of Contents

1. Executive Summary

The Six Month Study on the Feasibility of the Facility

The goal of this study was to investigate and document the technical feasibility of an intense Neutrino Source Based on a Muon Storage Ring. Colleagues from several national and international laboratories with expertise in the different areas were asked to work closely together with the study group at Fermilab and the members of the *Neutrino Factory and Muon Collider Collaboration.* The charge from the Fermilab directorate to the study group represents questions which are of basic interest for a laboratory that is trying to define a future program: What is the design concept and can it meet the performance goals? What is the R&D that is required to bring us from the state that exists today to the point where a conceptual design can be proposed? What are the most likely cost drivers and where are the potential technical risks? And, finally: What are the Environment, Safety and Health issues that have to be addressed during construction and operation?

The basic question about feasibility is addressed throughout the report and the answer is: yes. The result of this study clearly indicates that a neutrino source based on the concepts presented here is technically feasible [1]. According to our present understanding it will not quite meet the intensity specified and it should probably have an energy lower than initially specified (50 GeV). There is clear indication though that we would and should improve the performance and also how it could be done, but it will need appropriate support for the ongoing R&D. The study summarizes the R&D required that would lead to a conceptual design. The identified topics worth mentioning here are certainly, the proton driver and the target area, the performance and the construction of an induction linac, the uncertainties in the simulation of emittance cooling together with the performance of the associated hardware for the cooling channel, and finally the development of the superconducting rf cavities required for acceleration. All these subjects will have to be addressed in parallel in order to arrive, on a reasonably rapid time scale, at a point where a laboratory could initiate a conceptual design report. These subjects are equally critical for the performance of the facility and focusing on only one of them at a time, perhaps due to resource limitations, will severely impact the time scale. As requested in the charge, the cost drivers have been identified. Finally, many of the ES&H issues associated with the facility are very similar to those that have been encountered and solved during the construction and operation of other facilities at Fermilab and elsewhere while others are quite novel. It is concluded here that with adequate planning in the design stages, these problems can be adequately addressed.

The Basic Advantages of a Neutrino Factory

A neutrino factory as a facility has a number of advantages that are worth pointing out. The most essential one is that it is a unique facility, whose physics justification is becoming increasingly clear. In addition, an intense cold muon source will open up new windows of research in a manner similar to what has happened with lasers, synchrotron light sources, FEL's, and neutron sources. An intense neutrino beam will most probably be the first application and is considered in this report. Staged upgrades of the cooling channel can lead to increased intensity neutrino beams, and perhaps ultimately as the technology improves, to muon colliders. In a similar way the final energy of the facility can be upgraded in steps. Both parameters can be adjusted to meet the funding realities that will have to be imposed at some point to make the first step affordable.

Another unique characteristic arises from the fact that the cost of the total facility can be balanced between the detector and the accelerator. Over a wide range the measure of the quality of physics is proportional to the product of $\mathbf{E}.\mathbf{I}.\mathbf{M}$ = constant, where **E** is the energy of the muon beam, **I** is the intensity of the muon beam and **M** is the fiducial mass of the detector. Minimizing the cost for the product requires equal investment into accelerator (acceleration = **E)**, the cold muon source (proton driver through emittance cooling channel = **I)** and the detector (=**M**). Balancing $\mathbf{E}.\mathbf{I}$ with **M** will minimize the total cost and will require the development of accelerator as well as detector technology. A more general advantage is that the small footprint of the facility which will allow it to fit under an existing laboratory site. The same is true for the detectors, one of which could be in a different US Laboratory or, for a very long baseline experiment in Europe or Japan, other laboratory sites could be used. The international nature of the *Neutrino Factory and Muon Collider Collaboration* leads naturally to this collaborative approach. DOE (Department of Energy) and NSF (National Science Foundation) are endorsing this approach given the large number of universities already involved. Responsibilities and cost can be shared between different groups, laboratories or even countries.

The Interest of the Laboratory

All the arguments stated above on the basic advantages are useful only if the proposed program fits the mission of the laboratory, its specific situation and its ongoing program. The question of mission is addressed by the contemporaneous study [2] that investigated the physics program which would accompany this facility. With the strong ongoing program at Fermilab today and over the next couple of years, a balance between supporting the present operation and developing a plan for the future has to be found. The limited resources available to Fermilab make it imperative to use the resources that have been collected under the umbrella of the *Neutrino Factory and Muon Collider Collaboration* and the other organizations supporting this program. Funding has come from DOE, NSF, the State of Illinois, the different universities within the state of Illinois and the additional national and international laboratories which have all made their expertise available. Many of these groups have assumed responsibilities within the R&D program already and their contributions can be found throughout the report. For the ongoing program, it is obvious that an intense proton source would further empower the laboratory to better exploit its investments in Run II, NuMI/MINOS, Mini BooNE, fixed target etc. The existence of an intense muon source would define an interesting and new program, with many opportunities in addition to those offered by a neutrino source.

Norbert Holtkamp　　　　　David Finley

Fermilab, March 31st 2000

REFERENCES

[1] Neutrino factory technical study coordinator: N. Holtkamp and D. Finley. See http://www.fnal.gov/projects/muon_collider/nu-factory/nu-factory.html

[2] Neutrino factory physics study coordinators: S. Geer and H. Schellman. See http://www.fnal.gov/projects/muon_collider/nu/study/study.html

Acknowledgements

We would like to thank all the contributors to this study for the enthusiasm they have shown and for their patience in finally writing up all the work which was done and finally condensing into 10$\pm$x pages. Especially we want to thank Bob Palmer who contributed many of the ideas that were used for this study. Together with him, Eberhard Keil and Collin Johnson wrote up an early design, which was used as the basis for many of the parameters throughout this report. Also we would like to thank Andy Sessler for his patience and successful efforts in focussing the Neutrino Source/Muon Collider collaboration onto this specific Fermilab request. We believe that the interaction with the Collaboration and the result will both serve as positive examples for future studies. Jonathan Wurtele and Mike Zisman deserve credit for organizing the simulation effort for the cooling channel and many other things, which should never be written down publicly. Finally we want to especially thank the contributors from laboratories and universities which are not presently officially part of the Collaboration: CERN, INP, Protvino, Dubna, MRTI, TJNAF, Cornell University, Oak Ridge National Laboratory, Michigan State University, and the National High Magnetic Field Laboratory. We also thank their management for their support and interest, and we certainly hope that the ongoing good work will continue. We also would like to express our gratitude to Mike Witherell, Steve Holmes, Mike Shaevitz, John Marriner and Peter Limon for giving us the opportunity to organize this study and for their continuous support. They gave us a very exciting six months.

2. Introduction

A muon storage ring as a source of intense neutrino beams supersedes a standard neutrino source in many ways. Classical neutrino sources have long decay channels which are used to generate $\bar{\nu}_{\mu,e},\nu_{\mu,e}$ beams from pions coming from a target that is hit with an intense proton beam. In a muon storage ring the muons circulate after injection until they decay. A fraction of these muons will decay in the straight section, which will produce an intense, well collimated neutrino beam. If the muon beam divergence in the straight section is small compared to the decay angle, the opening angle of the neutrino beam is completely dominated by the decay kinematics. Given the energy of the muons this angle basically equals $1/\gamma_{muon}$. From the requirement to have the divergence of the muon beam in the straight section to be small compared to the divergence of the neutrino beam, an emittance goal for the muon source and the cooling channel can easily be defined.

A muon storage ring used to produce very intense and clean neutrino beams is most probably the first application of an intense muon source. After being generated from pion decay and cooled in an ionization cooling channel, the muon beam is accelerated and injected into a storage ring, where the muons decay while circulating. The neutrinos from the decay muons in the storage ring form a very intense and well collimated beam of electron and muon neutrinos (ν_e,ν_μ). The idea for such a neutrino source has been described many times (see section 2.1), but only recently with the progress being made on ionization cooling concepts within the Neutrino Factory and Muon Collider Collaboration, does an intense source seem feasible. With a new proton driver and a target that can withstand the power density and the intense radiation from the impinging proton beam, the source will produce enough muons to achieve $2\text{x}10^{20}$ muons decaying into neutrinos in one of the straight sections of the storage ring. In order to achieve this goal, very efficient and large aperture focusing solenoids and rf accelerating systems must be developed for the ionization cooling channel. The transverse emittance that has to be achieved in this channel, to be sufficient for a neutrino source on the other hand, has to be reduced by only a factor of approximately ten in both transverse dimensions. The longitudinal emittance coming from the source is almost of no importance, which makes longitudinal cooling unnecessary. Given the intensity goal of $2\text{x}10^{20}$ muons/year decaying in one straight section, an attempt has been made to investigate the technical feasibility of such a facility as a whole (see also [2]). This is reflected in the charge that was given to the study group and is summarized in the box to the right.

Charge for the purpose of this study

1. A design concept for a muon storage ring and associated support facilities that could, with reasonable assurance, meet performance goals required to support a compelling neutrino based research program.
2. Identification of the likely cost drivers within such a facility.
3. Identification of an R&D program that would be required to address key areas of technological uncertainty and cost/performance optimization within this design, and that would, upon successful completion, allow one to move with confidence into the conceptual design stage of such a facility.
4. Identification of any specific environmental, safety, and health issues that will require our attention.

Even though we have done our best to be complete and consistent in this report, the careful reader will note some inconsistencies throughout this report, particularly from chapter to chapter. The reason is that, early on, we had to specify many of the parameters so that we could make reasonably rapid progress on the engineering designs. However, optimization of the various subsystems continued vigorously during the six months of this study. The resulting inconsistencies are indications of ongoing progress in the design of this complicated and intertwined facility.

Later on in Table 2 the design parameters for the Neutrino Factory are presented in more detail. One of the main parameters, the neutrino flux that can be achieved as a measure of the performance, is worth discussing at this point. The goal was to achieve 2×10^{20} muon decays per year in one straight section of the storage ring. Given the numbers for muon survival from the different subsystems that will be described later in the report, the presented scenario will instead provide 6.0×10^{19} muon decays per year. This assumes perfect transmission between the different subsystems. Detailed error analyses still have to be done and are not included in the present performance.

2.1 Physics Motivation for a Neutrino Source Based on a Muon Storage Ring

Recent measurements of atmospheric muon neutrino (ν_μ) fluxes from the Super—Kamiokande (SuperK) collaboration have shown an azimuth—dependent ($\rightarrow$ baseline dependent) depletion that strongly suggests neutrino oscillations of the type $\nu_\mu \rightarrow \nu_x$. Since the atmospheric ν_e flux is not similarly depleted, ν_x cannot be ν_e and must therefore be either ν_τ, or ν_s (a sterile neutrino). These observations have inspired many theoretical papers, several neutrino oscillation experiment proposals, and much interest in the physics community. This interest is well motivated. Understanding the neutrino-mass hierarchy and the mixing matrix that drives flavor oscillations may provide clues that lead to a deeper understanding of physics at very high mass-scales and insights into the physics associated with the existence of more than one lepton flavor. Hence, there is a strong incentive to find a way of measuring the neutrino flavor mixing matrix, confirm the oscillation scheme (three—flavor mixing, four—flavor, n-flavor ?), and determine which mass eigenstate is the heaviest (and which is the lightest). This will require a further generation of accelerator based experiments beyond those currently proposed.

High energy neutrino beams are currently produced by creating a beam of charged pions that decay in a long channel pointing in the desired direction. This results in a beam of muon neutrinos ($\pi^+ \rightarrow \mu^+ + \nu_\mu$) or muon anti—neutrinos ($\pi^- \rightarrow \mu^- + \bar{\nu}_\mu$). In the future, we will need ν_e and $\bar{\nu}_e$ (as well as ν_μ and $\bar{\nu}_\mu$) beams to adequately unravel the mixing matrix. To illustrate this, consider neutrino oscillations within the framework of three-flavor mixing, and adopt the simplifying approximation that only the leading oscillations contribute (those driven by the largest Δm^2_{ij} defined as $\Delta m^2_{32} \equiv \Delta m^2_3 - \Delta m^2_2$, where m_i is the mass associated with mass eigenstate **i**.) The probability that a neutrino of energy E~(GeV) and flavor α oscillates into a neutrino of flavor β whilst traversing a distance L~(km) is given by:

$$P(\nu_e \rightarrow \nu_\mu) = \sin^2(q_{23}); \sin^2(2q_{13}); \sin^2(1.267\Delta m^2_{32}\, L/E)$$

$$P(\nu_e \rightarrow \nu_\tau) = \cos^2(q_{23}); \sin^2(2q_{13}); \sin^2(1.267\Delta m^2_{32}\, L/E)$$

$$P(\nu_\mu \rightarrow \nu_\tau) = \cos^4(q_{13}); \sin^2(2q_{23}); \sin^2(1.267\Delta m^2_{32}\, L/E)$$

Each of the oscillation probabilities depends on Δm^2_{32} and two mixing angles q_{ij}. To adequately determine all the q_{ij} and sort out the various factors contributing to the $P(\nu_\alpha \rightarrow \nu_\beta)$ will require ν_e as well as ν_μ beams. In addition, there is a bonus in using ν_e beams since electron neutrinos can elastically forward scatter off electrons in matter by the charged current (CC) interaction. This introduces a term in the mixing matrix corresponding to $\nu_e \rightarrow \nu_e$ transitions that is not present for neutrinos of other flavors. Hence, if electron—neutrinos travel sufficiently far through the Earth, matter effects modify the oscillation probabilities. This modification depends on the sign of Δm^2_{32}, and provides a unique way of measuring which mass eigenstate is heaviest and which is lightest. We conclude that if we can find a way of producing ν_e beams *of sufficient intensity*, we are highly motivated to do so.

The obvious way to produce high energy ν_e beams is to exploit muon decays. Since muons live 100 times longer than pions, we need to avoid using a linear decay channel, which would be impractically long for high energy muons. The solution is to use a muon storage ring with long straight sections, one of which points in the desired direction. This yields a neutrino beam consisting of 50% ν_e and 50% $\bar{\nu}_\mu$ if μ^+ are stored, or 50% ν_μ and 50% $\bar{\nu}_e$ if μ^- are stored. Using a storage ring to produce secondary beams of $\mu^\pm$, $e^\pm$, $\bar{p}$ and ν was proposed by Koshkarev [3] in 1974. The idea is also ascribed to Wojcicki [4] as well as Collins [5]. The muons were to be produced by allowing high-energy pions to decay within the ring. The key questions that need to be addressed in order to produce a viable proposal for the production of secondary beams by this method are:

- How can enough particles be stored ?
- How can their phase-space be compressed to produce sufficiently intense beams for physics ?

The calculated beam fluxes used in [3], [4] and [5] were too low to motivate the construction of a secondary beam storage ring. A viable solution to the key question (how to make sufficiently intense beams) was implemented at the beginning of the 1980's for antiproton production, leading directly to the CERN proton—antiproton collider and the discovery of the weak Intermediate Vector Bosons. The solution to the intensity question involved using lithium lenses to collect as many negative particles as possible, and stochastic cooling to reduce the phase-space of the $\bar{p}$ beam before acceleration. In 1980 it was suggested [6] that the negative particle collection ring (the Debuncher) at the proposed

Fermilab antiproton source could be used to provide a neutrino beam downstream of one of its long straight sections. The Debuncher collects negative pions (as well as antiprotons) which decay to produce a flux of captured negative muons. The muon flux in the Debuncher was subsequently measured and found to be modest. The short baseline neutrino oscillation experiment proposal (P860 [7]) that was developed following these ideas was not approved ... the problem of intensity had not been solved!

In order to make progress we need a method of cooling muon beams and a way of producing more muons. Stochastic cooling cannot be used since the cooling time is much longer than the muon lifetime. Ionization cooling was proposed as a possible solution (see [8]). A way of collecting more pions (that subsequently decay into muons) using a very high-field solenoid was proposed by Djilkibaev and Lobashev [9] in 1989. Thus by the end of the 1980's the conceptual ingredients required for very intense muon sources were in place, but the technical details had not been developed. Fortunately in the 1990's the desire to exploit an intense muon source to produce muon beams for a high energy muon collider motivated the formation of a collaboration (back then, the *Muon Collider Collaboration,* subsequently renamed as *The Neutrino Factory and Muon Collider Collaboration*). This has resulted in a more complete technical understanding of the design of an intense muon source [10]. In 1997 it was proposed by Geer [11] to use a muon collider type muon source to produce an intense beam of muons at low energy, rapidly accelerator the muons to high energies, and inject them into a dedicated muon storage ring with long straight sections, to produce a very intense neutrino source. It was shown that this "neutrino factory" was sufficiently intense to produce thousands of events per year in a reasonably sized detector on the other side of the earth! The intensity problem had been solved! In addition, it was shown that the ring could be tilted at large angles to provide beams for very long (trans-earth) neutrino oscillation experiments, and that muon polarization could in principle be exploited to turn on/off the initial ν_e flux [11]. This proposal came at a time of increasing interest in neutrino oscillation experiments due to the SuperK results, and also at a time when the particle physics community was/is considering possible facilities needed at its laboratories in the future [12]. Thus, the neutrino factory concept quickly caught the imagination of the physics community. At the very beginning a specific scenario was picked to investigate the technical feasibility of many of the components necessary for such a source. Given the knowledge at that time about the intensity that would be required to have a compelling physics program, the energy and the baseline length was specified as well. These parameters, the basis for the accelerator facility feasibility study, are presented in Table 1. The physics study [1] on the other hand, investigated a much broader spectrum of experiments, which most probably would lead to a reconsidered set of parameters that would be used later on.

Energy of the Storage Ring should be 50 GeV

Number of neutrinos/straight section is $2x10^{20}$ per year

No polarization

Capability to switch between μ^+ and μ^+

Baseline for facility Fermilab to SLAC/LBNL

Table 1: Set of parameters chosen for the feasibility study following a very early assessment of the goals for the physics study.

2.2 Basis for the Accelerator Facility Layout

If the μ-beam divergence in the straight section is small compared to the decay angle, the opening angle of the neutrino beam is dominated by the decay kinematics. Given the energy of the muons this angle equals $\approx 1/\gamma_{muon}$, where γ_{muon} is the muon energy in units of $m_{muon}c^2$. Thus, the opening angle of the muon beam in the storage ring, in order to not contribute significantly to the divergence of the neutrino beam, has to be small compared to $1/\gamma_{muon}$. A reasonably large β-function in the decay straight allows therefore a comfortably large emittance which in our case has to be approximately a factor of 10 smaller (in both dimensions) than the emittance coming from the target. This defines the goal for transverse emittance cooling. The total flux which can be achieved defines the performance of a neutrino source. (This is quite different from a muon collider where the luminosity is proportional to the square of the number of particles per bunch.) Therefore the longitudinal emittance is of no direct interest and the flux is simply proportional to the number of particles per pulse - independent of the longitudinal distribution. The longitudinal emittance has to be small enough to manipulate and finally cool the beam, which is the only requirement that has to be met.

In the simple version of a racetrack shaped storage ring with two long straight sections considered in this study, more than one third of the muons will decay in each straight section. Given the large number of different and technically demanding sub-systems required for the entire facility, the charge for the feasibility study was focused on basic questions one would have to answer for such an facility (see charge in the box on the first page). Given the large variety of possibilities for short (~500 km), long (~3000 km) and very long baseline (>8000 km) experiments which all influence the technical layout one way or the other, a choice had to be made to focus on one design. A specific set of accelerator parameters was chosen based on the physics goals known at that time. Other boundary conditions were:

1) Given the experience with the simulations being done for the Muon Collider and earlier studies of a neutrino source [13], a reasonable assumption had to be made for the number of muons one could obtain per incident proton on target. This number, which includes all the decay losses and the beam loss during cooling and acceleration, is a very critical number because it defines the requirements on the proton driver and target. The goal for this study is to achieve 0.1 muon injected into the ring per incident proton on target.
2) We required at least one third of the muons circulating in the ring to decay in each straight section, given the available space and assuming a racetrack shape for the storage ring.
3) Because this is a pulsed accelerator, the average current that has to be accelerated to achieve 2×10^{20} neutrinos/year, critically depends on the accumulated operating time per year. More operating time reduces the investment cost in the high power rf systems which are expected to dominate the cost. An optimistic assumption led to 2×10^{7} sec/year assumed for the purpose of this study.
4) A storage ring tunnel with an acceptable slope would be the only possible design that could reasonably be investigated over the time scale that was available. This choice is particularly relevant since cryogenics and civil engineering would be based on experience with other more standard type installations.
5) Abandoning polarization for this study had two advantages. A very low frequency, high gradient rf system that was proposed directly after the target [13] would not be necessary, because the correlation in longitudinal phase space for the forward and backward polarized pions does not have to be preserved. For the same reason the proton bunch length in the proton accelerator could go up to 3 nsec instead of 1 nsec, which is a significant relief.

The final list of parameters for this study is shown in Table 1. This table, together with assumptions 1, 2 and 3 above, led to most of the specifications that were necessary to start the design work on the accelerator complex. These specifications are summarized in Table 2.

1. Given the ongoing study at Fermilab for a fast cycling proton synchrotron (15 Hz) with 16 GeV extraction energy, the number of protons per pulse required on target is at least 2×10^{13}. This as approximately 1 MW beam power on target.
2. The transverse emittance of the muon beam after the cooling channel has to be small enough, in order to have the beam divergence in the straight section to be less then 1/10 of the decay angle, which is $1/\gamma = 2$ mrad. Given an invariant emittance of $\gamma\cdot\varepsilon=3.2\pi\cdot$mm$\cdot$rad the β-function would be ~400 m. This seemed reasonable.
3. Following the assumption of having ten protons per one muon injected in the storage ring, 2×10^{12} muons per pulse are required after the cooling channel and have to be accelerated.
4. No polarization.
5. The Neutrino beam is directed from Fermilab to SLAC/LBNL with a distance of ~3000 km. This sets the slope of the storage ring with respect to the earth surface at 22% or 13 deg. Gentle enough to think of conventional installation methods.

Table 2: Specifications for the accelerator complex of the neutrino source.

It was also recognized very early, and it is worth noting here, that because of the high energy (50 GeV) and high average current ($6\text{x}10^{20}$ muons per year in $2\text{x}10^{7}$ seconds) the average muon beam power would be 240 kW during operation. One of the highest pulsed power lepton beams in the world. This would clearly be a cost driver and led very soon to a focus on lower energy. A unique and very interesting feature of neutrino sources was identified as a result of this discussion, namely the possibility to balance cost between higher energy and higher intensity (basically a more expensive accelerator) and a larger and more advanced detector. This will certainly be used for cost optimization in later studies.

For the storage ring an acceptance which is twice as large as the expected emittance from the cooling channel was chosen, because of the uncertainties in the cooling channel design. The aperture was designed to accommodate ±3σ of 3.2 π mm-rad rms normalized emittance. This allows for a total emittance growth of approximately a factor of 2 in the accelerating systems, once the muon beam has been cooled down to the goal value of 1.6 π mm-rad or it would allow for a somewhat larger emittance coming out of the cooling channel.

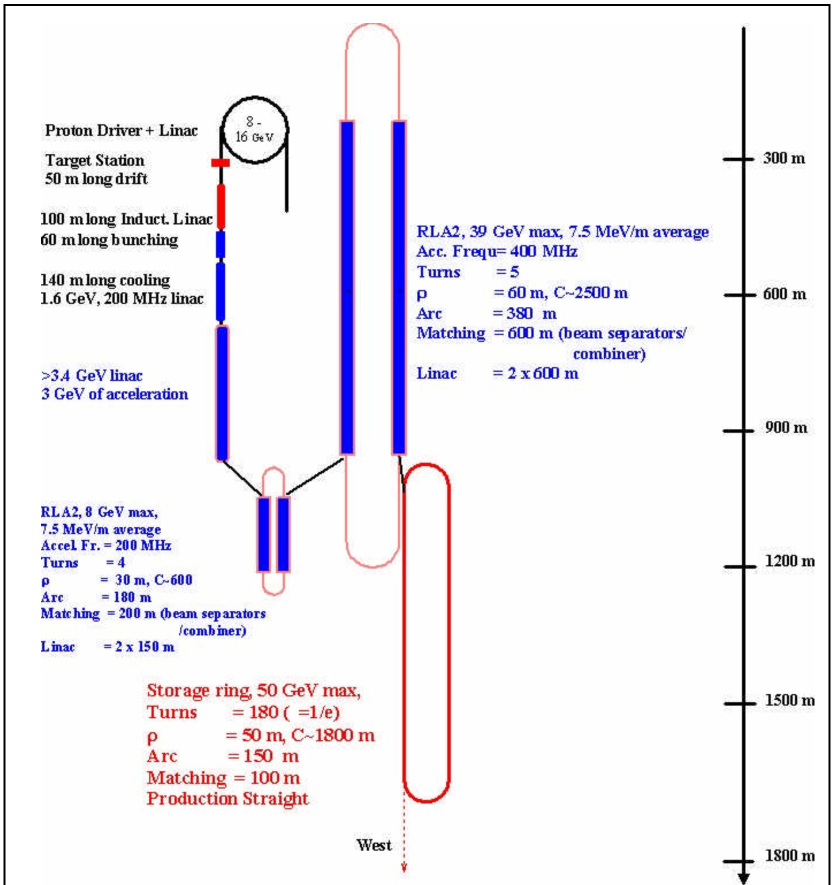

Figure 1: Footprint (to scale) of the whole facility.

The footprint of the total facility is comparatively small and fits easily under several existing laboratory sites. The same is certainly true for any detector that could be considered. A generic sketch of the accelerator facility which is made to scale is shown in Figure 1. This figure shows the logical relationships between the various subsystems. The largest subsystems are the accelerating linac in the cooling channel, the superconducting linac after the cooling and the recirculating accelerators (RLA1 and RLA2). The total area required in order to provide a 50 GeV muon beam to a storage ring is approximately 1.0×2.0 km. A more elaborate, site specific picture is shown in Chapter 13. There, using minimal deviations from this logical layout, we have integrated the facility onto the Fermilab site. The proton driver is placed near the Main Injector, and the rest of the facility easily fits inside the Tevatron.

The basic argument leading to the generic layout is that bending between the different subsystems should be minimized. This will minimize muon loss because of the large transverse emittance that will have to be transported. The same number of passes through each linac of the RLAs is another criterion that was applied to make the beam loading equal on both sides of each RLA, which leads to identical rf system requirements for both sides. Coming out of the last RLA, the muon beam would be gently bent downward into the storage ring tunnel and injected into the straight section pointing to the long baseline experiment. Another remarkable result of this layout, given the earlier boundary conditions, is that the direction the proton beam hits the target defines the natural direction of the neutrino beam going to the experiment. Therefore once the location of the detector is fixed, the layout is constrained, or one of the boundary conditions have to be given up, which will most probably increase cost or decrease performance.

REFERENCES

[1] Neutrino factory physics study coordinators: S. Geer and H. Schellman. See http://www.fnal.gov/projects/muon_collider/nu/study/study.html

[2] Neutrino factory technical study coordinators: N.Holtkamp and D. Finley. See http://www.fnal.gov/projects/muon_collider/nu-factory/nu-factory.html

[3] D.G.Koshkarev, Preprint ITEP-33, 1974 and “Proposal for a decay ring to produce intense secondary particle beams st the SPS”, CERN/ISR-DI/74-62.
[4] S. Wojcicki, unpublished (1974).
[5] T. Collins, unpublished (1975).
[6] D. Cline and D. Neuffer, AIP Conf. Proc. 68, 846 (1980).
[7] W. Lee (spokesperson) et al., FNAL Proposal P860, “A Search for neutrino oscillations using the Fermilab Debuncher”, 1992.
[8] A.A. Kolomensky, Sov. Atomic Energy Vol. 19, 1511 (1965).
[9] R.M. Djilkibaev and V.M. Lobashev, Sov. J. Nucl. Phys. {\bf 49(2)}, 384 (1989).
[10] "$\mu^+\mu^-$ Collider: A Feasibility Study", BNL-52503, Fermilab-Conf. 96/092, LBNL-38946, and C. Ankenbrandt et al. (Muon Collider Collaboration), Phys. Rev. ST Accel. Beams 2, 081001 (1999).
[11] S. Geer, “Neutrino beams from muon storage rings: characteristics and physics potential”, FERMILAB-PUB-97-389, 1997; Presented in the Workshop on Physics at the First Muon Collider and Front-End of a Muon Collider (Editors: S. Geer and R. Raja), November, 1997, and published in S. Geer, Phys.Rev.D57:6989-6997,1998.
[12] J. Ellis, E. Keil, G. Rolandi, “Options for future colliders at CERN”, CERN—SL/98-004 (1998)., B. Autin, A. Blondel, J. Ellis (editors), “Prospective study of muon storage rings at CERN”, CERN 99-02, April (1999).,D. Finley, S. Geer, J. Sims, “Muon Colliders: A vision for the future of Fermilab”, FERMILAB-TM-2072, Jun 1999., S.-C. Ahn et al., “Muon Colliders: A Scenario for the evolution of the Fermilab accelerator complex”, FERMILAB-FN-677, Aug 1999.
[13] "The Cost Effective Design for a Neutrino Factory", R. Palmer, C .Johnson, E. Keil, CERN-SL-99-070-AP, Nov 1999. 22pp, CERN Library, MUCOOL note Nr. 67.
[14]

3. **Proton Driver**

3.1 Introduction

The proton driver under design at Fermilab is a high intensity rapid cycling proton synchrotron. Its function is to deliver intense short proton bunches to the target for muon production. These muons will be captured, phase rotated, bunched, cooled, accelerated and finally, injected into a storage ring for neutrino experiments. In this sense, the proton driver is *the front end* of a neutrino factory. In addition to serving a neutrino factory, the proton driver may serve other needs. For example, it would replace the present Fermilab Booster as a high intensity new booster. As such it could be the platform for providing 6 times as high proton flux and 12 times as high beam power to experiments. It could also increase the beam intensity in the Main Injector by a factor of 4, where it may begin to have intensity limitations. The antiproton production rate and Tevatron luminosity could be enhanced accordingly, after comparatively modest upgrades in other machines.

The first serious effort for designing a new proton driver at Fermilab started around 1995 and was summarized in 1997 [1]. That work has continued, and a complete design report for such a machine is being prepared for the end of 2000. It is not appropriate to include the details here, and in the following, we only discuss the interaction between the Booster design parameters and those of the Neutrino source.

There are two primary requirements of the proton driver:

1. High beam power: $P_{\mathrm{beam}} = 1.2$ MW
This requirement is similar to other high intensity proton machines that are presently under design or construction, e.g. the SNS at the ORNL, the ESS in Europe and the Joint Project (formerly known as the JHF) in Japan. This similarity makes it possible to establish a worldwide collaboration for tackling various technical design issues in a coherent manner.

2. Short bunch length at exit: $\sigma_b = 3$ ns.
This requirement is particular to the proton driver. It brings up a number of interesting and challenging beam physics issues that must be solved. The bunch length is related to the longitudinal emittance ε_L and momentum spread Δp by:

$$\sigma_b \propto \frac{e_L}{\Delta p}$$

In order to get short bunch length, it is essential to have:

- small longitudinal emittance (emittance preservation during the cycle);
- large momentum acceptance (in the rf and as well as in the lattice);
- bunch compression at the end of the cycle.

3. Low beam loss during acceleration to keep the activation of machine components low enough to allow maintenance. The above requirements on the machine design make this a major challenge.

3.2 Choice of Major Design Parameters

The design goal of the neutrino factory at Fermilab is 2×10^{20} muons per year to the neutrino experiments. This requires 4.5×10^{14} protons per second (see chapter 2). At a repetition rate of 15 Hz, 3×10^{13} protons per cycle are required. The average beam current is 72 μA. At 16 GeV, this provides a beam power of about 1.2 MW.

The beam power is the product of three parameters – proton energy E_p, number of protons per cycle N_p and the repetition rate f_{rep}:

$$P_{beam} = E_p \times N_p \times f_{rep}$$

The rep rate is chosen to be 15 Hz for two reasons: (1) Fermilab has a 15 Hz linac. A repetition rate higher than 15 Hz would require a major change in the present linac set-up. (2) A repetition rate lower than 15 Hz would mean more protons per cycle, which will be difficult in the present linac.

A proton energy of 16 GeV was chosen for the proton driver study. The choice of beam energy is a compromise resulting from the following considerations:

1) All other things being equal, higher energy synchrotrons most probably require higher investment cost.

2) At the outset of this study, the calculations being made so far indicated that muon flux scales with beam power over a fairly wide range of proton energies. For a fixed repetition rate and a specified beam power, reducing the beam energy would require a proportional increase in beam intensity. Those changes in turn would cause the following undesirable parameter changes: higher longitudinal phase space density N_b/ε_L (in which N_b is the number of protons per bunch), higher space charge tune shift ΔQ at top energy (which would make bunch compression more difficult) and large momentum spread $\Delta p/p$.

3) The present Fermilab linac should be able to deliver the intensity required for a 16 GeV synchrotron, 3×10^{13} particles per cycle at 15 Hz, after upgrades of modest scope. More substantial upgrades would be necessary for higher intensities.

4) Higher intensities will exacerbate space-charge effects at low energy in the synchrotron, and it would probably be necessary to raise the linac energy to alleviate these effects, perhaps to 1 GeV.

5) For the present 400 MeV linac and a 16 GeV synchrotron, the ratio of input and output momenta for the synchrotron is about 18, which is a rather large but probably tolerable dynamic range for a rapid cycling synchrotron.

There are a number of open questions regarding the design energy for the booster that can only be answered by looking at the overall service that the Booster must provide in support of the laboratory physics programs. These broader questions were not addressed at this time, and the parameters shown in Table 1 below were determined to be adequate for the purposes of this study.

The proton driver for the neutrino factory is called Phase I. Details of Phase I design will be described in the following sections. A possible future upgrade of the proton driver to serve a muon collider is called Phase II. Table 1 lists the main parameters of the two phases. However, Phase II design will not be discussed in this report. For comparison, the present proton source parameters are also listed in Table 1.

3.3 Technical Systems

The central part of the proton driver is a new 16 GeV synchrotron that would be installed in a new tunnel. There are eleven main technical systems: a new linac front end, a chopper, 400 MeV line, 16 GeV lines, 16 GeV ring lattice, injection and extraction systems, RF systems, magnets, power supplies, vacuum and collimators. The design of each system has been worked out to some detail and will be briefly described below.

3.3.1 New Linac Front End

In order to use much of the present linac as an injector for the first stage of the proton driver, the linac must provide H^- ions in excess of 4800 mA-μs (60 mA and 80 μs). Although both the beam current and pulse length are within the capability of the system, the beam loss and induced radiation in the structure at high intensity operation would become an issue. The front end of the linac will be changed to increase the transverse brightness of the beam. The new front end consists of a brighter source (either a modified magnetron or a DESY rf type volume source), a short electrostatic focusing structure (LEBT) and a 201

MHz RFQ from 30 keV to 1 MeV. In addition, an isochronous transport line made of two 270° bending magnets (the α-magnets) and five quads, a second 201 MHz RFQ from 1 MeV to 2.235 MeV and a modified Drift Tube Linac (DTL) section, in which the first existing 18 drift tubes will be eliminated, are required. The rest of the linac (*i.e.*, Tank 2 to 5 of the DTL and the Coupled Cavity Linac) will remain the way it is now. With these modifications the transverse beam emittance ε_T at 400 MeV is expected to decrease from 8 π mm-mrad (present value) to 3 π mm-mrad. This would greatly reduce beam losses in the linac due to the aperture limitations in the system.

	PRESENT	(ν-FACTORY) PHASE I	UPGRADE PHASE II
Linac (operating at 15 Hz)			
Kinetic energy (MeV)	400	400	1000
Peak current (mA)	40	60	80
Pulse length (μs)	25	80	200
H^- per pulse	6.3×10^{12}	3×10^{13}	1×10^{14}
Average beam current (μA)	15	72	240
Beam power (kW)	6	29	240
Pre-booster (operating at 15 Hz)			
Extraction kinetic energy (GeV)			3
Protons per bunch			2.5×10^{13}
Number of bunches			4
Total number of protons			1×10^{14}
Norm. transverse emittance (mm-mrad)			200π
Longitudinal emittance (eV-s)			2
RF frequency (MHz)			7.5
Average beam current (μA)			240
Beam power (kW)			720
Booster (operating at 15 Hz)			
Extraction kinetic energy (GeV)	8	16	16
Protons per bunch	6×10^{10}	7.5×10^{12}	2.5×10^{13}
Number of bunches	84	4	4
Total number of protons	5×10^{12}	3×10^{13}	1×10^{14}
Norm. transverse emittance (mm-mrad)	15π	60π	200π
Longitudinal emittance (eV-s)	0.1	2	2
RF frequency (MHz)	53	1.7	7.5
Extracted bunch length σ_b (ns)	0.2	3	1
Average beam current (μA)	12	72	240
Target beam power (kW)	100	1200	4000

Table 1: Proton Driver Parameters of Present, Phase I and Phase II.

3.3.2 Chopper

A new type of chopper has been designed and built in collaboration with the KEK 2. This is a pulsed beam transformer made of three 1”-thick Finemet cores. It is driven by two HTS 81-09 transistors for bipolar operation. It is placed in front of the RFQ and modulates the injection beam energy by ± 10%. The rise- and fall-time of the chopper is about 30 ns. A prototype has been installed and successfully tested with beam on the linac at HIMAC, a medical center in Japan operating a high intensity accelerator.

3.3.3 400 MeV Line

The 400 MeV line connects the linac to the 16 GeV ring. It could be made of permanent magnets, similar to the present 8 GeV line used at Fermilab.

3.3.4 16 GeV Line

In the present layout, the 16 GeV transport line is about 2 km long and connects the driver to the target station. A major portion of it would be in the Tevatron tunnel. A preliminary design using FODO lattice has been worked out. One concern about transporting intense ($N_b = 7.5 \times 10^{12}$) short ($\sigma_b = 3$ ns) bunches in this long line is possible bunch lengthening due to space charge and lack of longitudinal focusing. However, simulation shows that the longitudinal emittance growth is negligible in this line [3].

3.3.5 16 GeV Ring Lattice

In order to minimize longitudinal emittance dilution a lattice design should be chosen which does not require to go through transition. This excludes the traditional FODO lattice for a 16 GeV ring. Flexible momentum compaction (FMC) type lattice have to be considered. Other requirements include: $B_{max} \leq 1.5$ T, large dynamic aperture (> 100π mm-mrad), large momentum acceptance ($\Delta p/p = \pm 2.5\%$), and dispersion free straight sections for rf. A collimation system is definitely required and the collimator design must be coupled to the lattice design.

There are presently two FMC lattices under study. One with a triangular shape is shown in Figure 1. The circumference is 711.3 m, which is 1.5 times the size of the present booster. Another lattice has a racetrack shape. Both provide a large or imaginary γ_t and use sextupoles to increase the momentum acceptance. A choice will be made after more careful comparisons between the two lattices.

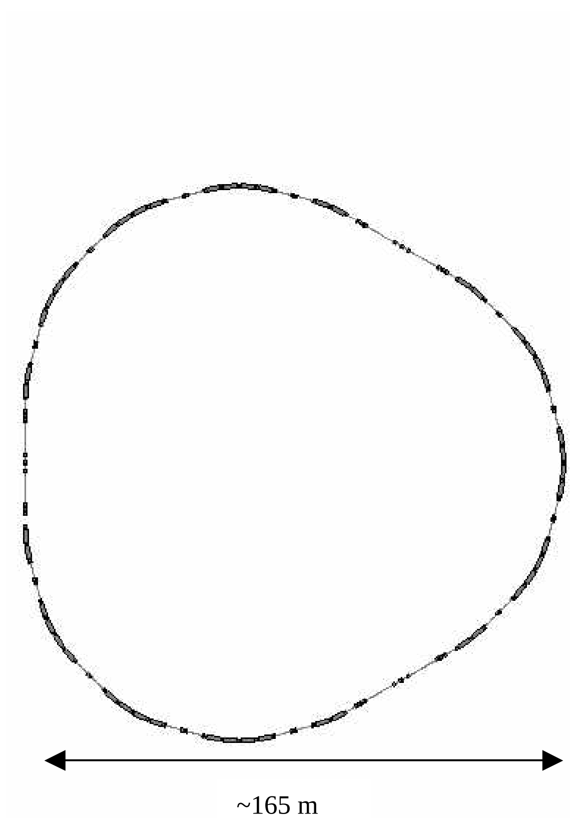

Figure 1: Footprint of the proton driver showing the triangular lattice.

3.3.6 Injection and Extraction

In order to reduce space charge effects, the injected beam will be painted in both transverse and longitudinal phase space. The horizontal injection system consists of 4 orbit bumpers and 2 fast kickers. The latter are used for painting and are located 90°apart (in phase) on each side of the foil. The foil temperature rise and beam emittance dilution during multiple passes through the foil have been calculated and seem tolerable.

Because this accelerator requires a resonant power supply, 1-turn fast extraction is considered. So far only one extraction point has been designed. A second extraction point is possible if placing the rf in dispersive regions (*i.e.*, in the arcs) turns out to be feasible.

3.3.7 The RF System

The required total rf voltage is about 1.4 MV. Due to the small circumference of this machine, the cavities must have a high gradient (30 kV/m). A study showed that Finemet cores (which is a new type of magnetic alloy) can withstand higher rf B-field than regular ferrite and thus provide higher gradient. The disadvantage is higher losses and lower Q. This can be partially compensated by cutting the core to two halves. In order to reduce eddy current heating, the sharp edges of the cut core should be shaped in order to minimize the radial B-field. A prototype 20 kV, 7.5 MHz Finemet cavity has been built at Fermilab in collaboration with the KEK and is shown in Figure 2. It will be tested in the Main Injector for 132 ns bunch spacing coalescing experiment.

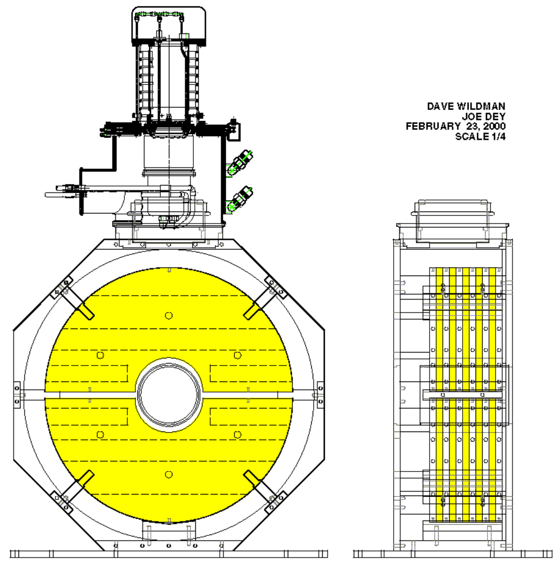

Figure 2: An rf cavity loaded with Finemet cores.

In addition to this acceleration rf system, a second rf system for bunch compression is considered 4. The main difference between the two systems is the duty factor. The one for acceleration will be used throughout the cycle. The second used for bunch compression is turned on for a few hundred microseconds in the cycle. Therefore, the latter could work at much higher gradient (0.5-1 MV/m).

3.3.8 Magnets

The main requirements are a large aperture (dipole: 12.7×31.8 cm^2, quad: 8.56 cm pole tip radius) and a large good field region (dipole: $\Delta B/B < 10^{-3}$ within ±10 cm). The lamination uses 0.014" silicon steel M17. The quadrupole design is similar to the large quadrupoles in the Fermilab Accumulator, except that it will use 4-piece laminations instead of 2-piece.

3.3.9 Power Supplies

A dual-resonance (15 Hz plus 12.5% 30 Hz component) is proposed. In addition to the main power supply, a second power supply for correcting the tracking error between dipole and quadrupole has also been designed. It drives the correction coils in the quadrupoles and uses a bucking choke in order to cancel the voltage and current induced by the main coils.

3.3.10 Vacuum System

In a rapid cycling machine, the eddy current in the beam pipe is a major problem. The ISIS solution, which is a ceramic pipe equipped with a metallic cage inside, works well. However, it requires additional vertical aperture within the magnet. The alternative is to use a thin metallic pipe. Three designs are being pursued: a 0.05" Inconel pipe with cooling tubes, a 0.005" Inconel pipe with ribs, and a composite material pipe with a thin Inconel (or Ti-Al) sheet inside. The pipe size is 5" × 9". The vacuum system design would give a vacuum of 10^{-8} Torr or lower. Such a vacuum would eliminate the concern about possible *e-p* instability as observed in the PSR at LANL.

3.3.11 Collimators

A 2-stage collimator system has been designed. Calculation shows that it can dump 99% of the lost particles in a controlled manner. With such a high efficiency, even for 10% loss at injection or 1% loss at ejection, the activation level in most of the tunnel would be around 1 W/m. Therefore, hands-on maintenance will be possible. The area near the collimators will require special local shielding.

3.4 Technical Design Issues

3.4.1 High Longitudinal Brightness

One of the most demanding issues in the proton driver design is the required longitudinal brightness. Table 2 is a comparison of the longitudinal brightness N_b/ε_L in existing as well as planned proton accelerators.

Machine	E_{max} (GeV)	N_{tot} (10^{12})	N_b (10^{12})	ε_L (eV-s)	N_b/ε_L (10^{12}/eV-s)
Existing:					
CERN SPS	450	46	0.012	0.5	0.024
FNAL MR	150	20	0.03	0.2	0.15
FNAL Booster	8	4	0.05	0.1	0.5
PETRA II	40	5	0.08	0.12	0.7
KEK PS	12	3.6	0.4	0.4	1
DESY III	7.5	1.2	0.11	0.09	1.2
FNAL Main Inj	150	60	0.12	0.1	1.2
CERN PS	14	25	1.25	0.7	1.8
BNL AGS	24	63	8	4	2
LANL PSR	0.797	23	23	1.25	18
RAL ISIS	0.8	25	12.5	0.6	21
Planned:					
Proton Driver Phase I	16	30	7.5	2	3.8
Proton Driver Phase II	16	100	25	2	12.5
Japan JHF	50	200	12.5	5	2.5
AGS for RHIC	25	0.4	0.4	0.3	1.3
PS for LHC	26	14	0.9	1.0	0.9
SPS for LHC	450	24	0.1	0.5	0.2

Table 2: Longitudinal Brightness of Proton Machines

The first phase for the proton driver (see Table 1) requires $3.8\text{x}10^{12}$ particles per eV-s, which is higher than most of the existing proton accelerators, with the exception of the PSR and ISIS. (The PSR is an 800 MeV accumulator ring. The ISIS, although an 800 MeV synchrotron, uses low field magnets, a small rf system, and has no sextupoles.)

In order to achieve high longitudinal brightness, one has to preserve ε_L, which is in contrast to the controlled blow-up of ε_L in many high intensity machines for keeping beam stable. The following measures are taken to preserve the longitudinal emittance ε_L:

1. Avoiding transition crossing in the lattice design. This eliminates a major source of emittance dilution.
2. Avoiding longitudinal microwave instability by keeping the beam below transition (The capacitive space charge impedance helps stabilize the beam below transition) and keeping the resistive impedance small (using a uniform metallic beam pipe).
3. Avoiding coupled bunch instability by using low Q rf cavity.
4. Applying inductive inserts for space charge compensation.
5. Applying longitudinal feedback system.

3.4.2 Bunch Compression

Bunch compression is required at the end of the cycle in order to shorten the bunch length to 3 ns. There are at least three possible methods to achieve this: (1) RF amplitude jump, (2) RF phase jump and, (3) the so called γt manipulation. The achieved compression ratio of either of these methods is about 3-5. Method (1) is the most common one. Although Fermilab has many years of experience with this operation, the high bunch intensity imposes new challenges:

1. During debunching, the beam momentum spread will decrease. This may give rise to excitation of the microwave instability.
2. During debunching, the rf voltage will decrease. This may exacerbate beam-loading effects.
3. In a regular bunch rotation simulation, the momentum compaction is assumed to be a constant α_0. However, the proton driver lattice is nearly isochronous ($\alpha_0 \approx 0$). The higher order terms (α_1, α_2,...) become important. Thus, particles with different $\Delta p/p$ have different path length ΔL. This complicates the bunch rotation process.
4. Due to short bunch length, the tune shift ΔQ from direct space charge and image charge remains large even at 16 GeV. This ΔQ also gives different path length ΔL. In other words, the path length of each particle depends not only on its longitudinal position but also on its transverse amplitude. This effect couples the longitudinal and transverse motion and is a new challenge to beam dynamics study.

Items 3 and 4 causes the so-called "η-spread" (η is the slip factor), which must be taken into account in theoretical modeling as well as in numerical simulations.

Several laboratories (Fermilab, BNL, KEK, CERN, GSI and Indiana Univ.) have decided to investigate methods to achieve the highest possible peak current, longitudinal brightness and compression ratio. An experiment in collaboration with BNL using the AGS has shown that bunches of σ_b = 2 ns can be produced for a bunch intensity of 4 X 10^{12} protons. The bunches were stable for the times measured during the experiment. [5]

3.4.3 Transient Beamloading

Transient beamloading can impose severe limitations on intense short bunch operation if not being compensated. A single bunch intensity of 7.5 X 10^{12} corresponds to a charge of q = 1.2 μC. With a gap capacitance of C = 300 pF, the single pass beamloading voltage q/C is 4 kV. Given the gap voltage of 20 kV the beamloading has to be compensated. However, because the bunch is very short (σ_b = 3 ns), it will be to difficult apply a short current pulse to perform direct compensation. This subject is a high priority R&D item in the proton driver study. RF feedforward systems for global compensation and an rf feedback system to reduce the bunch to bunch and turn by turn variation for a total reduction of 20-30 dB is required.

3.4.4 Space Charge and Instabilities

Space charge is a main limitation to achieve high intensity proton beams, in particular at injection. In order to reduce the Laslett tune shift, a large transverse emittance (60π mm-mrad, normalized, 95%) is used. Both the transverse and the longitudinal phase space will be diluted (painted) for a uniform particle distribution. Inductive inserts are foreseen to reduce the potential well distortion from space charge. An experiment is going on at the PSR/LANL using inductive insert modules provided by Fermilab. The results are encouraging. For a given rf voltage, the achievable beam intensity is increased when the inserts are in place. More measurements will be done to study the effects of the inserts on the beam.

There are two categories of instabilities in the proton driver which have been identified. One is the "conventional" type, for instance, impedance budget, resistive wall, slow head-tail, Robinson, coupled bunch, etc. These are by no means trivial. However, methods for compensation are well understood. Another type is "non-conventional," which is not well understood but is important for the proton driver.

For example, the longitudinal microwave instability below transition, fast head-tail instability (transverse mode coupling) in the presence of strong space charge, and synchro-betatron coupling when rf is placed in dispersive region. Both analytical and numerical studies are being carried out on these effects. Machine experiments are also being planned.

3.4.5 Particle Loss, Collimation Shielding

Here the main concern is the residual activity, which requires the residual dose to be below a certain level. Monte Carlo simulations using the code MARS show that, assuming an average particle loss rate of 1 W/m, the residual dose after 30 days irradiation and 4 hours cool down would be below 100 mrem/hr which is considered to be acceptable. This result agrees with other simulations done at LANL and ORNL. To meet these requirements, a collimation system has been designed with a capture efficiency better than 99% and would allow 10% particle loss at injection and 1% loss at extraction during normal operation. Shielding calculations have been performed as well. The needed berm thickness for shielding for a 1-hour accidental full beam loss is 29 feet.

3.5 Summary

Significant progress has been made to achieve the Phase I design goals. The proton driver consists of a modest improvement of the linac front end, a new 16 GeV synchrotron in a new tunnel and two new beam lines (400 MeV and 16 GeV). The synchrotron meets the needs of a neutrino factory and can provide a 1.2 MW proton beam with 3 ns bunch length. It also allows an upgrade path to a beam power of 4 MW and eventually a bunch length of 1 ns. The proton driver would also serve as a complete functional replacement for the Fermilab Booster, providing upgraded capabilities for the ongoing programs.

REFERENCES

1. S. Holmes, editor, "A Development Plan for the Fermilab Proton Source," FERMILAB-TM-2021 (1997).
2. W. Chou et al., KEK Report 98-10 (September 1998), also see FERMILAB-Conf-99/102, which is published in the PAC'99 proceedings.
3. M. Popovic, MUCOOL Note 106 (March, 2000).
4. W. Chou and A. Van Ginneken, "Phase Rotation Using Low Frequency (Few MHz) RF," Fermilab MUCOOL Note 90 (February, 2000).
5. C. Ankenbrandt *et al*., Phys. Rev. ST Accel. Beams 1, 030101 (1998).

4. Target System and Support Facility

4.1 Overview

The target facility extends from the pre-target primary beam focusing to the end of the decay channel. Technical components include the target, beam absorber, and solenoid magnetic field focusing system. While the ultimate goal is to target approximately 4 MW of proton beam in the target area, smaller values and different target materials (low Z etc.) are considered for the first phase of operation. Chosen initially is a carbon target with incident primary beam power of 1.5 MW. The target is embedded in a high field solenoid magnet of 20 Tesla, and followed by a matching section channel, where the field tapers down to 1.25 T. An iterative design process has been carried out in optimizing Monte Carlo code flux projections with realistic magnetic field parameters. The severe radiation environment and component shielding requirements strongly influence design choices.

The system design includes capture and decay channel solenoids. A cost design optimization for the 20 T capture solenoid is provided, balancing resistive and superconducting magnet contributions. Facility requirements, including shielding, remote handling, radioactive water system, etc. are based on the final design goal of 4 MW. Extent of the Target Support Facility and radiation handling equipment includes the 50 meter decay channel, where remote handling operations are also required, because of intense neutron fluxes.

4.2 MARS Simulation of Captured Meson Beam, Radiation in the Solenoid and the Shielding

4.2.1 Captured π / μ Beam vs Target and Beam Parameters

Realistic 3-D geometry, material and magnetic field distributions [1] based on solenoid magnet design optimization have been implemented into the MARS14(2000) Monte Carlo code [2]. Carbon and mercury tilted targets of various lengths and radii were studied. A variation in the 20 T solenoid region of B_z and B_r with z results in the reduction of the π/μ yield in the decay channel by about 7% for a long carbon target and by 10–14% for a short mercury target compared to the ideal case. Results of a detailed optimization of the π/μ yield vs. target material with the MARS14(2000) code are as follows.

For the given parameters the kinetic energy interval of 30 MeV<E<230 MeV (around the spectrum maximum at z ≥ 9 m from the target) has to be considered as the one to be captured by a phase rotation system. The yield grows with the proton energy E_p, but the yield per beam power is almost independent of E_p for high-Z targets at $6<E_p<24$ GeV, and drops by 30% at 16 GeV from a 6-GeV peak for graphite (see Figure 1). The higher E_p reduces the number of protons on target, but results in more severe energy deposition in the target. The yield is higher by up to 30% for the target tilted by 50 to 150 mrad. A tilt angle of 50 mrad is chosen to locate the primary beam dump at ~6 m from the carbon target.

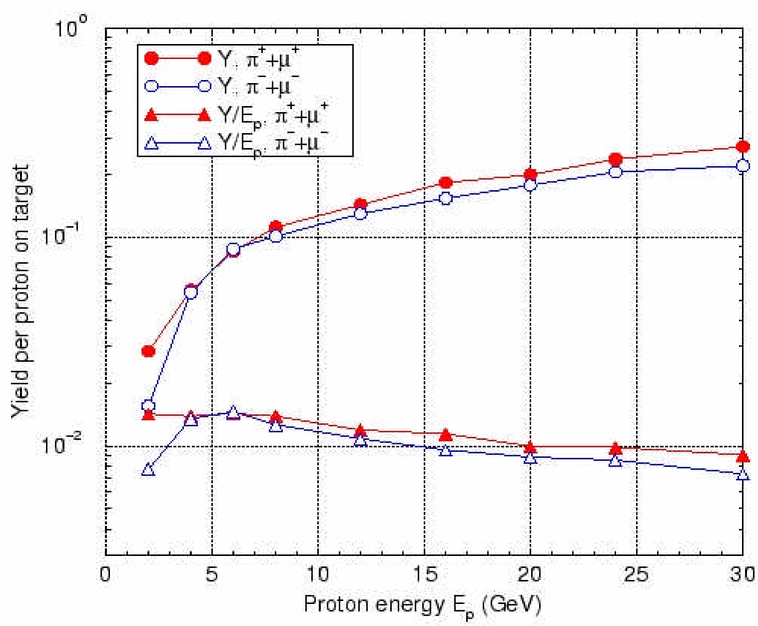

Figure 1: The number of $\pi^+ + \mu^+$ (filled symbols) and $\pi^- + \mu^-$ (open symbols) at 30 MeV<E<230 MeV, as a function of proton energy in the decay channel. Yields are at 9 m downstream of an 80-cm long and 0.75-cm radius carbon target, tilted by 50 mrad with respect to the solenoid axis. RMS beam spot size $\sigma_{x,y}$=0.214 cm. Triangles represent the yield per beam energy.

Maximum yield occurs at $R_{target} = 7.5$ mm for carbon and $R_{target} = 5$ mm for mercury targets with $R_{target} = 3.5\sigma_{x,y}$ and $R_{target} = 4\sigma_{x,y}$ conditions for the beam spot size, respectively. The often used criteria $R_{target} = 2.5\sigma_{x,y}$ reduces the yield by about 10% for the carbon target, but might be more optimal from the energy deposition point of view. Captured yield saturates at the target length of ~2 interaction lengths, i.e. 80 cm of graphite or 30 cm of mercury.

The ratio of mercury to carbon yields varies with the beam energy, as well as with other beam/target parameters. At 16 GeV it is in the range of 1.7 for positives and 2.2 for negatives. Optimizing beam/target parameters, it is found that the best results for the $(\pi+\mu)/p$ ratio at 16 GeV in the decay channel with the given cut are: $Y_{\pi^+ + \mu^+} = 0.182$ and $Y_{\pi^- + \mu^-} = 0.153$ for the 80-cm carbon target and $Y_{\pi^+ + \mu^+} = 0.309$ and $Y_{\pi^- + \mu^-} = 0.315$ for the 30-cm mercury target; i.e., at 16 GeV (best Hg)/(best C) = 1.7 (+) and 2.06 (-).

To provide 2×10^{20} muon decays per year in the straight section at 15 Hz, one needs to have 6×10^{12} muons per pulse in the decay channel. With that, needed are 3.30×10^{13} (and 3.92×10^{13}) protons per pulse at 16 GeV on optimal carbon target for positives (and negatives), respectively. This corresponds to 1.27 (1.51) MW beam. For a mercury target these numbers are 1.7 (2.06) times lower. Figure 2 shows the required number of protons and beam power as a function of the beam energy, for the carbon target. At 16 GeV, the peak instantaneous temperature rise is 60-70 ^{o}C and power dissipation is 34.3 (40.7) kW. For mercury targets the required beam power is lower, 0.72 MW; however, peak temperature rise per pulse is 750 ^{o}C, because of higher energy deposition.

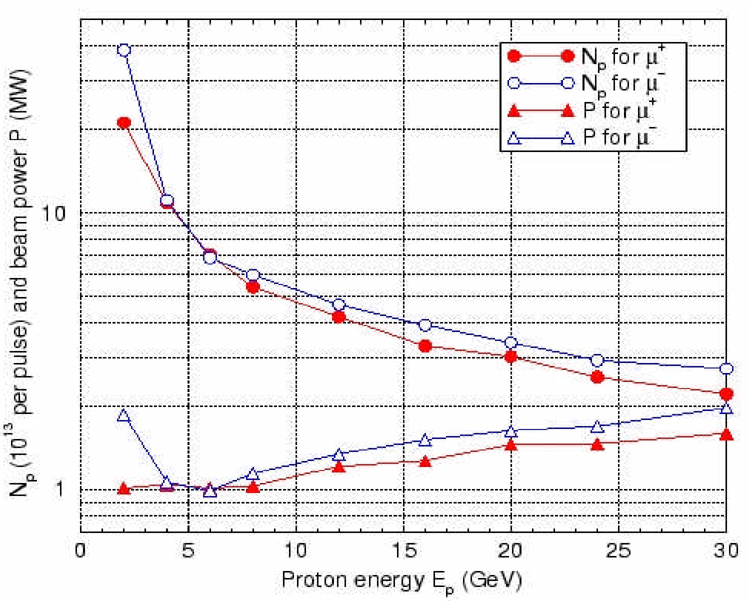

Figure 2: The number of protons per pulse on an 80-cm carbon target required to get 2×10^{20} positive (filled symbols) and negative (open symbols) muons per year in the storage ring straight section vs. proton energy. Triangles represent corresponding beam power.

Study of the final focus optics on target for the primary beam has shown that the optimal targeted beam size of $R_{target}=3.5\sigma_{x,y}$ can be achieved on a 7.5mm radius target using conventional magnets. Considered is a 16 GeV proton beam with a 60 π mm-mrad normalized emittance (for a 1.5 MW beam), and $\Delta E/E = \pm 2\%$.

4.2.2 Radiation Load and Shielding

Full MARS14(2000) simulations have been performed to calculate the accumulated dose and particle flux in the target, and in the resistive and superconducting coils in the high-field, transition and low-field regions. These calculations enable determination of adequate tungsten-based shielding, the residual dose rates on the system components and ground water and personnel radiation shielding. Figure 3 shows the calculated radial distribution of particle flux ($cm^{-2}\ yr^{1}$) and absorbed dose (Gy/yr) for a 1.5 MW 16 GeV beam on a carbon target. Similar distributions are calculated for the beam dump region, at about 6 m downstream of the target in the decay channel.

For a 1.5 MW beam, the annual hadron flux in a stationary graphite target is $5\times10^{21}cm^{-2}$, which corresponds to several months of target lifetime. The annual hadron flux (E>0.1 MeV) and dose in the hottest spot of the inner resistive coil are $1.2\times10^{20}cm^{-2}$ and 3×10^{10} Gy, respectively. This corresponds to ~3 year lifetime limit for copper and ceramic. As discussed later, other considerations also severely limit the lifetime of the resistive coil. The annual neutron flux (E>0.1 MeV) and the dose in the hottest spot of the high field superconducting coil are $8\times10^{17}cm^{-2}$ and 1.3×10^{7} Gy, respectively, or 15 to 20 year lifetime. The annual neutron flux (E>0.1 MeV) and dose in the hottest spot of the potted superconducting coil at the beam dump are $7.6\times10^{17}cm^{-2}$ and 4.1×10^{7} Gy, respectively, or 7-10 year lifetime with the current shielding. The lifetime numbers are rather uncertain, due to lack of data for radiation damage to superconducting materials at neutron energies above 14 MeV. With better understanding of these effects, a shielding design can be adapted that provides longer coil lifetime.

Residual dose rates for a 1.5 MW beam are up to 10^7 mSv/hr (10^6 R/hr) on the target, bore tube and inner resistive coil, 10^3 mSv/hr (100 R/hr) on the CICC (cable-in-conduit conductor) coil and 10^2 mSv/hr (10 R/hr) on the vessel, with the requirement for remote control and robotics. Radiation shielding requirements based on these rates are presented as part of the target support facility design.

4.3 Conceptual Design and Cost Estimate for the Capture and Decay-Channel Solenoids

4.3.1 Requirements

There are straightforward requirements for capture and decay-channel magnet systems but these must be achieved in a difficult radiation environment. The radiation is intense, requiring that the magnet systems incorporate a significant quantity of shielding, especially in the immediate vicinity of the target and the beam absorber.

A field of 20 T is required on-axis in the target region, which should be uniform to within ± 5% over the length of the target (800-mm). The beam and target are inclined relative to the magnetic axis, requiring a clear bore in the capture solenoid (with integral shield) of 150-mm diameter for access. From the target region, the field should drop smoothly over the next 2 m to 1.25 T, which is then held constant over the next 48 m. A simplified representation of the required field profile is shown in Figure 4. It was found that if a realistic profile matches the ideal field to within ±5% (also shown in Figure 4) it is satisfactory for achieving the desired beam flux. The required system lifetime is 20 years**.**

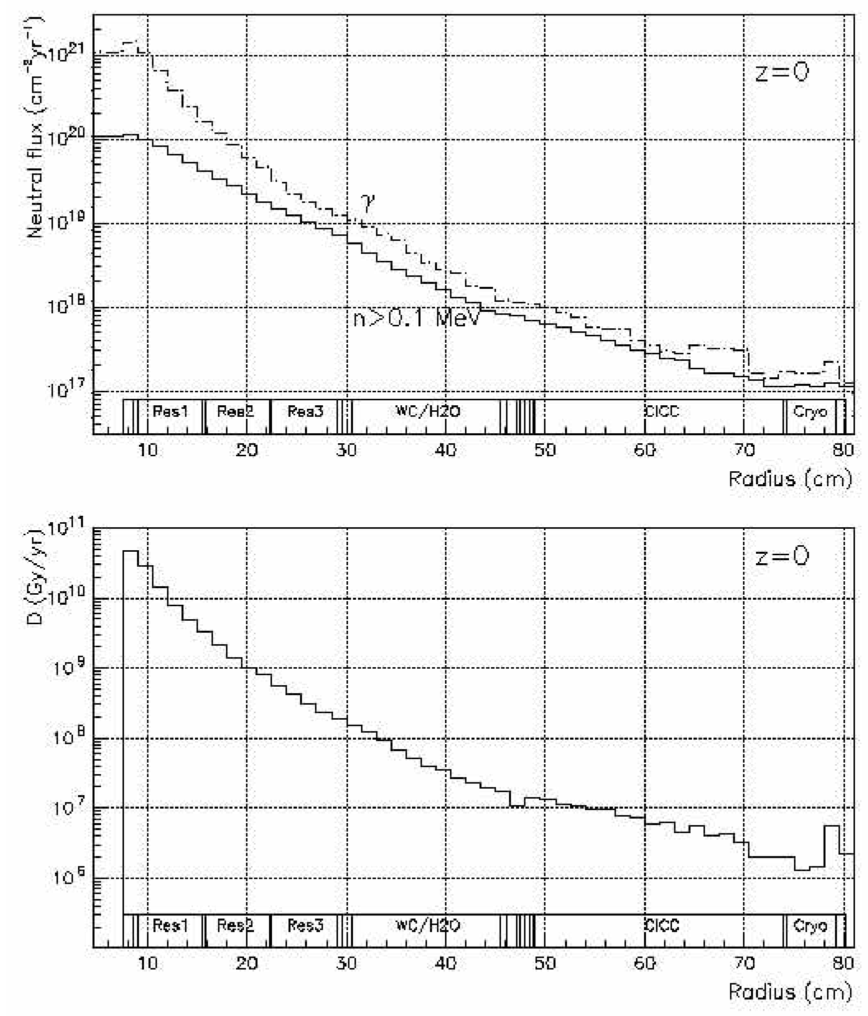

Figure 3: Radial distribution of annual neutron and photon flux (top) and accumulated dose (bottom) at the hottest spot in the high-field solenoid (downstream end of an 80-cm long carbon target) for a 1.5 MW 16 GeV proton beam.

4.3.2 Approach

Achieving the desired field profile requires the specification of coil geometries using feasible coil-pack current densities, which in turn requires that certain engineering constraints be satisfied. The operative engineering constraints depend upon the particular magnet technologies employed in the design, and settling on design details involves an assessment of relative costs. Therefore, the basic approach has been to:

- review the potentially applicable magnet technologies,
- establish the appropriate engineering constraints,
- perform a benchmark design wherein operating conditions are clarified, and establish critical design criteria,
- construct appropriate cost algorithms, and
- use these to optimize the system design.

During the limited time available for this study, three design iteration cycles have been made.

In the target region where 20 T on-axis field is required, this is achieved with a resistive magnet close to the bore, a water-cooled shield outside of this, and an outside superconducting magnet. The principles underlying this choice are:

- The resistive coil pack can be made with reasonable radiation tolerance.
- The resistive magnet will be more cost effective closer to the bore.
- In that position it can also provide some nuclear shielding to the superconducting coil.
- The resistive magnet has a finite life in any case caused by cavitation due to forced water flow.
- To minimize costs, it is expected that a superconducting magnet on the outside would provide a field as high as 10 T.
- To ensure that the superconducting magnet will survive approximately 20 years, a minimum amount of shielding must be provided which includes the resistive magnet plus other material.

4.3.3 Resistive-Magnet Technologies

The technology options considered for the resistive magnet are hollow-conductor, poly-helix, and poly-Bitter (other options, typically those invoked for more specialized or challenging applications than we have here, were not pursued). Hollow-conductor technology offers simple construction and long life but is severely limited in attainable current density because of inherently long cooling passages. High current densities are attainable with poly-helix technology, but this technology is less well developed and, in particular, the insulation is subjected to complex stresses, making it even more problematic in a radiation environment. We have chosen to design with poly-Bitter technology, which is highly developed, capable of very high current densities, and subjects the insulation to predominantly compressive stress. However, the life-time of poly-Bitter magnets is limited (in designs appropriate for the present application, primarily by water erosion of insulating materials and degradation of electrical contacts).

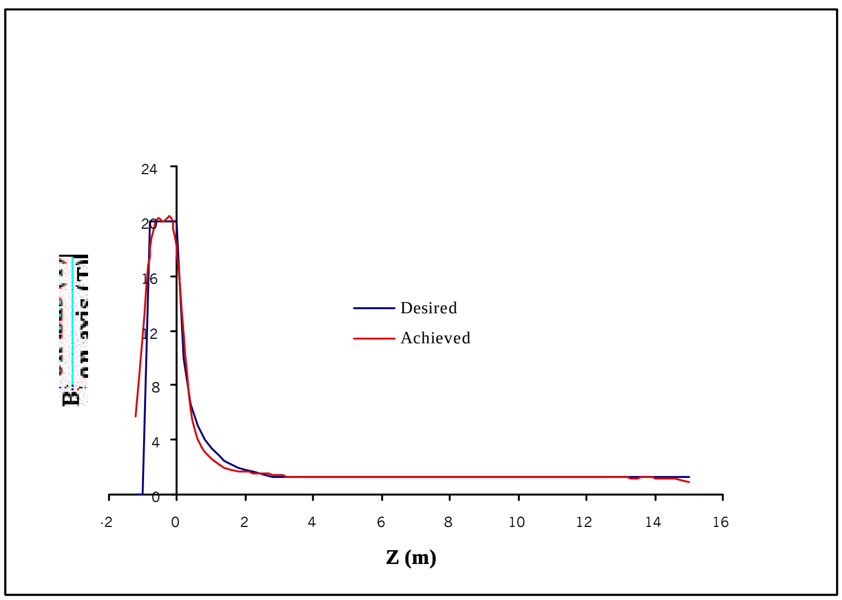

Figure 4. Field profile for the target solenoid system.

4.3.4 Shield Technologies

For the shield, the concept is a toroidal cannister with stainless steel walls filling the annular space between the resistive insert and the superconducting outsert magnet. The cannister will be filled with tungsten-carbide (WC) balls (approximately 80% filling factor). Cooling will be achieved by circulating water through the interstices of the packed bed of WC balls.

4.3.5 Superconducting Magnet Technologies

Operating the superconducting magnet near the damage limit of the insulation and the superconductor results in an appreciable heat load in the windings, significantly higher than what can be accommodated without direct cooling. Two well-developed options for cooling are bath cooling with ventilated windings and forced-flow cooling using cable-in-conduit conductors (CICC).

Bath cooling is a simple and passive technology wherein the windings remain nearly isothermal at the saturation temperature. However, the potential for vapor locking the channels within the windings, especially in coils with appreciable thickness, may be a concern.

A design with forced-flow cooling using CICC technology was chosen. It is somewhat more complex and requires a finite temperature margin, but using an active cooling approach is generally capable of much higher and more predictable heat removal. For most applications, a design using CICC technology is limited by radiation damage rather than by heat removal. Since the windings are not isothermal at the bath temperature, this approach benefits from the use of a superconductor with higher critical temperature (T_C) such as Nb_3Sn, which is also the choice here.

4.3.6 Engineering Constraints

The National High Magnetic Field Laboratory (NHMFL) [3] has been very successful in applying the combination of poly-Bitter technology for resistive magnets and CICC technology for superconducting magnets. The recently completed 45 T Hybrid uses both. The resistive insert of this magnet is designed to contribute 31 T and the superconducting outsert, 14 T. Except for the radiation environment, the requirements of the capture solenoid are relatively less demanding. The NHMFL experience on the 45 T Hybrid Magnet provides a good feel for the critical engineering constraints for the resistive and superconducting technologies that were chosen here.

4.3.7 Resistive Magnet

For poly-Bitter technology applied to the capture solenoid the critical constraints are:

- Heating < 5 W/mm^3
- Hoop stress < 300 MPa
- Lifetime 4000 h
- Radiation damage (no limit has been set but should be less limiting than the normal lifetime of 4000 h)

4.3.8 Superconducting Magnet

For the superconducting solenoid, the critical constraints are:

- Membrane stress in the conduit (von Mises) < 800 MPa
- Hoop strain < 0.3%
- Temperature margin > 0.5 K at any point in the coil in the presence of heating
- Hot-spot temperature during a quench < 150 K, assuming the quench is detected within 1 s and the coil is discharged with a time constant of 5 s
- Absorbed dose $< 10^8$ Gy to preclude radiation damage to the insulation

4.3.9 Benchmark Design

Many of the operating conditions for the magnets could not be assessed without first establishing a benchmark design, with specifications not greatly different than a fully qualified or a fully optimized design. The benchmark design was established simply by using educated guesses for achievable current densities, coil-pack compositions, and appropriate field contributions of the resistive and superconducting magnets. The benchmark design was then used as a vehicle for establishing such critical conditions as intercoil forces, radiation-flux/heating profiles, radiation fluence/dose, etc. as well as a basis for constructing simple analytic expressions for these, which could then be used in the design optimization process. In addition, the benchmark design provided a degree of visualization that permitted the establishment of critical assembly tolerances and gaps, the placement of structural components, etc., all of which were important design constraints and which significantly impact the design process.

4.3.10 Cost Algorithms and Design Optimization

The heart of the design process are the estimates and scalings of system costs. Given that the system is feasible, this is the most important issue. Cost algorithms were constructed that are applicable to a wide range of magnet system configurations. The underlying principle is the decomposition of the system into components, materials, processes, or services for which there is a reasonable experience base of cost. From that experience base, a judgement is made of the most appropriate scaling parameter (mass, length, volume, etc.) for each. The cost of a system is then just the sum of these. The optimum design is the one that satisfies all the physics requirements and meets all the engineering constraints for the least overall cost. Establishing that design is then a straightforward exercise in non-linear optimization of a function of many variables with both equality and inequality constraints on the variables.

4.3.11 System Description

The capture solenoid is a complex system with a number of design parameters that can be varied to minimize the total cost. In comparison, the coils for the decay channel and transition region are far less challenging. These coils will be constructed with epoxy-impregnated windings of Cu/NbTi composite wire and conduction cooled. Although their design feasibility will not be an issue, the length of the channel results in a total cost that is not insignificant. On the other hand, these coils are essentially identical and can be built with relatively mature, commercial technology. Therefore, little variation is anticipated in the projected cost, which is estimated to be approximately 256 k$ for the transition coil (including cryostat) and approximately 175 k$/m for the coils in the decay channel (including cryostat). Results of the cost optimization for the capture solenoid are displayed in Table 1. The system description is essentially the same whether the optimization is based on capital cost or capital plus 20-year operating cost.

Although the optimization resulted in a significantly larger resistive magnet, the resulting optimal value for the build is less than the constrained value. The balance between resistive and superconducting magnet contributions depends heavily on the rate of energy deposition in the latter. For the “Optimized” case, the Bitter coil contributes 11 T and the superconducting coil contributes 9 T.

		Base	**Optimized**
Key Parameters/Variables:	Current [kA]:	10	10
	Build of sc magnet [m]:	0.250	0.231
	Build of outer res. magnet [m]:	0.065	0.088
	Estimated heat load on sc [W]:	903	312
Resistive System	Total Capital costs (k$):	7,266	7,708
	Operating/maintenance costs (k$):	45,843	49,164
Shield	Total capital costs (k$):	735	639
	Operating/maintenance costs (k$):	1.4	0.5
Superconducting System	Total capital costs (k$):	8,039	5,686
	Total operating/maintenance costs (k$):	20,980	9,700
Ensemble:	Total costs (k$):	82,864	72,899
	Capital cost (k$):	16,039	14,034
Low-Field System	Capital costs (k$):	8,331	8,331

Table 1. Results of system optimization compared to the base case. Virtually no differences were found between cost optimizations performed on capital cost and on total system cost; hence only the capital-cost optimized results are shown. The “Ensemble” cost refers to the 20 T capture solenoids and does not include the low-field coils.

4.4 Target Support Facility

The Target Support Facility for the neutrino source consists of the target region, crane hall, hot cell, and radiation handling equipment. It comprises a structure that is 8.4 meters wide by 80 meters in length and is located over the proton beam window (PBW) region, the target region, and the decay channel. The 16 GeV proton beam-target interaction produces significant levels of neutrons and neutron-induced gamma activation; herefore, the facility requires significant shielding, provisions for remote handling equipment, and a hot cell. The radiation handling equipment that is used to replace the target and remotely handle life-limited components is arranged to have minimal impact on the facility design. A linear crane hall provides lift coverage to the areas over the target region, the decay channel, and the hot cell. There is ample laydown space for storing shield blocks that are removed to gain access to components in the target region and the decay channel. A 40-ton bridge crane and a bridge-mounted manipulator operate along the full length of the crane hall.   Figure 5 is a cutaway view of the overall facility.

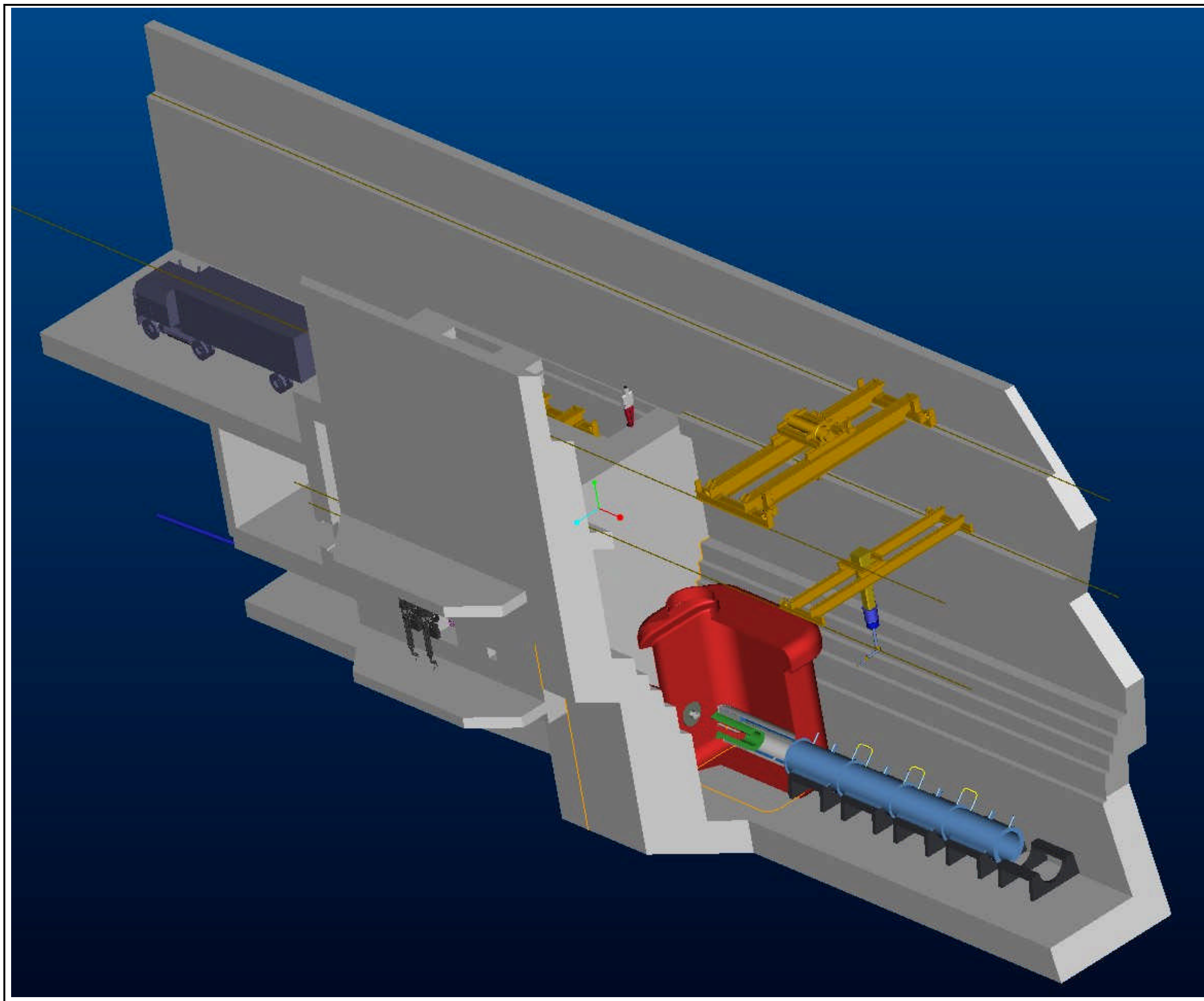

Figure 5. Overview of the Target Support Facility.

4.4.1 Design Requirements and Assumptions

The shielding for the target area is designed for a 16 GeV, 4 MW proton beam, although initial operations will be at 1.5 MW. The Neutrino Source Facility should have an operating availability of 2 x 10^7 s/y for all systems; therefore, annual downtime for scheduled and unscheduled maintenance activities, including those of the Target System, is 133 days per calendar year.

The major components in the Target Support Facility consist of components that are expected to survive for the life of the facility, i.e. >20 years, and life-limited components that require periodic replacement. Table 2 lists the expected component lifetimes based primarily on radiation damage criteria and a preliminary allocation of downtime for their replacement. The life-limited components greatly influenced design of the Target Support Facility. The design also utilizes the extensive Oak Ridge National Laboratory (ORNL) experience with high beam power target facilities[4].

Component	Expected Lifetime	Replacement Time
Target	3 mos	6 days
Target + Bitter Coil	6 mos	7 days
Target +Bitter Coil + PBW	1 yr	8 days
PB Instrumentation	1 yr	5-7 days
Beam Dump	5 yrs	1.5 mos
High Field S/C Coils	>20 yrs	9-12 mos
Low Field S/C Coils	>20 yrs	9-12 mos

Table 2. Component Lifetimes for the Target Support Facility

4.4.2 Target Region

The target region is the focus of remote handling activities that occur every three months. It consists of a helium-atmosphere vessel that contains steel shielding, a passively cooled graphite target module, a high field solenoid magnet assembly and the proton beam window. The vessel is approximately 4 x 6 x 7 meters with a removable lid. The smaller 2 meter diameter port on the lid is removed for routine replacement of the components listed in Table 2. The large lid can be removed if a superconducting coil in the first cryostat module ever needs replacing. The magnet assembly consists of a demountable resistive solenoid (Bitter coil) that is replaced every 6 months, a lifetime tungsten/steel shield, and a lifetime superconducting solenoid. These components are contained in a helium atmosphere. The He atmosphere prevents air-activation when the proton beam is on and minimizes evaporation of the graphite target.

The target is a graphite rod 1.5 cm diameter x 80 cm long, held in place by two spoke-like graphite supports, in a 15 cm diameter stainless steel support tube. The target is radiatively-cooled to the water-cooled surface of the support tube. The axis of the target is parallel to the proton beam line but is oriented at 50 milliradians relative to the axis of the support tube. The support tube is aligned with the magnetic axis of the solenoid coils and is mounted into the bore of the Bitter coil. (Therefore, the overall axis of the target support facility has a 50 milliradian offset to the proton beam tunnel, in the horizontal plane.) Figure 6 is a cutaway view of the target module mounted in the solenoid coil structure.

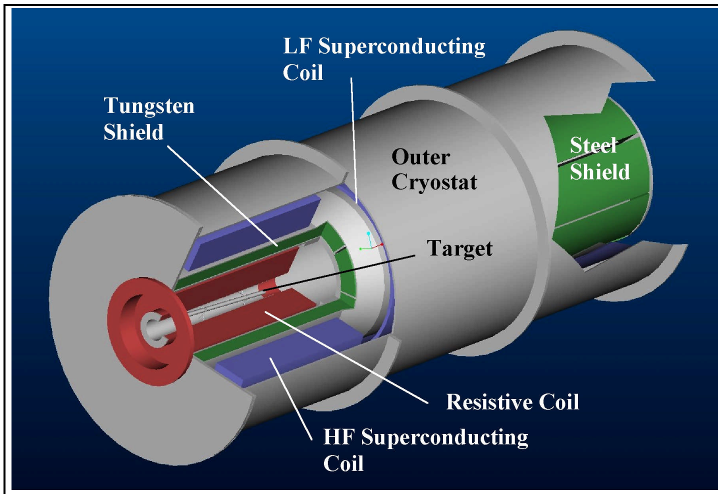

Figure 6. Cutaway view of the high-field solenoid, target, and shielding in the cryostat module.

Preliminary analysis of the target indicates that radiative cooling and low thermal stresses are achievable for a beam power on target of up to 1.5 MW. For a uniform heating distribution throughout the target, internal thermal stresses were determined to be 1/5 the strength of graphite. Most probably, radiation damage will limit the target lifetime. A damage criterion of 5 displacements per atom (dpa) was chosen to be a reasonable limit; this equates to approximately 3 calendar months before the target must be replaced. (Sublimation of the target is not an issue since it operates at a temperature of about 1850^0 C and is in a He environment.) Additional analysis is required to better understand an important remaining issue, shock wave effects from the 3 ns duration beam spill.

The Bitter solenoid is mounted within the bore of a tungsten radiation shield. The shield limits neutron heating to the high field superconducting coil (HFSC), protects the coil from radiation damage, and because of its high density, minimizes the diameter of this costly superconducting magnet. The shield is a stainless steel structure filled with water-cooled tungsten-carbide balls under the HFSC, but contains steel balls under the other three coils. The HFSC and the first three low field coils are assembled in a common cryostat located within the He vessel. Figure 6 shows the arrangement of the coils and shielding. Use of a common cryostat was employed so that the coil-to-coil axial magnetic forces could be reacted within the cryostat, thereby avoiding external structure with its inherent thermal leaks to the coils.

The target is surrounded by steel shield blocks, which limit the prompt radiation effects to the surrounding area. Two meters of steel are required on the sides and bottom of the target module to meet the requirement for ground water protection, and approximately 4.5 meters of steel and 0.5 meter of concrete are needed above the target to limit the dose rate at the crane hall floor to 0.25 mr/h.

4.4.3 Decay Channel

The 50-meter long decay channel is a tunnel-like structure below the crane hall, located under approximately 5 meters of removable shield slabs. Figure 7 shows a cross section of the decay channel. The shield slabs are removable to gain access to the 12 cryostat modules that each contain 4 low field superconducting coils (LFSC). Under normal operations the decay channel does not require access since the LFSC are lifetime components. Each of the cryostat modules are mechanically joined together so that the inner cryostat surface makes up the vacuum boundary of the muon decay channel, but the outer cryostat surface is in an air atmosphere. The LFSC cryostat modules are similar to that shown in Figure 6.

The low field solenoids are protected from nuclear heating and radiation damage by a 30 cm thick, water cooled stainless steel shield. The first low field cryostat in the decay channel also contains a beam dump at $5.5<Z<6.5$ meters to absorb the portion of proton beam that passes through the target. In this region, the LFSC may require a diameter larger than the adjacent coils to accommodate the thickness of the beam absorber module, coolant lines and a suitable nuclear shield thickness. Downstream of the beam dump at the end of the first low field cryostat, a 60 cm diameter titanium window is in place to separate the helium atmosphere from the vacuum in the remainder of the decay channel. The shield requirements in the decay channel are virtually the same as those in the vicinity of the target because of the large diameter of the muon channel. Access into the decay channel requires lifting shield slabs weighing up to 40 tons and storing them in the crane hall.

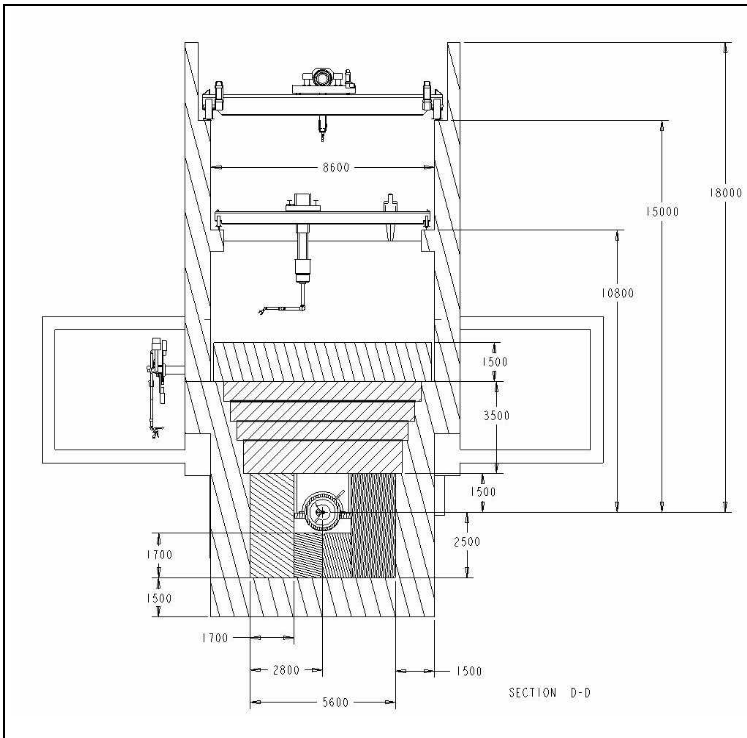

Figure 7: Typical cross section of the Decay Channel

4.4.4 Crane Hall and Hot Cell

The crane hall is located over the entire target support facility. It is 12 meters above the floor level, 80 meters long and contains a 40-ton overhead crane and a bridge-mounted manipulator system. The floor of the hall consists of removable shield slabs that provide access into the target region and the decay channel.

The hot cell contains a 20-ton bridge crane, overhead manipulator, through-the-wall manipulator, shield window, and CCTV and lighting. There are provisions to add up to three additional wall manipulators and windows. The hot cell size is determined by the floor space needed for the routine replacements shown in Table 2 plus handling a 4 meter long cryostat for the possible replacement of a solenoid coil. The operations in the cell are primarily handling the rad waste created by periodic replacement of the target, Bitter magnet, and proton beam window. These life-limited components are not repairable due to the nature of their radiation damage and are temporarily stored in the hot cell prior to disposal. They are brought into the hot cell with the 40-ton crane by removing any of the three roof plugs. The hot cell floor contains shielded storage areas for up to 4 targets, 2 Bitter coils, and 1 proton beam window. The hot cell is partially located over the proton beam tunnel and has floor plugs that provide access to the proton beam focusing magnets/instrument module. Remote replacement of the instrumentation on this module is done in the hot cell annually.

4.4.5 Remote Handling

Remote handling operations are required on all of the components located in the target region and the decay channel. However, when the crane hall floor shielding is in place, unlimited personnel access is permitted in the crane hall even with the beam on. This is the most cost-effective way to design the shield since meeting site-boundary radiation criteria are efficiently met by placing shield material as close to the source of radiation as possible.

4.4.6 Equipment

The equipment for lifting and remotely handling components listed in Table 3 is determined by their weight and size. For example, the crane capacity is established by the high field cryostat module, which is the heaviest component that could require handling during the facility lifetime. Table 3 is a listing of the size and weight of the key components.

The bridge-mounted manipulators located in the crane hall and hot cell are commercially available, single arm, dexterous, force reflecting systems. They are used in conjunction with special fixtures for lifting and handling the target module, Bitter coil, PBW, etc. These manipulators are operated from control stations located in the hot cell gallery and their operations require remote viewing. The through-the-wall manipulator in the hot cell is used in conjunction with a shielded viewing window for operations that can be done at a work station.

4.4.7 Operations

The maintenance philosophy for dealing with the life-limited components is to replace them at scheduled intervals with new modular components. Since they are not repairable, they will be handled as rad waste. Therefore, the need for special purpose tools and handling fixtures is minimal. Furthermore, almost all of the components that require periodic replacement are located in the target region; hence, many of the remote handling tasks are common. As a result, a preliminary estimate of downtime to replace life-limited components (Table 2) was found to be within a reasonable allocation of time for scheduled maintenance activities.

Component	Weight (lbs)	Size (m)
HF Cryostat	72,500	1.5 dia x 4.2
HF S/C Coil	18,000	1.5 dia x 1.2
Tungsten Shield Module	44,000	1.0 dia x 4.0
LF Cryostat/Steel Shield	44,000	1.3 dia x 4.0
Steel Shield Slabs	72,000	0.4 x 1.0 x 3.0
Vert. Steel Shield Blocks	28,000	0.6 x 1.2 x 2.0

Table 3. Component Weights and Sizes

The typical tasks for replacing the target, Bitter coil, and PBW are as follows:

- remove the stacked shielding above the He vessel (crane and personnel)
- remove the 2-meter port cover (crane and personnel)
- decouple water connectors for each steel shield block and remove the blocks that surround the target (this task and the remainder are remote)
- decouple instrument and water line connectors to the target, unbolt the target module, disengage and remove with the bridge manipulator
- decouple instrument connectors and water lines to the Bitter magnet, unbolt from the tungsten shield flange, engage a crane-mounted handling fixture for removal
- decouple instrument connectors and water lines to the PBW, disengage the commercial remote-connector with manipulator tools, remove with the bridge manipulator and holding fixture
- replacement of these components follows the reverse order.

4.5 Summary

Current design status of the target system and support facility provides a system plan for targeting a 1.5 MW beam, and providing a solenoid magnetic field focusing system which meets rigorous design requirements, including 20 T target region fields. Support facility design will enable safe handling of components and environmental protection for the severe radiation conditions encountered. While new capabilities beyond current state of the art are not required, significant "engineering" type R&D efforts are needed for better understanding of graphite target survivability, beam absorber design, and magnet radiation tolerance.

We would like to address these issues beginning with a near term focused R&D program. This effort is complementary to the R&D plans now underway with the Brookhaven National Laboratory (BNL) experiment E9511 [5].

REFERENCES:

[1] N.V. Mokhov, 'π/μ Yield and Power Dissipation for Carbon and Mercury Targets in 20-Tesla Solenoid with Matching Section', Mucool Note MUC0061 (1999), http://www-ap.fnal.gov/mokhov/mumu/target99/muc0061 and updates at http://www-ap.fnal.gov/mokhov/mumu/target00.

[2] N.V. Mokhov, 'The MARS Code System User Guide, Version 13(95)', Fermilab-FN-628 (1995); N.V. Mokhov et al., Fermilab-Conf-98/379 (1998); LANL Report LA-UR-98-5716 (1998); nucl-th/9812038 v2, 16 Dec 1998; http://www-ap.fnal.gov/MARS/.

[3] J.R. Miller et al., Teion Kogaku (Cryogenic Engineering – Japan), 31 (1996) 240, J.R. Miller, 'The Superconducting Outsert for the NHMFL 45 T Hybrid Magnet System', abstract to Applied Superconductivity Conference, Virgina Beach,VA, 17-22 Sep 2000.

[4] Spallation Neutron Source Design Manual, Chapter 6, Target Systems, 12 Oct 1998, http://www.ornl.gov/sns/dm/DesignManual.html .

[5] An R\&D Program for Targetry at a Muon Collider, J.Alessi etal, proposal to the BNL AGS (Sept. 1998); also:

[6] http://puhep1.princeton.edu/mumu/target/targetprop.ps

5. π-Decay, μ-Capture and Bunching Section

5.1 Introduction

Following the target, each proton bunch from the four bunches extracted from the proton driver produces a cloud of pions that is transported downstream within a focusing channel, where the pions decay to muons following $\pi \to \mu + \nu$. The initial pions, and the product muons, are produced with a large energy spread. Due to this energy spread the length of the beam bunch increases in this transport and a longitudinal position-energy correlation develops with the lower-energy end of the beam trailing behind the higher-energy muons. This energy spread is much larger than the acceptance of the following cooling system. The plan is to reduce this energy spread by an acceleration system that decelerates the high-energy head of the bunch while accelerating the low-energy tail, obtaining at the end of this "phase-rotation" system a beam with minimal energy spread and a relatively long bunch length.

In the previously developed μ^+-μ^- collider scenarios [1], the phase-rotation system was constrained by the need to keep the entire muon beam from an initial proton bunch within a single bunch throughout the system. The bunch length had to be short, in order to fit into the longitudinal acceptance of the cooling and bunching system which was based on ~30MHz rf. For a neutrino source, the long bunch can be split into a string of higher-frequency bunches (with that frequency matched to the following acceleration systems) [1].

In the ν-source, a phase-rotation system is used to obtain a very long bunch and that greater length coupled with a long acceleration pulse (obtained from an induction linac) obtains a much-reduced energy spread. The long bunch is then inserted into an RF system, which forms the beam into 201.25 MHz bunches matched to the following cooling system. A design goal of the present scenario is to obtain an energy spread small enough so that the following cooling system can capture and cool a maximal number of muons without any additional energy cooling.

5.2 Baseline Scenario Description

A schematic overview of the precooling decay, RF capture and bunching section is displayed [2] in Figure 1. It shows a 50m decay channel following the target and capture solenoid. This channel is matched into an induction linac phase-energy rotation system (100m long), which is followed by a "minicool" energy absorber (2.45m of liquid hydrogen), and a bunching section (16.4m long) matching the beam into a 201.25 MHz cooling system. Simulation results are displayed in Table 1.

A critical parameter for this channel is the total voltage difference that can be provided by the induction linac, since that also determines the energy range which can be accepted by the capture system. Our baseline scenario contains a voltage difference of 200 MV (+150 to –50 MV). With that range, we can accept the $\pi\to\mu$ particles with energies centered about the maximal production energy of ~130 MeV kinetic energy, obtaining an acceptance range of about 30 to 230 MeV. The transverse focusing magnets and the apertures are selected to accept most of the particles produced within that energy range. The acceptance of the overall system is matched to the precooling design goal, which is to provide ~0.1μ per initial proton from the target to the cooling system, and our simulations

Region	**Position**	**π+μ/proton**	**E-window**	**$\varepsilon_{t,n}$(mm)**	**σ_x(m)**	**σ_{px}(MeV/c)**
After Target	0	0.242	<500 MeV	15.1	0.090	23.0
Decay Channel	47 m	0.226	<500 MeV	15.9	0.092	22.5
Matching (D)	50 m	0.222	<500 MeV	16.5	0.057	34.2
Induction Linac	150 m	0.191	<450 MeV	16.3	0.060	44.9
"Mini-Cool"	153.45 m	0.191	<375 MeV	12.6	0.055	32.6
Buncher(all μ's)	170.9 m	0.188	<375 MeV	12.4	0.046	32.2
Buncher (in bucket)	170.9 m	0.123	In bucket	12.0	0.046	31.4

Table 1: Beam Properties along the Capture and Bunching Section.

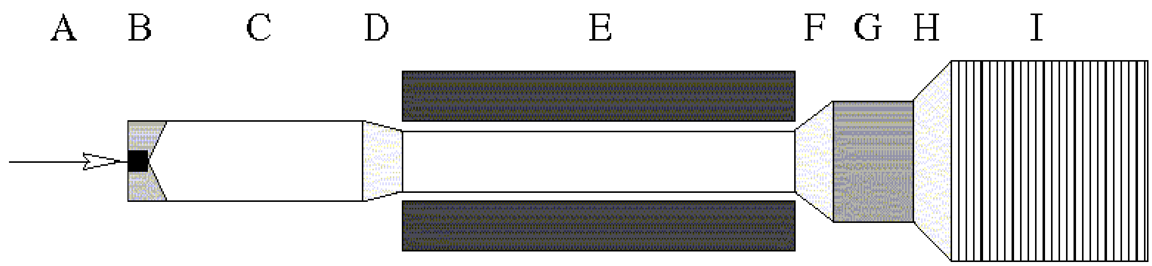

Figure 1: Schematic overview of the $\pi \to \mu$ production, capture and bunching system, showing:

A: proton beam (16 GeV, 4bunches)
B: Target station (Carbon target)
C: Drift- $\pi \to \mu$ decay region (L=47 m, B=1.25 T)
D: Matching section (L=3 m)
E: Induction Linac (L=100 m, B_{ave} = 3T, V′ = -0.5—1.5 MV/m)
F. Matching section (L=1 m)
G: Minicooling (2.45m liquid H_2, B = 5 T)
H: Matching section (L=1m)
I: Buncher (L=16.432 m, B=5 T, includes three 2 m RF accelerating cells)
(Lengths of sections are not to scale.)

show that performance at this level should be possible.

In the following subsections we describe the various subcomponents of this "precooling" system in greater detail: the decay channel, the induction linac, the minicooling section and the buncher, and discuss matching into the following cooling section. Results of tracking simulations will be presented to estimate the performance of the various sections [2][3]. The simulation results are summarized in Table 1 and these results are discussed in the remainder of the chapter.

5.2.1 The Decay Channel

As discussed in the previous section, in the baseline scenario 16 GeV proton beam bunches collide with a 0.8m long graphite (C) target, that is immersed in a 20 T solenoidal focusing field. π's produced in the target are captured in the solenoidal field and directed into a decay channel for $\pi \to \mu + \nu$ decay. The focusing solenoidal field is gradually reduced to 1.25 T over a ~3m transition region, while the transport region radius is increased to 30cm. At the end of transition region ~0.242 $\pi + \mu$ per initial proton are both within the energy acceptance cut (E < 500 MeV) and captured within the transport. The rms transverse emittance matched into the decay channel is ~15 mm, corresponding to a beam size of $\sigma_x = \sigma_y \cong 9$ cm, and $\sigma_{Pt} \cong 30$ MeV/c. The decay channel immediately follows this transition region.

The decay channel consists simply of a long large-diameter beam pipe with a 30cm radius and with a solenoidal focusing field of 1.25 T. In the present baseline, the total length of this decay channel is 50 m, including a final 3 m subsection for matching into the following induction linac.

By the end of the 50m decay channel section, ~95% of the π's in the initial beam have decayed to μ's. Simulations show that very few (< ~10%) of the initially captured $\pi + \mu$'s (compared to 3 m after the target) are lost in this section. The transverse momentum introduced by decay is smaller than the intrinsic beam momentum spread and adds little to the beam emittance. The transverse emittance increase is only ~10% to $\varepsilon_{t,rms} \cong 16.5$ mm.

Figure 2 shows projections of the beam phase space distribution at the end of the decay channel. The initial energy spread of ~300 MeV is stretched over a ~50 m length. The transverse phase space projections (x-P_x and x-P_y) are also displayed.

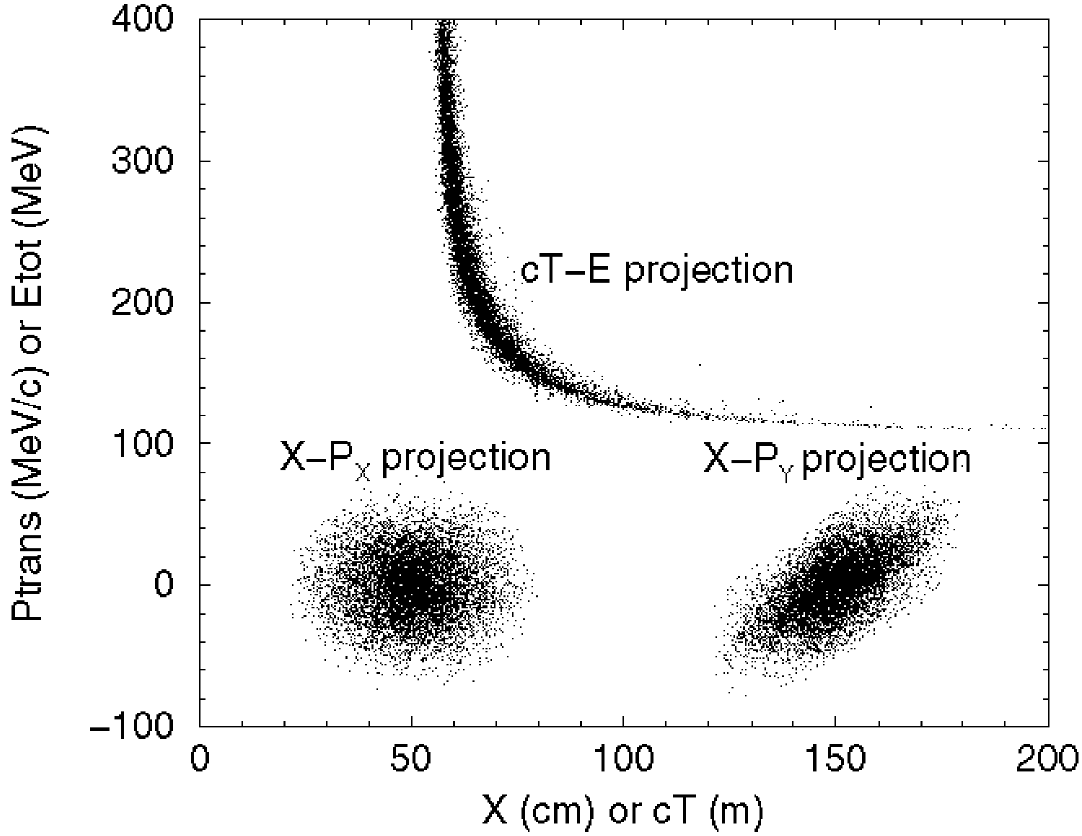

Figure 2: Beam at the end of the 47 m decay channel. Three projections of the 6-D phase space distributions of a simulated beam are displayed. The cT-E projection shows the energy-dependent bunch lengthening. The X-P_x projection indicates the beam phase-space size ($\sigma_x \cong 9$ cm, $\sigma_{Px} \cong 22$ MeV/c). The X-P_y projection indicates the beam angular momentum associated with the 1.25T solenoidal focusing field.

At the end of the decay channel the focusing magnetic field is gradually increased from 1.25 T to 3 T over a 3m length, while the beam transport radius is reduced from 30 cm to 20 cm. This change matches the beam dimensions and focusing system to that used in the following induction linac capture system. Figure 3 shows a cross section of this matching section. The rms beam size is reduced from $\sigma_x = \sigma_y = 9$ cm in the decay channel to ~5.7 cm at the end of the matching section. This fits easily within the 20 cm radius aperture of the induction linac.

5.2.2 The Induction Linac

The decay channel is followed by an induction linac. The channel consists of 100 1m modules of the form displayed schematically in Figure 4. Each module has an accelerating gap of 10cm, which provides an accelerating voltage of between –0.5 and 1.5 MV to the particles. The focusing, longitudinal magnetic field is provided by an array of superconducting solenoids placed in separate cryostats inside the induction modules. The gaps between the cryostats are shaped to serve as accelerating gaps

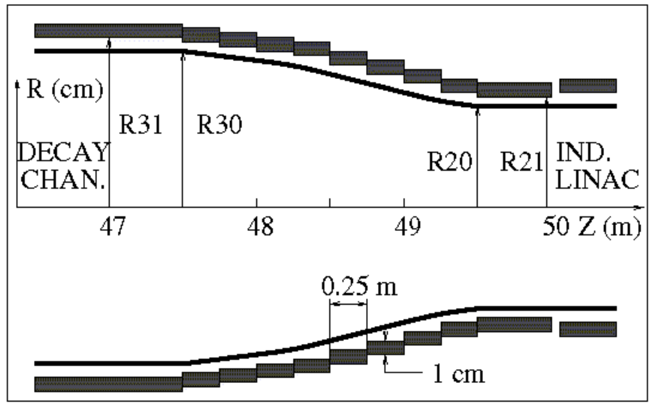

Figure 3: The 3m long matching section between decay channel and induction linac. Focusing solenoidal field increases gradually from 1.25T to 3T, while the aperture reduces from 30cm radius to 20cm radius.

Figure 4 shows cylindrical coils with 22.2 cm inner radius and 1.46 cm thickness separated by the induction gap of 14 cm length and spacers of length a. Cylindrical magnetic induction cores surround these coils. The coils provide a mean focusing of 3 T on axis, with a periodic fluctuation of ~10% due to the coil position. The 1 m, ~3 T periodic focusing system has betatron oscillation resonance's for ~200 MeV/c particles, which would lead to particle losses. However, these resonances are eliminated if the inter-coil spacing length is chosen to be a=14cm, the same as the induction gap coil spacing. This changes the transverse focusing period to 0.5m and removes the medium energy resonance condition [2]. A preliminary engineering layout of an integrated superconducting coil will be discussed later on (see also Figure 12).

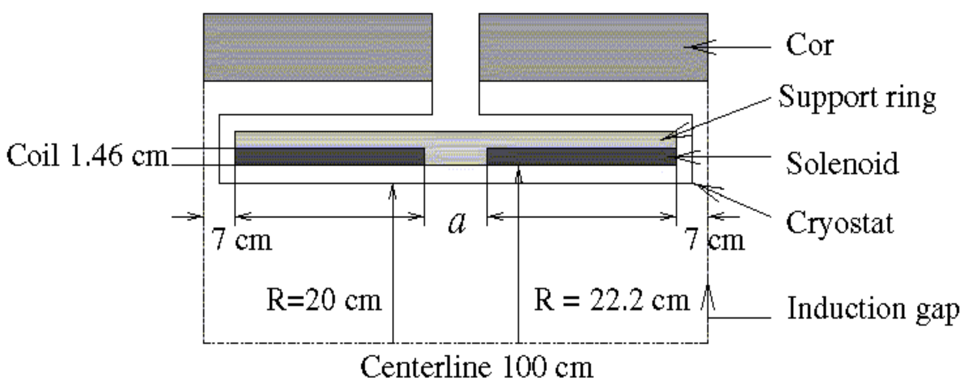

Figure 4: Schematic cross section of an induction linac cell.

The cores are excited by a waveform matched to the beam energy-phase distribution, with a voltage range from –0.5 MV/gap for the high-energy head of the bunch to ~1.5 MV for the low energy tail. This asymmetric form, which accelerates the beam centroid by ~0.5 MV/gap, was chosen as a preferred mode for the pulse forming network, since it facilitates a fast reset of the cores, which enables sequential very fast excitation of the 4 primary bunches [3][4]. The pulse lengthens from 150 ns to 200 ns along the linac, matching the bunch lengthening. Figure 5 shows the desired module waveforms along the linac (from gap 1 to 100).

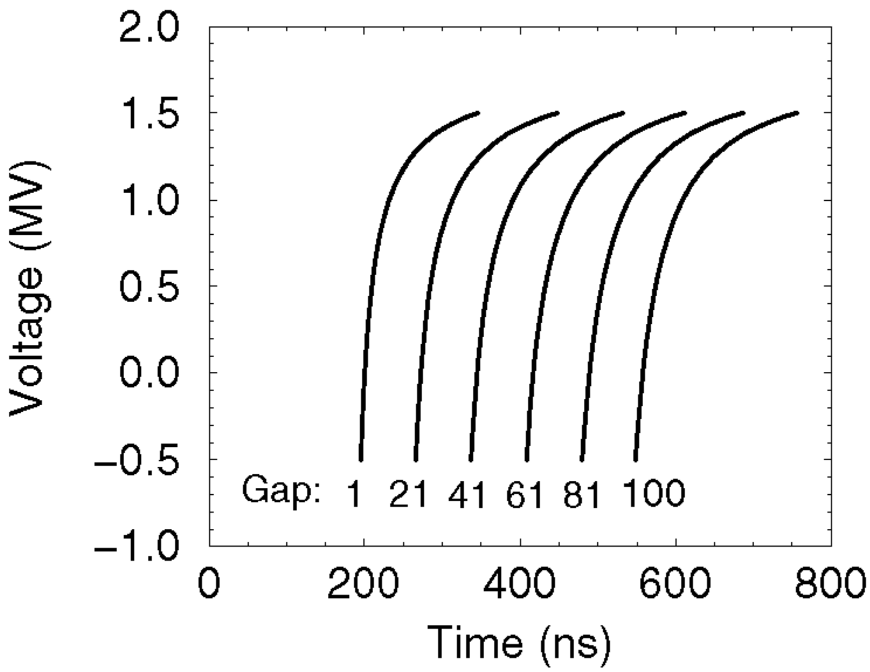

Figure 5: Induction Linac waveforms along the induction linac. Pulses for gaps 1, 21, 61, 81, and 100 are displayed.

Energy-phase distributions of the beam along the induction linac are displayed in Figure 6. The bunch lengthening with energy spread flattening of the captured beam is displayed. A core of a beam with a full energy width of ~300 MeV and a bunch length of ~50 m (with a curved position-energy correlation) is phase rotated into a ~80 m long bunch centered about ~280 MeV beam energy (~175MeV kinetic energy) with a full-width of ~100 MeV. The

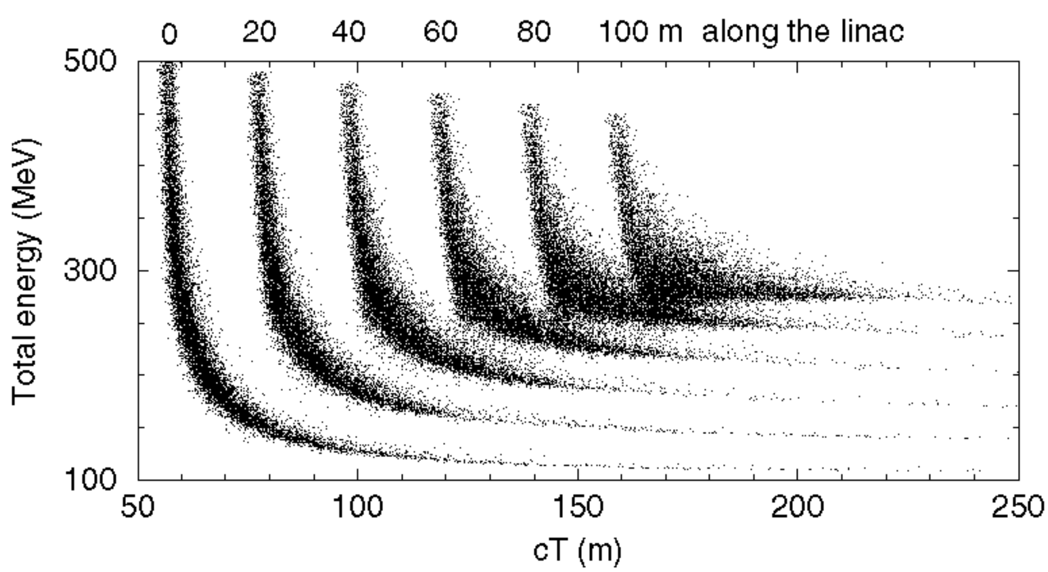

Figure 6: Beam distributions in E-cT phase space along the induction linac. Distributions from L = 0, 20, 40, 60, 80, and 100 m are shown.

width is correlated with position along the bunch, but the mean beam energy is not. About 10% of the initial beam is lost in the transport. The beam transverse emittance and beam size are approximately unchanged in the RF rotation. The rms transverse emittance ε_T remains at ~16 mm (rms, normalized) while the beam radius remains $\sigma_x \cong 6$ cm.

In the baseline design a string of 4 proton bunches, spaced by ~500 ns, is sent onto the target. The induction cells must provide approximately identical waveforms for the muons from each proton bunch coming from the proton driver. Thus, the induction cells must be driven by a 4-pulse waveform, with each pulse ~150—200 ns long, spaced by 500 ns. Note that the four-pulse design at these parameters was selected because it is estimated that this was within demonstrated induction linac capabilities [6]. The induction linac itself will be discussed in greater detail later on in this chapter.

5.2.3 "Minicool" Absorber Section

At the end of the induction linac the mean beam kinetic energy is $T_\mu \sim 175$ MeV (total energy $E_\mu \cong 280$ MeV), while the following bunching and cooling section is designed for muons with a kinetic energy of ~100 MeV. In order to match these central energies the beam passes through an energy-loss absorber. This absorber also provides some transverse cooling.

Following the induction linac a 3 m transition region is placed with coils matching the beam optics into a solenoidal magnetic field of 5 T at the absorber. The physical aperture is increased to a radius of 30cm to minimize possible losses. The absorber is a 2.45 m long liquid H_2 bottle, which lowers the mean beam kinetic energy from 175 MeV to 100 MeV. Simulations show that this insert decreases the rms transverse emittance $\varepsilon_{t,rms}$ from 16.4 mm to 12.4 mm. However, the rms energy spread is somewhat increased by the absorber. Figure 7 shows the longitudinal (E-cτ) phase space distributions of the beam before and after the minicool insert; the energy spread increase is not large compared to the large intrinsic beam energy spread.

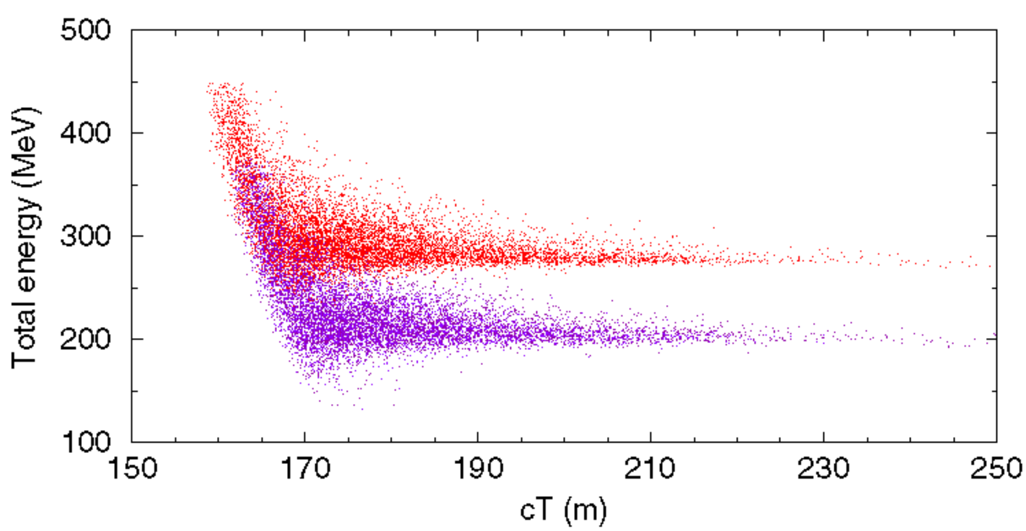

Figure 7: Longitudinal phase space distributions of the μ-beam before (above, red) and after (below, violet) the minicool energy loss insert.

In our baseline scenario the "minicool" energy loss is used primarily to reduce the central energy of the phase-rotated beam to that of the cooling channel, but it also provides some initial transverse cooling. If a longer energy loss section is used, more transverse cooling is obtained and the beam energy could be lowered to the level where an adiabatic capture and acceleration with a 201.25 MHz section can match the beam energy to the cooling rf. However, at present parameters the energy spread of the beam is initially large and energy loss at low energies would increase that energy spread far beyond the acceptance of the cooling channel. This limitation could be removed if energy cooling were incorporated into the scenario.

5.2.4 Buncher

After the mean energy is reduced by the "minicool" absorber to the cooling kinetic energy of $T_\mu \cong 120$ MeV ($P_\mu \cong 200$ MeV/c), the bunches from the induction linac must be formed into 200 MHz bunches. Several scenarios for transforming a long-bunch beam from the induction linac into a string of short bunches have been proposed and these options have been described in [8]. The optimal scenario depends on the beam properties at the exit of the induction linac as well as the beam cooling scenario requirements. Two styles of matching have been considered:

- An adiabatic match obtained by gradual bunching of the beam with 200 MHz RF. This can be done at a fixed energy corresponding to the mean μ capture and cooling energy, or by lowering the energy to a level where the beam longitudinal motion is enhanced, and then bunching and accelerating the beam to cooling energy. An adiabatic match could minimize phase space dilution, and maintain a small longitudinal phase space.

- A short bunching RF section followed by a drift in which bunch length is minimized to match the cooling acceptance. This drift incorporates transverse matching. This option can be modified to include multiple steps (2 or 3).

Since in the baseline scenario (as currently implemented) the beam energy spread (and longitudinal emittance) is large and not well matched to adiabatic scenario parameters, we have decided to minimize length and cost of the buncher by choosing a short buncher scenario as our baseline.

The buncher used in the baseline scenario is displayed schematically in Figure 8. It has a total length of 16.4 m and contains three 1.944m 201.25 MHz RF modules. The longitudinal beam distributions at the end of the buncher are displayed in Figure 9. It shows the longitudinal distribution of the entire beam; the 201 MHz structure can be seen. The energy width of the beam has been increased, but the degree of increase depends upon position along the bunch. The RF system has partially formed the ~80 m long beam distribution into a string of about fifty 201 MHz bunches. Figure 9 also shows the distribution folded over the 201 MHz period. A 201MHz RF bucket corresponding to the estimated acceptance of a $E_\mu \cong 200$ MeV, f=201MHz cooling system is displayed overlapping the distribution. About 2/3 of the μ's are within that acceptance.

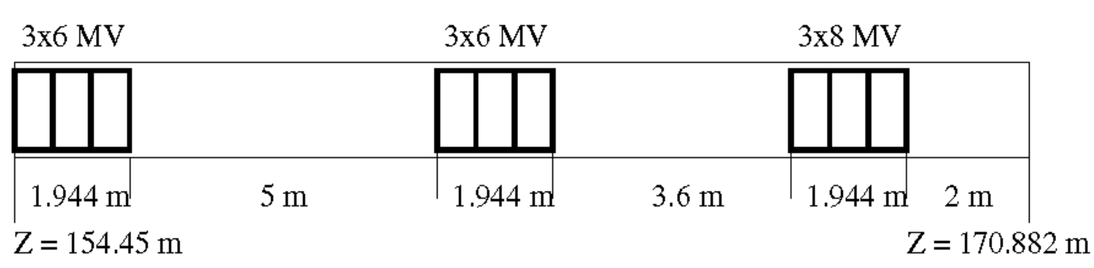

Figure 8: Buncher layout, showing three RF insertions distributed over a 16.5 m length**.**

At the end of the buncher the beam is matched into a 5 T focusing system, and has a transverse emittance of $\varepsilon_{t,rms} \cong 12$ mm. Longitudinally the beam overflows the expected acceptances of the cooling channel. However, ~0.123 μ per initial proton are within that acceptance, indicating that the precooling section is able to meet the goal of ~0.1 μ/p.

This buncher has not yet been fully optimized. Ref. [8] discusses some of the possible variations, and these will be studied in more detail. Some significant improvements may be expected from future parameter optimization studies, which will include more complete integration with the upstream phase rotation and downstream cooling systems.

5.2.5 Integration with Cooling Section

The optimal beam capture and bunching parameters depend critically on the acceptance and parameters of the downstream cooling and acceleration sections. The cooling channel and some of its design options are described in more detail in the following cooling chapter.

If there is no energy cooling in the scenario, the most critical parameter in downstream acceptance is the longitudinal emittance for the beam entering the cooling channel. A cooling channel has a longitudinal acceptance corresponding to an rf bucket determined by the average accelerating gradient eV′ and stable phase ϕ_0 set such that the energy gain (eV′ sinϕ_0) cancels the mean energy loss rate from absorbers. Figure 9 shows a cooling bucket acceptance superimposed on a simulated μ-distribution. The smaller size of the bucket implies a significant design mismatch.

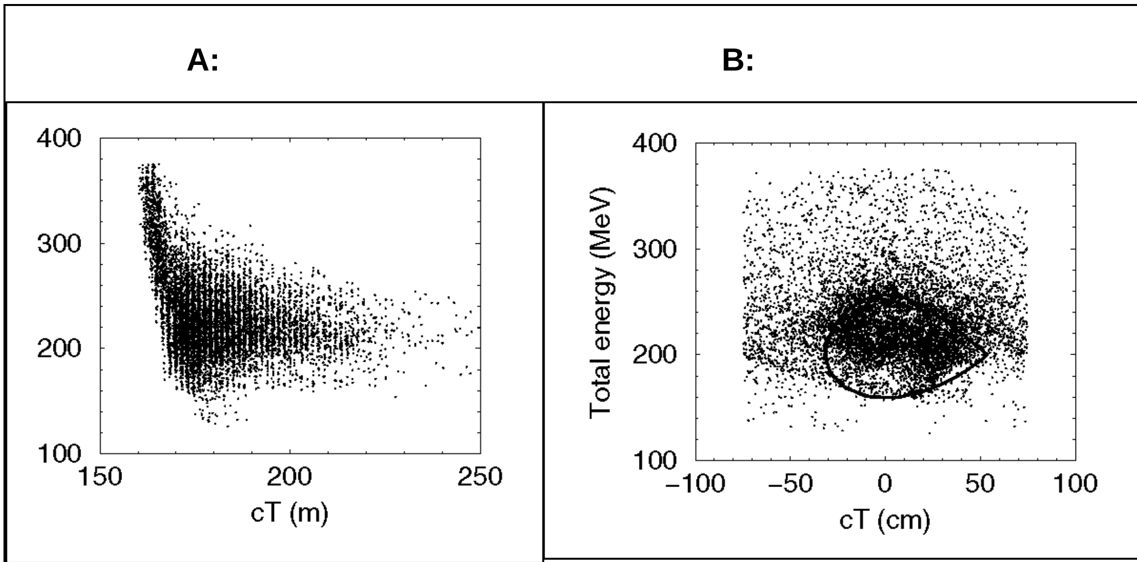

Figure 9: Beam distributions in energy –distance coordinates. A shows the full beam length; B shows the distribution folded over the 201.25 MHz periodicity, with an RF bucket for 200 MeV, 200 MHz cooling.

In the present example we have centered the final beam energy of the precooling section at $E_\mu \cong 200$ MeV, since that is the expected energy for the cooling channel. However it is not known whether that is an optimum cooling energy. A larger longitudinal acceptance with less longitudinal heating would be obtained by a higher energy cooling system; however, it would also have a reduced cooling rate. Variation of the cooling energy within the context of global scenario optimization would be an important goal of future research. Other parameters of the precooling (and cooling) systems may also be varied to improve the match.

5.2.6 Discussion: Variations and Alternatives

A number of variations and improvements on the baseline scenario could be considered and studied. Many of these could improve μ-acceptance. In addition to incremental improvements, greatly different μ-capture scenarios (using different technologies) could be considered. We first consider some incremental improvements.

The present precooling scenario has been shown by simulations to provide ~0.12 μ per initial 16 GeV proton into the acceptance of the cooling channel from an initial Carbon target. Optimization of this scenario should continue with the attempt to increase the yield as much as possible without increasing technical complexity of the system significantly.

One critical parameter (discussed above) is the target material; a high-Z target could provide up to twice as many μ's from the same primary beam. However, because of the much more demanding technology that would be required to build and operate high-Z targets, they are not considered for this study but do provide an obvious upgrade path.

Acceptance could be somewhat improved by increasing the voltage bandwidth of the RF capture system, although the current bandwidth does cover the production peak. Increasing the induction linac voltage range from 200 MV to 300 MV could increase the number of accepted μ's by ~25% but would lengthen the induction linac by 50%.

The energy spread at the end of the precooling region can be reduced by lengthening the decay channel + induction linac system (including lengthening the induction linac pulse beyond 200 ns). In principle the energy spread can be reduced inversely proportional to the final macrobunch width. (For example, A. Van Ginneken has presented a simulation that obtains an energy spread a factor of two smaller, when using a 200 m decay drift together with a 400 ns induction linac pulse. [9])

The energy spread (and longitudinal emittance) at the end of the induction linac, and the subsequent energy spread after the 200MHz buncher, is much larger than desired for the cooling system, and is significantly larger than the longitudinal acceptance of the cooling channel. Thus large particle losses occur at the beginning of the cooling channel. The difficulty is exacerbated by the fact that the cooling system increases the energy spread (and longitudinal emittance), which means increased beam losses in the cooling system. Modification of the capture section to reduce energy spreads (with further scenario optimization and/or more acceleration modules) and modification of the cooling system to include some energy cooling would both be very desirable.

An alternative collection system is described in the PJK scenario [10] and more recently in an updated version of [10]. This scenario begins with a low frequency rf capture section, obtained by 42m of 30—90MHz RF at (~5 MV/m), immediately after the target. This initial capture section obtains a ~1.5m long (rms) μ-bunch with ~15% rms momentum spread. This is followed by an energy loss "minicool" section, a drift section (~100m), and an induction linac (~100m), to obtain a long bunch with much smaller energy spread. Since this system has more total rf capture voltage, and has an initial rf capture section reducing the energy spread closer to the target, the capture efficiency will be larger. Recent calculation indicate [11] that total efficiency could be up to 0.15μ/proton. The final energy spread will be somewhat smaller than our baseline scenario. Also, this RF enables better sorting of the beam polarization, obtaining higher initial μ-beam polarization (25→45% or so). However, the PJK scenario adds significant complexity and power requirement to the capture scenario, requiring development and construction of 30—80 MHz RF systems as well as induction linacs, which will increase risk and cost.

The present scenario uses induction linac systems, which have the great advantage that the acceleration waveform can in principle be tailored to match the phase-energy distribution of the beam, and thereby provide an ideal phase-rotation system. However it is possible that the actual performance of an induction linac system may be deficient in acceleration waveform quality, gradient, reliability, and/or lifetime or simply be too expensive. Alternative acceleration systems such as the ~30 MHz RF system used in the baseline μ^+-μ^- Collider scenarios could be used, without an additional induction linac. Recently scenarios using ~5MHz RF systems (at ~1MV/m) have also been suggested, and are investigated [12]. These (higher-frequency) alternatives may not develop energy spreads as small as those that can be developed from very long induction linac pulses; they may require additional energy cooling in a complete scenario.

5.3 The Technical Design of the Induction Linac

Since the induction linac modules are the primary component of the precooling (phase-energy rotation) system, we include a more detailed discussion of the properties of these modules. Several designs for such an induction linac [4] have been presented and different designs for pulse power production have been studied[5][6]. Figure 10 shows a detailed view of an induction linac module from ref. [4], including acceleration and focusing components. Some parameters are included in Table 2. The 1 m long induction module consists of a set of toroidal magnetic cores surrounding an induction gap. A pulser sends high-current pulses to the module that change the core magnetic fields, and the changing magnetic field generates an accelerating voltage across the induction gap. As compared to the design discussed in the first part of this chapter technical detail, like for example the exact cell length etc may vary. This is a result of the ongoing optimization with the technical design going on simultaneously.

The induction module includes a 3 T solenoidal field for transverse beam focusing. To minimize the leakage of magnetic field into cores (to < ~0.1 T), the superconducting solenoidal coils are placed inside the cores. It is essential to investigate early on what the maximum tolerable field is going to be at the cores. Separate cryostats and current leads are required for each magnet. A ~20 cm annular gap between the coils and the induction cores is sufficient for cryogenic and magnetic separation.

A number of materials can be considered for the magnetic cores of the induction modules, such as Finemet, Metglas and nanocrystalline compounds. In the baseline design of ref. [4] Finemet and Metglas 2605 are preferred materials.

PARAMETER	VALUE	UNIT
Induction linac length	110	m
Length of induction modules	1	m
Acceleration Gap	0.1	m
Induction pulse length	150—200	ns
Induction pulse voltage	-0.5—1.5	MV
Pulse structure	15×4	Hz $\times$ pulses
Induction core material	Finemet or Metglas 2605C	
Core inner radius	45	cm
Core outer radius	77	cm
Core cross section (L=6 cm)	300	cm^2
Core magnetic field change (ΔB)	1	T
Amount of Metglas (100 m)	500000	kg
Peak pulsed power /1 m module	5.5	GW/m
cw Power requirements (100 m)	5	MW
Solenoidal Focusing Field	3	T
Beam Channel aperture	20	cm

Table 2: General Parameters for the Induction Linac.

5.3.1 Overall Topology

Each Induction Linac cell is 1m long operated at 2.00 MeV (-0.50 MeV, +1.50 MeV _ head to tail). This allows the pulsed power pulse train to be delivered to the 10 induction cores per cell at 150 kV, a reasonable voltage level for cables. The cathode of the accelerating gap is located upstream to provide the proper polarity to the beam, but the center conductor of the cables are connected to the cores in the sense that allows the pulse generator to operate in negative polarity, which minimizes the size of its components. The configuration of the major cell components was dictated by the need to maintain a high acceleration gradient at conservative electric field stress levels on the vacuum insulator and cathode surfaces in vacuum, and to minimize the perturbation of the axial magnetic field of the superconducting magnets caused by the acceleration gap. A 1 m long inter-cell module is positioned every 10 cells to provide vacuum pumping for the beam tube and beam position/net current monitors. A constant solenoid gap pitch is maintained by choosing the inter-cell module length to be the same as that of the acceleration cells.

A cross section view of a pair of cells is shown in Figure 10. The bore radius of 20 cm corresponds to an axial magnetic field of 3.0 T. The induction cell's acceleration gap is 10 cm and its solenoid gap is 14 cm, which allows 2 cm per side for thermal isolation between the end of the superconducting coil and the vacuum feed conductor. The superconducting solenoid is 1.46 cm thick with an inside radius of 22.2 cm. The Mycalex insulator stack is 82 cm long by 5 cm thick with an inside radius of 36.4 cm. The induction cores are located outboard of the insulator with an inside radius of 45 cm and an outside radius of 77 cm.

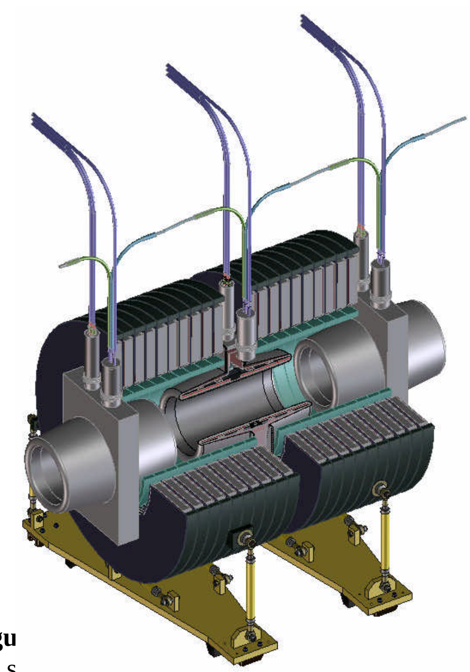

Figu cut
out s

5.3.2 Electric Field Stresses

An equipotential plot of the electric field distribution in the induction cell is shown in Figure 11. The field in the oil dielectric, radial feeds between individual cores is 150 kV/cm or 42 % of the calculated breakdown strength of 345 kV/cm. The peak axial field along the Mycalex insulator is 23 kV/cm for an effective stress time of 50 ns (89% of peak). This value compares to a measured breakdown field of > 33 kV/cm for a 2.2 μs pulse on the Mycalex insulator of the DARHT 2nd axis injector, which scales to >55 kV/cm at 50 ns (33 * (1000 ns/50 ns)$^{1/6}$). On the DAHRT and AIRIX 1st axis injectors vacuum cathode surfaces have been operated in a non-emitting mode at fields of 250 kV/cm, pulse lengths of 60 ns, and areas of 1000 cm^2. With some preliminary cathode conductor shaping the peak field in the accelerating gap is only 183 kV/cm, and in the region where emitted electrons could impact the insulator it is further reduced to 103 kV/cm.

5.3.3 Induction Cell Cores

Each 2.0 MV cell contains 10 individual 200 kV cores. Diametrically opposed cables drive alternate cores, and these core pairs are then clocked azimuthally to provide clearance for the pulse shaping network enclosures that couple the cables to the cell.

The induction cores provide the dominant load to the pulse train generator (2.5 kA of core current versus ~0.1 kA of beam current). Minimizing the core losses reduces pulsed power system costs, but lower core losses require the use of either more expensive core material or larger core volumes. The results of a scan which optimizes system costs are summarized in Table 3. Two types of Metglas manufactured by Allied Signal (USA) were considered, 2605SC and 2714A. 2605SC is the least expensive with the largest losses and 2714A is the most expensive with the lowest losses. A compromise between these extremes, which minimized system costs, was obtained with Finemet FT-1H, a nano-crystalline alloy manufactured by Hitachi (Japan) at a flux density swing of 1.0 T. This optimum gave a mean core loss current of 2.5 kA, which defined a core load impedance of 80 Ω used for the pulsed power design.

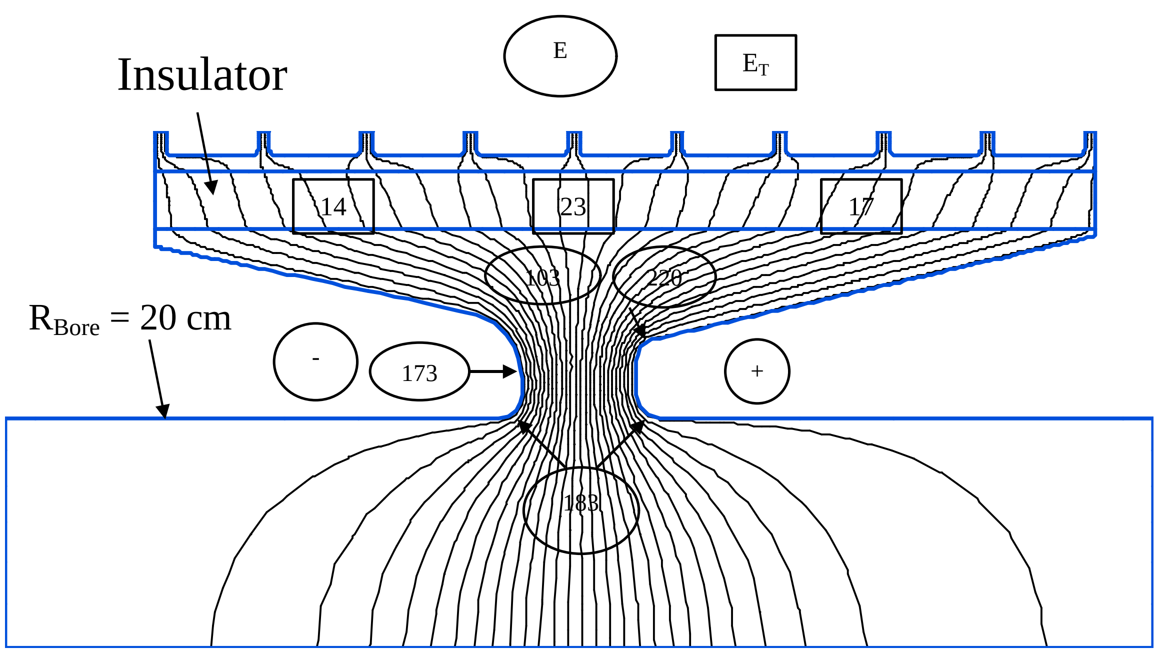

Figure 11: Cell Equipotential Plot. Electric Field Stress on the cell.

ΔV	V_{eff}	τ_r	τ_{flat}	τ_{eff}	$v\tau$	Type	δ	PF_r	ΔB_{max}	Cost	
kV	kV	µs	µs	µs	mV-s	gm/cc			T	Norm	
200	**142**	0.070	0.030	**0.07**	**12.6**	**Finemet**	7.32	0.70	**1.95**	**1.00**	**<-- Finemet**
200	**142**	0.070	0.030	**0.07**	**12.6**	**2605SC**	7.32	0.70	**2.90**	**0.36**	**<-- 2605SC**
200	**142**	0.070	0.030	**0.07**	**12.6**	**2605SC**	7.32	0.70	**1.10**	**2.00**	**<-- 2714A**

ΔB	A_{Met}	A_{Core}	$\Delta B/\Delta t$	L		Δr	r_i	r_o	r_o / r_i	r_{Mean}	H	I_{Core}	E_{core}	k	U_{Met}	V_{Met}	W_{Met}	System $
T	cm^2	cm^2	T/µs	"	cm	cm	cm	cm	cm	cm	kA/m	kA	J	J-µs/T-m^3	J/m^3	cm^3	kgm	Norm
0.97	130	185	**13.2**	2.28	5.8	32.0	45	**77**	1.71	61.0	0.65	**2.50**	31.5	**107**	**634**	49670	363.6	**1.00**
0.82	154	220	11.1	2.28	5.8	37.9	45	**83**	1.84	64.0	0.55	**2.23**	28.1	107	454	61744	452.0	1.02
1.48	85	122	20.1	2.28	5.8	21.0	45	66	1.47	55.5	0.98	3.41	42.9	107	1445	29688	217.3	1.07
0.82	154	220	**11.1**	2.28	5.8	38.0	45	**83**	1.84	64.0	0.98	**3.94**	49.6	**282**	**801**	61946	453.4	**1.13**
2.20	57	82	29.8	2.28	5.8	14.1	45	59	1.31	52.1	2.53	8.28	104.4	282	5571	18736	137.1	2.07
0.82	154	220	**11.1**	2.28	5.8	38.0	45	**83**	1.84	64.0	0.37	**1.50**	18.9	**41**	**306**	61946	453.4	**1.35**
0.86	147	209	11.7	2.28	5.8	36.1	46	82	1.79	64.1	0.39	1.59	20.0	41	339	58981	431.7	1.33

Table 3: Summary of Induction Core Parameters.

5.3.4 Superconducting Magnet for the Induction Cell

The requirements for the phase rotation linac solenoids are as follows: 1) the solenoid outside diameter should minimized. This means that the magnetic induction in the channel should be maximized. 2) The radial thickness of the solenoid cryostat should also be minimized. This allows the induction linac acceleration structure to be brought closer to the axis of the machine. As the magnetic field increases, the thickness of the superconducting magnet that creates the field must also increase. 3) The space between the induction linac cells must be minimized. This means that the space used for the cold mass support system, the electrical leads and the cryogen feed system

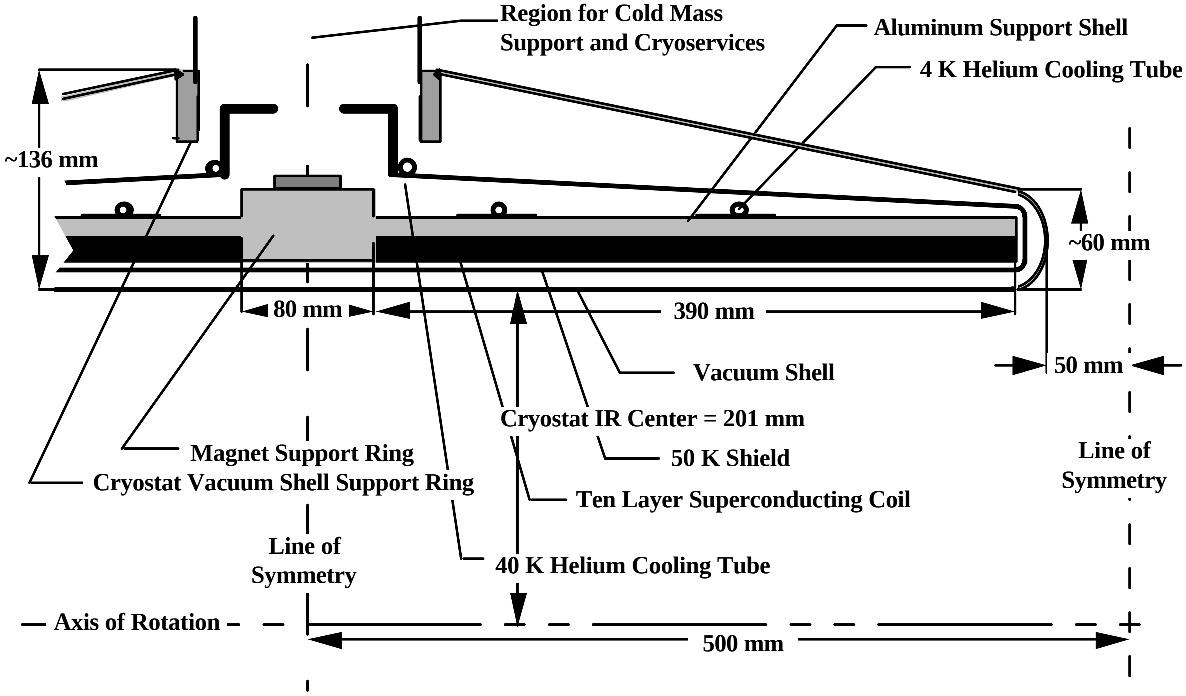

Figure 12: A cross-section of the Induction Linac Superconducting Coil and Cryostat

must fit in this minimum space. To further reduce the space occupied by the cryostat, the solenoid was designed to be cooled indirectly using flowing two-phase helium in a cooling tube attached to the support structure. The 40 K helium used to cool the shield is carried in tubes attached to the shields.

Figure 12 below shows a cross-section of a superconducting solenoid that is designed to generate an average induction of 3 T on the axis of the phase rotation linac. The inner bore of the solenoid cryostat is 400 mm. This allows a 200 MeV muon beam with a nominal diameter of 384 mm (at 3 T) to pass through the solenoid without loss (except from muon decay). The distance from the end of the superconducting coil to the outside end of the cryostat can be reduced to 20 mm. If an additional support clip is needed at the end of the coil, it can be accommodated in the space shown.

Magnet Physical Parameters	
Induction Linac Cell Length (mm)	1000.0
Magnet Cryostat Length (mm)	900.0
Magnet Coil Package Length (mm)	860.0
Number of Coils in the Coil Package	2
Length of Each Superconducting Coil (mm)	390.0
Inner Cryostat Radius (mm)	201.0
Superconducting Coil Inner Radius (mm)	224.3
Superconducting Coil Thickness (mm)	14.55
Support Structure Thickness (mm)	12.7
Magnet Cryostat Thickness at Ends (mm)	60.0
Magnet Cryostat Thickness at Center (mm)	136.0
Cold Mass per Magnet Cell (kg)	247.0
Overall Mass per Magnet Cell (kg)	292.0
Magnet Electrical Parameters	
Average Central Induction (T)	3.00
Peak Induction in the Windings (T)	~4.5
Number of Turns per Cell	4580
Magnet Design Current (A)	521.27
Magnet Design Operating Temperature (K)	4.4
Conductor Critical Current at Operating T (A)	~790
Magnet Stored Energy per Cell E (kJ)	618
Magnet Self Inductance per Cell (H)	4.55
Superconductor Matrix J (A mm^{-2})	331
E J^2 Limit per Magnet Cell (J A^2 m^{-4})	6.76×10^{22}

Table 4: Phase Rotation Solenoid Parameters.

The proposed conductor for the coil shown in Figure 12 above is a standard MRI magnet conductor that is 1 part NbTi and 4 parts RRR=70 copper. This conductor has fifty-five 85-μm filaments twisted with a twist pitch of 12.7 mm. The bare matrix dimensions of the conductor are 0.955 mm by 1.65 mm. The insulation on the conductor is 0.025 mm thick. At an average design induction of 3.0 T on axis, the coil design current is about 521.3 A. As a result, the coil would be a 10 layer coil that is 14.6 mm thick (including 2 mm of ground plane insulation).

It is proposed that the coils be wound and cast on a form that is removed after the coil is cured. After curing the coils are removed from the mold and machined at the ends and on the outer radial surface. After the coils are machined they can be shrunk fit into a 6061 aluminum support structure that has been machined so that the coils closely fit with in it. Table 4 on the next page shows the design parameters for the induction linac solenoids.

The 6061-aluminum support structure on the outside of coils serves the following functions: 1) It limits the coil strain by carrying some of the magnet hoop forces, and 2) it serves as a shorted secondary to protect the magnet during a quench. A single magnet is entirely self-protected through quench back from the support structure. One can use quench back to protect a string of these magnet as well. When a quench is detected in one magnet, the current in the string can be discharged through a varistor resistor, causing all coils to go normal through quench back from the support structure.

The space available longitudinally for leads, cryogenic services and cold mass supports is about 85 mm wide at the center of the magnet. The cold mass of phase-rotation solenoid (including the 40 K shield and lower lead assembly) is estimated to be about 250 kg. The primary forces that will be seen between the cold mass and room

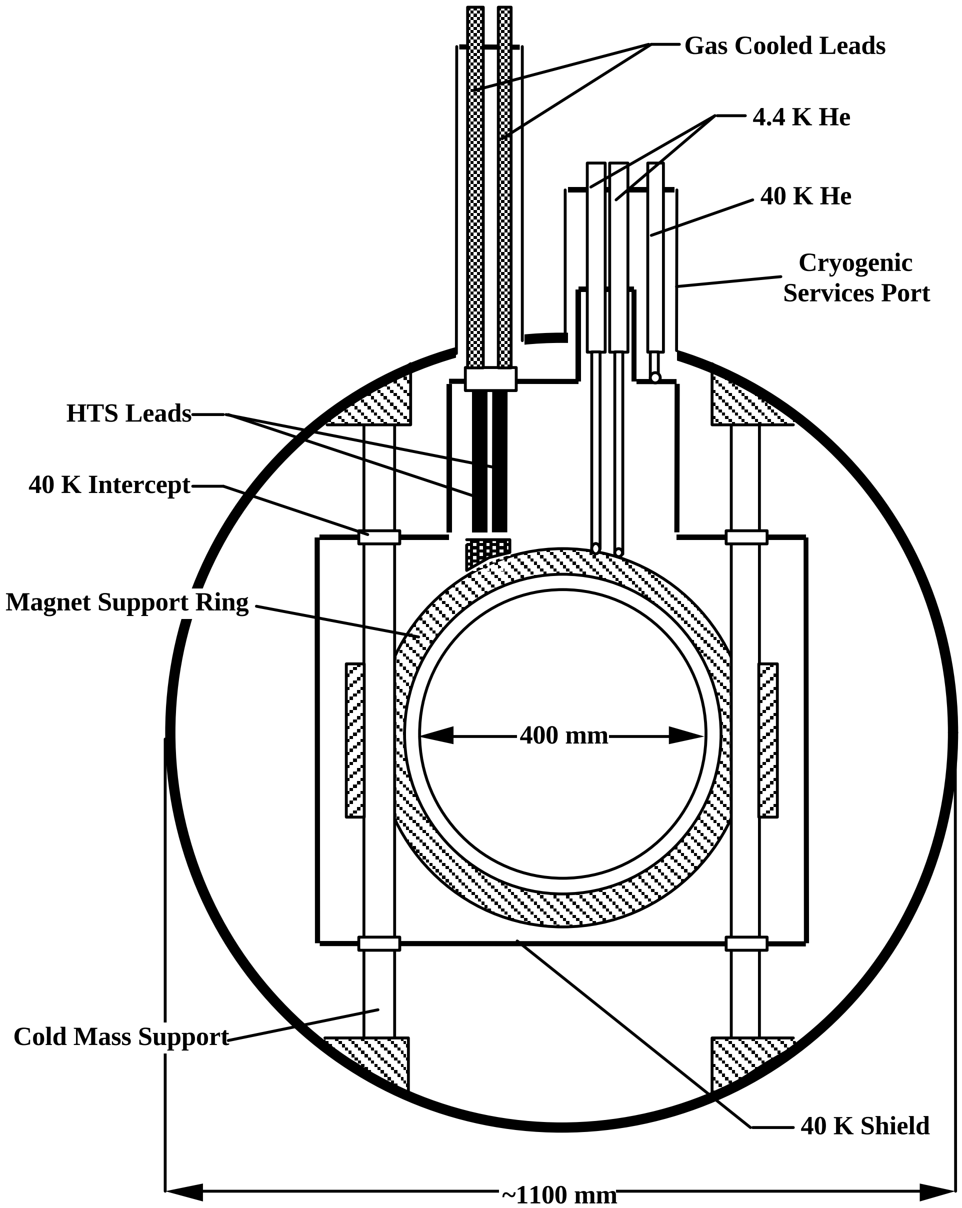

Figure 13: Induction Linac Solenoid Cold mass Support System and Leads.

temperature will be forces do to shipping and forces introduced due to unbalanced magnetic fields. The magnet cold mass supports are designed for a force of 10000 N in any direction. It is proposed that a pair of 60 mm diameter oriented carbon fiber tubes (with a wall thickness of about 3 mm) be used to carry forces from the cold mass to room temperature.

Since there is a solenoid magnet every meter down the phase rotation channels and the drift spaces between the phase rotation linac sections, leads must be brought out of each of these magnets. One has two choices: 1) All of the magnets or 20 to 25 meter long subsets can be hooked in series and run off of a common power supply. Inter-connects between the solenoids can be either superconducting or conventional copper cable. 2) Each magnet can have its own set of leads to room temperature and its own power supply, so individual cells can be tuned. It is proposed that the leads between 4 K and 40 K be made from high temperature superconductor (HTS). The leads from room temperature to the top of the HTS leads at 40 K should be gas-cooled. Gas from the refrigerator that is used to cool the magnet shields and cold mass support intercepts can be used to cool the gas-cooled leads. This gas must be returned to the refrigerator compressor intake at room temperature. Figure 13 shows a schematic representation of the cold mass support system, the helium supply system, and the current leads.

The induction linac superconducting solenoids are cooled by conduction from the 6061-aluminum support structure. The aluminum support structure will be cooled by two-phase helium flowing in tubes attached to the support structure. Two-phase helium cooling is commonly used to cool detector magnets and magnets that are used in physics detectors. The advantages of two-phase tubular cooling are as follows: 1) There is very little helium inventory within the magnet. 2) The two-phase helium tubes have a high-pressure rating. This means that the magnet cryostat is not a pressure vessel. 3) Two-phase helium cooling does not require a cold compressor or a helium pump to circulate the helium through the magnet cooling system. 4) The helium in a two-phase helium cooling circuit decreases as along the flow circuit. 5) The pressure drop along a two-phase helium flow circuit is lower than for a supercritical helium flow circuit. A large number of superconducting solenoid magnets have been cooled using force flow two phase helium in tubes.
It is assumed that the magnet shown is one of twenty to twenty-five magnets that are cooled in series from the two-phase helium refrigerator and control cryostat. If twenty to twenty-five magnets are cooled, the mass flow rate through the flow circuit should be about 2.5 grams per second. The two-phase helium tube would be attached to the superconducting coil support structure, the base of the HTS leads and the attachment points of the cold mass supports. The heat that is added to the two-phase helium flow stream in each of the solenoid is expected to be about 0.5 W.

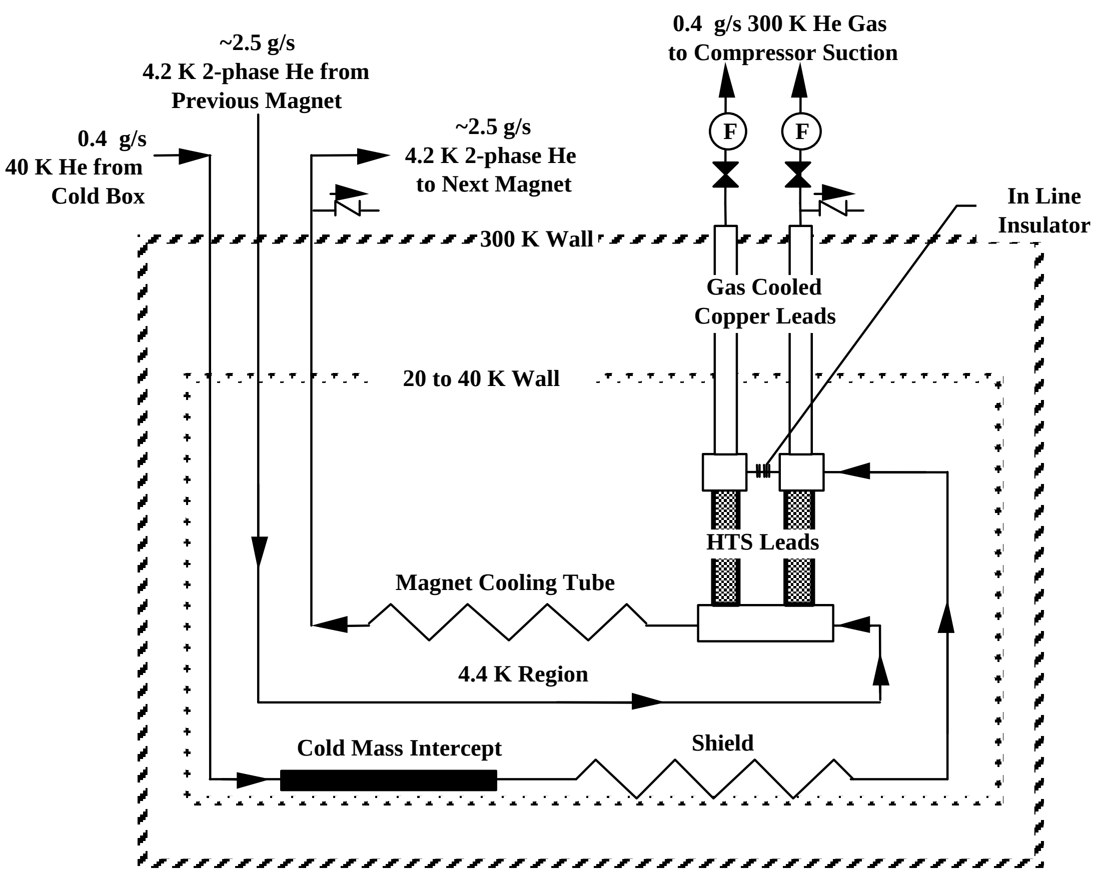

Figure 14: Cryogen Distribution within the Induction Linac Solenoid Cryostat.

5.3.5 4 Pulse per Booster Cycle System Architecture

The pulser system is certainly the most ambitious piece of hardware for the induction linac layout. While single pulse a comparatively easy to provide, multiple pulses at the required voltage rating are difficult to produce. Although two approaches have been considered, the first one presented here is our present baseline. Figure 15 represents a layout of the pulsed power system showing the major components to scale. They consist of cell cables, a water dielectric delay line, four series pulse forming lines, PFLs, magnetic compressor pulse charge modules, MCPCs, and a thyristor switched prime power unit. One of these units is required per induction module, overall 100 of them.

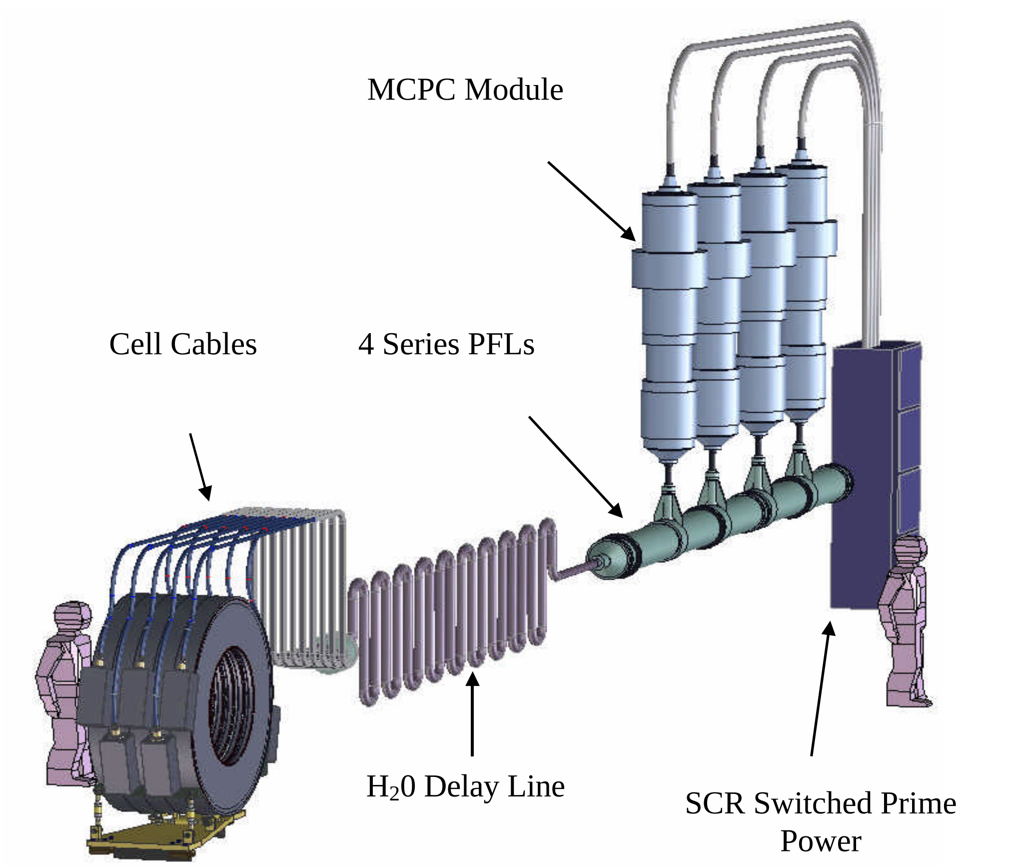

Figure 15: Pulsed Power System layout

Figure 16 is a block diagram of the system that documents key parameters of the components. The generation of four bipolar, 100 ns pulses spaced 400 ns apart is made possible by the use of rapid cell core reset that returns them to the same state between the pulses. 8.3 kA of cell reset current is supplied via a 17 μH inductor housed in a cable adapter at the end of the water delay line. The inductor energy is supplied in 220 μs by a simple Thyristor switched capacitor bank (72 μF at 4.0 kV). The reset current resets the cell cores towards – saturation, blocking leakage current from the four pulse generator, and allowing voltage to develop across the accelerating gap. A + 1.5

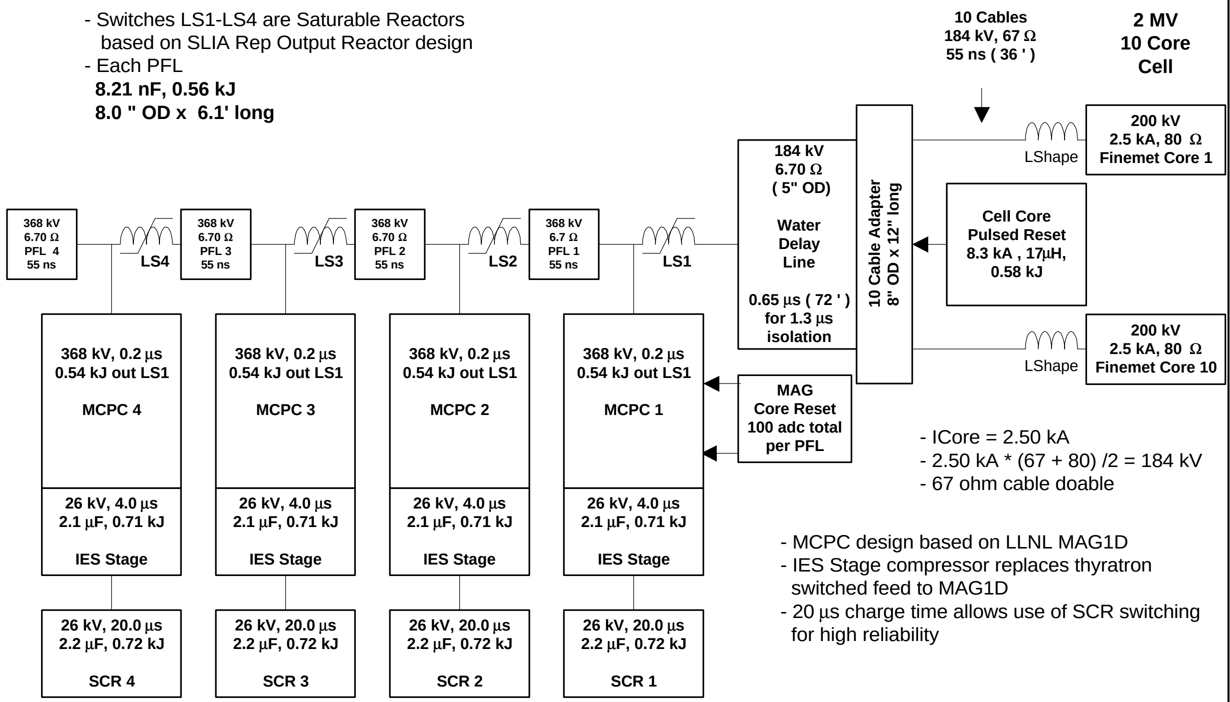

Figure 16: Pulsed Power System Block Diagram

MV pulse from the 4 pulse generator drives the cores towards + saturation. When the pulse disappears, the reset current produces –0.5 MV across the accelerating gap while providing rapid seset of the cores in preparation for the next pulse. Without rapid reset the core area would have to be a factor of four larger, a significant cost impact, and the pulse generator would have to produce the bipolar pulse. It is desirable that the volt-second product of both the acceleration pulse and the reset pulse be equal so that the cell cores are in the same state for each pulse to ensure pulse to pulse reproducibility. Even more importantly the reset pulse must not drive the cell cores completely into saturation before the arrival of the next acceleration pulse or the head of the beam will see 0.0 MV instead of –0.5 MV. The reset pulse width must also be at least 3 times the acceleration pulse width to allow switching transients from the pulse generator to be damped out to an acceptable level. These criteria lead to the asymmetric bipolar acceleration pulse and a net acceleration of 0.5 MV per cell. They also lead to the addition, of a pre-pulse generator not shown in Figure 15 and Figure 16 that will be attached in parallel with LS1 at the entrance to the delay line. Without it, the cell cores would be at – saturation when the first pulse arrived, because of the long time scale of the reset circuit. The pre-pulse generator will supply a > 8.3 kA pulse to the cell cores to overcome the reset current, and drive the cores towards + saturation past their desired operating point. When this +80 kV, 100 ns long pre-pulse ends 100 ns before the beginning of the 1st pulse, the reset current will develop – 50 kV across each cell core and return the cores to the desired operating point for the start of the 1st pulse. The pre-pulse PFL energy is only 42% of the individual main pulse PFLs.

The 1st pulse of the 4 pulse train is generated by the closure of the saturable reactor LS1, which discharges PFL1, launching a 184 kV, 100 ns square wave pulse with a 20 ns risetime into the water dielectric delay line. At the end of the delay line the pulse is routed via ten 67 Ω cables to the ten 80 Ω cores of the cell. The cable to core mismatch developes a change in core voltage of 200 kV superimposed on the reset voltage of –50 kV. The pulse shaping networks at the cable/cell interface convert the fast risetime square wave to the required hyperbolic shape. For this study a simple inductor was used to approximate the required shape. The delay line prevents first pulse reflections from this mismatch from returning to the cell for the pulse train length of 1.3 µs. Once discharged, PFL1 acts as a matched output line for the PFL2 when LS2 closes launching the 2nd pulse into the delay line 400 ns later. The sequence repeats until the 4th pulse of the train is generated by closure of LS4. The risetime of the 4th pulse is slowed to ~40 ns because it has to trnsverse the saturated inductance of 4 switches, but this is largely compensated for by the pulseshaping network at the cell.

Each series PFLs is pulse charged to 368 kV by a MCPC. For this study the MCPC design was based a MAG1D currently in use at 1 pule per second at LLNL so that realistic costs could be developed. A modified version of a MAG1D was run at 100 Hz at PSI. As part of the R&D effort the MCPC design would be optimized for this application. An intemediate energy store, IES, magnetic compression stage was added to the back end of the MAG1D to replace its thyratron switched feed. Extension of the charge time from 4.0 μs to 20 μs allows the use of commercially available thyristors for high reliability switching.

5.3.6 Preliminary Circuit Simulations

A simple circuit simulation of the four series PFLs with realistic saturated switch inductances, the delay line, cables, simple inductor waveshape network, and a resistive load for the core was done to check the feasibility of producing the required pulse waveshape with this approach. Figure 17 shows a four pulse train of the square-wave injected into the delay at the top and the cell voltage on the bottom. Although the 4th pulse of the top pulse train shows significant distortion on the top of the waveform and a slower risetime, much of this is integrated out on the core voltage waveform. Figure 17 shows an overlay of the 1st and 4th pulse of the core voltage pulse train with the

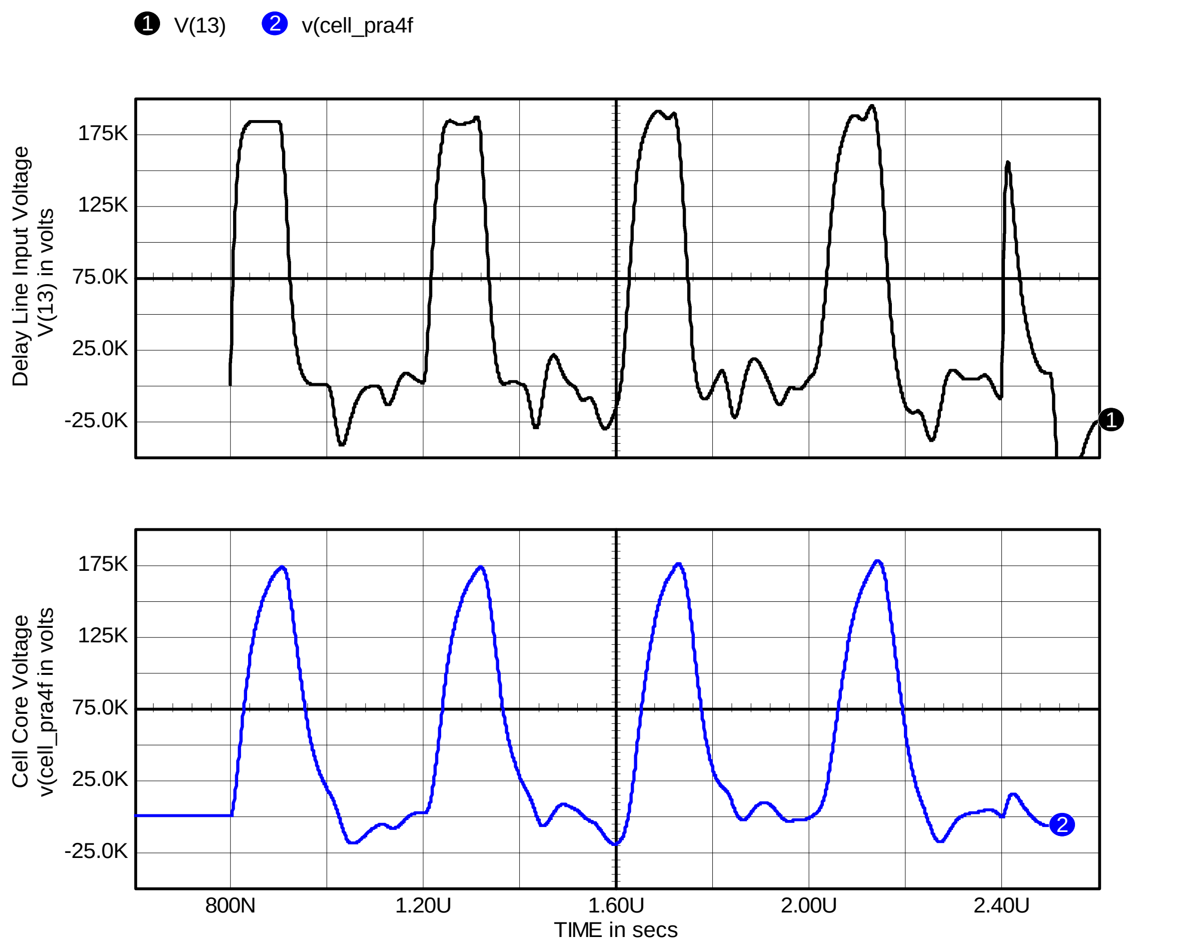

Figure 17: Delay Line & Core Pulse Train Voltage Waveforms

pulses time shifted for comparison. Based on these results it seems reasonable that a combination of rear PFL impedance tailoring and special pulse train generators along the Induction Linac will allow matching of the four pulses in the train.

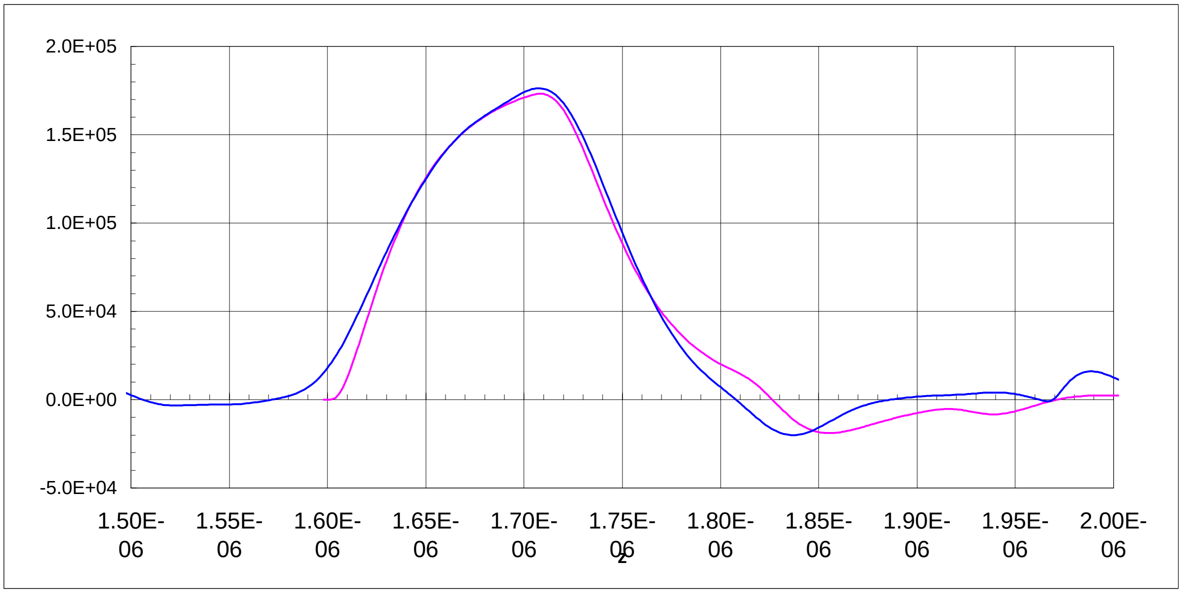

Figure 18: Overlay of the 1st & 4th Pulse of the Train

5.3.7 Alternative Approach for the Pulsing System

A second design for the pulser system was initiated in order to investigate alternative methods for generating the power pulse driving the induction cores. Figure 19 shows a simplified electronic layout for the pulse power generator[4]. The inductor voltage is formed by the common discharge of the forming capacitor C0 and pulse

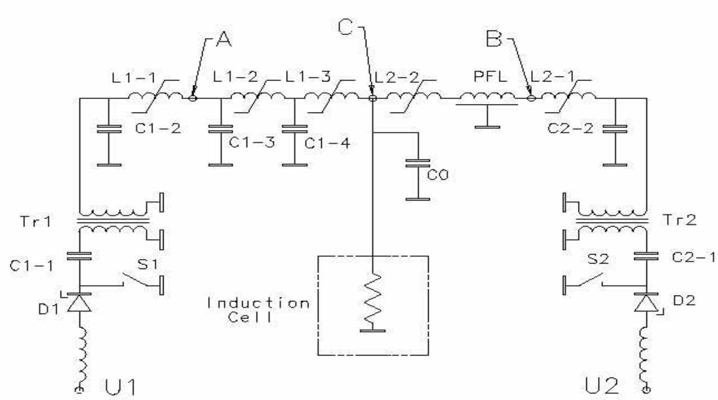

Figure 19: Conceptual scheme of the voltage pulse power generator.

forming line (PFL) into the inductor. A detailed scheme description is provided in [7], and the resulting pulse shape is shown in Figure 20. For this power system approach, LIA accelerating gradient changes from -1.5 MV/m in the beginning of the cycle to 0.5 MV/m in the end, which is similar to what was found optimal in [5]. The time duration of the negative and the positive parts of the voltage pulse are chosen so that the volt-second areas are equal. As a result, magnetic reset of the induction cell core is reached automatically, and after one voltage pulse ends, the system is ready to accept the next one. This power system approach allows generation of several pulses by adding fast charging circuits in parallel at points A and B in Figure 19.

The impedance of the circuit in Figure 19 can not be made arbitrarily small. Nevertheless, it appears possible to use one generator to feed ten inductors (0.5-m of total length) in parallel. Core power loss is the major factor that dictates the size and the cost of a pulsed power system. It was shown in [6] that it is important not to underestimate core power loss because it scales nonlinearly with applied voltage. In order to calculate the average power loss, careful calculation of the instant power loss has to be made followed by integration over the pulse length. Calculations made according to this scheme resulted in a minimal induction core weight of about 100 Tons and an average power required for the total system of about 5 MW. The next step of the development will include thorough simulation of pulsed power circuits that take the nonlinear induction cell impedance into account, as well as stray inductance, and stray capacitance of each section element.

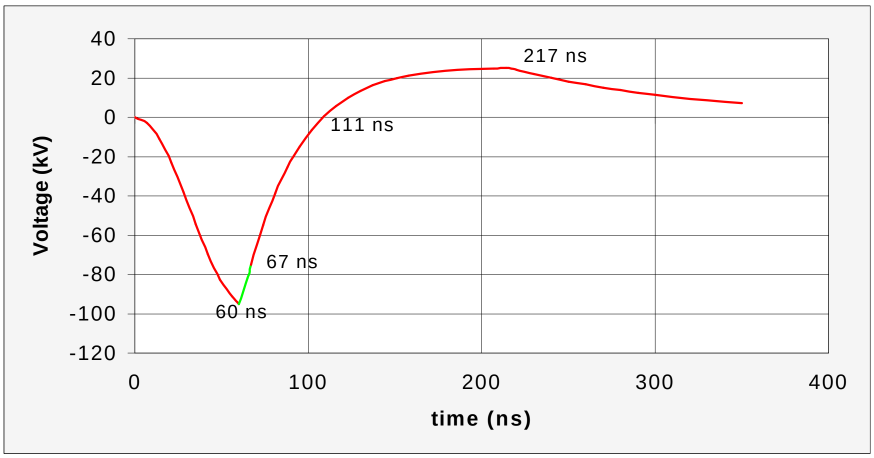

Figure 20: Output voltage pulse applied to an inductor in the LIA section.

5.4 Summary

The reduction of the energy spread of the muon beam is the primary goal of this phase rotation section. The central component that provides the necessary time dependent voltage, is the induction linac. All the other technical components (solenoids in the decay channel, mini cooling absorber, buncher cavities) are simple compared to the induction linac. The superconducting coils inside the induction cores are an additional technical complication. The assessment of all these difficulties and the initial design approach being presented here indicate that the technical problems are solvable with a reasonable amount of R&D.

The phase rotation design presented here performance of the phase rotation on the other hand, as being presented here, meets our intensity performance goal, however the energy spread is still too large in order to guarantee good performance through the buncher section and the cooling channel. More work is needed.

REFERENCES

[1] C. Ankenbrandt et al., "Status of Muon Collider Research and Development and Future Plans", Phys. Rev. ST Accel. Beams 2, 081001 (1999)

[1] S. Geer, C. Johnstone, and D. Neuffer, “Muon Storage Ring Neutrino Source: The Path to a Muon Collider?", FN-2073, March 1999.
[2] V. Balbekov, “Pre-cooling Stage of Neutrino Factory”, MUCOOL note 96, March 2000.
[3] V. Balbekov, “Optimization of Phase Rotation Using an Induction Linac”, MUCOOL note 63, October 1999
[4] J. Fockler et al., “Induction Linac Technology for Muon Beam Phase Rotation”, Neutrino Factory Feasibility Study Workshop, February 2000.
[5] Terechkine, “Neutrino Factory Phase Rotation LIA: Pulsed Power System Optimization”, January 2000 http://www.fnal.gov/projects/muon_collider/nu-factory/subsys/ss-phrot/Optimization.pdf.
[6] S. Yu, LBNL, private communication, Jan. 2000.
[7] V. Kazacha, A. Sidorov, I. Terechkine "Pulsed Power System of Linear Induction Accelerator for FNAL Neutrino Factory".http://www.fnal.gov/projects/muon_collider/nu-factory/subsys/ss-phrot/proposal_inductl.pdf.
[8] D. Neuffer, “RF Capture Variations for the Muon Collider Neutrino Source”, MUCOOL note 52, October, 1999.
[9] A. Van Ginneken, unpublished, January 2000.
[10] R. B. Palmer, C. Johnson, and E. Keil, “A Cost-Effective Design for a Neutrino Factory”, MUCOOL-67, November 1999, Proc. NuFact99, Lyon, 1999.
[11] Bob Palmer, The draft of the current results of this paper are now at <http://pubweb.bnl.gov/people/palmer/nu/pjksim/pjksim.ps>, and will appear shortly as a MUC note.
[12] W. Chou and A. Van Ginneken, “Phase Rotation Using Low-frequency RF”, MUCOOL note 90, February 2000.

6. Cooling

6.1 Introduction

The goal of this six-month study is an integrated design for a neutrino source, subject to realistic engineering constraints. As will become evident, the coupling between the cooling-channel design and the design of the upstream components is critical to achieving the best performance. Nevertheless, to make sufficiently rapid progress it has been necessary to design the various components semi-independently, then optimize and iterate to converge towards an integrated design. While we have not yet arrived at a fully optimized design, we have studied sufficiently the cooling channels described below to determine that their performance is limited primarily by the performance of the current phase-rotation and buncher designs. While the designs presented here suffice for an entry-level neutrino factory (10^{19} neutrinos /year) our overall conclusion is that further iteration of the integrated design is called for.

6.1.1 Theory

The successful design of a high-intensity neutrino source requires that the transverse phase space occupied by the muon beam after the capture, phase-rotation, and buncher channels be reduced by a factor of ~10 in each plane before it enters the acceleration section.

The technique which could accomplish this "beam-cooling" task within the time limit imposed by the finite lifetime of the muon is ionization cooling [1],[2],[3]. In ionization cooling, the beam, while passing through material, loses both transverse and longitudinal momentum by ionization energy loss (*dE/dx*). The longitudinal momentum is then restored by passing the beam through accelerating cavities. This sequence results in a reduction of the angular spread of the beam particles and thus a reduction of the transverse emittance. However, multiple Coulomb scattering in the energy-absorbing medium heats the beam. To minimize this heating effect, the absorbers have to be placed in a strong focusing field. An approximate differential equation for the rate of change of the normalized transverse emittance ε_n is

$$\frac{d\varepsilon_n}{ds} = -\frac{1}{\beta^2}\frac{dE_\mu}{ds}\frac{\varepsilon_n}{E_\mu} + \frac{1}{\beta^3}\frac{\beta_\perp (0.014)^2}{2E_\mu m_\mu L_R} \quad ,$$

where s is the path-length, E_μ is the beam energy, $\beta = v/c$, L_R is the radiation length of the absorber medium, and $\beta_\perp$ is the betatron function of the beam (the size of the beam is given by $\sigma_z = \sqrt{(\varepsilon_n \beta_\perp / \beta\gamma)}$). Since the heating term is proportional to $\beta_\perp$ and inversely proportional to L_R, we need to place the absorbers in low-$\beta_\perp$ regions (strong focusing) and use material with high L_R (hydrogen) in order to maximize cooling. A detailed discussion of the principles of ionization cooling is presented in Refs [1] and [4].

To obtain the strong beam focusing needed for optimal cooling in the absorber, several lattice configurations have been considered. Focusing by solenoids has been selected based on the results of design studies, and on the engineering constraints imposed for a realistic cooling-channel design. Solenoidal focusing has the advantage of naturally focusing equally in both transverse planes, simplifying the design of the transverse beam optics. Solenoids could focus the beam to small $\beta_\perp$ at absorbers in field-free regions, or could provide continuous focusing, with the absorbers placed inside the magnet, allowing the use of extended absorber lengths. The complication with the use of solenoids arises from the fact that a particle entering such a magnet acquires angular momentum, by its interaction with the radial component of the field at the entrance of the solenoid. In the absence of absorbers, this effect is reversible, since at the exit of the solenoid the particle receives an opposite kick from the radial field there, canceling the angular momentum acquired at the entrance. With an absorber within the solenoid, the beam loses angular momentum in the absorber, so at the exit the cancellation is not exact, and the beam retains a net angular momentum. If this angular momentum is not compensated, it results in emittance dilution. In the designs presented here, the technique used to compensate for this effect is to alternate the sign of the solenoidal field so that the sign of the residual angular momentum changes. In an ideal case, where this "field flip" is a step function, the solution would be to alternate the sign after every absorber, which implies variable focusing. Since the longitudinal and transverse motions are coupled, noticeable longitudinal emittance dilution can occur. As a result, the frequency with which we switch the sign of the field is one subject of optimization for each channel.

Each cooling channel is characterized by an optimum length. In the absence of longitudinal-transverse correlation, and at a fixed $\beta_\perp$-min, the transverse emittance settles to an equilibrium value, where additional cooling is compensated by re-heating due to multiple scattering. However, in practice, beyond that quasi-equilibrium point, the transverse emittance starts to increase with channel length, due to the continuous increase of the longitudinal emittance and this correlation.

Three sets of constraints on the design optimization of the cooling channels are imposed by 1) the beam coming from the upstream components of the front end, 2) the beam which the acceleration system that follows can accept, and 3) the engineering requirements for realistic component parameters. For instance, the cooling channel should not be configured independently of the buncher. This is because both the numbers and lengths of matching sections (longitudinal or transverse) must be minimized. In addition, with such large-emittance beams, matching sections are often difficult to design without beam losses. Hence, a significant part of the effort has been devoted to studying integrated solutions, in which a beam is propagated all the way from the pion production target to the beginning of the first accelerating linac.

6.1.2 Design Goals

An initial design study of all the components of a neutrino factory by Palmer, Johnson, and Keil (PJK) [5] concluded that the cooling needed is approximately one order of magnitude in each transverse plane. Our goal is to obtain this transverse cooling without unmanageable longitudinal dilution of the bunch. A factor ~1.4 was to come from minicooling, thus the input emittance into the cooling channel was assumed to be ~10π mm.rad, and we targeted an output emittance of about 1.5π mm.rad. The input rms bunch length was ~10 cm and the momentum spread was ~10%. The buncher was assumed to provide a beneficial longitudinal-transverse correlation (discussed in more detail below) since the bunching is done in a lattice similar to the ones used in the cooling channels.

While rms emittance provides a useful gauge of cooling performance, for a neutrino factory what counts most is the number of muons decaying in the straight sections of the storage ring. Thus the most directly useful measure of performance is the number of muons exiting the cooling channel within the acceptance of the acceleration system. This acceptance has been specified by the TJNAF group as a four-dimensional hypersphere in transverse phase space with radius equal to 2.5σ, where $\sigma^2 = 1.5\pi$ mm.rad, and an ellipse in longitudinal phase space with area of 150π mm. Within these limits 99% of muons are expected to be accelerated and delivered to the storage ring, while a negligible fraction of muons lying outside of these limits will be accelerated. We regard the yield into this acceptance as our main figure of merit and will present it below for each cooling channel studied.

The buncher simulations available at present do not provide the beam just described, with consequent degradation of the performance of the cooling channels. The specifications of the input beams actually used in the cooling simulations are discussed in Sections 6.2.1 and 6.3.1.

6.1.3 Cooling Channel Lattices or Types

As of about a year and a half ago, our collaboration had studied basically one type of cooling channel, the Alternating Solenoid (AltSol) cooling channel. Since then, we have improved our understanding of this type of lattice, with analytical solution of the beam envelope equations in solenoidal channels [3][4][6] and detailed numerical simulations of AltSol at transverse emittances ranging from 12 cm down to 1.5 cm with linacs running at 175 MHz or 201 MHz. The LBL group has proposed a simpler sinusoidal-focusing-field configuration (FOFO). A biperiodic version of this lattice has also been studied, where the more pronounced $\beta_\perp$-min is at the absorber and the tamer one in the middle of the linac where a necessary cavity window sits. V. Balbekov and Ya. Derbenev propose a lattice featuring two constant solenoidal fields, running with opposite current such the total canonical angular momentum of the beam is preserved through cooling (Single-Flip). The FOFO channel is conceptually the most straightforward and has been simulated in great detail with two distinct codes (ICOOL [7]and DPGeant[8]). This is our baseline, or reference design. The optimization – currently in progress – of this FOFO channel is tightly coupled to the performance of the upstream components of the front-end complex and engineering constraints. Since the performance of a realistic design (all constraints applied) could be worse than expected from the initial design, we have chosen to study (first with a less-detailed standalone Monte Carlo program, then with DPGeant) a second channel as a backup. This channel uses the single-flip lattice, chosen primarily because of the simplicity of its design. At this stage, both configurations have been reviewed from an engineering standpoint (more extensively in the FOFO case), and both succeed in cooling transversely without unacceptable dilution of the longitudinal phase space.

6.2 The Baseline FOFO Channel

6.2.1 The Input Beam

The design of the FOFO cooling channel was initially optimized using an idealized beam, since the design of the components of the machine upstream of the cooling channel was not completed at the time. The parameters of this idealized beam are given in Table 1. The final ("integrated-front-end") optimization, currently in progress, uses the beam at the exit of the buncher. It is important to note that the integrated-front-end design (including the induction linac and the buncher) used for the FOFO simulation differs from the baseline design presented in the preceding chapter and is based on an earlier design of the phase-rotation channel.

PARAMETER	**VALUE**
Global	-
Length of a section (1/2 of a lattice period)	1.1 m
Maximum magnetic field on axis	3.4 T
Number of sections	150
$\beta_\perp$–min	35 cm
$\beta_\perp$–max	88 cm
Absorber	-
Length of liquid-hydrogen (LH2) absorber	12.6 $\rightarrow$ 13.2 cm
Density of LH2	0.0708 g/cm^3
Absorber window thickness	400 $\rightarrow$ 200 μm
Absorber window material	Aluminum (6061-T6)
Energy loss per section, nominal	4.0 MeV
Radial aperture, in LH2	15.0 $\rightarrow$ 10.0 cm
Linac	-
Length of linac (per section)	66 cm (π/2) or 74.56 cm (π)
Number of rf cells	2 (π/2) or 1 (π)
Frequency	201.25 MHz
Peak electric field, on axis	15 MV/m (π/2) or 18 MV/m (π)
Optimum synchronous phase (ϕ_s)	~ 30 degrees
Acceleration at ϕ_s	~ 4.0 MeV
Beryllium-window thickness (pillbox)	125 μm
Radial aperture, linac	17 cm
Beam	-
Nominal momentum p_0	200 MeV/c
Normalized transverse emittance ε_n	~15π mm rad
$\sigma(p_x)$	~25 MeV/c
Longitudinal bunch spread σ_z	~ 310 ps = 8.14 cm
Normalized longitudinal emittance ε_{Ln}	~ 35π mm
Average momentum	~200 MeV/c
Momentum spread	~ 7 to 10 %
Longitudinal-transverse correlation	0

Table 1: Parameters of the FOFO cooling channel. The idealized input-beam parameters are given, although simulations have also been done with the beam coming out of the buncher, which has slightly different parameters and correlations.

As in the baseline design, in the integrated-front-end simulation, the cooling-channel input beam has been bunched at 201.25 MHz rf frequency, but it is matched to a beta function of ~35 cm at the null of the magnetic field. The central momentum is 200 MeV/c and the rms energy spread is 17 MeV (momentum spread of 20 MeV/c). The normalized rms transverse emittance is 9.1π mm.rad and the longitudinal emittance is 58 π mm. There is negligible canonical angular momentum in the beam. The longitudinal phase space occupied by the particles spreads out beyond the separatrix of the rf bucket. There are 0.07 muons per proton overall, a factor 3 fewer than in the baseline design, and 0.05 muons per proton within a longitudinal phase-space area of 150 π mm, which is the acceptance of the acceleration section. There is negligible correlation between the transverse amplitude and energy. This implies an additional mismatch into the rf system, as the FOFO channel is tuned for an energy-amplitude correlation $\langle \Delta E \rangle / \langle A_\perp \rangle = 0.5$ GeV/m.

6.2.2 Technical Description

The lattice is periodic, characterized by a solenoidal magnetic field whose magnitude on axis varies sinusoidally with 2.2-m period and 3.4-T amplitude (Figure 3). The betatron phase advance per magnetic period is quite large by normal standards. This allows a relatively low $\beta_{\perp}$-min to be achieved with reasonable values for the on-axis field. However, the betatron resonance characteristic of such a simple and compact optical system leads to beam instabilities: as particles undergo synchrotron motion, their momentum can get close to the resonant momentum, leading to dramatic increase of the radial excursions. Unless favorable multiple scattering or straggling occurs, such particles are lost. The cooling process *de facto* weakens the impact of such betatron resonances.

Engineering feasibility is a complicated function that depends on such parameters as field, current density, and stress on the conductor. While a detailed engineering study has yet to be performed, a conservative rule of thumb (based on keeping the hoop stress within manageable limits) for solenoids built from Nb_3Sn superconductor is [9] $BJR < 350$ MPa, where B is the field at the coil, J the area current density, and R the radius, all evaluated at the location within the coils where the above product is at a maximum. Coils satisfying this inequality should have forces on the windings that are within acceptable engineering limits. The maximum magnetic field occurs on the facing surfaces of the "bucked" coil packs (see Figure 1), and this is also where the force on the windings will be greatest. For the 3.4-T FOFO the relevant values are $B = 7.0$ T, $J = 49$ A/mm^2, $R = 0.9$ m, giving $BJR = 310$ MPa.

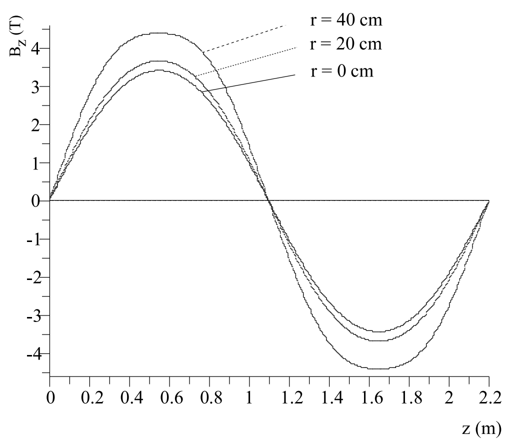

Figure 3: The profile of the longitudinal component of the magnetic field in the FOFO channel on axis and at 20- and 40-cm radius.

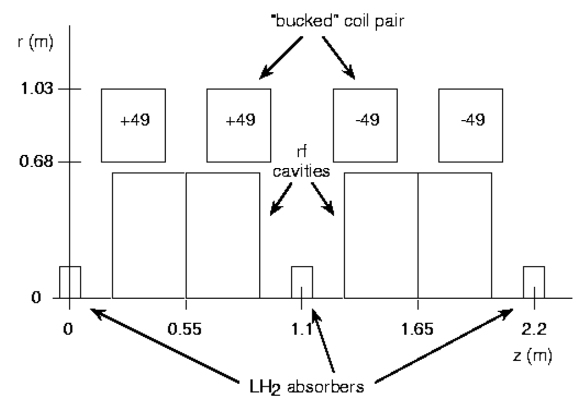

Figure 1: Sketch of a FOFO lattice period showing the relative locations of the coils, linac and absorbers. The LH_2 vessel and the linac are centered on the symmetry points of the section, at $z = 0$ and 0.55 m, respectively.

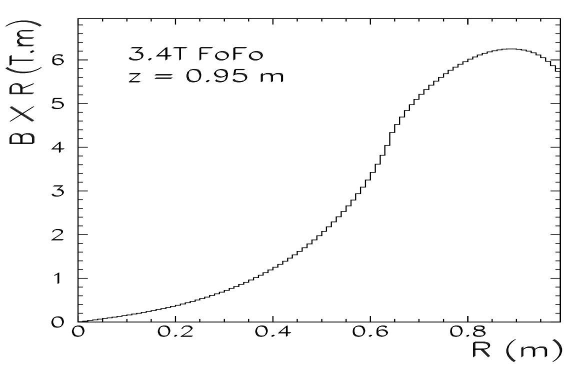

Figure 2: The magnetic field times the radius on the inner faces of the "bucked" coils (one of the critical factors entering into the design of such solenoids) vs. radius.

(see Figure 2). While the forgoing cannot substitute for a full engineering study, comparisons with existing magnets of similar size, function, and field production suggest that such current density can be reliably achieved in these magnets The absorbers and linac structure are inserted into the lattice as shown in the engineering drawing of

Figure 4. Liquid-hydrogen (LH_2) absorbers are used to minimize multiple scattering. The specifications of the absorbers are given in Table 1.

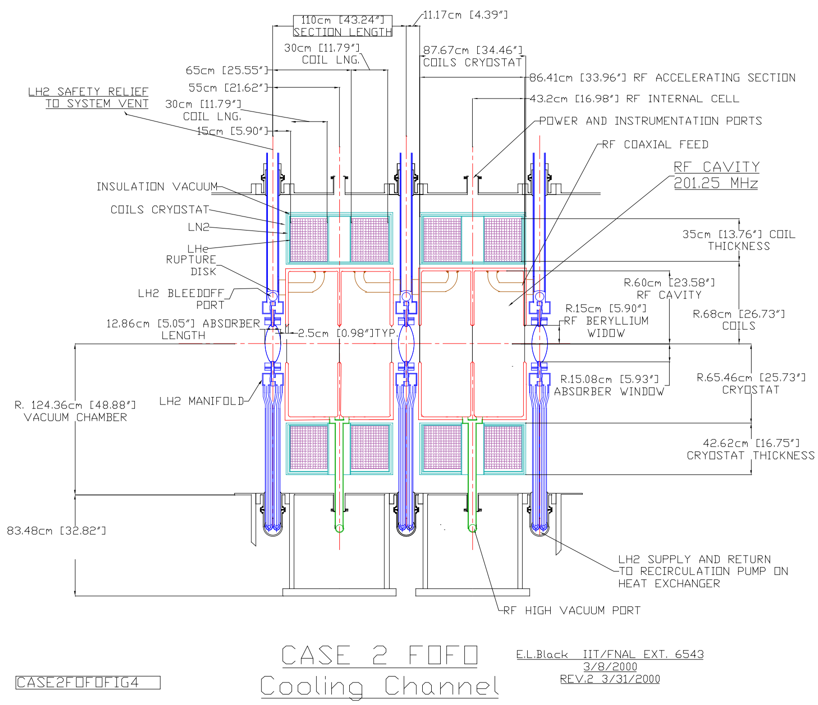

Figure 4: Engineering drawing of two sections of the FOFO lattice (one lattice period), showing all components of the lattice including the pillbox type beryllium window cavity.

The thickness of the absorber windows is a critical parameter. They must be thick enough to sustain the pressure from the LH_2 yet as thin as possible to reduce multiple scattering. The window thicknesses have been chosen based on the ASME standard for pressure vessels [10]. This choice also satisfies the Fermilab safety code for liquid-hydrogen targets [11]. Given the oblate shape of the absorbers, of three standard window profiles specified by ASME (hemispherical, ellipsoidal, and torispherical), the torispherical profile is chosen in order to minimize the sagitta and leave sufficient room for absorber connections and support structure (see Figure 6Figure 5). For this case, the minimum window thickness is given by

$$t = 4\frac{0.885PD}{SE} ,$$

where P is the pressure differential, D the absorber diameter, S the ultimate strength of the window material, and E the weld efficiency. (This formula includes the safety factor of 4 mandated by ASME.) We have used S = 289 MPa as given by ASME for 6061-T6 aluminum alloy and E = 0.9. We assume operation of the absorbers at an internal pressure of 1 atm, giving a 1-atm pressure differential on the windows.

Assuming that aluminum-alloy windows are used, the LH_2 and absorber windows in each cell correspond respectively to 1.45% and 0.90% of a radiation length in the first part of the channel, and 1.52% and 0.45% in the second. The reduction in window thickness from part 1 to part 2 of the channel is made possible by the reduction in transverse size of the beam and a corresponding reduction in the diameter of the absorber. It results in a lowering of the equilibrium emittance from 2.6π mm.rad to 2.2π mm.rad and a corresponding increase in the cooling rate. While beryllium or AlBeMet (a composite of 62% beryllium/38% aluminum) could reduce the impact of the windows on the cooling performance, based on the CEA bubble-chamber accident, beryllium is believed to be incompatible with liquid hydrogen, and an R&D program would be required to establish safe design parameters for these materials.

In passing through the absorber, a 200-MeV/c muon loses on average 4 MeV of energy. Thus at the beginning of the channel, where bunches of up to 10^{13} muons may be incident at a 15-Hz repetition rate, up to 100 W of power will be dissipated in each absorber. While larger than the power dissipations at which hydrogen targets have been operated at Fermilab, this is within the range of dissipation that has been handled successfully at SLAC [12] and Bates [13], utilizing a flow-through cooling-loop design with external heat exchanger. Engineering studies are ongoing to certify the power-handling performance of the absorber design which will be tested in a high-intensity beam as part of the R&D program for a neutrino factory or muon collider.

6.2.3 The Normal Conducting Accelerating Structure for the Cooling Channel

The linac has two functions: it provides the longitudinal focusing and compensates for the energy loss in the absorber. These linacs must be relatively compact in order to minimize the decay loss, hence relatively high accelerating gradient must be used. The number of cells per linac (or section) is driven by the period of the lattice, the resonating mode, the frequency and the momentum. These last two parameters are dictated by the bunch properties coming out of the buncher. The most straightforward option is to use the same frequency, 201.25 MHz.

The accelerating field provided by the rf systems in the cooling channel requires substantial rf power. Using closed-end accelerating cell structures, which allow arbitrary phase variation from cell-to-cell, allows the shunt impedance of multi-cell cavities to be increased significantly over open-cell structures, hence reducing rf power requirements. The

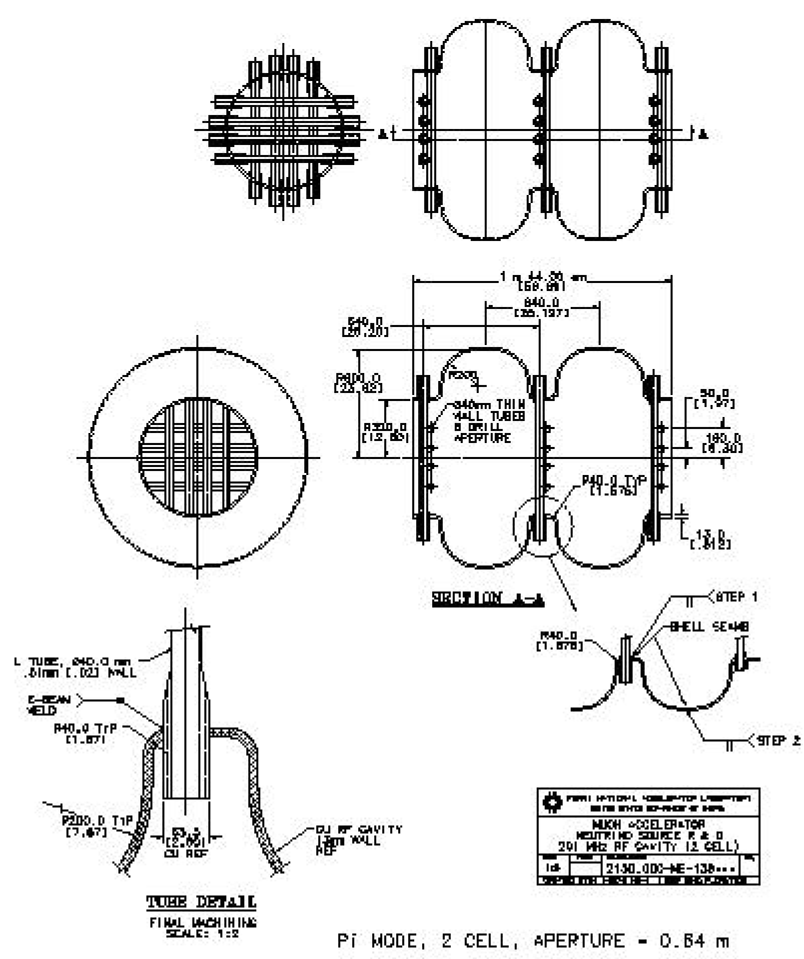

Figure 5: Sketch of a 2 cell π-mode cavity with aluminum tubes installed inside the iris.

challenges in cell design and in rf power sources remain key technological areas. While the rf power sources are discussed in more detail in chapter 10, the cavities an integral part of the cooling system.

There are two types of cavities under consideration for the ionization cooling channel. One is a pillbox cavity with thin beryllium windows covering the iris. The other is a cylindrical rf cavity with rounded ends and thin walled hollow aluminum tubes covering the beam aperture. Both cavities fit in the proposed cooling channel and have a outside radius, including copper wall thickness, of ≤ 0.60 m. The numbers of cells in the cooling channel is determined by the total ionization loss and the rf phase at which the muon bunch is accelerated

The design with beryllium windows (pillbox type) has a 10 to 15 % larger optimized shunt impedance. This is important because the larger shunt impedance would require less rf power installed. A second advantage of the beryllium cavity design is that it achieves high accelerating gradients without increasing the peak surface electric field. However, because the beryllium needs to be thin, 125 microns, to reduce beam scattering, mechanical strength and thermal stability due to surface current heating are of major concern. The thin walled aluminum tube design, on the other hand, may be easily cooled by forced air or helium gas flow through the tubes. The tubes are mechanically more stable and less prone to rupture than are the beryllium windows. The diameter of the tubes is 4 cm and the walls range in thickness from ~ 100 μm at the beam center up to 150 μm. A sketch of a π-mode cavity with tubes inside the iris is shown in Figure 5. The thin beryllium windows of large radius can only support a small pressure differential. In addition the aluminum tube design is expected to be less expensive. Its mechanical strength can be designed to operate with beam apertures as large as 0.64m. This may be important in the early stages of the cooling channel where the muon beam is the largest. There are currently draft mechanical designs for both cavity designs (one example is shown in Figure 4). The thin walled aluminum tube design comes at the expense of a higher peak surface electric field gradient. At the surface of the tubes, the surface electric field is increased by a factor 1.5 relative to the accelerating gradient. This could limit the peak achievable accelerating gradient due to vacuum electrical breakdown in the cavity, and perhaps multipacting.

Both designs should achieve the design gradient of 15 MV/m. In fact experiments performed on the Fermilab 200 MHz linac have achieved gradients of 40 MV/m in pulsed operation. Using closed-end structures (with Be window or Al tubes), allow the shunt impedance of multi-cell cavities to be increased over open-cell structures, hence reducing rf power requirements. The beryllium design requires an rf power of 5.6 MW for an accelerating gradient of 15 MV/m. The aluminum tube design requires an rf power of 6.2 MW and has a peak surface electric field of 22.5 MV/m. The peak power production and distribution is discussed in more detail in chapter 10. An example is given in Table 2. While the pillbox has a relatively short transit time, the muons always go through three windows per linac structure. Detailed simulations based on 3D particle tracing are needed to estimate the beam dynamics and the scattering probability in the grid or window. This effort is ongoing.

Parameter	Crossed Tube	Pill Box
Frequency	201.25 MHz	201.25 MHz
Accelerating Phase Angle	Sin(25 degrees)	
Peak Accelerating Field	15.0 MV/m	15 MV/m
Peak Surface Field	22.5 MV/m	15 MV/m
Kilpatrick Limit	14.8 MV/m	14.8 MV/m
Cavity Type	Open Cell with crossed tubes over aperture	Beryllium foil windows over 15 cm radius apertures
Cavity Dimensions	internal r is 0.600 m internal cell length, λβ/3, is 0.432 m.	internal radius is 0.600 m, internal cell length, λβ/3, is 0.432 m. length of accelera-ting section is 0.864 m.
Impedance	28.4 MΩ/m	34.1 MΩ/m
Shunt Impedance	20.3 MΩ/m	23.3
Transit Time Factor T	0.845	0.827
Peak Voltage per Cell	6.5 MV	5.7 MV
Q	47,500	52,600
Fill Time	38 μs, critically coupled	42 μs
rf Pulse	114 μs	125 μs
Peak Power per Cell	3.45 MW	2.8 MW
Average Power per Cell	8.0 kW	5.3 kW
Window Type	4 cm diameter Al crossed tubes	15 cm radius, 127 μm thick Be foil
Average Power on Tubes	30 W (worst tube)	53 W (heated from both sides)

Table 2: Example rf cavity parameters for a 1.1 m channel with an aperture of 34 cm and 2π/3 phase advance per cell.

We take the Pillbox type, running in the TM010 mode, with $\pi/2$ phase advance per cell, equipped with thin beryllium windows, with two cells per linac as the baseline for this study. For cooling simulations it is interesting to note, that while the first cavity has a relatively short transit time, the muons always go through three windows per linac structure. Detailed simulations based on 3D particle tracing are needed to estimate the beam dynamics and the scattering probability in the grid or window. This effort is ongoing. We take the pillbox-type cavity as the baseline for this study.

6.2.4 Performance

As mentioned above, the cooling channel cannot be designed in isolation but must be optimized together with the muon source “front-end” components that precede it. This work has not yet been completed to our satisfaction, and what we present here is in the nature of a status report. Prior to availability of a simulated output beam from the buncher and matching section, we explored the optimization of the FOFO channel using an approximation of the expected beam that would be input to it, and Figure 7 summarizes the resulting cooling performance for this idealized beam. The parameters of the channel are similar to those described above. Muon decay losses have been turned off in the simulation in order to isolate optics and matching issues but contribute an additional 12% loss.

The large (50%) losses in the first 25 m of the channel reflect the need for further optimization, and in particular the need to incorporate a realistic longitudinal-transverse correlation in the incoming beam, such as would be present in the beam from the buncher but is absent in this simulation. The desired correlation ameliorates the differential path length through the lattice for muons at large transverse amplitude (which follow helical trajectories with large radii) compared to those at small transverse amplitude (whose helices have small radii) by raising the average muon energy in proportion to transverse amplitude. Despite the absence of such correlation, Figure 7b shows that the transverse emittance is cooled by a factor of 7 over the 150 m of the cooling channel, approaching the PJK goal [5].

Figure 7c shows the number of muons within the acceptance of the acceleration system (see Section 6.1.2), which is seen to increase by a factor 4.5 within the first 120 m of the channel and then to decline with continued longitudinal phase-space dilution and beam losses. Better performance is expected once the losses at the beginning of the channel have been optimized.

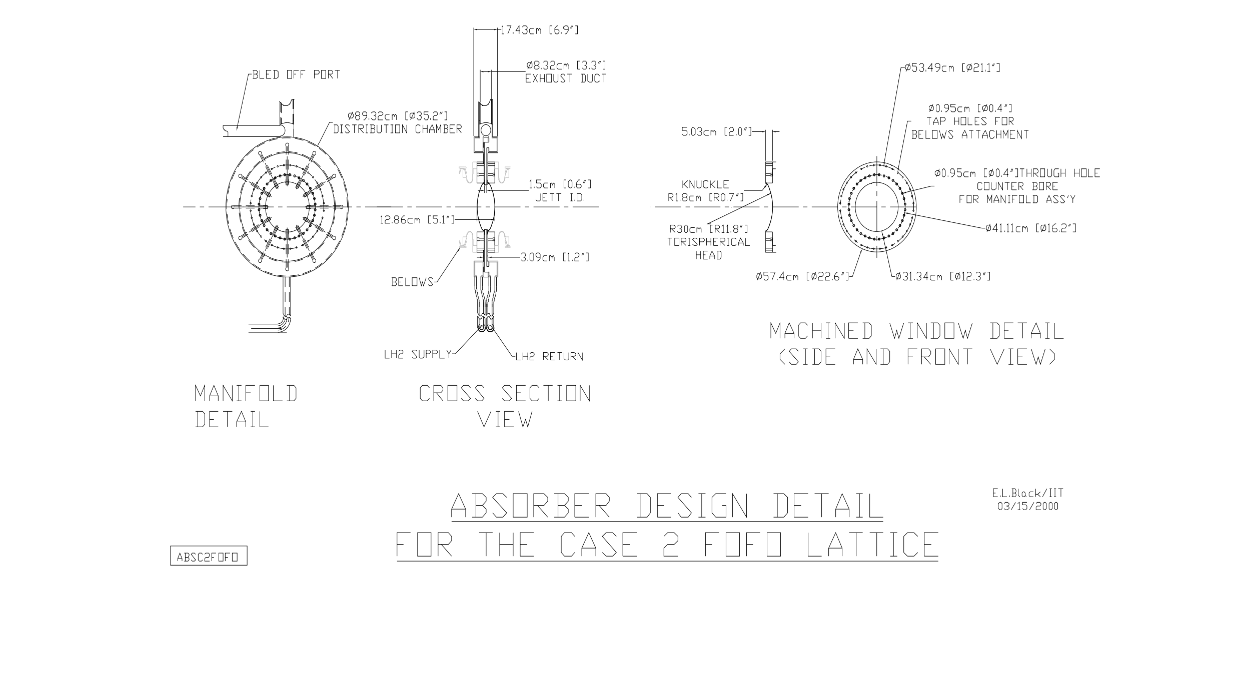

Figure 6: Detail of the liquid-hydrogen absorber and related piping, constrained by the coil placement and the rf feeds

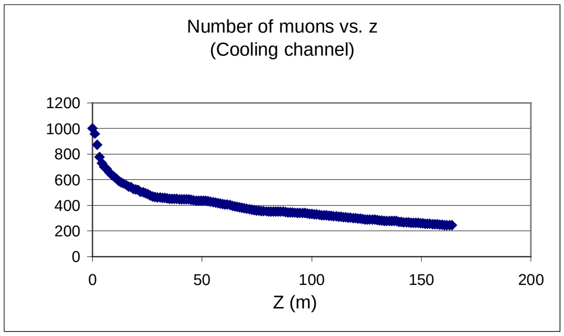

Figure 7a: Transmission in the FOFO channel vs. distance using the idealized beam described in the text.

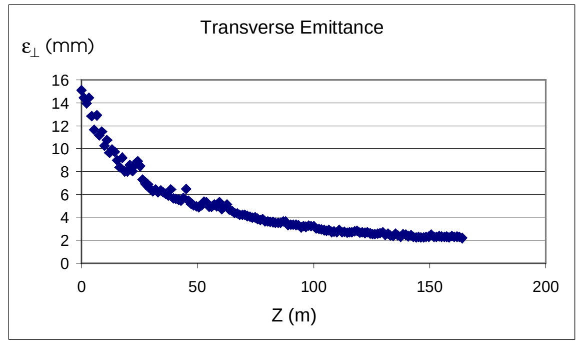

Figure 7b: Transverse emittance vs. distance for the idealized beam.

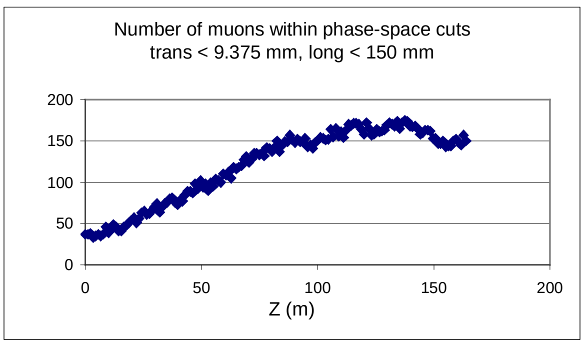

Figure 7c: Relative yield increase within the acceptance of the accelerator (9.375π mm.rad transverse, 150π mm longitudinal) using the idealized beam.

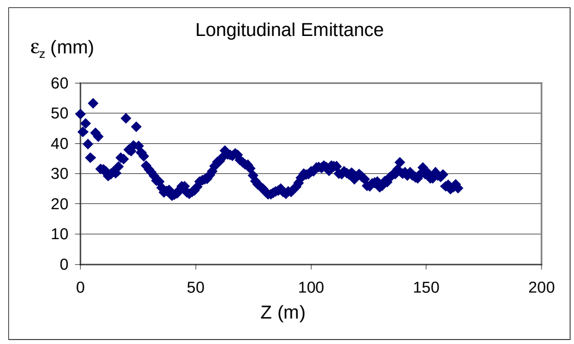

Figure 7d: The longitudinal emittance of the idealized beam in the FOFO channel.

Figure 7: Summary of cooling performance of the channel with an idealized beam.

We next present results from the integrated-front-end simulation. The parameters of the channel have been given above. Figure 8 summarizes its performance. While the final transverse emittance obtained is similar to that with the idealized beam, the cooling factor is smaller since the beam begins with a smaller emittance (9.2π mm rad). The losses are also worse, with the total yield into the acceleration system increasing by a factor of only 2 within the first 100 m of the channel, to 0.018 muons/proton. While the number of muons within the acceleration acceptance declines in the last 50 m, we have left the length of the cooling channel at 150 m in the cost estimate, both to be conservative and to leave room for possible additional beam manipulations.

Insight into the large losses and poor performance of these simulations so far is provided by Figure 9, which shows the longitudinal phase plane at the input of the cooling channel and 65 m further downstream. The input beam has a time spread that extends well beyond the separatrix, thus the large initial losses are not surprising. The continued losses along the entire length of the channel reflect the behavior expected when an overfull bunch is presented at the input, since the longitudinal emittance dilution due to stochastic effects in the absorber necessarily causes particles near the separatrix to cross into the unstable region of the phase plane.

This performance represents a notable shortfall relative to the PJK design sketch [5], but we are confident that there is substantial room for improvement with further optimization work and R&D. As an example, we have simulated a FOFO channel with parameters similar to those described above except that the absorber windows have been eliminated. While liquid-hydrogen absorbers do require containment, this case indicates how much might be gained by R&D on exotic window materials such as beryllium or AlBeMet. The yield within the acceleration acceptance is increased by 50%. Moreover, the FOFO lattice may not be the optimal choice for muon cooling in this emittance range, an issue that will be elucidated by further work on the single-flip and alternating-solenoid options.

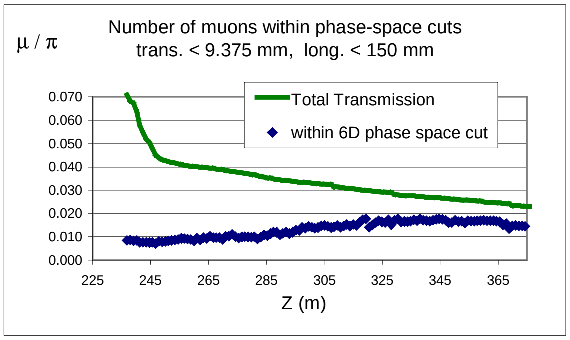

Figure 8a: The transmission vs. distance and the muon yield within the acceptance of the accelerator.

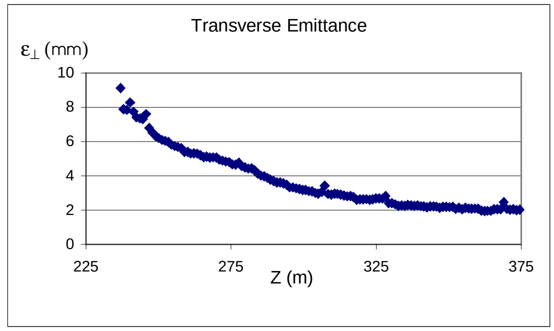

Figure 8b: The transverse emittance vs. distance in the FOFO cooling channel.

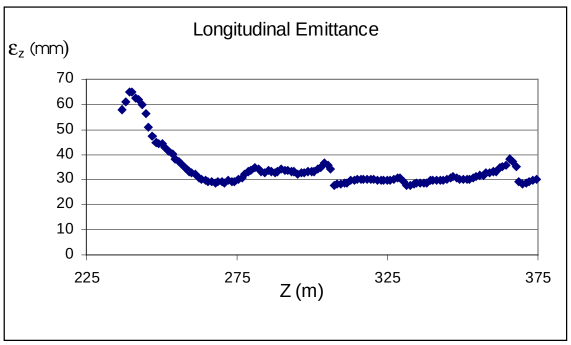

Figure 8c: The longitudinal emittance.

Figure 8: Summary of the integrated-front-end simulation.

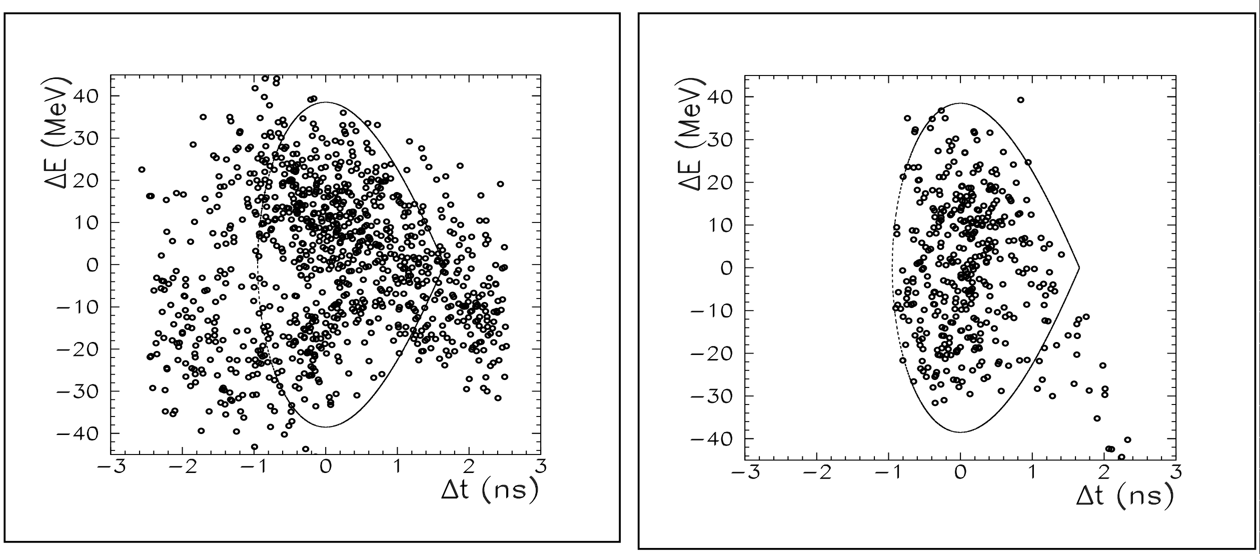

Figure 9: The longitudinal phase space of the bunch entering the FOFO cooling channel (left) and 65m further downstream (right). Muons from the integrated simulation are shown together with an approximate representation of the separatrix.

6.3 The Single-Flip-Channel Option

Unlike the baseline FOFO channel, this channel has a very simple lattice (Figure 10): the cooling sections use continuous focusing from long solenoids, with the absorbers placed inside the magnets. Such a configuration provides simple transverse optics: for a matched beam there is no modulation of the beam envelope in the channel. The field of the long solenoid is reversed in the middle of the lattice, in order to control angular-momentum growth (see section 6.1.1). A special matching section is used at this point, both to minimize the length of the region affected by the polarity change, and to mitigate particle loss due to the excitation of synchrotron oscillations. These oscillations arise from the longitudinal-transverse phase-space correlations that develop due to the dependence of the time of flight on the transverse amplitude of the particles in a solenoid. The transverse momentum and thus the transverse amplitude changes at the field reversal; this change has to occur in a spatial region smaller than the Larmor wavelength of the beam in order to control these effects.

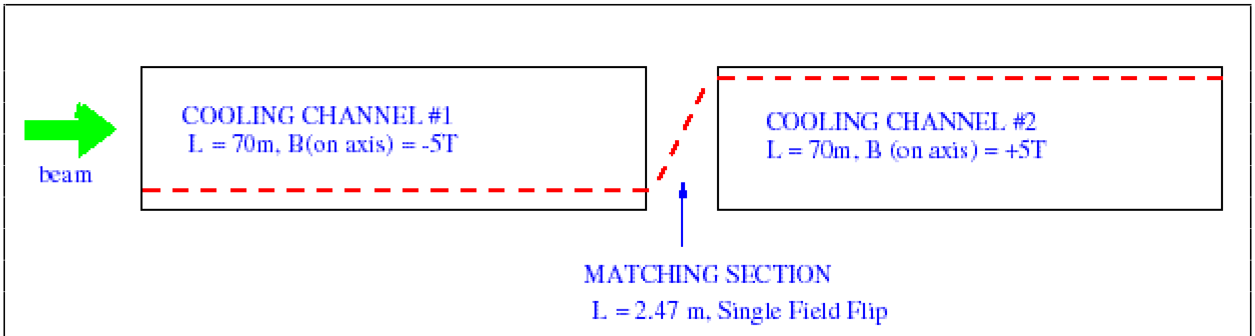

Figure 10: Sketch of single-flip-channel concept.

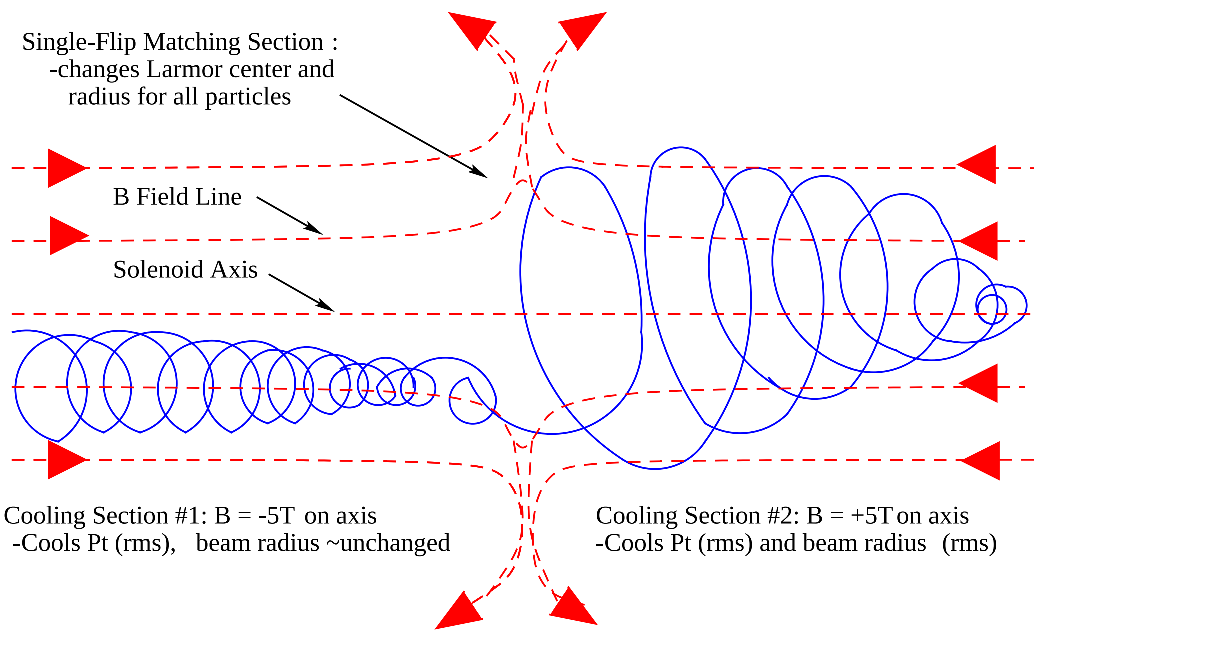

Figure 11: Illustration of particle motion in the single flip channel.

Figure 11 illustrates the cooling principle of the single-flip channel. Channel 1 cools the transverse momenta of the muons, to first order without affecting the transverse size of the beam (to second order the beam grows slightly due to multiple scattering). (For an infinitely long channel, neglecting scattering, the muon helices would shrink to lines.) In the matching section between channels 1 and 2, the centers of the Larmor orbits are displaced such that in channel 2 the muons to first order execute Larmor motion about the solenoid axis. As this motion cools, both the beam size and transverse momenta are reduced.

6.3.1 Initial constraints and the input beam

The design of this channel is optimized to maximize the transmission and the cooling performance for the exact input beam produced at the end of the buncher described in the preceding chapter. As noted above, the optimization of any cooling channel is strongly coupled to the front-end design. The beam is relatively large: σ_x = 4.5 cm, σ_{px} = 30 MeV/c, σ_E = 40 MeV, but it is the result of our initial global optimization given the constraints of all subsystems.

6.3.2 Technical description of the channel

This cooling lattice consists of two supersections: the first contains 28 cooling sections, 2.47m long, in an almost-constant magnetic field of –5T on axis. Between the two supersections there is one 2.47-m-long matching section in which the field changes polarity. The field flip is followed by a second supersection of 28 sections, 2.47-m long, at +5T on axis. Within each supersection the magnetic field varies as little as possible. A perfectly constant field would be ideal, however this cannot be achieved due to engineering constraints. Gaps in the solenoids required for rf power feeds and absorber cooling equipment are included in the simulation (see Figure 12).

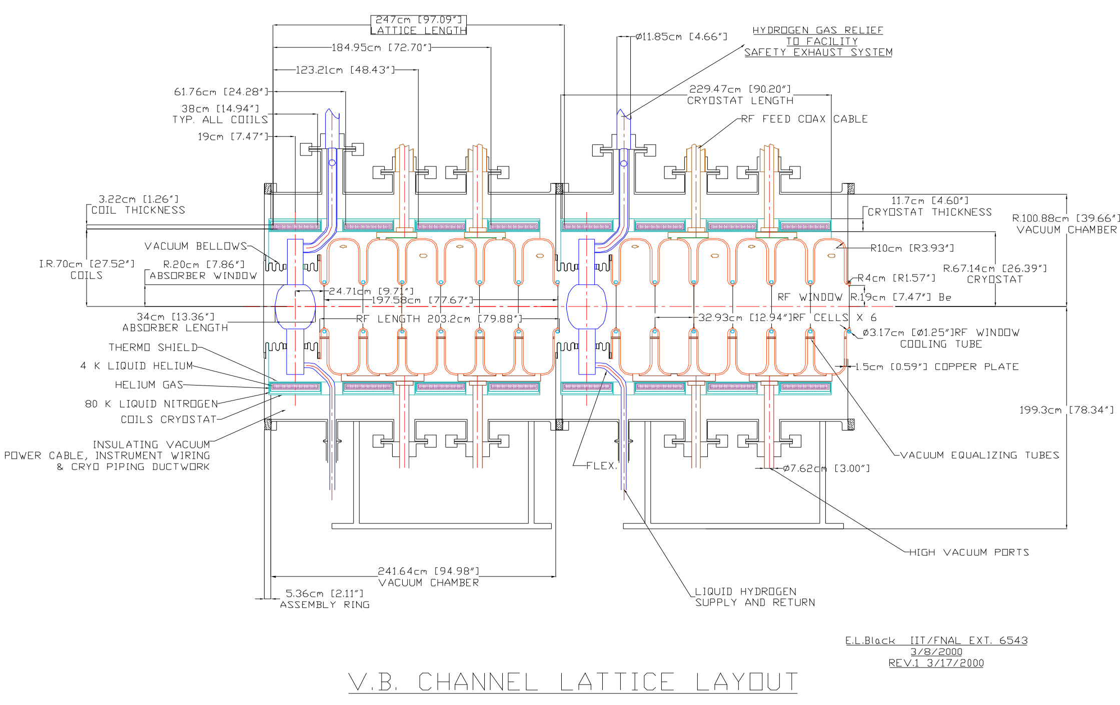

Figure 12: Engineering drawing of two sections of the single-flip cooling channel

The specifications of the cooling sections are given in Table 3. Each cooling section contains one liquid-hydrogen absorber and one linac consisting of 6 $\pi/2$ TM010-mode pillbox cavities. The absorbers are wider in diameter than they are long, but they are longer than in the FOFO case, allowing use of the ellipsoidal window profile and a concomitant decrease in window thickness. For ellipsoidal windows, the minimum thickness is given by [10]

$$t = 4\frac{0.5PD}{SE} \ ,$$

giving t = 300 μm as shown in the table. Note that the preliminary design for the cooling solenoids specifies 3-cm-thick coils at a current density of 400 A/mm^2. While this current density is within the specifications of NbTi superconductor for fields below 7 T [14], it implies a hoop stress BJR = 1800 MPa, exceeding the conservative limit used for the FOFO coil design (see Section 6.2.2). If hoop stresses need to be reduced, thicker coils at reduced current density could easily be used.

An absorber of length 32 cm will scatter the beam with an rms angle of approximately 0.016 rad. The initial rms angular spread of the beam is 0.160 rad. At the end of the first supersection, the rms angular divergence of the beam is 0.048, still larger than the multiple-scattering contribution. The length of this supersection could be extended to reach the multiple-scattering limit. However, the length is chosen both to minimize the length of the cooling channel and to compensate for the expansion of the beam envelope in the matching section. The length of the second supersection is additionally constrained by the requirement that the beam be canonical after the cooling channel. By design, the nominal particle gains 12.5 MeV per linac and loses 10 MeV per absorber, thus the nominal channel momentum increases linearly by 2.5 MeV per 2.47-m-long section. This acceleration is chosen to increase the size of the rf bucket and compensate for the increase of the rms energy spread through the channel. In 28 sections, the rms momentum increases from 30 to 36 MeV/c due to the range of path lengths in the absorbers. The goal of increasing the bucket size is to avoid particle loss due to this longitudinal phase-space dilution.

Given the momentum dependence of ionization energy loss, to lose 10 MeV per absorber, the absorber lengths must increase with longitudinal position as the beam momentum increases. In the first supersection, absorber lengths increase from 31.6 cm in the first cell to 33.8 cm in the 28th cell. The absorber length is constant at 34 cm in the second supersection. The beam starts out at a momentum of about 200 MeV/c, enters the matching section around 280 MeV/c, and exits the second supersection at 340 MeV/c.

The most sensitive parameter of the cooling channel is the gradient of the magnetic field in the field-flip region. This gradient must be maximized in order to stabilize the longitudinal motion. This is achieved by inserting two sets of coils, at differing radii, in the region of the field flip. The

PARAMETER	**VALUE**
Global	-
Length of a section, ΔL	2.47 m
Magnetic field on axis	5.0 Tesla
Magnetic field at the coil	6.3 Tesla
Field variation	0.02%
Current density	4,000,000 A/m
Coil radius	70 cm
$\beta_\perp$ min (z = 0)	21 cm
Number of sections per supersection	28
Absorber	-
Length of hydrogen (LH2) absorber	31 $\rightarrow$ 34 cm
Density of LH2	0.0708 g/cm^3
Thickness of absorber windows	300 μm
Material for absorber windows	Aluminum
Energy loss per section, nominal	~10 MeV
Radial aperture, in LH2	r = 20.0 cm
Linac	-
Length of linac (per section)	1.974 m
Number of rf cells	6
Frequency	201.25 MHz
Peak electric field, on axis	15 MV/m
Acceleration at ϕ_s = 90 degrees	13.4 MeV
Optimum synchronous phase ϕ_s	28.65 degrees
$\Delta\phi_s$ per section	0 to few deg.
Acceleration at optimum ϕ_s	12.5 MeV
Beryllium-window thickness	125 μm
Radial aperture, linac	r = 19 cm
Beam from buncher	-
Mean momentum	200 MeV/c
ε_N Normalized transverse emittance, initial	16.9π mm-rad
σ_x (lab frame), initial	4.5 cm
σ_{px} (lab frame), initial	32 MeV/c
Longitudinal bunch spread (full width)	±50 cm

Table 3: List of parameters for the 5T single-flip cooler with pillbox cavities. The hydrogen vessel and the linac are centered on the symmetry points of the section, at z = 0 and z =ΔL/2, respectively. The parameters of the input beam are listed at the end of the table.

matching section is the most technically challenging component of this cooling channel. The magnetic field at the large-radius coils (r = 70 cm), which run in opposite polarity, is ~9 T, while the current density is 375 A/mm^2. The field on the small-radius coils (r = 20 cm) is only 3 T, due to the near-zero average value of the field on axis in this region. The current density for these coils is 510 A/mm^2. While these current densities are reasonable for Nb_3Sn [14], the hoop stresses on the large-radius coils and the repulsive forces between them are large. This problem will require detailed engineering studies, however, since there is only one field flip in this channel the problem is considered tractable.

6.3.3 Performance

The performance of the channel is summarized in Figure 13. This channel cools in 2D by a factor of ~4 transversely, from 16.9π to 3.1π mm-rad, and heats longitudinally by a factor of ~2. As seen in the figure, the first half of the channel reduces the rms transverse momentum of the beam from 32 to 17 MeV/c without changing the size of the beam envelope. The change of field polarity in the matching section causes σ_{px} to grow by a factor of ~ 3. Due to the displacement of the Larmor orbits, the second supersection cools both σ_x and σ_{px}, to final values of 20 mm and 25 MeV/c, respectively. The second half recovers from the emittance growth in the field-flip region, cools the transverse size of the beam, and restores angular momentum such that the beam is canonical when it exits the cooling section.

Fractional transmission through this channel is approximately 50%. The bunch fills the 201.25-MHz rf bucket from the start, with a full width of ±1.8 ns (±50 cm). About half of the lost particles are muons that are not captured into the bucket; these are lost in the first few meters of the cooling channel. The remaining particle loss is due to the excitation of longitudinal motion in the field-flip region, where the longitudinal emittance grows by a factor of 4. Low-momentum muons are lost at the maximum of this synchrotron oscillation, ~10 – 15 meters after the matching section. Thus the second part of the channel scrapes longitudinally, resulting in a final full width of ±2 ns (±60 cm). At the current stage of optimization the yield within the acceptance of the acceleration (see section 6.1.2) is similar to or slightly better than that in the FOFO case.

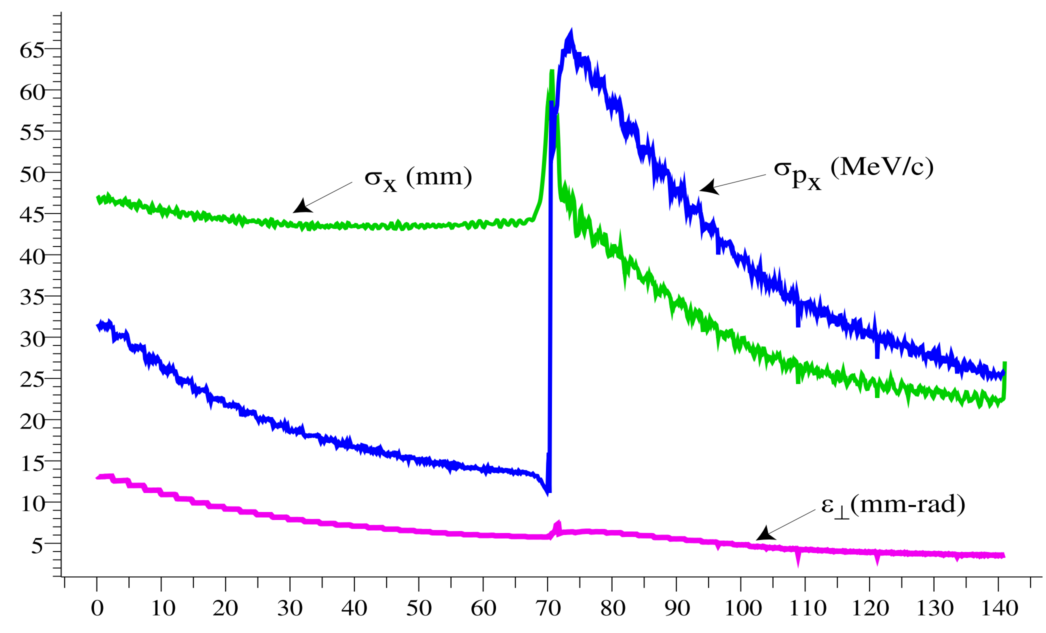

Figure 13: Performance of the 5T single-flip channel: rms transverse momentum ("σ_{px}"), rms transverse beam size ("σ_x"), transverse emittance $\sqrt{\varepsilon_{4D,n}}$ ("$\varepsilon_\perp$").

6.4 Summary

We have studied proposed designs for FOFO and single-flip cooling channels. The FOFO design has been extensively simulated using both DPGeant and ICOOL, and initial simulations of the single-flip channel have been performed using DPGeant. While the two channels have comparable cooling performance within the acceptance of the muon-acceleration system, they achieve that performance in differing ways that will be subject to differing engineering constraints. For example, the single-flip channel offers greater mechanical simplicity, since it has only one field reversal and uses longer absorbers with fewer windows. The two designs also make differing trade-offs between final transverse emittance and longitudinal bucket size: the single-flip channel studied here accelerates the beam during cooling, resulting in a larger bucket and reducing longitudinal losses at the expense of greater losses from the transverse cut imposed by the acceleration system. The implications of these sorts of trade-off are under investigation.

While both designs have adequate performance for an entry-level neutrino factory, both fall short of the PJK benchmark. In both cases, the performance of the cooling channel is limited by the parameters of the input beam provided at the end of the buncher. We expect that ongoing work on tuning and optimization will improve the muon yield by a substantial factor. We note in this regard the very recent work by Palmer *et al.* [15], which suggests that an additional factor 4 or more may be achievable by improvements in the phase rotation and buncher.

6.5 Future Steps

6.5.1 Cooling theory, simulation, and optimization

Although considerable progress has been made in understanding the problems involved in applying ionization cooling, and designing realistic cooling channels, more work is needed to optimize performance and to minimize cost. In particular, cooling the longitudinal phase space would ease the design requirements for all components of the machine downstream of the cooling section, thus helping to reduce the cost and to design more efficient components. We plan to continue simulation studies and optimizations of existing emittance-exchange concepts [1]. We would also like to consider other configurations, for example, one based on the helicoidal-channel proposal [16]. We plan to continue our work towards eliminating model uncertainties present in our current simulations of the ionization-cooling process. These include the correlations between straggling and large-angle-scattering, the atomic form factors that enter into the calculation of multiple scattering, and the effect of intense magnetic fields on these processes.

In this report we have presented two ionization cooling schemes based on differing design principles. The objective of our study is to design an efficient transverse cooling channel with components that can be built at the present time, or could be developed with a well-defined R&D plan. Detailed simulation studies are required to obtain the optimal solution for each of the available cooling channels. These studies will be crucial in selecting the best design, based on performance, engineering constraints, and cost. In particular, the engineering details of the design of the rf-cavity grids or windows (see Section 6.2.2), and their corresponding electric fields, will be implemented in our simulations. This project will require the use of full 3-dimensional codes and diagnostics to estimate reliably both the effects of scattering off these complicated shapes and the effects of the field on the longitudinal phase space. Evaluating the effect of alignment errors also requires 3D codes. Another project which requires this code development is the study of cooling channels that can achieve longitudinal cooling, because they involve elliptical or wedge-shaped absorbers. In addition, the optimization of each design must respect the engineering constraints on coil current densities, coil placement, and forces on the coils. Successive iterations of our simulation studies with the engineering analysis of each of the design variants will achieve the best solution. The performance of any cooling channel is tightly coupled to the performance of the machine components upstream of it and to the acceptance of the acceleration section that follows. For this reason, the optimization of the cooling channel will have to be iterated with the evolution of the designs of these other components.

6.5.2 Magnetic focusing system

The cooling channels described above require high magnetic field strength to reach low $\beta_\perp$ and precise field shape to control the beam dynamics. While we do not plan to rely on new superconducting materials or techniques, the optimization of the magnets demands proper engineering. For instance, a critical limit is the hoop stress on the windings for coils running with opposite currents. We therefore plan to tightly control future designs by obeying these design rules. Improving our knowledge and technical expertise in this area is critical.

6.5.3 Absorbers

The baseline (FOFO) cooling design requires liquid-hydrogen absorbers that are thin (~13 cm) relative to their diameter (20 - 30 cm). For a given pressure differential, hemispherical windows are thinnest, however, with this oblate shape thicker ellipsoidal or torispherical windows are required to provide a sufficiently short sagitta (see Section 6.2.2). For such absorbers scattering in the windows is of key importance, requiring R&D on exotic window materials (beryllium and/or AlBeMet) whose safety for LH_2 containment has yet to be established. While the lore within high-energy physics is that beryllium and LH_2 are incompatible, a less absolute view prevails in industry. A program of design studies backed up by carefully-designed tests will be needed to establish safe design and operating parameters for beryllium-containing windows for LH_2containment. With 40% greater strength than aluminum and 2.1 times the radiation length, AlBeMet has the potential to lower the total radiation-length fraction per absorber from ~2.4% to 1.8% or less, depending on the detailed optimization of absorber dimensions. (While beryllium windows may also be feasible, there appears to be little additional gain in going beyond AlBeMet.)

Other cooling scenarios use absorbers that are thicker compared to their diameter. Here effects of windows on cooling performance are reduced, and aluminum windows may be adequate. Whether R&D on exotic window materials is worthwhile may thus depend on which cooling approach prevails.

In all scenarios the specific power dissipation in the absorbers is large and represents a substantial portion of the cryogenic load of the cooling channel. Handling this heat load is a significant design challenge. An R&D program is already in place at IIT to understand the thermal and fluid-flow aspects of maintaining a constant temperature within the absorber volume despite the large spatial and temporal variations in power density. This program is beginning with computational-fluid-dynamics studies and is planned to proceed to bench tests and high-power beam tests of absorber prototypes over the next year.

In some scenarios (especially those with emittance exchange), lithium hydride (LiH) absorbers may be called for. Since it is a solid, LiH in principle can be fabricated in arbitrary shapes. In emittance-exchange channels, dispersion in the lattice spatially separates muons according to their energies, whereupon specially shaped absorbers can be used to absorb more energy from muons of higher energy and less from those of low energy. However, solid LiH shapes are not commercially available, and procedures for their fabrication would need to be developed. Such an effort is challenging since LiH reacts with water, releasing hydrogen gas and creating an explosion hazard.

6.5.4 Beam Diagnostics

Techniques for optimizing the operation of a physical cooling channel must also be developed. Alignment errors in constructing the magnetic system need to be tracked. The beam emittances and particle losses in these cooling channels must be measured in order to optimize running conditions. These beam measurements will be complicated by the large size of the beam, the poor access (see

Figure 4 and Figure 10), high magnetic fields, need for low-temperature insulation, and short bunch structure. This subject has not received attention comparable to other parts of the study, although a preliminary examination of some of these issues has been done [17].

Although measurements of muon beams have been done for years, the high precision, high intensities, limited access, and large backgrounds associated with the cooling channel may make the required measurements difficult.There are a number of measurements that seem to be required in order to optimize the performance of the cooling system. These requirements include: 1) initial matching of the cooling optics to the beam parameters, 2) maintaining this match down the length of the cooling channel, 3) producing and maintaining the physical alignment of beam components, 4) identifying and minimizing transverse and longitudinal loss mechanisms, and 5) measurement of the emittance at various stages of cooling. Since the emittance will only change by a few percent in each cooling section, it may be desirable to have a few special diagnostic sections interspersed with cooling sections to make precise measurements.

One would ideally like high-precision measurements of the six-dimensional muon phase space at a variety of locations along the cooling channel and acceleration system, although the only experimentally available quantities are the transverse and longitudinal bunch profiles. Measurement of the muon emittance from a beam profile is complicated by possible mismatches in the cooling optics which could produce uncertainties in the beta function and the calculated emittance. Measurements could also be complicated by pion and other backgrounds, particularly at the upstream end of the cooling channel.

While many conventional accelerator diagnostics may be appropriate for some applications, it seems desirable to look carefully at secondary emission monitors (SEM's) and Faraday cups. The intense muon beams expected would produce large signals without amplification, and the short range of low-energy muons would permit the option of stopping the beam in a transmission line and looking at the electrical pulse directly. Using one possibly appropriate geometry, Beck and Schutt [18] have demonstrated an 18-ps rise time with good dynamic range. A variety of options may be available for destructive and non-destructive diagnostics using these principles.

REFERENCES

[1] C. M. Ankenbrandt *et al*., "Status of Muon Collider Research and Development and Future Plans," Phys. Rev. ST Accel. Beams, **2,** 081001, (1999).

[2] G.I.Budker and A.N.Skrinsky, "Electron cooling and new possibilities in elementary particle physics," Sov. Phys. Usp. **21**, 277 (1978).

[3] D.Neuffer, Particle Accelerators **14,** 75 (1983).

[4] G. Penn, "Beam Envelope equations in a Solenoidal Field," MUCOOL Note 71 (http: www-mucool.fnal.gov/mcnotes/muc0071.ps).

[5] R. B. Palmer, C. Johnson and E. Keil, "A cost effective design for a neutrino factory," **BNL-66971, CERN SL/99-070**, also available at http: www-mucool.fnal.gov/mcnotes/muc0067.ps.

[6] K. J. Kim and C. X. Wang, "Formulae for Transverse Ionization Cooling in Solenoidal Focusing Channels," MUCOOL Note 92 (http: www-mucool.fnal.gov/mcnotes/muc0092.ps).

[7] R. Fernow, "ICOOL, A simulation Code for Ionization Cooling of Muon Beams," **Proceedings of the 1999 Particle Accelerator Conference,** A. Luccio, and W. MacKay, eds. (IEEE, Piscataway, NJ, 1999), p. 3020.

[8] DPGeant is based on the Geant3 simulation tool kit, see http: www-pat/simulations/muc; also the "Geant3 User Manual," http://wwwinfo.cern.ch/asd/geant/index.html .

[9] J. Miller (National High Magnetic Field Laboratory, Florida State University), private communication.

[10] "ASME Boiler and Pressure Vessel Code," ANSI/ASME BPV-VIII-1 (American Society of Mechanical Engineers, New York, 1980), part UG-32.

[11] "Guidelines for the Design, Fabrication, Testing, Installation and Operation of Liquid Hydrogen Targets," Fermilab, Rev. May 20, 1997; J. Kilmer, private communication.

[12] J. W. Mark, SLAC-PUB-3169 (1984) and references therein.

[13] E. J. Beise *et al*., Nucl. Instrum. Meth. A378, 383 (1996).

[14] I. Bogdanov *et al*. (IHEP Protvino), private communication. Hoop-stress limits [9] may require a design with lower current density.

[15] See R. B. Palmer *et al*., http://pubweb.bnl.gov/people/palmer/nu/pjksim/pjksim.ps.

[16] Ya. Derbenev, talk given at the 1999 conference on Muon Collider, San Francisco.

[17] J. Norem, "Muon Diagnostic issues for the Neutrino Source," MUCOOL Note 85 (http: www-mucool.fnal.gov/mcnotes/muc0085.ps).

[18] G. Beck and D. W. Schutt, Rev. Sci. Instr. **43** (1972) 341.

7. Design of a Muon Accelerator for the Neutrino Factory

7.1 Introduction

The muon accelerator must deliver a pulsed 50 GeV beam to the storage ring with an intensity of 6×10^{20} charged particles per year delivered in 2×10^{7} seconds, an average beam power of 240 kW. Large transverse and longitudinal acceptances are required, and they drive the design toward low rf frequency, especially in the early stages of acceleration. This is reflected in the layout (for example Figure 1 in the introduction), in which the second recirculating linac (RLA2) is seen to be the dominant subsystem of the whole facility. High accelerating gradients are necessary to preserve the muon flux given the short muon lifetime. Were normal-conducting cavities used, achieving high gradients would require high peak power, higher than is available in low-frequency rf sources. The number of sources would be large and the installation would become prohibitively expensive. Superconducting rf (srf) cavities are a much more attractive solution. SRF offers additional advantages: rf power can be delivered to the cavities over an extended time, and power dissipation is of much less concern given the very high cavity quality factor (Q). The muon accelerator is therefore baselined on srf technology.

PARAMETER	BASELINE VALUE
$p_{injection}$	190 MeV/c
E_{final}	50 GeV
$\varepsilon_N^{injected}$	1.5 mm-rad
$\varepsilon_N^{extracted}$	3.2 mm-rad
$\Delta E/E_{final}$	$< \pm 2\%$
σ_l^{bunch}, injected	12 cm
$\sigma_{\delta p/p}^{bunch}$, injected	11%
macropulse length	four 150 nsec pulses with 250 nsec pulse-to-pulse separation
N_{bunch}/macropulse	30 x 4 = 120
N_μ/macropulse, extracted	$(1.5\times$design$)$ 3 x 10^{12}
$f_{macropulse}$	15 Hz

Table 1: System Parameters

The accelerator will capture 190 MeV muons from the cooling channel and accelerate them to 50 GeV. Table 1 lists the input parameters, and Table 2 presents derived machine parameters (such as average and peak currents) used in subsequent discussion.

Parameter	Derived Value	Comments
I_{ave}	7.2 μA	Macroscopic average current
$I_{in\ pulse}$	0.8 A	Current in quarter-macropulse
P_{ave} $(1.5\times$design$)$	360 kW	Macroscopic average beam power
$P_{in\ pulse}$	40 GW	Beam power in quarter-macropulse
$\beta_{injection}=v/c$	0.87	
$\varepsilon_{injected}^{geometric}=\varepsilon_N^{injected}/\beta\gamma$	9 x 10^{-4} m-rad	Injected geometric emittance
$\varepsilon_{extracted}^{geometric}=\varepsilon_N^{extracted}/\beta\gamma$	6.4 x 10^{-6} m-rad	Extracted geometric emittance
$\sigma_{betatron}^{injected}(\beta=1\text{ m})$	3 cm	Injected rms spot size at beam envelope of 1 m
$\sigma_{betatron}^{extracted}(\beta=10\text{ m})$	8 mm	Extracted rms spot size at beam envelope of 10 m

Table 2: Derived Parameters

7.2 Fundamental Issues

The primary technical issues, to be discussed in this chapter, are:

- muon survival,
- choice of accelerating technology and frequency,
- accelerator acceptance – capture, acceleration, and transport of the large muon phase space, and
- accelerator performance – issues such as potential collective effects (e.g., cumulative beam breakup) resulting from the relatively high peak current during the muon macropulse.

7.2.1 Muon Survival

Given their intrinsic lifetime of 2.2 ìs, one must fight muon decay d uring acceleration. Figure 1 shows the fractional muon survival as a function of distance along the machine for various rf real-estate gradients. An average gradient of 5 MV/m ensures >80% of the initial beam survives for injection into the storage ring.

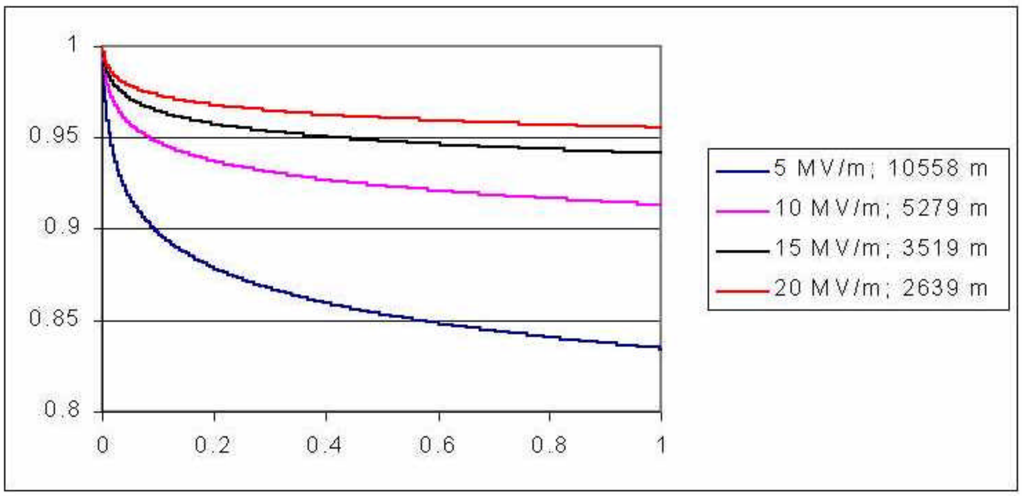

Figure 1: Muon survival during acceleration from 190 MeV to 50 GeV versus real-estate gradient and fractional distance along machine.

7.2.2 Selection of Acceleration Technology

Muon survival demands either a high-gradient linac or high-gradient recirculating linac. The large acceptances (longitudinal and transverse) required as a product of muon cooling, combined with the fact that the source beam is bunched at 200 MHz, lead to the choice of 200 MHz rf for the first part of the accelerating system and to possibly higher-harmonic rf frequencies at higher beam energies. Several technology choices are available; they are summarized as follows:

- Straight and/or recirculating linacs, or a combination of both;
- Pulsed and/or cw rf:
  1. "fast" – on microsecond time scales, with high peak power and short pulses, or
  2. "slow" – on millisecond time scales, filling cavities slowly between pulses and accelerating the beam using the stored energy.

The desire to keep wall losses low and rf-power requirements manageable excludes recirculation and "slow-pulse" scenarios with copper linacs. Gradients achievable with conventional cw rf are too low for adequate muon survival. "Fast-fill" pulsed (conventional or srf) systems involve prohibitively high peak power (~0.8 A x 50 GeV = 40 GW in each quarter of the macropulse) with associated high cost. The scenario of choice is therefore "slow-fill" pulsed or cw srf, with either straight or recirculated transport, the idea being to fill at 15 Hz while the beam is off and accelerate using only a small fraction of the stored energy.

Recirculation saves money over a single linac. Cost considerations favor multiple passes per stage, but practical experience commissioning and operating recirculating linacs dictates prudence. Experience with recirculating linacs at Jefferson Lab suggests that recirculation should be possible once the muon energy is larger than 3 GeV. Given the large initial emittance and energy spread, a ratio of final-to-injected energy well below 10-to-1 is deemed prudent [1]. We therefore propose a machine architecture featuring a 0.2-to-3 GeV straight "preaccelerator" linac, a 3-to-11 GeV recirculating "compressor" linac (RLA1), and a 11-to-50 GeV recirculating "primary" linac (RLA2). The *preaccelerator* captures the large phase space coming from the cooling channel and accelerates it to relativistic energies. At this point, the increased muon lifetime ($\gamma\tau$) allows use of a *compressor* (RLA1). During compression, the longitudinal and transverse phase spaces are shaped (while further raising the energy) for injection into the high-energy *primary* (RLA2), which then generates the 50 GeV injection energy for the storage ring.

The 200 MHz microbunch spacing from the cooling channel imposes an rf-frequency requirement of 200 MHz or one of its harmonics. The frequency of choice for both the preaccelerator and the compressor is 200 MHz, as it provides large physical apertures (well in excess of the spot sizes given in Table 2) and adequate transverse and longitudinal acceptances for the source beam. It also provides adequate stored energy to accelerate multiple passes of a single-pulse bunch train without need to refill the extracted energy between turns. Thus, the "slow-fill" pulsed scenario is viable.

The choice is less obvious for the primary (RLA2), inasmuch as the phase space is smaller and rather more manageable. Preliminary studies suggest that the first harmonic, 400 MHz, may provide an adequate aperture and acceptance. If so, the higher frequency is desirable in that it provides significant cost savings during operation (compare chapter 10). Detailed calculations affirm that the larger stored energy at 200 MHz (in contrast to 400 MHz, where the stored energy per unit length is 4 times smaller) and the longer rf wavelength generate a smaller momentum spread through the acceleration cycle. This is due to the smaller ratio of bunch length to wavelength, as well as smaller gradient sag during energy extraction over the macropulse. Accordingly, the acceptance requirement is relaxed. However, it is not clear that 200 MHz is necessary. The following "solution in progress" attempts to provide adequate recirculator acceptance to manage the larger momentum spread (and tighter bunch-length tolerances) associated with 400 MHz. Preliminary results suggest the required performance can be met. Because of significant cost savings, it is therefore our baseline frequency for RLA2. If further studies indicate that 400 MHz will not provide an adequate performance, the 200 MHz solution used in the preaccelerator and compressor will be used for the primary as well.

7.3 Machine Architecture

The proposed machine architecture is based on the aforementioned chain of three accelerators. The preaccelerator brings the beam to relativistic energies where recirculation can be invoked. The compressor (RLA1) then conditions the phase space by raising the beam energy and adiabatically damping the geometric emittance, relative momentum spread, and bunch length, so as to render the phase space volume manageable for the primary (RLA2). The principal beam dynamics issues are:

- capturing the large longitudinal and transverse emittances of the injected beam;
- minimizing the recirculatable energy;
- devising acceleration/longitudinal matching scenarios in the compressor to optimize the phase space for subsequent acceleration to full energy;
- designing RLAs 1 and 2, to include: initial and final energies, numbers of passes, and transport optics for adequate acceptance in the presence of the required longitudinal manipulations; and
- potential instabilities (such as beam breakup) at the relatively high (amp-level) peak currents present in the macropulses.

An "existence proof" with sufficient (though perhaps better than necessary) performance to address these issues has evolved based on the machine concept described above. The large injected phase space is a primary concern, and a longitudinal capture and acceleration scenario was developed first during the design process [1]. This indicated that a 200 MHz, 3 GeV preaccelerator would provide adequate capture and a high enough energy to guarantee longitudinal matching into RLA1. A 3-to-11 GeV RLA1 concept based on 4 recirculations with 200 MHz rf was then developed. The energy range and pass number were chosen to be prudently conservative from a geometric and beam-dynamics point of view, given the need to accommodate beam splitting, recirculation, and recombination of the large phase space on multiple passes while providing adequate opportunity for longitudinal matching. The acceleration phases and momentum compactions were selected to compress both the relative momentum spread and bunch length. A notional view of the cryomodule layouts appears in Figure 2. A similar process was applied to RLA2, resulting in 5-pass primary acceleration from 11 to 50 GeV. As mentioned before, preliminary results suggest that a 400 MHz system provides adequate performance for RLA2, though with larger intermediate momentum spreads than in a 200 MHz system.

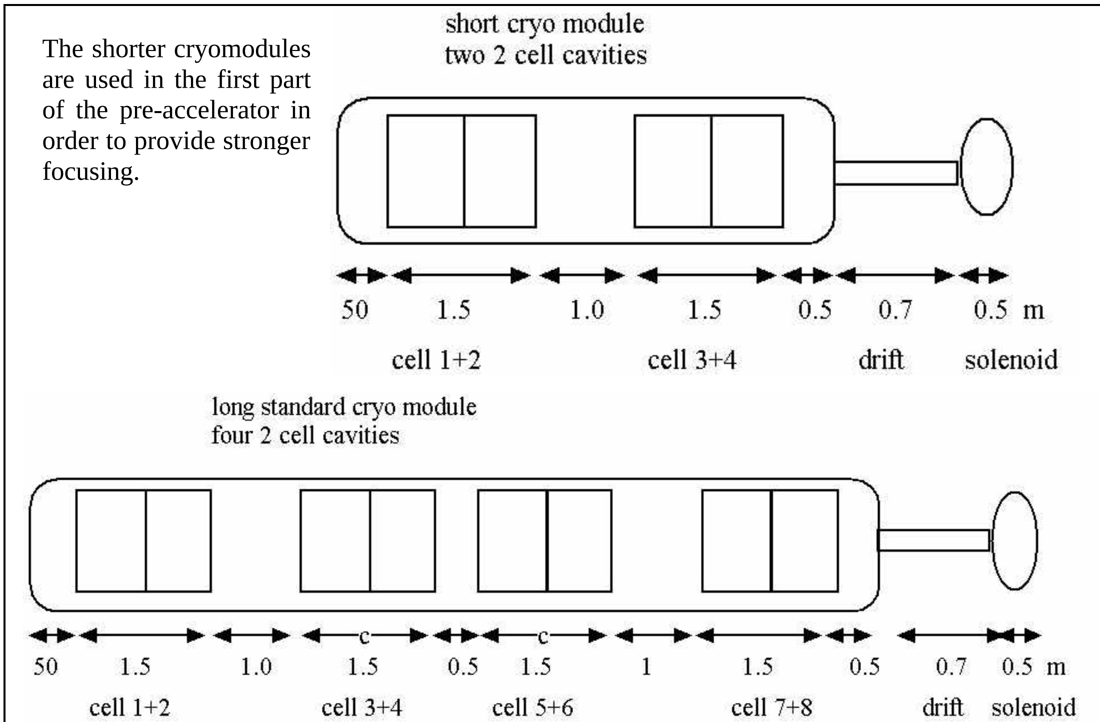

Figure 2: Sketch of the cryomodule layout for the first part of the preaccelerator and for the later part as well as RLA1.

For the tracking studies an initial distribution function is generated using the following procedure. First, for each particle six random numbers, (j is the particle number, and i = 1,…6), are used to generate an initial particle position in the 6D-phase space. The random number generator generates numbers with a Gaussian distribution, which has a mean value equal to zero and a standard deviation equal to one. Second, for each particle its radius (distance from the coordinate system center),

$$r_j = \sqrt{\sum_{i=1}^{6} u_i^2}$$

is computed, and all particles for which the radius is more than 2.5 are discarded. Third, real particle coordinates are computed using following formulas:

$$\begin{bmatrix} x_\beta \\ x'_\beta \\ y_\beta \\ y' \\ s \\ \Delta p/p \end{bmatrix}_j = \begin{bmatrix} \sqrt{\varepsilon_x \beta_x} & 0 & 0 & 0 & 0 & D_x \sigma_p \\ -\alpha_x \sqrt{\frac{\varepsilon_x}{\beta_x}} & \sqrt{\frac{\varepsilon_x}{\beta_x}} & 0 & 0 & 0 & D'_x \sigma_p \\ 0 & 0 & \sqrt{\varepsilon_y \beta_y} & 0 & 0 & D_y \sigma_p \\ 0 & 0 & -\alpha_y \sqrt{\frac{\varepsilon_y}{\beta_y}} & \sqrt{\frac{\varepsilon_y}{\beta_y}} & 0 & D'_y \sigma \\ 0 & 0 & 0 & 0 & \sigma_s & 0 \\ 0 & 0 & 0 & 0 & \alpha_s \sigma_p & -\sigma_p \sqrt{1-\alpha_s^2} \end{bmatrix} \begin{bmatrix} u_1 \\ u_2 \\ u_3 \\ u_4 \\ u_5 \\ u_6 \end{bmatrix}_j$$

where ε_x and ε_y are the transverse rms beam emittances, β_x, β_y, α_x and α_y, are the initial beta-functions and their negative half-derivatives, σ_s is the rms bunch length, σ_p is the relative rms energy spread, and α_s characterizes the rotation of the ellipse in the longitudinal phase space so that the longitudinal emittance is $\sigma_s\sigma_p \sqrt{(1-\alpha_s^2)}$. At entrance of the linear preaccelerator the following parameters have been chosen:
$\beta_x=\beta_y$ = 8.03 m, $\alpha_x = \alpha_y$ = -0.122, σ_s =12.11 cm, σ_p =0.11, σ_p = -0.139, $D_x = D_y = 0$, $D'_x = D'_y = 0$. The particle ellipse in the longitudinal phase space is slightly tilted. Its axes will be coinciding with the coordinate frame axes after 0.65 m drift.

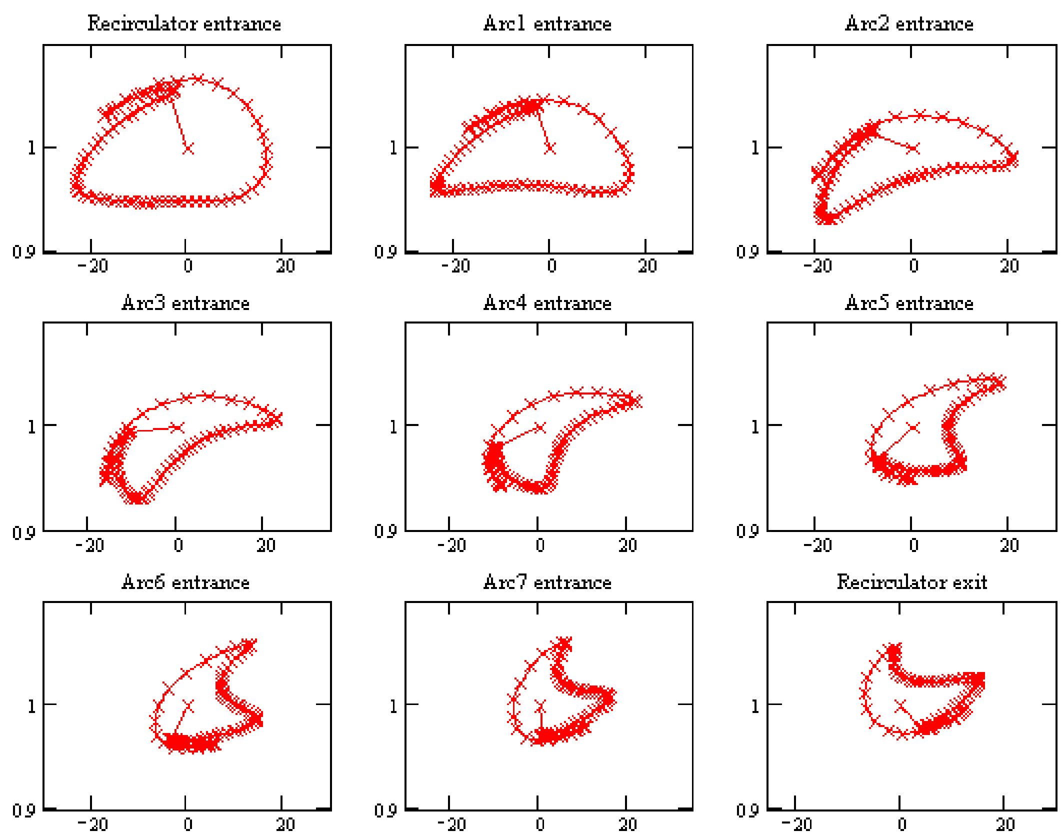

Figure 3: Longitudinal Phase space in RLA1. The units are p/p_o on the ordinates and rf phase in degrees on the absiccas.

Figure 3 and 4 illustrate the behavior of the longitudinal phase space through such a system; required acceleration phases and momentum compactions are shown in Table 3. Simulations of the 400 MHz scenario are at present incomplete, but they suggest that the higher frequency is feasible. A 200 MHz alternative has been studied in some detail [2] as well; it meets performance requirements and will be more robust, though at a higher initial investment and operational cost, and therefore the baseline frequency for RLA2 is taken to be 400 MHz.

Given a viable longitudinal scenario, a complete system solution was developed. The preaccelerator uses solenoid focusing between cryomodules. Beam envelopes are as shown in Figure 5. The compressor, RLA1, is a 4-pass machine comprising two 1.227 GeV linacs, with each pass split horizontally and

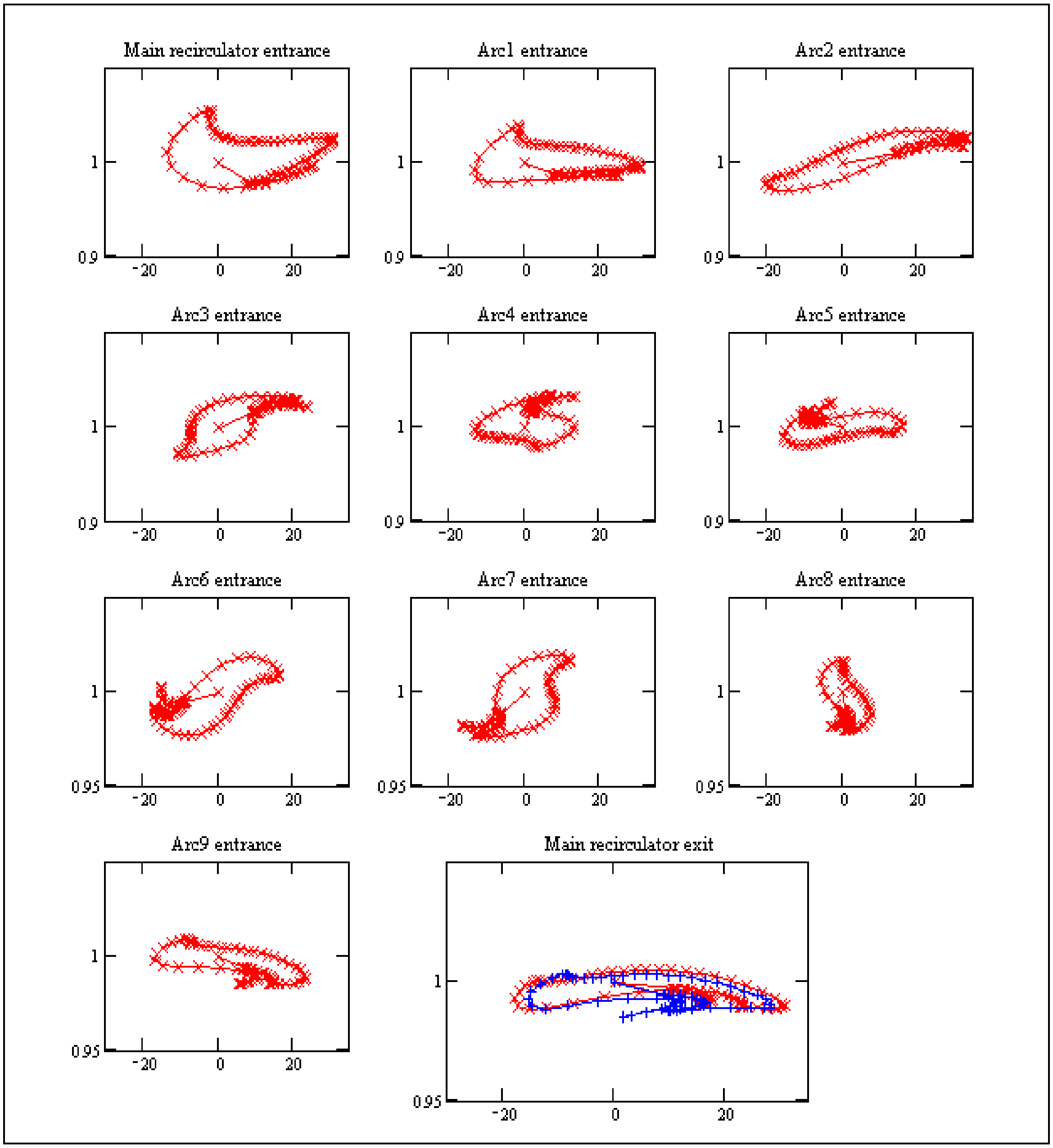

Figure 4: Longitudinal phase space in RLA2. The units are p/p_o on the ordinates and rf phase in degrees on the absiccas.

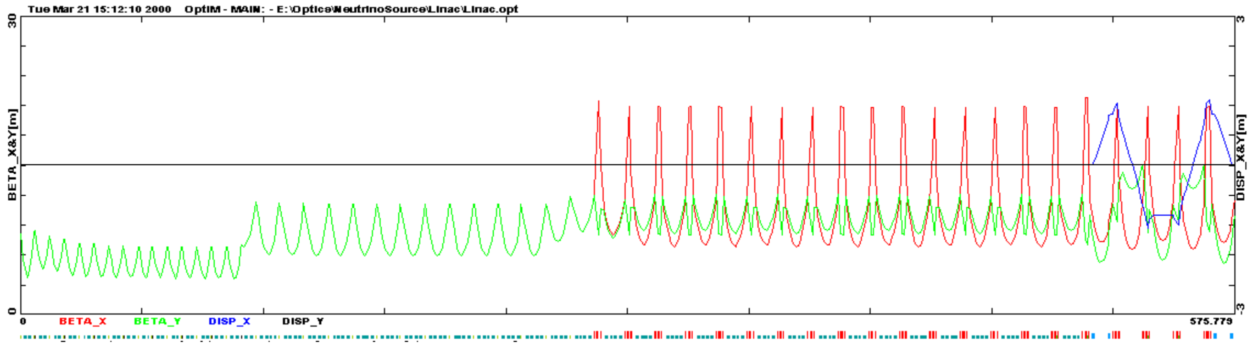

Figure 5: Beam envelopes in the pre-accelerator from injection to RLA1 at 2.8 GeV.

recombined using cascaded dipoles. Once separated, the individual beams are recirculated by periodic "bend-triplet-bend" arcs, producing typical beam envelopes as shown in Figure 6. Chromatic behavior is adequate to accept >10% momentum spread; no sextupole correction appears necessary.

Preaccelerator 200 MHz, 0.2→ 3 GeV energy; 15 MV/m gradient, accelerating phase -60°→ 0°				
RLA1 (Compressor) 200 MHz, 0.2→ 11 GeV energy; 15 MV/m gradient; total voltage/linac: 1.227 GV;				
	Kinetic energy (GeV)	M_{56} (m)	Gang Phase (deg)	Total energy spread 2Δp/p %
Entrance	2.89		6	11.7
Arc 1	4.11	0.6	-22	9.0
Arc 2	5.25	0.6	-25	9.9
Arc 3	6.36	0.6	-29	9.8
Arc 4	7.43	0.6	-38	9.2
Arc 5	8.40	0.5	-45	9.6
Arc 6	9.26	0.5	-45	9.9
Arc 7	10.13	0.5	-45	9.5
Exit	11.00	0.5		8.2
RLA2 (Primary) 400 MHz, 11→ 50 GeV; 15 MV/m gradient; total voltage/linac: 4.25 GV				
	Kinetic energy (GeV)	M_{56} (m)	Gang Phase (deg)	Total energy spread 2Δp/p %
Entrance	11.00	2.00	-7	8.2
Arc 1	15.22	2.00	-30	6.3
Arc 2	18.9	2.00	-17	6.3
Arc 3	22.96	2.00	-30	6.4
Arc 4	26.64	2.00	-30	5.4
Arc 5	30.32	2.00	-30	4.5
Arc 6	34.00	2.00	-30	4.1
Arc 7	3.68	2.60	-11	4.3
Arc 8	41.85	2.60	-16	3.7
Arc 9	45.94	2.60	-17	2.5
Exit	50.00			1.6

Table 3: Accelerator Parameters.

A similar approach was adopted for RLA2, a 5-pass machine. Cascaded dipoles (Figure 7) split the passes horizontally, bringing all beamlines parallel in a few tens of meters. Because the linacs are much longer than in RLA1, additional matching is provided following the beam separation: in each pass an array of quadrupoles provides matching of the pass-to-pass beam envelopes to the regular, horizontally separated FODO arcs. Again, because the focusing is modest and the structure regular, there is no obvious requirement for chromatic correction.
The machine footprint is presented in Figure 8. For clarity and ease of comparison, the segments (preaccelerator, RLA1, and RLA2) are all positioned sequentially. For actual construction, economy suggests a more compact layout, possibly with shared usage of tunnel and conventional facilities by multiple machine segments.

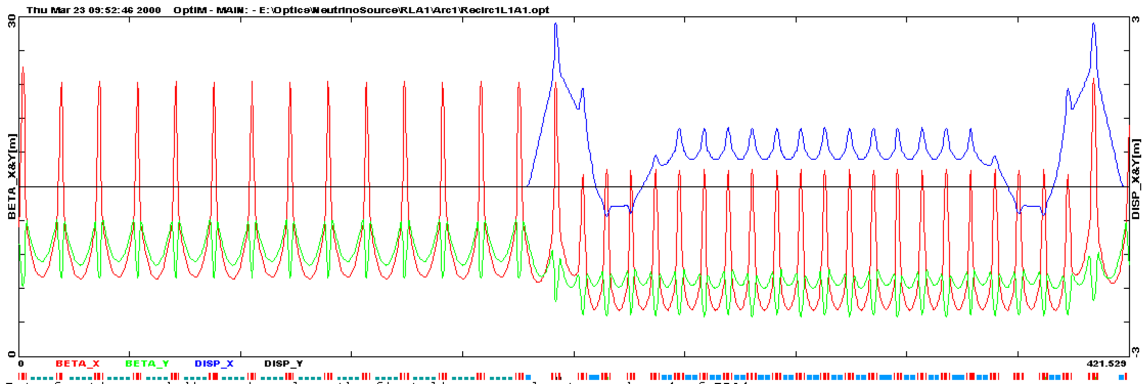

Figure 6: Typical RLA1 linac and arc beam-envelope functions.

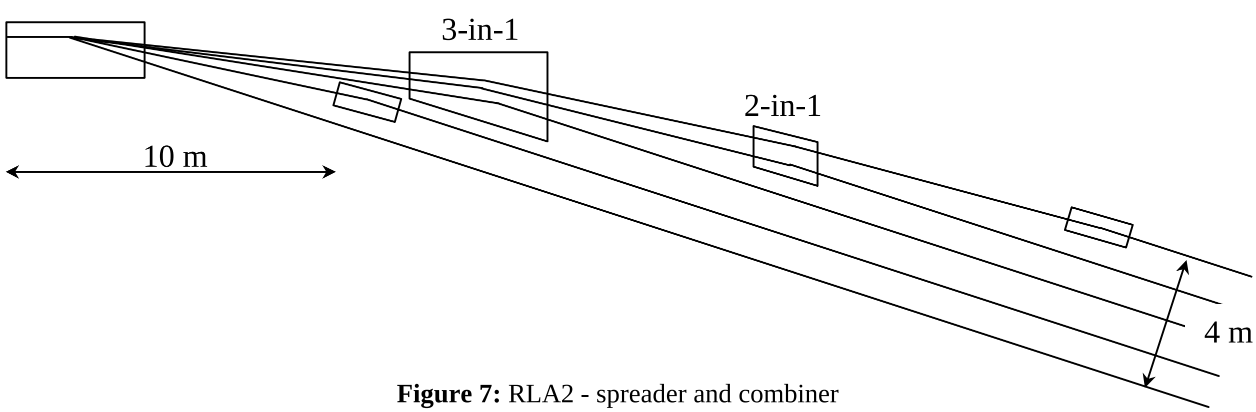

Figure 7: RLA2 - spreader and combiner

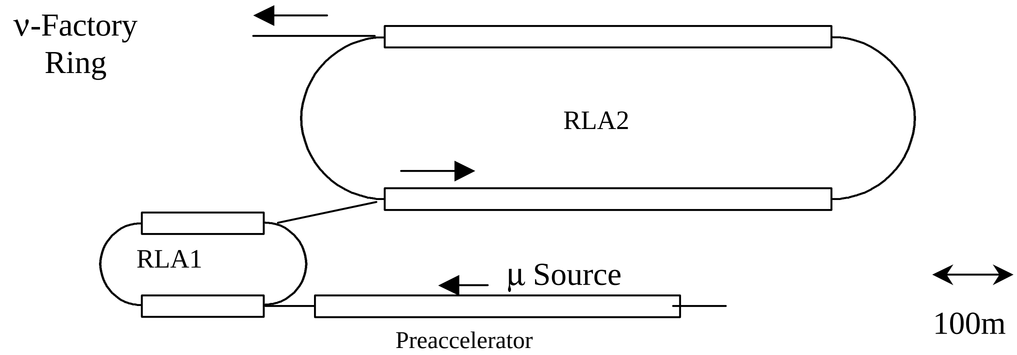

Figure 8: MAD accelerator concept.

7.4 Collective Effects

We examine two types of beam breakup (BBU) instabilities relevant to linacs, multipass BBU and cumulative BBU [4]. Multipass BBU is of most concern in accelerators in which the beam passes many times through the same linac structure. The important mechanism causing the instability is the fact that the recirculated beam can be displaced at a given cavity due to a kick it receives from a higher-order mode (HOM) in the same cavity on a previous pass. The displaced beam can then interact with the HOM fields on subsequent passes and feed energy into it, causing subsequent bunches to be kicked even harder. There is, therefore, a closed feedback loop between the beam and the HOMs formed within the structure. The M_{12} and M_{34} matrix elements (for the recirculation) are important for the feedback of the instability.

Cumulative beam breakup, on the other hand, results from the beam interacting with two or more cavities that make up the linac. Cumulative BBU begins when a bunch receives a transverse kick from a cavity HOM resulting in a transverse displacement in a downstream cavity. The displaced bunches can drive the HOM at the second cavity coherently thereby transferring kinetic energy into the HOM. Following bunches arriving at the downstream cavity are then more strongly deflected because of the additional energy contained in the HOM.

The important difference between cumulative and multipass beam breakup is that in cumulative beam breakup there is no feedback of the HOM energy of the driven cavity back to the cavity that initially deflects the beam. The cavities act to amplify the beam offsets due to the kick, and this amplification depends strongly on the beam current. The threshold current for cumulative BBU is the current where the offsets are amplified to the point where the beam hits the beam pipe.

The threshold current for multipass beam breakup (BBU) in CEBAF had been calculated to be ~20 mA for external Q's of the higher-order modes (HOMs) less than 10^5. Extensive simulations with TDBBU (a BBU code specially configured for recirculating linacs) seem to indicate that the threshold current scales approximately as the square-root of the product of the injection and final energies [4]. The muon linacs will require roughly an order of magnitude more cavities than the CEBAF linac; therefore, the impedance will be higher by an order of magnitude. Scaling with the rf frequency has been shown to be inversely proportional to the square of the frequency provided the accelerating gradient is frequency-independent, but it is inversely proportional to the frequency if the gradient varies linearly with frequency. Assuming the more pessimistic 1/ù scaling, and given E_{in}=3 GeV, E_{fin}=50 GeV for the muon linac and E_{in}=45 MeV and E_{fin}=4 GeV for CEBAF, we arrive at

$$I_{th} = 20mA \times \frac{1}{10} \times \frac{\sqrt{3GeV \times 50GeV}}{\sqrt{45MeV \times 4GeV}} \times \frac{1500}{200} \approx 433mA.$$

Note that if this were a truly cw linac, the average operating current would be ~50 mA, an order of magnitude lower than the threshold current. The damping time of the HOMs is $2Q/\omega$ = 16 μs for $Q=10^4$ and $\omega=2\pi\cdot$(200 MHz). Therefore, during the 10 μs between pulses, the fields will have almost decayed, implying a somewhat higher threshold for the pulsed machine than for cw.

Cumulative BBU also needs to be examined as it is typical in an S-band linac in the 100-mA range. At 200 MHz the shunt impedance and gradient scaling combined with the larger apertures should result in a factor of 10-20 higher threshold current. At ~1% duty factor, the equivalent threshold is ~100 A. In conclusion, these rough estimates based on scaling from existing accelerators indicate BBU will probably not be an issue for the muon linac if external Q's of HOMs are damped to 10^4 or lower. However, detailed simulations are needed to quantify more rigorously the points outlined here.

7.5 Superconducting RF Technology Issues

We now turn to srf considerations for a slowly pulsed, recirculating srf linac in which the macropulse acceleration is based solely on the stored energy in the cavity and not on refilling the cavities between turns or even within the macropulse. Recent technology developments suggest that one can assume the availability of superconducting cavities with single-cell properties similar to those summarized in Table 4. Here, we assume the availability of 15 MV/m gradients at both 200 and 400 MHz. The assumed unloaded quality factors (Q_0's) are consistent with those achieved in presently available srf systems. The stored energy is given by:

$$U_{stored} = \frac{E^2 l^3}{R/Q} \frac{10^4}{24p}$$

with λ the free-space wavelength, R/Q a geometric constant for the chosen cavity, and E the gradient. The data derived specifies the cw power deposited in the cryogenic system as a result of the rf power input. A summary is given in Table 5 for cw operation at 4.2 K. The number of cells is simply the installed voltage divided by the single-cell voltage in Table 4. The dynamic load is the number of cells times the power loss per cell given in Table 4.

Machine Stage	f (MHz)	l_{cell} (m)	E (MV/m)	V (MV)	U_{stored}/cell (J)	Q_0	R/Q (Ω/cell)	P_{lost} (cw, W/cell)
Pre-accelerator	200	0.75	15	11.25	1000	6×10^9	100	209
RLA1	200	0.75	15	11.25	1000	6×10^9	100	209
RLA2	400	0.375	15	5.625	125	6×10^9	100	52

Table 4: SRF cavities for muon accelerator: single-cell properties.

Machine Stage	Installed Voltage (GeV)	#cells	CW load (kW) @ 4.2 K
Preaccelerator	3.6	320	67
RLA1	2.6	231	48
RLA2	8.5	1079	56

Table 5: Dynamic load, 4.2 K operation

The total cw load is ~170 kW at 4.2 K. However, the linac is to operate in pulsed mode, filling prior to injection of the macropulse and using the stored energy to accelerate the beam for multiple turns. Pulsing will significantly reduce the dynamic heat load, roughly by the rf duty cycle. Considering this operating mode, we present in Table 6 a summary of the energy extracted by the macropulse as it traverses each accelerator segment. Table 6 gives, in particular, the energy and gradient sag due to extraction of rf energy by the beam.

Machine Stage	Charge/macropulse (μC)	# passes	V (MV)	ΔU (J)	$\Delta U/U_{stored}$ (%)	ΔV/V across pulse (%)
Preaccelerator	0.48	1	11.25	5.4	0.5	0.25
RLA1	0.48	4	11.25	21.6	2.2	1.1
RLA2	0.48	5	5.625	13.5	10.8	5.6

Table 6: Energy extraction per single cell during one macropulse.

The relative gradient sag is only half the stored-energy sag because the energy scales as the square of the gradient. The gradient sag imposes an energy slope along the macropulse, with the tail of the pulse experiencing less acceleration than the head. Given the large inherent energy spread of the beam, this sag will not be a problem in the preaccelerator or RLA1. However, it could become significant in RLA2 where the stored energy at the higher frequency is smaller and therefore more susceptible to the energy extracted by the macropulse. This might be accommodated as a part of the rf manipulations performed during longitudinal matching. For example, RLA2 arc momentum compactions and path lengths might be adjusted not only to do the required microbunch compression, but also to offset the energy slope induced across the macropulse. This possibility in principle is illustrated in Figure 3; the final frame in both Figure 3 and 4 includes data illustrating the beam-loading-induced energy slope from the head to the tail of the bunch train. The longitudinal match used to manage the large phase space similarly controls the spread across the macropulse. Once a final design is established, a methodology to implement this process operationally must be developed.

Also critical to this scenario is the availability of ~15 MV/m gradient at 200 and 400 MHz. If the gradient were lower, the stored energy would drop quadratically, and the gradient droop would increase significantly, unless the charge per macropulse were reduced. This may ultimately motivate the use of 200 MHz rf in RLA2 with an associated increase in dynamic load but with less risk to machine performance. A detailed design study must evaluate this cost/risk/benefit tradeoff. Given, however, the availability of adequately high gradients and the development of an operationally appropriate longitudinal matching scenario both to compress the microbunch phase space and manage the gradient sag across the macropulse, the “slow-fill" scenario can be applied in this system with adequate performance. Moreover, use of 200 MHz in all machine stages (as a contingency) clearly allows this mode of operation.

Details of pulsed operation evolve from consideration of rf-power requirements. Table 7 presents power demands for each of the machine stages. The average beam-loading current is just the product of the macropulse charge (0.48 μC), the repetition rate (15 Hz), and the number of passes through the segment; the average extracted power is the product of the single-cell voltage and the average beam loading current. The power to control microphonics and detuning is the product of the stored energy and the detuning bandwidth $\delta\omega$ (U_{stored} x $\delta\omega$), here taken to be 2π x 80 Hz. Though only an approximation, this result is valid provided the detuning bandwidth is much greater than the intrinsic bandwidth, which is certainly true for the case under consideration. This power requirement corresponds to an infinite time to fill the cavity, and therefore differs from the particular rf power demanded. Rather, at low average current the required power is determined by the necessity to establish and maintain the fields in the presence of detuning. It is therefore important to optimize the coupling by choosing the loaded Q (Q_L) carefully.

Machine Segment	# passes	$I_{average}$ (μA)	V (MV)	$P_{average}$ (W)	U_{stored}/cell (J)	$P_{control}$ for 80 Hz bandwidth, (kW)
Preaccelerator	1	7.2	11.25	81	1000	503
RLA1	4	28.8	11.25	324	1000	503
RLA2	5	36	5.625	203	125	63

Table 7: Single-cell rf power requirements.

Optimization of Q_L is typically accomplished by selecting a coupling that minimizes the required rf power given the anticipated operating parameters. For infinite fill time this is straightforward. The rf power is given in terms of cavity parameters by the following expression, in which $\Omega=\omega_0+\delta\omega$, with ω_0 being the cavity angular frequency and $\delta\omega$ the angular detuning bandwidth [5]:

$$P=\frac{(Q_0/Q_L)^2}{4(Q_0/Q_L-1)Q_0}\frac{V^2}{(R/Q)}\left\{\sqrt{1+Q_L^2\left(\frac{w_0}{\Omega}-\frac{\Omega}{w_0}\right)^2}+\frac{(R/Q)Q_L\,I_{average}}{V}\right\}^2$$

Other parameters are as specified in Tables 4 through 7. Figure 9 presents the required rf power versus Q_L for several detuning bandwidths at 200 MHz for preaccelerator parameters and 400 MHz for RLA2 parameters (Figure 10). The RLA1 result will be virtually identical to that of the preaccelerator. This is because, as mentioned before, at these low average currents the required rf power is dominated by the need to establish and control the field in the presence of static and dynamic detuning, and not by the beam loading. The optimum Q_L is simply the value providing the minimum required power; it can be either read off Figure 9 or Figure 10 or derived analytically by minimizing the above power expression with respect to Q_L for the desired parameter set.

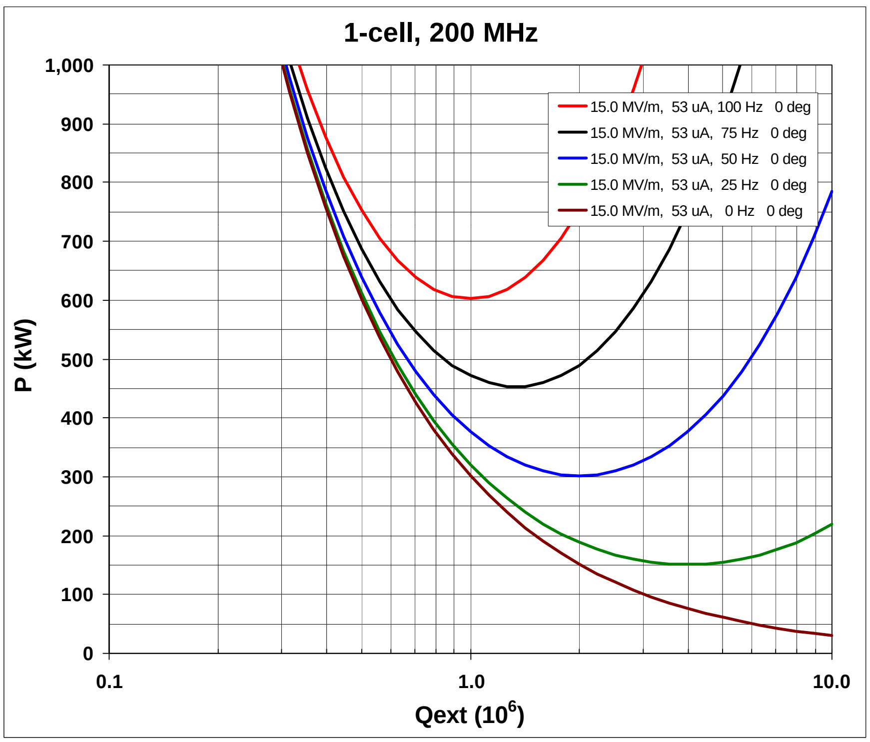

Figure 9: RF power requirements for 200 MHz single cells. 200 MHz, $Q_0=5\times10^9$, V=11.25 MV, R/Q=105 Ω, $I_{average}=7.2$ µA. Calculated for infinite filling time.

The preaccelerator (and by implication RLA1) system will handle ~80 Hz detuning with under 500 kW power provided coupling is chosen such that Q_L~1.25×10^6. This rf power is within the limits of present technology and can be delivered to the cell through existing, albeit state-of-the-art, couplers. Similarly, the RLA2 system will manage ~80 Hz detuning with ~125 kW power when the coupling is chosen so that

Q_L~2.5x10^6. The power requirements are similar to the estimates given above; they are very preliminary. They are again based on the assumption that the system operates with very small currents and even more on the fact that a detuning bandwidth of 80 Hz is feasible. Especially the second part can only be answered by an R&D program, which would emphasize this question by constructing a cavity especially suited for this purpose (i.e., minimizing Lorentz-force detuning and microphonics) .

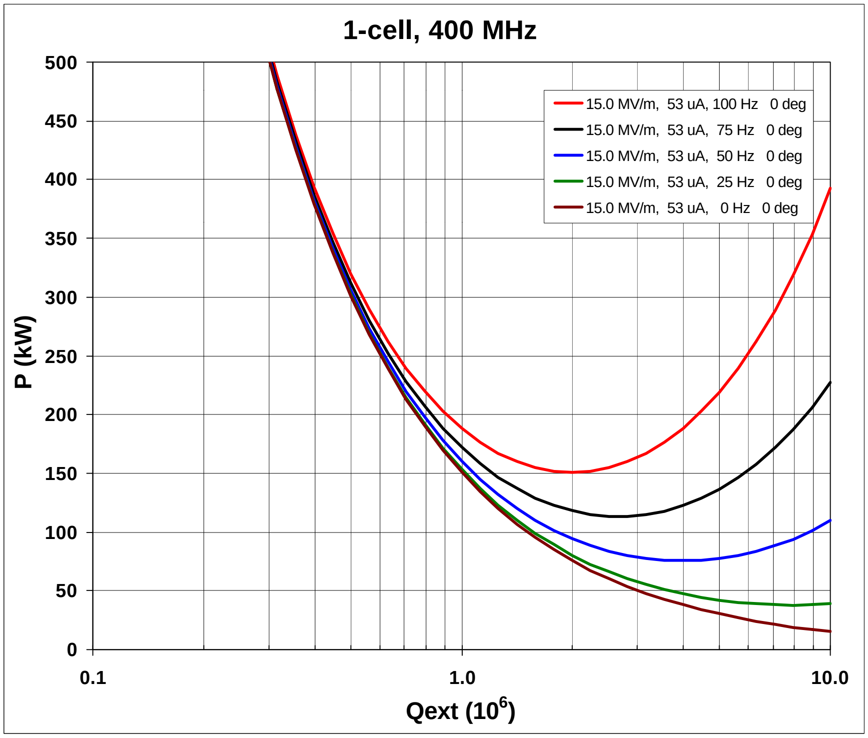

Figure 10: RF power requirements for 400 MHz single cells, Q_0=5x10^9, V=5.625 MV, R/Q=52.5 Ω, $I_{average}$=36 μA. Calculated for infinite filling time

For finite filling times, the analysis is less transparent. In this case (in the zero-current limit applicable to this machine), the power as a function of fill time T, coupling $\beta=Q_0/Q_L-1$, stored energy U, detuning bandwidth δω, and intrinsic bandwidth $\Delta\omega_0=\omega_0/Q_0$ can be derived from

$$P = \frac{U\ \Delta w_0}{\left[1-\exp\left(-\frac{T\Delta w_0(b+1)}{2}\right)\right]^2}\frac{1}{4b}\left[(b+1)^2+\left(\frac{2dw}{\Delta w_0}\right)^2\right]$$

The optimum Q_L (or coupling β) is that which minimizes the required power. This case is not amenable to simple analytic treatment because of the time dependence. Instead, a numerical solution is used to minimize the power as a function of coupling. Figure 11 presents the optimum power, coupling, and detuning as functions of fill time (fill time ≡ rf pulse length in this case) for parameter sets appropriate to this machine. The asymptotic limit is simply that given above; as the fill time decreases to below ~10 ms, the required power rises, and the optimum coupling and bandwidth change.

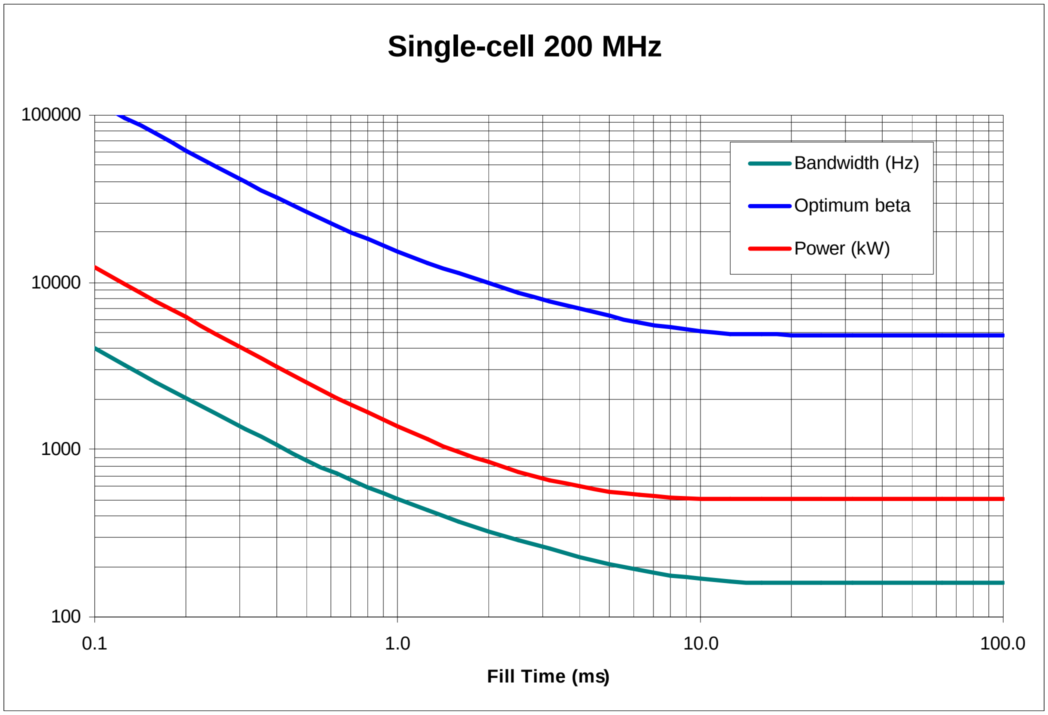

Figure 11: Optimized power, coupling, and bandwidth as a function of fill time. (200 MHz system case).

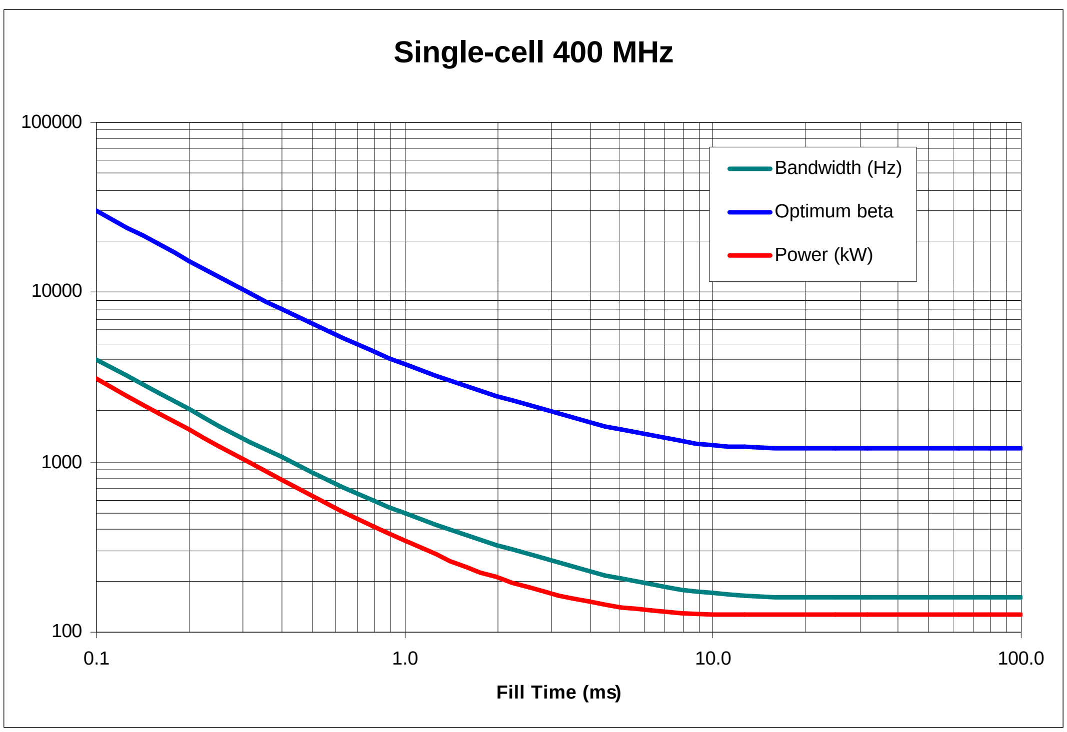

Figure 12: Optimized power, coupling, and bandwidth as a function of fill time. (400 MHz system case)

For a more detailed design a filling time (or duty cycle) must be chosen consistent not only with rf power requirements, but also with the constraint of cryogenic loads in place. For this study, we examine a fill time of 2 ms, which corresponds to a duty cycle of 3% at 15 Hz macropulse repetition rate. The preaccelerator and RLA1 will optimally require 820 kW at a coupling of about 9750, corresponding to a Q_L of 6.1 x 10^5, while RLA2 will require 200 kW at a coupling of 2500, and a Q_L of 2 x 10^6. At this duty cycle, the dynamic heat load for the full machine is 3% of the 171 kW cw load quoted in Table 5, or 5 kW. Given the details of a full design, this type of analysis should be done to establish the cost optimum of the rf drive and cryogenic systems.

The use of modestly long (2 ms) rf pulses and relying on the stored energy in the cavity to accelerate the beam thus allows use of almost available (not quite state-of-the-art) couplers, with an associated small dynamic cryogenic load of 5 kW. The required rf power is specified not by the beam but rather by the control system (to manage static and dynamic detuning) as well as filling the volume of the cavity with enough energy to establish the gradient. The primary issues for this scenario are the availability of sufficiently high gradients (to provide adequate stored energy) and proper specification of the cavity external Q (to optimize rf power and duty-cycle/cryogenic requirements). The rf systems which are anticipated for the accelerator are described in Chapter 10.

We note that alternative scenarios are possible. The above discussion details a system in which the beam is accelerated entirely by energy “slowly” stored in srf cavities between macropulses. Earlier discussions have noted that directly driving the beam with rf power (“fast”-pulse scenarios) during the macropulse requires prohibitively large peak power. We have not, however, determined the system-wide optimum fill time. It may be possible, for example, to reduce beam-loading-induced momentum spread across the macropulse by adopting a fill time that replenishes the stored energy between individual *turns* of the macropulse [7]. Though requiring more peak power than refilling between macropulses, this scheme does not require the peak power demanded by “fast”-pulse scenarios such as those used in copper linacs. In addition, it provides better momentum spread through the acceleration cycle and allows use of a lower rf duty cycle. It may also reduce the required average rf power and thereby provide (through reduced transport and cryogenic demands) lower costs. A detailed system design must incorporate a cost/performance optimization between peak-power and average-power demands, momentum-spread-driven transport-system requirements, and dynamic heat load/cryogenic-system loads.

7.6 Conclusions

A first, but preliminary, design concept for the muon accelerator has been devised. Based on the analyses presented here, it seems feasible in that it meets the performance requirements. Nonetheless, acceleration of a large-emittance muon beam is clearly challenging. Moreover, the need to achieve high energy makes this system a cost driver. SRF technology minimizes the total cost because it circumvents development of rf-power sources that would be needed for normal-conducting technology, which would be, even if they already existed, the major part of the cost. An unconventional way of using the large stored energy in a low-frequency, high-gradient srf cavity has been delineated. Acceleration based solely on the stored energy in the cavity allows filling the cavity extremely slowly which reduces peak-power demands. On the other hand, a very small detuning bandwidth, driven by microphonics, is required, which will not be easy to achieve in large cavities.

REFERENCES

[1] For a discussion of linac dynamic range (injected-to-final energy ratio) see, *e.g.* D. Douglas, “Lattice Design Principles for a Recirculated, High Energy, SRF Electron Accelerator”, Proceedings of the 1993 Particle Accelerator Conference, IEEE Catalog No. 93CH3279-7, p. 584 (1993).

[1] Various similar solutions were independently developed by D. Neuffer, S. Berg, and V. Lebedev; the latter is presented here and is documented on the Web at http://www.jlab.org/~lebedev.

[2] V. Lebedev, *op. cit.*
[3] This section was kindly provided by L. Merminga.
[4] J. J. Bisognano, private communication.
[5] G. A. Krafft, S. N. Simrock, and K. L. Mahoney, “Beam Loading Studies at CEBAF”, Proceedings of the 1990 Linear Accelerator Conference, LANL Report LA-12004-C, p. 300 (1990).
[6] G. A. Krafft, JLAB-TN (in preparation)

8. The Muon Storage Ring

8.1 Introduction

The 50-GeV storage ring for neutrino production has been designed using a racetrack configuration. A racetrack is the optimal geometry for maximizing the proportional length of a single straight section to circumference, hence maximizing the number of muons converted into a neutrino beam. Although this particular ring was designed to meet limitations and target physics detectors specific to the Fermilab site, its design concepts, parameters, components, and dynamics are generally applicable. The racetrack design is simple, containing a downward straight, called the production straight, a return straight pointed towards the surface and two arcs with their associated matching and dispersion suppression sections.

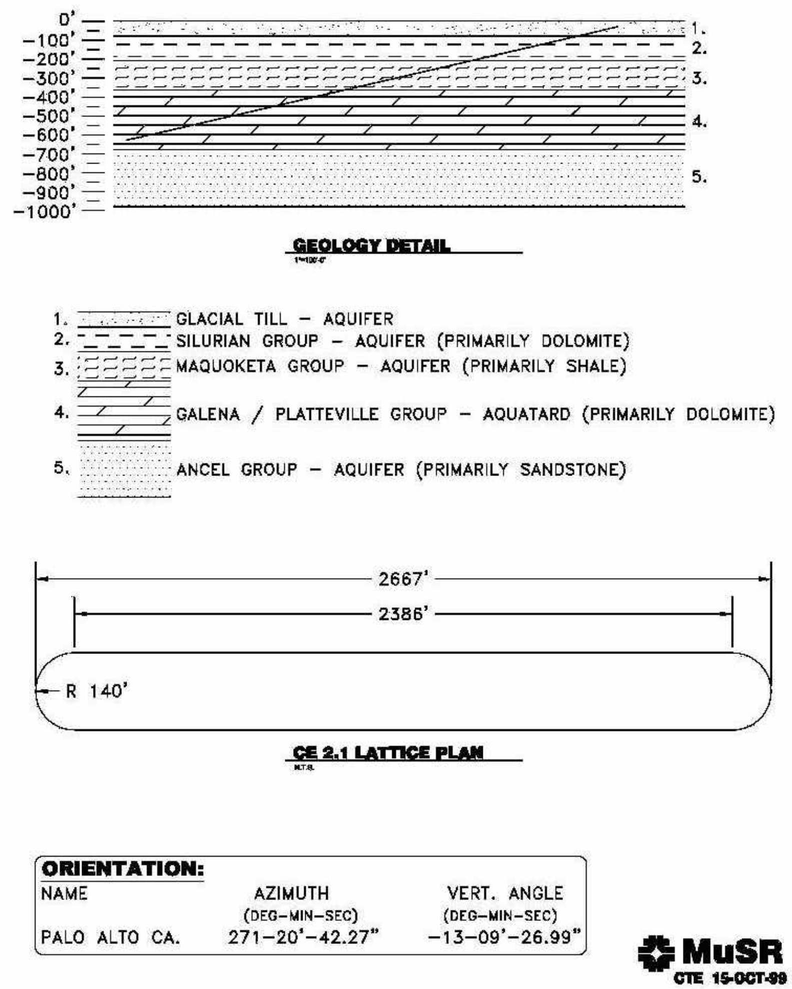

Figure 1: Constraints on the storage ring due to the geology under the Fermilab site. The 2667' (or 813 meter) limit on the cross-section profile of the ring shown in the lower drawing is given by the 600 foot available for the ring's vertical drop the and 13 degree angle between Fermilab and the West Coast.

One of the parameter constraints of the design arises from the underlying geology of the site as shown in Figure 1. The vertical distance between the surface of the site and the bottom of the Galena Platteville rock layer is approximately 680 feet. Below this dolomite layer is a sandstone layer, which must be avoided because it is a poor substrate for tunnel construction and it contains the water supply for the municipalities surrounding Fermilab. Of the 680 feet, 600 have been allocated to the ring for its vertical drop (Table 1). The "vertical drop" is the vertical distance between two parallel planes: one plane through the topmost part of the ring and a second plane through the bottommost part of the ring.

This vertical constraint is a limitation because at least part of the ring must be tilted at a vertical angle to direct the neutrino beam through the earth to a long-baseline detector. Tilting the entire ring obviates the need for additional, "out-of-plane" bending. For a significant angle of declination and vertical height restriction, tilting increases the relative arc length and matching and dispersion suppression sections, thereby decreasing the relative length of the production straight and the fraction of decays occurring in this straight.

An assumption used in designing this ring is the choice of the angle at which the ring must direct the neutrinos to illuminate the long-baseline physics detector. For directing the neutrino beam to the West Coast (including SLAC, LBNL, etc.), the downward angle corresponds to about 13°. This 13-degree angle combined with the vertical drop limit of 600 feet (183 meters) gives a cross-sectional profile of the ring (shown in the top part of Figure 1) of 813 meters. The "cross sectional profile" is the distance between the uppermost point of the ring and the bottommost point of the ring.

600	Feet	Ring Vertical Drop
10	Feet	Tunnel ceiling to floor
10	Feet	Shielding above ring
50	Feet	Undisturbed bottom layer of Galena Platteville
10	Feet	For uncertainties in the above three numbers
680	Feet	Total from Surface to Bottom of Galena Platteville

Table 1: Allocation of vertical distances under the Fermilab site.

The cross-sectional profile constraint, when combined with a dipole field of 6T and muon beam energy of 50 GeV, provides a straight section for neutrino production which is about 39% of the entire ring circumference. This is to be compared to a mathematical maximum possible value of 50%. The choice of 6T is based on Figure 2 which shows the production straight length divided by the circumference as a function of dipole bend field. The ratio is calculated based the 813 meter cross-sectional profile constraint and, thus, is specific to the geology under the Fermilab site. Releasing this constraint would allow one to increase the circumference. If, for example, one chooses to keep the arcs the same and increase the straight sections by a large factor, the ratio approaches the mathematical limit. On the other hand, one could use lower field magnets in larger arcs along with larger straight sections and still maintain a large decay fraction.

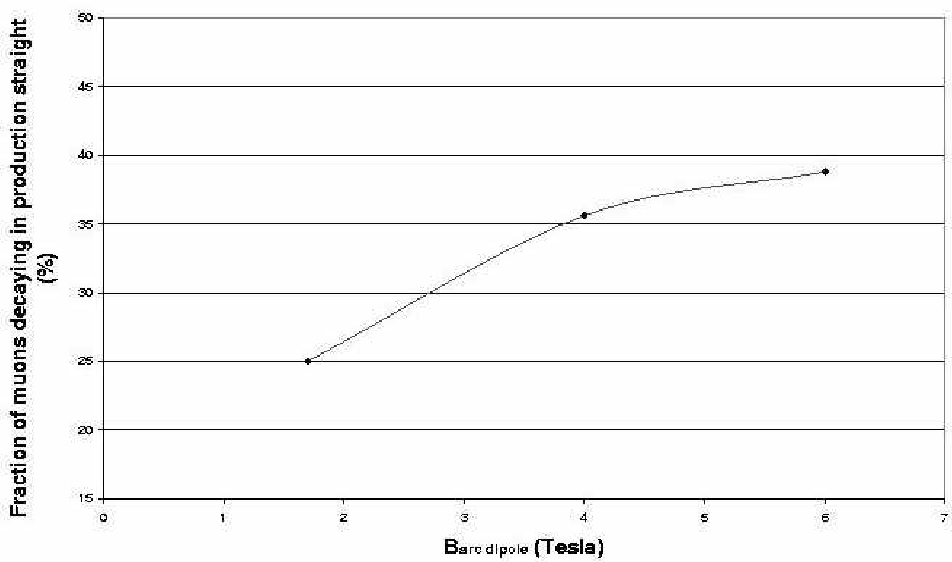

Figure 2: Fraction of muons decaying in straight section as function of dipole bend field.

In terms of the optics design, achieving a large admittance competes with the need to form a collinear neutrino beam—collinear, at least, to within limits set by the decay kinematics. To prevent the dynamics of the parent muon beam from contributing significantly to the angular spread of the secondary neutrino beam, the divergence of the muon beam in the production straight must be much less than the mean decay angle, which is 2 mr at 50 GeV. A straight with high-beta functions (implying large transverse beam sizes) is required. The challenge, then, in the design of the storage ring is to preserve the exceptionally large emittance transmission of the arc design through a transition to a high-beta region. The betatron function values are primarily determined by the transverse

$$\theta = \sqrt{\varepsilon \frac{(1 + \alpha^2)}{\beta}}.$$

emittance combined with a user-defined limit that the divergence in the high-beta straight be equal to or less than one tenth the rms decay angle, or 0.2 mr. In terms of the unnormalized emittance and the betatron functions, the angular divergence is given by:

The design conditions are summarized in Table 2. In the following paragraphs, details of the design are described.

Storage Ring Geometry	Unit	racetrack
Storage Ring Energy	GeV	50
Vertical Descent Limit	m	≈183
Declination Angle	Degrees	≈13
Cross-sectional Profile	m	813
ε(rms, normalized)	mm-rad	3.2π
dp/p(rms)	%	1.0
Maximum Poletip Field	T	6.0
Arc Cell Phase Advance	Degrees	90

Table 2: Muon Storage Ring Design Parameters and Constraints

8.2 The Lattice

8.2.1 The Arcs

Strong focussing FODO cells were chosen for the arcs to achieve a large momentum acceptance as compared with more complicated focussing structures. To shorten the arc lengths, high-field superconducting dipoles with 6T fields are assumed. Since strong gradients and large apertures are needed to accommodate and contain the large transverse emittance and the large displacement of off-momentum orbits, superconducting quadrupoles are also used.

The parameters of the magnets in the arc cells are listed in Table 3 along with calculated beam sizes based on the emittances in Table 2. The dimensions of the magnet apertures also include a 1-cm beam-stay-clear and a 1-cm thick tungsten liner for shielding. A 90° phase advance per cell was chosen so as to support strong sextupole correction of linear chromaticity while simultaneously maintaining an acceptable level of transverse acceptance. This phase advance is also the best choice to minimize transverse beam sizes both vertically and horizontally. The sextupole field has been superimposed on the quadrupole field (at the peak of the dispersion and betatron function) to minimize both the strength needed as well as the tune shift with amplitude aberration. Superconducting quadrupoles have been designed with a sextupole field component added. Each arc contains 31 half-cells, giving a total of 62 arc dipoles and 62 arc quadrupoles for the entire ring. For control purposes the defocusing and focusing quadrupoles are on separate buses. The arc lattice functions are plotted in Figure 3.

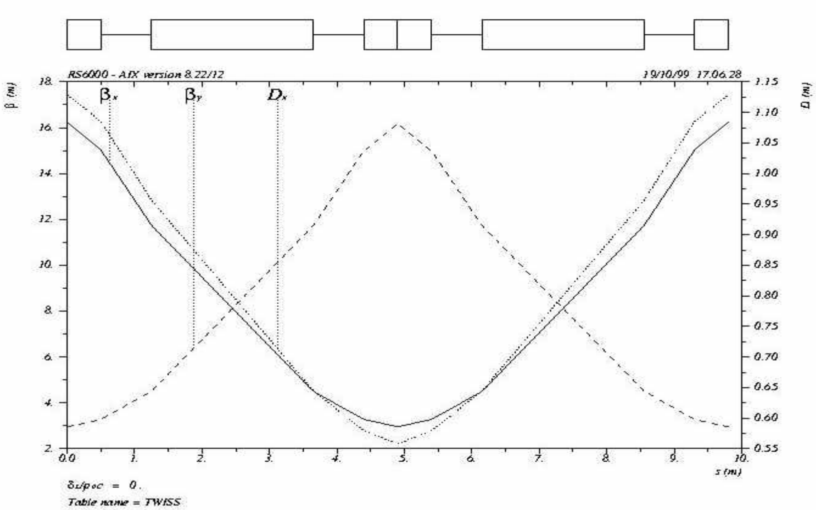

Figure 3: Lattice functions in the arcs of the storage ring.

8.2.2 Production Straight

The neutrino production straight, in contrast to the arcs, is a high-beta function, weak focussing structure. This production straight is matched to the arcs using a quadrupole doublet, and it has been designed to transmit a large momentum range in addition to forming a near parallel beam of muons. To form the insert, the short FODO cells of the arcs are matched into much longer, high-beta FODO cells that are the building blocks of the production straight. Use of a periodic unit allowed flexibility in the length of this region. The production straight represents about 39% of the 1.75-km ring circumference.

Table 5 gives the parameters of these production straight cells. The very low field gradient required by the quadrupoles in this region offers the possibility of using permanent magnets. The lattice functions for the production straight are shown in Figure 4.

General		
Tungsten shield thickness	cm	1.0
Beam-stay-clear	cm	1.0
Inter magnet spacing	m	0.75
Dipoles		
Dipole length	m	2.4
Dipole bend	rad	0.0859
Dipole field	T	6.0
Beam size (6σ) WxH	cm	8.0x5.3
Dipole full aperture, WxH	cm	12x9.3
Sagitta	cm	2.67
Quadrupoles		
Quadrupole length	m	1.0
Quadrupole strength	m-2	0.31
Quadrupole poletip field	T	3.6
Beam size (6σ) WxH:		
F quad	cm	9.2x2.6
D quad	cm	4.2x6.2
Quadrupole bore	cm	14
Sextupoles (overlay on quad field)		
Horiz. Sextupole strength	m-3	0.64
Vert. Sextupole strength	m-3	1.26
Horiz. Sextupole field	T	0.52
Vert. Sextupole field	T	1.03
Arc FODO cell parameters		
Cell length	m	9.8
Cell phase advance	deg	90
β(max)	m	16.2
Dx(max)	m	1.3
Total number of arc cells		31

Table 3: Parameters of the large-momentum acceptance arc cells for a 50-GeV muon storage ring.

8.2.3 Return Straight

The return straight is approximately equal in length and opposite to the production straight. It has been simply designed using 90° cells, 50-m long. The parameters of the return straight cells are shown in Table 4, and the lattice functions are shown in Figure 5. It cannot be identical to the production straight because of the anticipated need for higher order corrections for the ring. Tuneshift with amplitude corrections are planned using octupoles and /or sextupoles inserted in this straight. The cell parameters in the return straight will then be adjusted to enhance the dynamic aperture of the ring. It is planned that not only tuneshift-with-amplitude terms from the arc sextupoles will be corrected, but also those arising from the strong fringe fields associated with the unusually large bore of the quadrupoles.

Cell length	m	137.6
Quadrupole length	m	3
Quadrupole strength	m-2	0.0019
Quadrupole poletip field	T	0.05
Quadrupole bore	cm	33
Cell phase advance	deg	≈22
β(max)	m	436.0
rms divergence	mr	0.20
Number of cells		5

Table 5: Parameters of the high-beta FODO cells for the neutrino production straight section in the 50-GeV muon storage ring

Cell length	m	50.78
Quadrupole length	m	1
Quadrupole strength	m-2	0.056
Quadrupole poletip field	T	0.84
Quadrupole bore	cm	18
Cell phase advance	deg	90
β(max)	m	86.3
Rms divergence	mr	0.73
Number of cells		12

Table 4: Parameters of the FODO cells in the return straight of a 50-GeV muon storage ring.

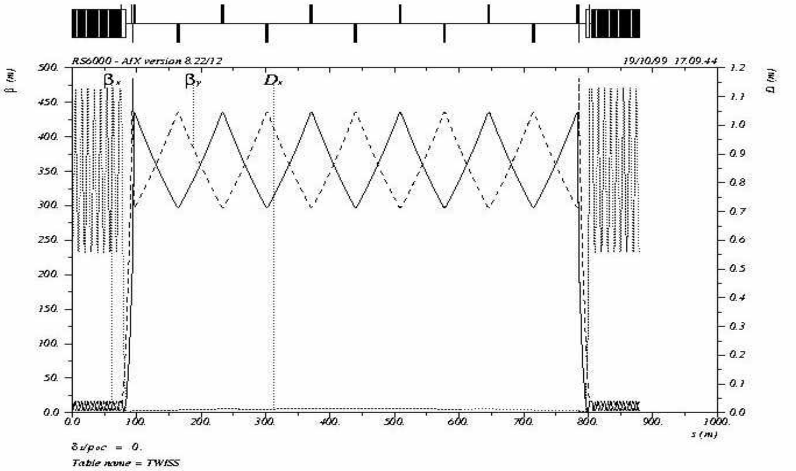

Figure 4: Lattice functions in the production straight.

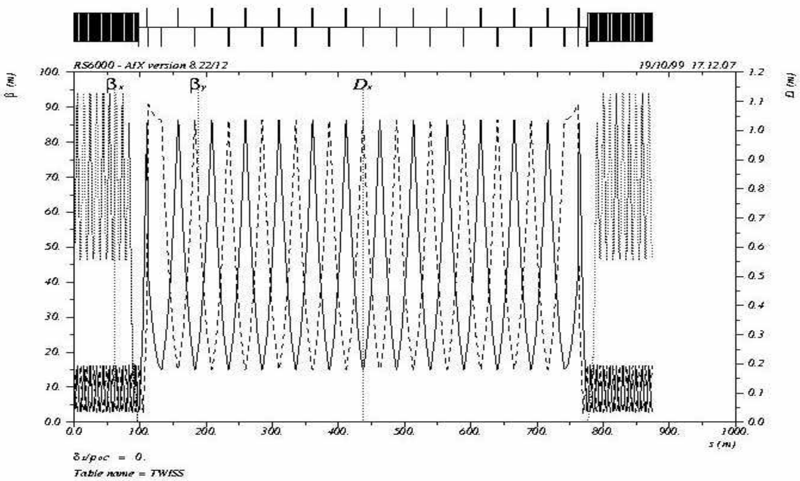

Figure 5: Lattice functions in the return straight.

8.2.4 Matching and Utility Sections

A combined matching section and dispersion suppressor was placed at each end of the arcs for efficient transition into the high-beta straight. A conventional two-cell dispersion suppressor was utilized for the return straight. Four more dipoles and sixteen quadrupoles are contained in the four matching/dispersion suppression sections. If conventional dispersion suppression is used for the high-beta straight, the length of the straight is reduced by about 4% of the total circumference, from 39% to about 35%.

8.2.5 Injection

The Muon Storage Ring has need of an injection kicker system that will deflect the incoming beam on orbit. The injection kickers are placed in the downward (or production) straight in order to inject into the ring at the top near the surface. Injection kickers with large apertures [2] will be needed for this purpose. The main parameters for the kicker system are given in Table 6.

Type		Horizontal
Clear Gap WxH	mm	308x246
Integral BL	Tesla-meter	0.6
Field Flattop	μsec	2.0
Field Fall	μsec	4.0
Field Variation	%	10
Rep Rate	Hz	15

Table 6: Injection kicker specifications.

The required total field integral is given by 24 magnets of length 1 meter and with a field of about 300 Gauss. This choice is based on two engineer-defined limits that were design constraints. Experience has suggested that the maximum system voltage should be limited to 50 kV and the maximum switch tube current should be limited to 5 k Amps. These two requirements imply a system impedance of 5 ohms.

The above constraints are such that the peak field will be:
$$\mathrm{B}_{\max} = \frac{\mu_0 \times \mathrm{I}_{\max}}{\mathrm{h}} \qquad B_{\max} = 0.0255\,Tesla$$

And the total length of the magnet system will be:
$$\text{Length} = \frac{\int \mathrm{Bdl}}{\mathrm{B}_{\max}} = 23.5\,\text{meters}$$

On a per meter basis the inductance, capacitance and the field drift time of the magnet are:
$$L = m_0 \times 1 \times \frac{w}{h} \qquad C = \frac{L}{Z_o^{\ 2}} \qquad drift = \sqrt{L \times C}$$
$$\mathrm{L} = 1.573\,\mu\mathrm{H/meter} \qquad C = 62.93\,nF\,/\,meter \qquad drift = 0.315\,m\,\mathrm{sec}/\,meter$$

In Figure 6 we show a proposal for the cross section of the magnet. The mechanical design for the support structure and vacuum vessel is non-existent and will need to be addressed for the next level design. The actual magnet length and number of pulsers will need to be nailed down at that time.

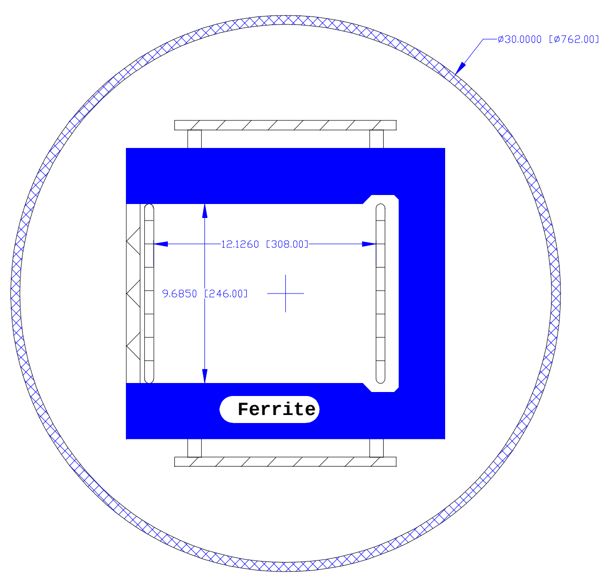

Figure 6: Proposed kicker magnet cross section. The dimensions are in inches [mm].

The PFN that will be used to drive each magnet will have an impedance of 5 ohms and a pulse length of 2.25 μsec. A ***SPICE*** simulation of both the PFN and magnet has been completed.

8.2.6 Superconducting Magnets for the Arcs

The two arcs of the Muon Storage Ring will be composed of superconducting magnets. The 31 identical arc-cells include 62 dipoles and 62 quadrupoles, with sextupoles combined with the quadrupole coils. All the magnets are designed to work at 4.5 K in one-phase liquid helium flow, and are also designed to work under the quite high beam losses heating of about 5 W/meter on average, with a peak value twice as high. The highest operating field for these magnets is 6 T, which allows the use of NbTi superconductor. Critical current data for the inner coil strands of the SSC 50 mm dipole were used as a reference for estimating the coil geometry and the superconductor volume. This critical current was ~ 340 Amps at 7 T and 4.2 K for the strands with 0.84 mm diameter. The average current density for the cable with insulation inside the coil was assumed to be 500 Amps/mm^2. The basic conceptual designs for all magnets use the single layer cosθ coil geometry and RHIC type mechanical structure for the cold mass design.

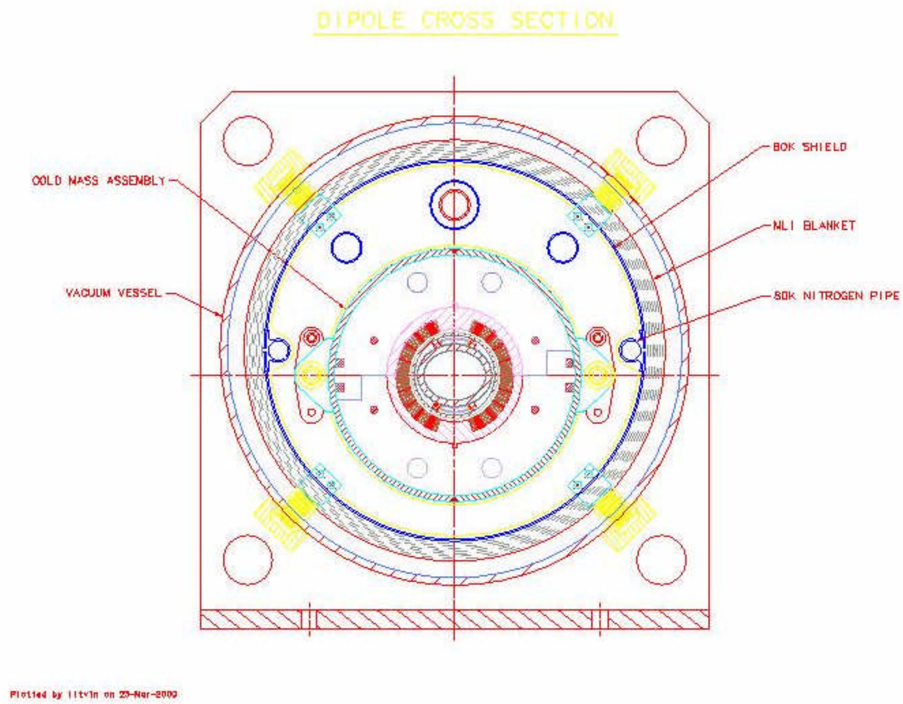

Figure 7: Arc Dipole Cross Section

The basic parameters of the magnets for the arcs of the storage ring are presented in Table 7.

A cross-section of the dipole cold mass inside the cryostat is shown in Figure 7. Here one sees the single layer superconductor coil surrounded by plastic spacers and collared by iron yoke laminations. Stainless steel shells that are welded around the yoke complete the cold mass assembly. The cold mass has two connections to the "spider" type suspension in the middle plane. This assembly is fixed to the vacuum vessel by four bolts. The thermo-shields that are placed around the cold mass will have a temperature of about 80 K and could be cooled by liquid nitrogen. Multi-layer insulation blankets are used to reduce the heating of the thermo-shields from the vacuum vessel. The vacuum vessel has reinforcement in the areas of the magnet suspensions.

The quadrupole and sextupole coils will be assembled like spool-pieces: that is, the sextupole coils will be placed around the quadrupole coils and will be collared together by iron yoke laminations. Stainless steel shells will be welded around the yoke. The complete cold mass assembly of the spool-piece and the dipole magnet assembly will be welded together in a common helium vessel. This vessel forms the basic half-cell unit of the arc. The longitudinal view of this arc half-cell cryostat is shown in Figure 8.

The cryostat has two suspensions along the length of the magnets. One is placed in the middle of the quadrupole and is an anchor point to keep the center point of the quadrupole in place during cool-down of the magnets. As shown in the top view of Figure 8, the dipole magnet has significant bending of the cold mass in the horizontal plane with a sagitta of about 68 mm. This bending should be done for the beam tube as well to preserve beam aperture. The superconductor coil must be protected from the electrons coming from muon decay, and is provided by a 10 mm cylindrical wall of tungsten as shown in Figure 7. As shown in section 8.4.1 below, the heat load on the tungsten will be about 50 W/meter on the average, with a peak value about twice as large. Cooling could be provided by two flattened tubes with liquid nitrogen flow or cold helium gas. Some additional tubes come through the suspension and are used for bus-bar returns and as a heat exchanger for the helium flow.

A summary of the mechanical dimensions and cryogenic loads of the arc-half cell are shown in Table 8.

Half-cell assembly		
Cold mass diameter	mm	410
Total length of cold mass	meter	4.6
Beam tube length	meter	4.9
Total weight of the common cold mass	tons	4.5
Outer diameter of cryostat	Mm	800
Total weight of arc half-cell assembly	Tons	5.5
Cryo loads		
to He level, at 4.5 K	W/cryostat	5
to N2 level, at 77 K	W/cryostat	30
Dynamic heat losses (including average beam losses)		
to He level, at 4.5 K	W/meter	7
to N2 level, at 77 K	W/meter	70

Table 8: Mechanical and cryogenic parameters of the arc half-cell.

Dipole		
Operating field	Tesla	6
Magnetic length	meter	2.4
Operating current	kA	15
Stored energy	MJ	1.4
Beam aperture (HxW)	mm	80x100
Tungsten beam tube thickness	mm	10
Cold mass diameter	mm	410
Length of cold mass	meter	3
Weight of cold mass	tons	3
Quadrupole		
Gradient	T/m	51.4
Magnetic length	meter	1.0
Operating current	kA	10
Coil inner diameter	mm	160
Beam aperture	mm	120
Sextupole coil		
Coil inner diameter	mm	220
Horizontal poletip field	T	0.52
Vertical poletip field	T	1.03
Magnetic length	meter	1.0
Common cold mass diameter	mm	410
Length of cold mass	meter	1.5
Weight of cold mass Quad+Sextupole	tons	1.5

Table 7: Arc magnet specifications

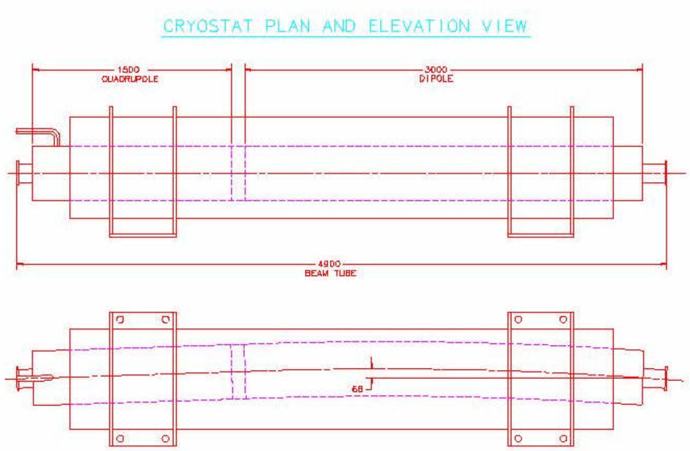

Figure 8: Cryostat Plan and Elevation Views. A half-cell is shown with a quadrupole and a dipole. The dimensions are in mm.

8.2.7 Power Supplies for the Muon Storage Ring

Schematics for the power supplies for the arcs of the storage ring are shown Figure 9. The power supply design assumes the dipole circuit requires 15 kAmp DC and each quadrupole (focusing and defocusing) circuit requires 10 kAmp DC. Since all circuits are superconducting, the resistance of the warm bus connecting the power supplies to the load and an acceptable ramp rate sets the voltage requirement. For the purposes of this study, the supplies were designed in units of 150 kWatt modules each capable of 30 volts and 5000 amps. Such supplies are common around Fermilab and have well known costs and operating characteristics. The dipole bus would require 3 of these supplies operating in parallel while the quad buses would each need 2. Assuming an 0.4 henry dipole circuit inductance yields a ramp rate of 75 Amps/sec (200 sec to ramp to 15 kAmp).

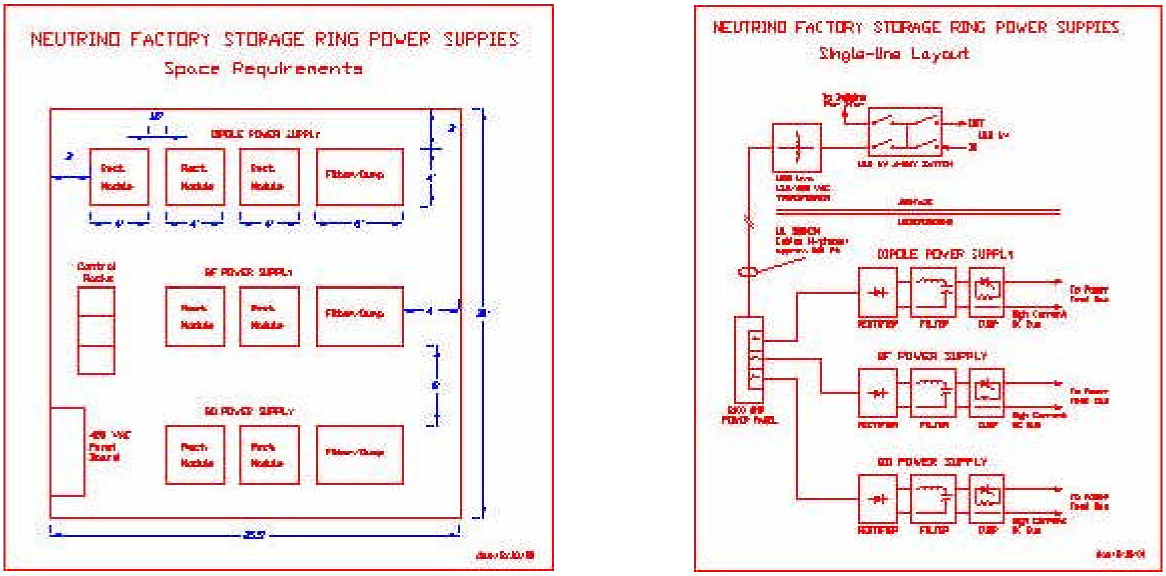

Figure 9: Schematics of Power Supplies for the Muon Storage Ring**.**

Since it is quite costly to transport 15 kAmp, the power supplies should be located near the feed cans in the beam enclosure. This should be no problem at the near-surface end of the ring, but requires some consideration for the deep end. The present plan is to locate the power supplies at the tunnel level and provide the 480 VAC power from the surface. The exceptionally high cost of a 15 kAmp, 800-foot long vertical DC bus system drove this decision. The cryogenic problems with operating a long vertical superconducting power transmission line ruled out the possibility of a superconducting feed from the surface. Further optimization studies may indicate additional cost or performance savings by installing the 13.8KV/480VAC transformer at the tunnel level. Presently, it is planned to use passive filters to smooth the output of the power supplies. This is the common practice at Fermilab for storage ring systems.

8.2.8 Quench Protection Dumps

This study assumes the quench protection dump switches and resistors will be integrated with the power supply filter. The switch itself will be similar to the 15 kAmp dump presently operating at the Fermilab magnet test facility. The resistors could be water-cooled stainless steal elements or air-cooled elements mounted to the wall of the vertical access shaft. The present plan does not include backup DC breakers in the dump switch because of the high cost of such devices. In the event that the dump switch fails, the Quench Protection Monitoring system would protect the magnets by firing all the magnet heaters in the string.

8.2.9 Muon Storage Ring Quench Detection & Protection

The MμSR will consist of 6 separately excited superconducting magnet strings. Each of the two arcs will have a dipole, and two quad circuits. The dipole circuits will store much more energy (45 MJ each) than the quad circuits, but quench protection will be implemented in the same manner for each. One embedded Quench Protection Monitor (QPM) will be needed in the “Power Supply Room” at each arc.

For quench detection, one voltage tap from each magnet will need to be connected with a coax to the QPM. VFC or technology can be used for data acquisition. For quench protection, each magnet will need an embedded heater connected to a capacitive discharge Heater Firing Unit located in the PS room. Also located in the PS room, will be the dump, dump switch, and two Quench Bypass Switches (QBS), as shown in Figure 10. Only one safety lead is needed in the center of each arc.

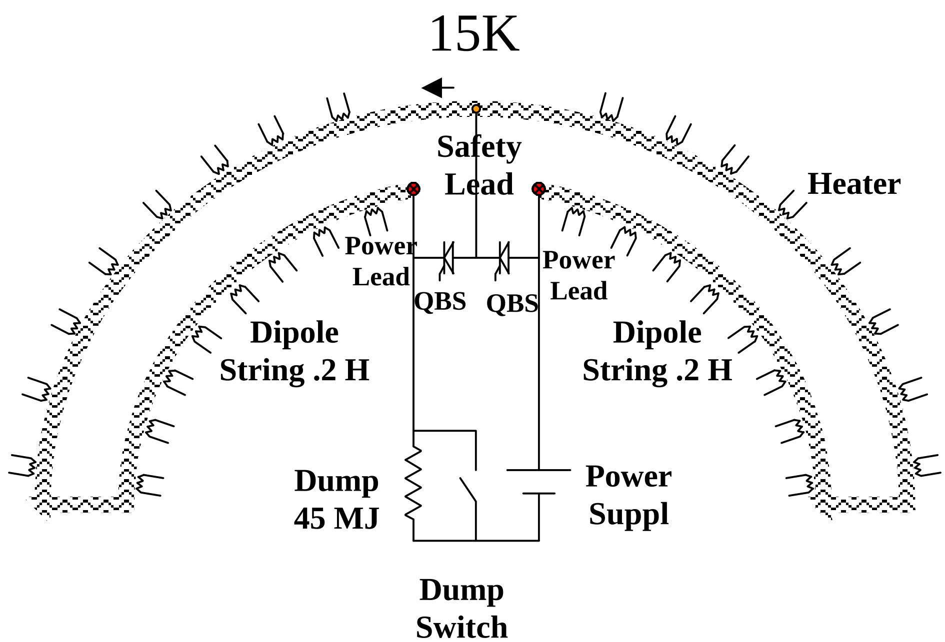

Figure 10: Dipole Quench Protection

8.3 Lattice Performance and Tracking

Overall physical characteristics of the storage ring are summarized in Table 9. The dynamic aperture and momentum performance of the ring lattice has been studied by tracking for 1000 turns to high order including not only full kinematical effects but also fringe field characterization of the large-bore quadrupoles [3]. This is a very conservative number of turns to track since the intensity of 50 GeV muons decays by 1/e in only 178 turns. Tracking plots are shown in Figure 11 in steps of 0.5 σ as given by a normalized emittance (rms) of 3200 π mm-mr. The top plots show the dynamic aperture of the storage ring with fringe fields of all quadrupoles included. Further study showed that only the fringe fields from four strong quadrupoles in the matching/dispersion suppression sections about the production straight caused a deterioration in dynamic aperture. Turning the fringe fields off in these four quadrupoles improved the dynamic aperture considerably as can be seen in the lower plots. Since fringe fields depend strongly on poletip field, the simplest solution is to lengthen these quadrupoles and reduce their poletip field correspondingly. To date, tracking has not included field and alignment errors. Given the relatively short lifetime of the beam, <1% field errors and all but the lowest-order resonances are not expected to be important.

Circumference	m	1752.8
Neutrino decay fraction	%	39.2
Production region		
Matching and dispersion suppression	m	44.1
High-beta FODO straight	m	688
General		
$\beta x(max)/\beta y(max)$		90
$\nu x/\nu y$		86.3
Natural chromaticity		12

Table 9: Overall parameters of the storage ring.

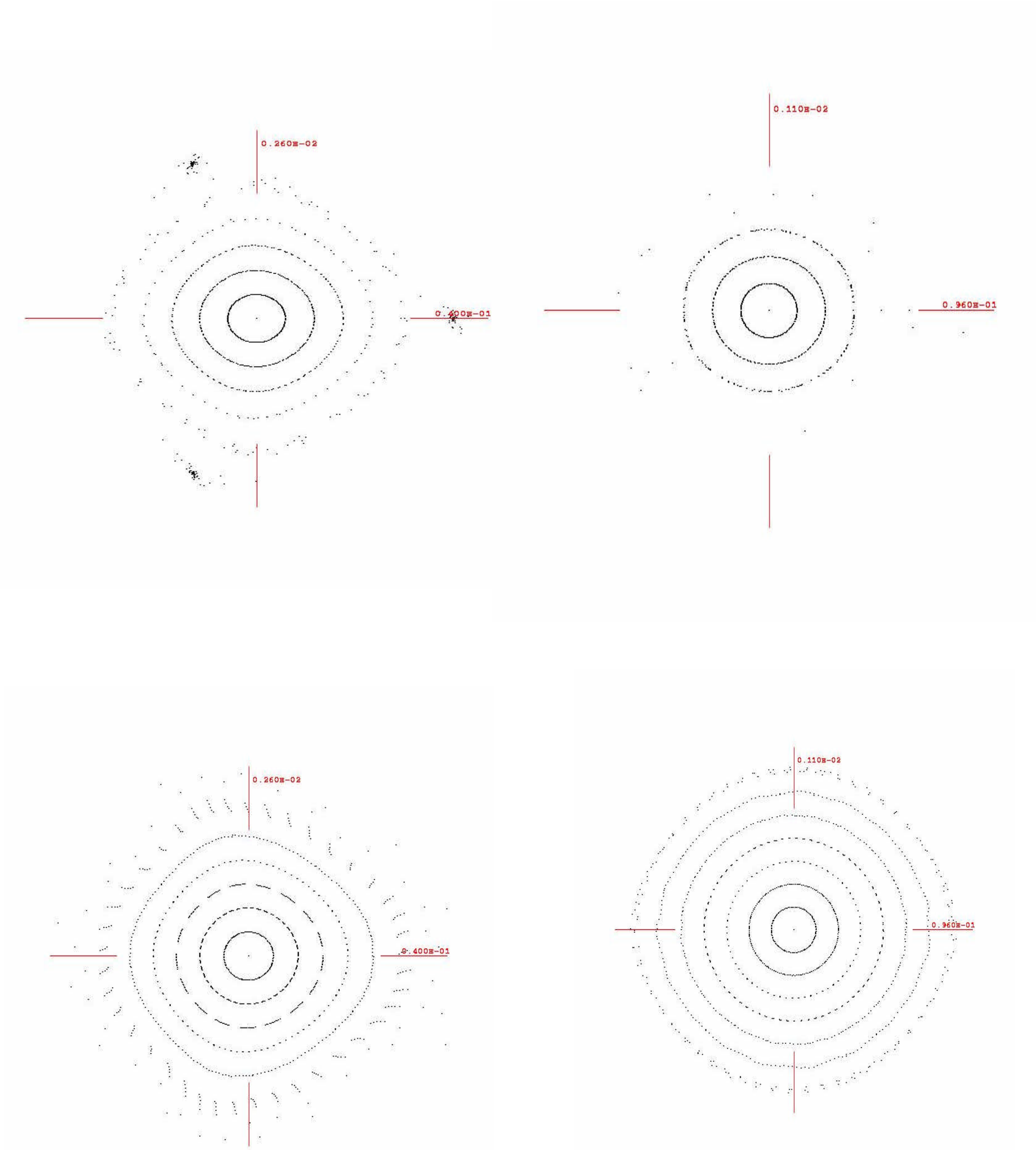

Figure 11: Top: Horizontal (left) and vertical (right) accepted phase space plots obtained by 9th order tracking through the full muon storage ring, including chromatic correction sextupoles and quadrupole fringe fields. Tracking is plotted in steps of 0.5 σ for an normalized emittance (rms) of 3200 π mm-mr. Bottom: Same as top plots but with quadrupole fringe fields in the matching sections to the production straight turned off.

8.4 Beam Induced Energy Deposition And Radiation Fields

Realistic Monte Carlo simulations have been performed with the MARS14(2000) code [1] for the arcs and straight sections of a muon storage ring using the above lattice for 30 and 50 GeV muon beams. Detailed analysis of radiation levels inside the magnets, around the arc tunnel and at large distances from the ring (neutrino hazard) is done.

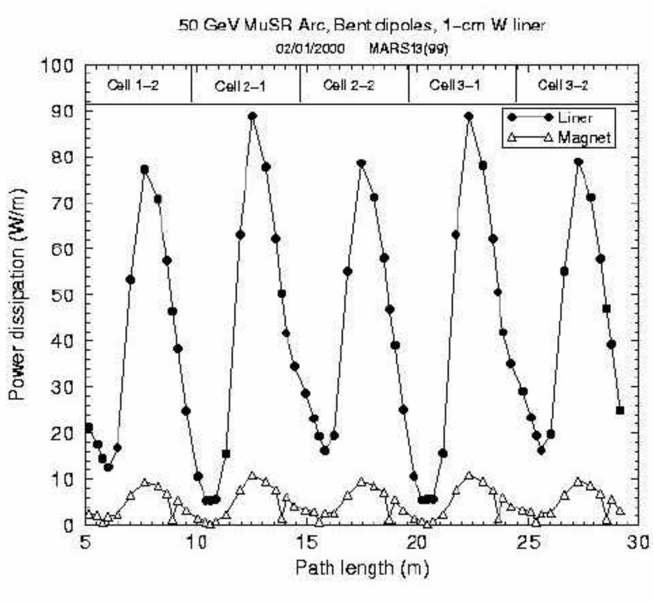

Figure 12: Longitudinal distribution of power dissipation in the arc magnets with 1 cm thick tungsten bore tubes.

8.4.1 Arc Magnets

Forced muon decays and shower simulation with MARS are done in the arc FODO cells. The cells are 9.8 m long each and made of 45 T/m 1-m quads and 6 T 2.4-m dipoles. At 50 GeV, the muon decay rate is 1.6×10^{10} decays/m/s. For a 240 kW beam, there is 84 kW power dissipation in the 1750 m storage ring, or 47.8 Watts per meter on average. A thick bore tube made - as calculations show - of tungsten must intercept most of this power. The longitudinal distributions of both power density and power dissipation oscillate in the arc cells (see Figure 12), with about 10% of power dissipated in the SC coils and 90% in the protective bore tube. The power density peaks in the orbit plane with a strong azimuthal variation (see Figure 13).

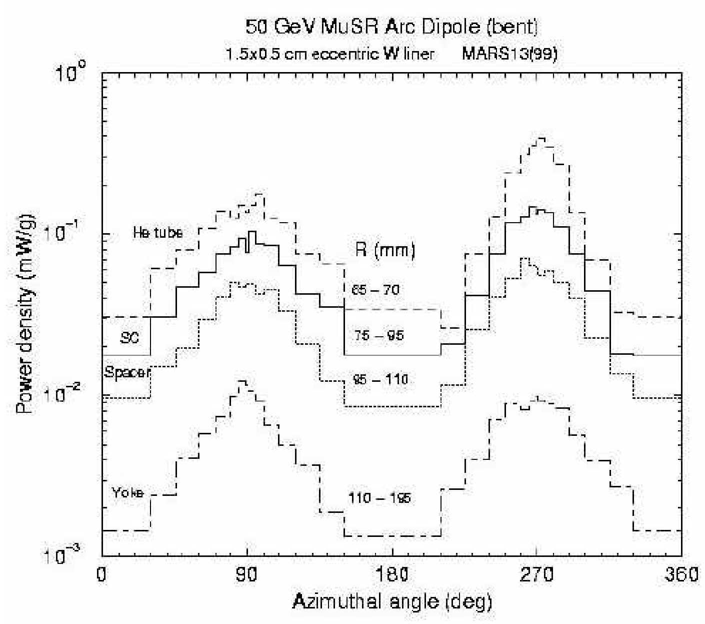

Figure 13: Power density in the bent arc dipole.

As a result of thorough optimizations, it was found that the radiation load to the superconducting coils of the arc magnets due to 50 GeV muon beam decays is reduced to tolerable levels if the dipole is bent and there is a tungsten eccentric bore tube. The latter can be made of a 1-mm thick SS pipe (100x80 mm elliptical aperture) and a 1-mm thick SS pipe (122x102 mm elliptical aperture) shifted inward by 5 mm with the space between filled with tungsten. With such a tube the peak power density in the coil is 0.15 mW/g and the peak power dissipation in the bore tube (at nitrogen temperature) and in the rest of the magnet (at helium temperature) is about 90 and 9 W/m, respectively. Averaged over the arc length values are about two times lower. Residual dose rates on the magnets are quite acceptable.

8.4.2 Radiation Around The Arc Tunnel And Downstream Of The Straight Sections

Full-scale MARS calculations have shown that the normal occupancy limit of 0.25 mR/hr is provided by 2 meters of dolomite type shielding below, above and radially inward from the arc tunnel enclosure walls. Six meters of such limit radially outward (see Figure). Power supply rooms and other underground enclosures should be placed inward from the arc tunnel.

The off site limit of 10 mR/yr due to neutrino induced radiation in the arcs is reached at 50 meters radially outward from

controlled disk is only +-
orbit plane.

Neutrino- nduced radiation downstream of the straight sections is more severe. The -site limit of 10 mR/yr is met at 4.2 km

GeV MuSR. The maximum half-
tolerable isocontour is 4.3 m and 2.7 m at 50 and 30 GeV, r

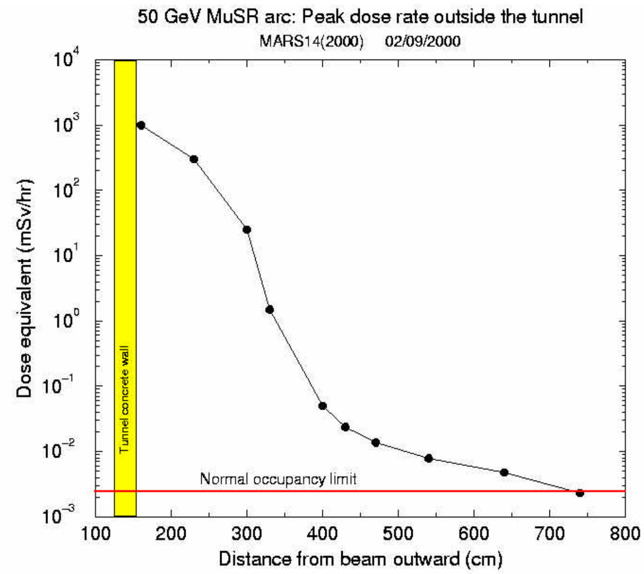

Figure : Dose distribution radially outward f tunnel enclosure.

REFRENCES

[1] N.V. Mokhov, "The MARS Code System User Guide, Version 13(95)", Fermilab- -628 (1995); N.V. Mokhov et -Conf 98/379 (1998); LANL Report LA- -98 5716 (1998); nucl- http://www- .

E. Keil, Muon Storage Ring Design with Simple Mathematica Packages, CERN SL- -053 AP, August 31, 1999.

F. Zimmerman et al, MUCOOL Note 95, March 3, 2000

9. Solenoids for Decay, Phase Rotation, and Cooling Channels

9.1 Introduction

For the neutrino factory study several magnetic channels are required, all based on solenoids. Four channels have been specified technically [1] with the goal to investigate their technical feasibility, the critical items for an R&D program and finally the cost. In total, about 300 m of solenoids with different magnetic field strengths and bore sizes must be built in order to prepare the beam for injection into the muon accelerator of the Neutrino Factory. The combination of beam size and longitudinal magnetic field strength satisfies a simple condition for the first three channels that will be considered in this paper:

$$B \cdot r^2 = 0.1125 T \cdot m^2 \quad (1)$$

Here B is the longitudinal magnetic field, r is the radius of the inner bore (1/2 the aperture) and the product given in formula (1) keeps the acceptance constant. A trade off between stored energy which is proportional to $B^2 r^2$ (= magnet cost) and the required acceptance given in equation (1) can be made. In our case the field on axis is 1.25 Tesla and the bore diameter 0.6 m.

Four channels will be described overall. The first channel is a 50 meter long drift channel, the second a 40 meter long drift channel which will not be used in our study but is of interest, if low frequency high gradient rf will be used within the decay channel. It would replace a part of channel 1 this case. The third channel is integrated into an induction linac with a length of 120 meters and the fourth channel is a cooling channel with a total length of 150 meter. This will be the most challenging one.

This chapter provides a preliminary layout of a magnetic system for each of the four channels. It helps to identify possible technical problems to work on during the R&D stage of the project. Also preliminary requirements on power supplies, cryogenic systems, and cooling systems are described

An inconsistency should be mentioned at this point. Because many things had to be specified at the beginning of the study, a number of parameters chosen for the magnetic channels do not necessarily fit the final solution described in other chapters. This inconsistency can not be removed in this report, because the presentation of a complete design is considered more useful. Instead of changing the design specifications after optimizing the beam dynamics the technical layout was finished on the basis of the specification provided at the beginning of the study. It should also be mentioned that the approach taken for solenoid design is more aggressive than what has been imposed as a limit when discussed in the cooling section in chapter 7. It will be part of the R&D program to study and test what the actual current density for a given field at the coil and the for the given force on the coil is going to be.

9.2 The Magnet Channels

9.2.1 The 50 m Long Drift Channel

The first channel has a length of 50 meters and can have either a cold bore or a warm bore. Cost trade offs for both solution have been made. The field interval can in principle be between 1.25 to 3 T and the field direction does not have to be changed within the channel. The radiation load from decay electrons and other particles is assumed to be negligible. Special care is necessary in the dump region (compare chapter 4) which will not be considered here. A preliminary study has shown that even if the magnet bore is getting smaller according to (1) the magnetic field has to increase, but magnet costs grow. This encourages us to choose a lower magnetic field in the channel. A reasonable compromise between magnetic field strength and bore size was achieved by choosing B = 1.25 T and R = 0.3 m for the first channel. The length of solenoids in the drift channel was chosen to be 4.7 m. A total of 10 magnets are used in the channel with 0.2-m gaps

Coil length, m	4.70
Bore diameter, m	0.6
Total ampere-turns, MA	4.69
Number of turns	780
Operating current, kA	6
$I_{nominal}/I_c$ ratio	0.3
Inductance, H	0.061
Cu/SC ratio	7:1
Coil inner radius, m	0.345
Cable length, km	1.7
Cryostat inner diameter, m	0.618
Cryostat outer diameter, m	0.935
Cryostat length, m	4.8
Cable mass, kg	370
Mass of magnet, ton	3.8
Stored energy, MJ	1.1

Table 1: Drift channel magnet parameters

between them. This leaves enough space for service ports that can also be used for installation of beam diagnostic equipment. The solenoid coil is placed in a cryostat that provides the required mechanical support to the coil structure and insures thermal insulation allowing the use of NbTi wire at 4.2 K. The required mechanical supports are different for magnets in the middle and at the ends of the magnet string. For example, the axial force on the magnet in the middle of the string is 170 kN. For the first and the last magnets in the string this force is 230 kN. Radial pressure developed at the coil location is about 0.6 MPa, and this makes the magnet design quite straightforward. The solenoid has a two-layer coil wound using NbTi cable. A stainless steel barrel is used to support the coil structure inside a stainless steel cryostat with a warm bore. Cable size is 12.0 x 2.1 mm^2, and the amount of copper used in the cable is defined by a Cu/SC ratio of 7:1. Dimensions of superconducting cable, quantity of copper for stabilization, and nominal-to-critical current ratio were determined taking into the account safe evacuation of energy stored in the magnet during a quench. The calculated temperature during a quench is less than 300 K and the maximal voltage does not exceed 1000 V. The cable in the coil is insulated using 0.1-mm kapton insulation. The coil is cooled by liquid helium flowing through copper piping soldered to copper shells and connected by collectors on the ends of the coil. A copper thermal shield cooled by liquid nitrogen is used to reduce heat leaks to the inner and outer surfaces of the superconducting coil. Super-insulation is installed between the coil and thermal shield and between the thermal shield and cryostat wall. Space inside the cryostat is pumped out to further improve thermal insulation. The main parameters of the solenoid magnet for the drift channel are listed in Table 1.

In the drift channel, all the magnets are connected in series using superconducting cable cooled by a pipe carrying liquid helium. It uses one 180 kW power supply, and it takes 200 seconds to reach the nominal current of 6 kA.

The protection system is shown schematically in Figure 1. When the quench detector sees an appearance of a normal zone in the coil, the dump resistor R_d is turned on by switch S_2 and the power supply is switched off by S_1. At that moment the stored energy of the string starts to dissipate in the dump resistor R_d. During extraction of energy out of the magnet, the maximum allowable voltage was 1000 V for R_d = 0.167 Ohm. A Simulation of a quench spreading through the coil was made for the case when the quench was provoked on the outer boundary of the inner layer of the coil. With a quench detector threshold of 1 V and a time delay of 100 ms, almost 97% of stored energy was dissipated outside the cryostat. The amount of energy dissipated in the coil was sufficient for adiabatic heating of the coil up to 180 K in the hottest area.

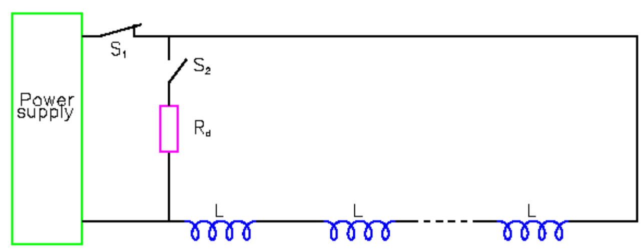

Figure 1. Quench protection scheme for the decay channel.

9.2.2 RF-based Phase Rotation Channel

The main idea of using RF cavities operating at low Frequency is, to have an early phase rotation stage that can simplify the requirements for the induction linac based phase rotation. The RF cavities are installed inside the magnets of this channel. The transverse dimensions of these cavities will determine the inner diameter of the magnets that generate the longitudinal magnetic field for beam transport. It is obvious that one must choose the magnets with the lowest field to reduce the channel cost. The RF frequency to be used in this channel is 30-60 MHz and the inner radius of the channel bore was chosen to be 0.7 m which will need very special cavity designs. The magnetic field in the channel is 1.25 T, and the field direction is the same for all solenoids in the channel. Length of a magnet in the channel must coincide with the length of the RF cavities. The cavities must be installed inside the magnet so feeding the cavities with RF power is possible. As the first approach, the magnet length was chosen to be about 1.8 m with 0.2 m gaps between the magnets, so in total 20 magnets are used in the channel. RF power dissipation in the channel is about 50 kW/meter, so an additional water-cooling system is required to reduce the power load on the inner wall of the magnet cryostat which will have to be a warm bore in this case. The cross-section of a magnet in the RF channel is significantly larger than a magnet cross-section in the drift or induction linac channel, and thus the axial magnetic forces are also higher, although

the radial pressure in the coil is at the same level of 0.6 MPa. For magnets in the middle of the magnet string, the axial force acting on the magnet end is about 550 kN. For the first and the last magnet in the channel, this force is about 900 kN. This force level requires strong support structures and a reliable protection system that can simultaneously and quickly remove all the energy stored in the magnets during a quench. The magnet design is similar to that of the drift and induction linac channel. The difference is that stronger banding is required to manage the higher longitudinal forces. Cable with 10.5 x 3.0 mm^2 cross-section made of NbTi wire is used for coil fabrication. The coil is cooled by liquid helium flowing through cooling pipes. A shell cooled by liquid nitrogen is used to lower heat leaks from the coil to cryostat walls, and superinsulation is used to further increase cryostat efficiency. The cryostat and coil support barrel are made of stainless steel. The inner space of the cryostat is pumped out.
The main parameters of a magnet in this channel are listed in Table 2.

Central field, T	1.25
Bore diameter, m	1.4
Total current, MA	2
Total number of turns	320
Operating current, kA	6
$I_{nominal}/I_c$ ratio	0.3
Stored energy, MJ	2.0
Inductance, H	0.1
Cu/SC ratio	9:1
Magnet length, m	1.8
Magnet coil length, m	1.7
Coil inner radius, m	0.745
Cable length, km	1.5
Cryostat inner diameter, m	1.4
Cryostat outer diameter, m	1.82
Cryostat length, m	1.8
Cable mass, kg	410
Mass of magnet, ton	5.0

Table 2: RF channel magnet parameters

The quench protection scheme is very similar to that of the induction linac channels. Twenty magnets of the channel store 40 MJ of energy. The magnets in the channel are subdivided into two groups. The magnets in each group are connected in series with their own power supply. The scheme of one string is presented in Figure 2. A 180 kW power supply is used in each string to raise the current up to 6 kA during 10 minutes. One magnet in each string is equipped with protective heaters like in the induction linac channel. These heaters are necessary for synchronizing the extraction of energy from the strings. The resistance growth rate stimulated by the heater is higher than that in the original normal zone, and this reduces the difference in resistances of the two strings. The two strings will have similar time constants for current decay and thus reduces the imbalance of forces in the string. After quench detection, the power supply is switched off by S_1, the dump resistor R_d is turned on by S_2, and the heater is connected to the heater power supply by S_h. The stored energy of all strings is dissipated on the dump resistors which have resistance R_d = 0.167 Ohm. The maximum voltage does not exceed 1000 V.

9.2.3 The Induction Linac Based Phase Rotation Channel

The main difference between the drift channel (=nr 1) and the channel inside the induction linac is, that these magnets are placed inside the accelerating structure. This sets a strict limitation on the magnet length, that cannot be exceeded. Moreover, the gaps of the induction linac are formed by the surfaces of the two neighboring magnet cryostats. For this study, a 1-m long induction linac section length was chosen with a bore diameter of 0.6 m and a longitudinal magnetic field of 1.25 T. The total number of magnets in the channel is 100. The length of each magnet is 0.85 m, and the gap between cryostats is 0.15 m. The bore has to be warm and the magnetic field direction does not have to change along the linac. Table 3 shows the main parameters of a magnet in the induction linac channel. Another critical issue for this channel is that the fringe magnetic field outside the channel must be rather low because induction linac inductor performance gets worse if the field level is higher than a certain limit. Some optimization of coil shape is required to have this fringe field as low as possible. This optimization includes but is not limited to coil thickness variation along the coil length. Nevertheless, because of the voltage gaps, some level of fringe field will form a part of the inductor's working environment. The coil design is very similar to that in the first channel. The NbTi cable cross-section is 8.3 x 3.0 mm^2. The radial pressure at the coil location is about 0.6 MPa. Axial forces depend on the magnet location in the string. For a magnet in the middle of the channel,

Bore diameter, m	0.6
Total current, MA	1.0
Total number of turns	180
Operating current, kA	6
$I_{nominal}/I_c$ ratio	0.3
Inductance, H	0.01
Cu/SC ratio	7:1
Cable length, km	0.4
Coil length, m	0.75
Coil inner radius, m	0.345
Cryostat length, m	0.85
Cryostat outer diameter, m	0.89
Cryostat inner diameter, m	0.618
Cable mass, kg	86
Mass of magnet, ton	1.0
Stored energy, MJ	0.2

Table 3: induction linac channel magnet parameters

the axial compressive force is about 150 kN; for the magnets at the ends, it is about 200 kN. So precautions must be made to keep magnet displacements within an acceptable limit, especially during a quench when axial forces can appear in the middle of the string if the quench protection scheme does not work properly.

The total energy stored in the channel is 20 MJ. This energy is about twice as large than that for the drift channel. To make an efficient quench protection system, all magnets in the channel are subdivided into two groups. In each group, magnets are connected in series and powered by a 180 kW power supply. The quench protection concept is shown in Figure 2.

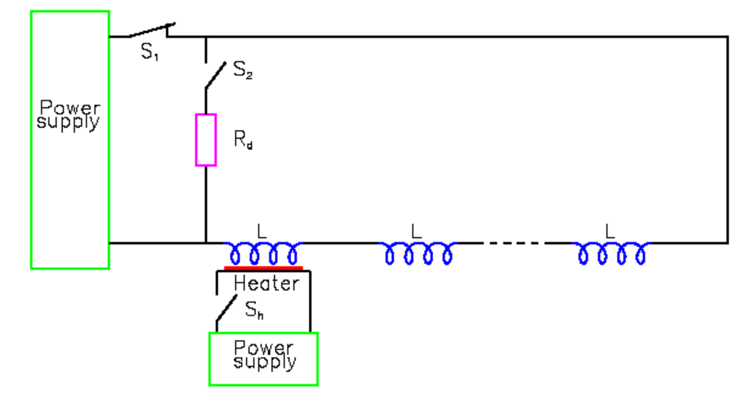

Figure 2: Quench protection scheme for the induction linac channel.

In each group of magnets there is only one magnet with protective heaters. After a quench is detected in each string, the power supply is switched off by S_1, the dump resistor R_d is turned on by switch S_2, and the heater is switched to heater power supply by S_h. Stored energy of both strings is dissipated in the dump resistors with resistance R_d = 0.167 Ohm. The maximum voltage does not exceed 1000 V. As a simulation of the quench process shows, the hot spot temperature does not exceed 200 K in the magnet where quench originates and 170 K in magnets with the heater-initiated quench.

9.2.4 Cooling channel

The channel is used to reduce the beam emittance to an acceptable level using ionization cooling. RF cavities installed inside the channel compensate for energy loss during the cooling process. The cavity transverse dimensions of about 1.4 m will determine the solenoid diameters in the channel. The length of the cooling channel was assumed to be 100 m, which is different from the final result presented in the chapter 7. Strong magnetic fields, alternating along the channel length, provide a field configuration optimized for cooling efficiency. The bore of the magnets has to be warm and very frequent changes of the magnetic field direction on axis are necessary. Also much higher fields are required. Several schemes of this channel type were considered that differ in magnetic field amplitudes and field period length. One of the latest schemes makes use of a magnetic field that changes following a sine law with a period of 2.2 m and field amplitude B_m = 3.6 T. Another channel configuration was proposed with period 1.5 m and amplitude B_m = 3.4 T. And increasing the field amplitude to 5.5 T was also considered. In this chapter, we will discuss the magnetic system with longitudinal period 2.2 m and amplitude B_m = 3.6 T, again, chosen very early in the study. The longitudinal period determines the length of a magnet, which in this case has to be less than 1 m. The construction of these magnets is

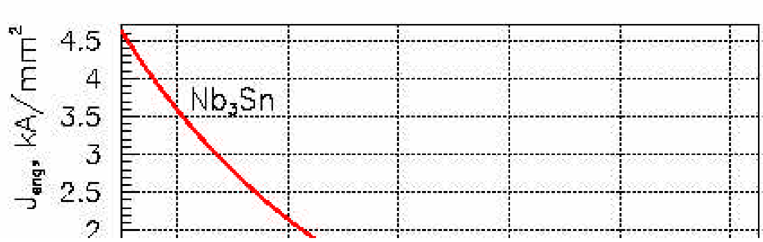

Figu

challenging. First of all, the magnetic field is rather high compared with the drift and phase rotation channels. Also, alternation of field direction along the channel length results in large longitudinal forces. Combination of both of these factors has significant impacts on the magnet design.
Figure 3 shows the engineering current density (that is, the critical current divided by the coil cross-section) for different superconducting materials.

It can be seen that NbTi can not be used in magnetic fields higher than 9 T at 5.2 K. Using NbTi at 2.2 K allows one to extend the field range up to 12 T. Nb_3Sn can work in fields up to 15 T at 5.2 K and has superior magnetic properties compared to NbTi at 2.2 K. High temperature superconductors (HTS) like Bi-2212 can work at much higher field (up to 30 T) practically without any reduction in critical current density, but it will take some time until long enough pieces of HTS superconducting cable will be available commercially.

For magnetic fields alternating in direction, magnetic fluxes from neighboring solenoids add in the gap between the magnets, so in the coil the maximal field can be higher than on the magnet axis. Figure 4 shows the longitudinal distribution of the magnetic field in the cooling channel for the case where the coil thickness **w** = 50 mm, and the solenoid length L = 1 m. The sine-like line shows the magnetic field along the axis of solenoid; the other lines show the field components $\mathbf{B_r}$, $\mathbf{B_z}$ and the absolute value $\mathbf{B_t}$ on the inner surface of the coil. One can see that the component $\mathbf{B_r}$ gives the main contribution to the edge field. Here the magnetic field reaches almost 10 T. According to Figure 3, NbTi wire cannot be used in such a field, and it is necessary to use Nb_3Sn alloy. From the same chart, it is clear that the Nb_3Sn coil thickness must be more than 65 mm.

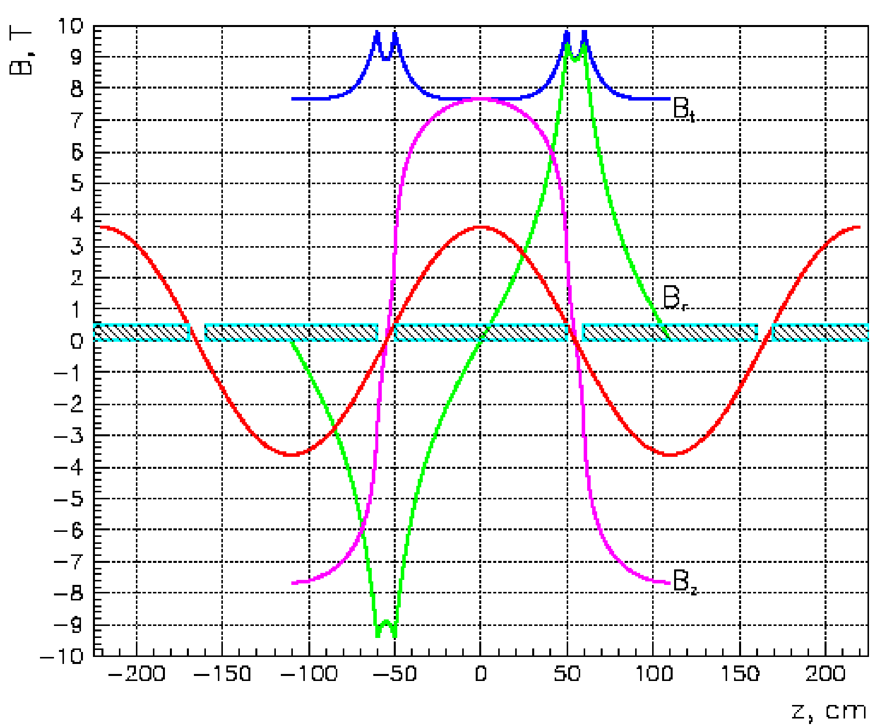

Figure 4. Magnetic field distribution in the cooling channel for solenoid length L = 1 m.

The choice of optimal coil length can reduce the magnetic field inside the magnet coil. Figure 5 shows how the maximal field in the coil depends on the solenoid length. The magnetic field near the edge of the coil (upper curve in Figure 5) is 9.2 T when the coil length is about 0.8 m. The magnetic field in the coil in the central area of the magnet (lower curve) is about 8.2 T with this coil length.

By increasing the coil thickness, it is possible to further reduce the field in the coil, as shown in Figure 6. Again, the upper curve here shows the magnetic field near the magnet edge and the lower curve shows the magnetic field in the coil in the center of the solenoid. It should be mentioned that the quantity of superconducting material does not necessary increase with coil thickness, because more copper can be added into superconducting wire to reduce the engineering current density. This addition can also be useful as a protective measure at a quench. The choice of coil thickness and wire and cable design must be finalized after the quench protection system is developed.

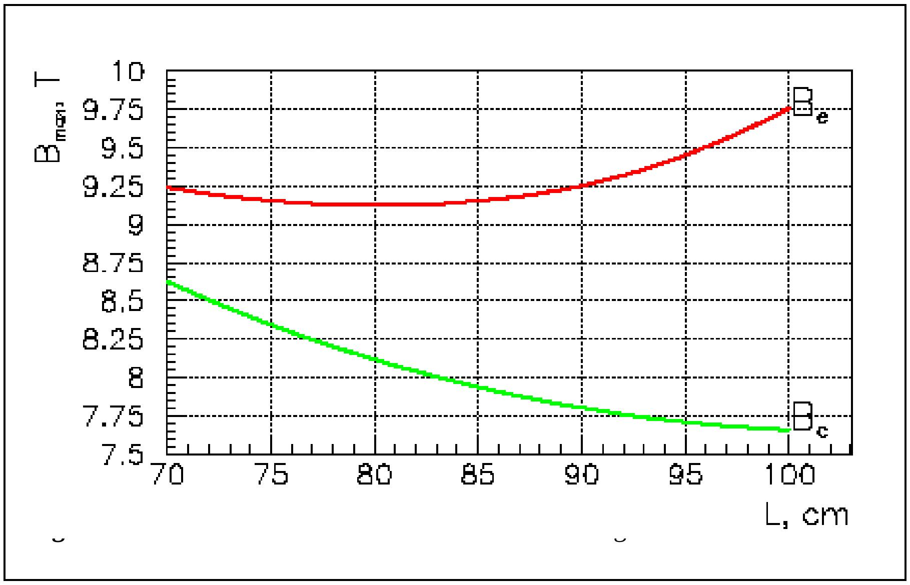

Figure 8 shows the longitudinal distribution of magnetic fields in a coil when with solenoid length L = 0.8 m and coil thickness w = 175 mm. One can see that the magnetic field in the coil now reaches only about 8.3 T, and the field does not change significantly along the length of the solenoid. It is also possible to see that the magnetic field near the edge of the solenoid is about 0.5 T higher than the field in the central part of the coil. An additional improvement of field distribution in the coil is possible if one uses a more elaborate optimization procedure.

The radial distribution of magnetic fields for this case is shown in Figure 7.For the case with L = 0.8 m and w = 175 mm, the calculated radial stress on the outer surface of the coil is about 15 MPa. This stress can be managed using strong banding. A simple mechanical analysis shows that to withstand the radial pressure, 6-mm stainless steel bands are required and does not seem to be a problem. Longitudinal stresses in the middle of the coil can be calculated given the magnetic field distribution and a detailed magnet design. Simple integration of forces along the length of the magnet gives an axial stress in the middle of the magnet of about 90 MPa. The use of external bonding introduces friction between turns and layers which reduces this stress to some extent depending on the initial coil pre-loading, although a mechanical design involving stress management features and elaborate mechanical analysis must be performed to insure proper coil performance. Probably, it will be useful to subdivide the solenoid coil into several sections using strong stainless steel walls so that the stress in the coil does not exceed the yield stress of copper in the superconducting wire. Epoxy impregnation will also help to improve coil mechanical stability.

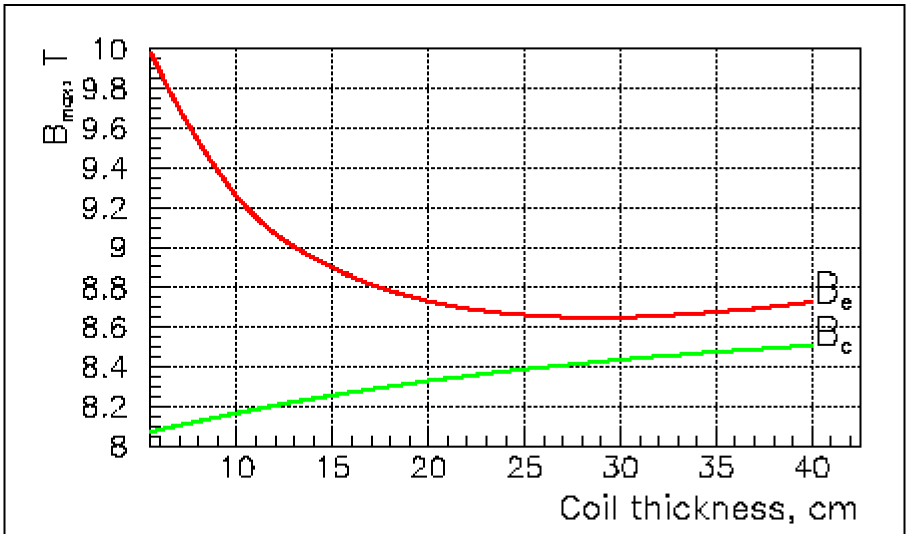

Figure 6: Maximal field in the center (B_c) and near the edge (B_e) of the solenoid versus coil thickness

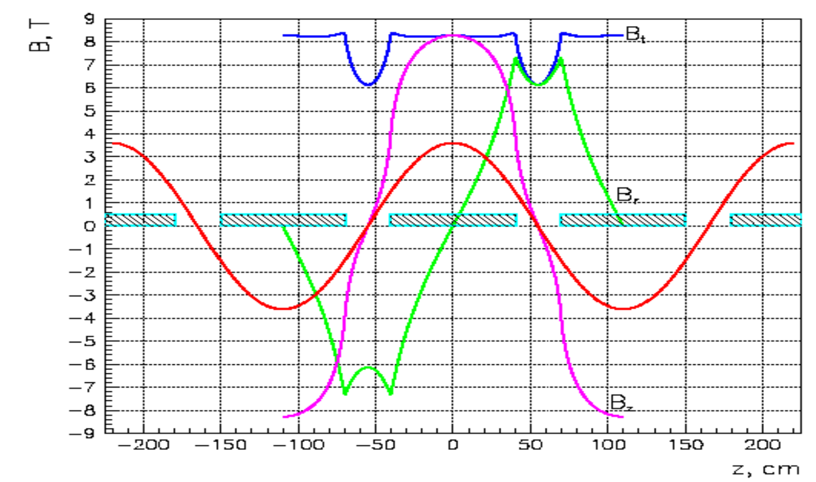

Figure 8: Magnetic field distribution for solenoid with L = 0.8 m and d = 175 mm

It is worth noting that the tensile yield strength of oxygen-free high conductivity soft copper is about 65 MPa at room temperature [2], so one can expect wire critical current degradation at the expected stress level. On the other hand, oxygen-free high conductivity hard copper has a tensile yield strength of about 230 MPa at room temperature, and the tensile yield strength of especially hardened copper can reach 340 MPa [[2], [3]]. Using copper with this high yield strength can help to solve the solenoid design problems. The large inner radii of the solenoids allow the use of "react and wind" technology that will help to keep the copper wire in the "hard" state. Fabrication and study of a wire that consists of Nb_3Sn superconductor in a copper matrix are subjects for R&D. Another way of solving the problem of stress in the magnet coil is increasing the coil thickness. For example, if the coil thickness increases from 175 mm to 350 mm, the axial pressure drops from 90 MPa to 55 MPa. However, stored energy, total current in magnet, and coil volume (the amount of superconducting material and copper) grow when the coil thickness increases. Coil geometry optimization, as an initial step will help to reduce the maximal magnetic field in the coil and improve other magnetic and physical parameters. This work can be done more efficiently if the cavity geometry and beam envelope are defined.

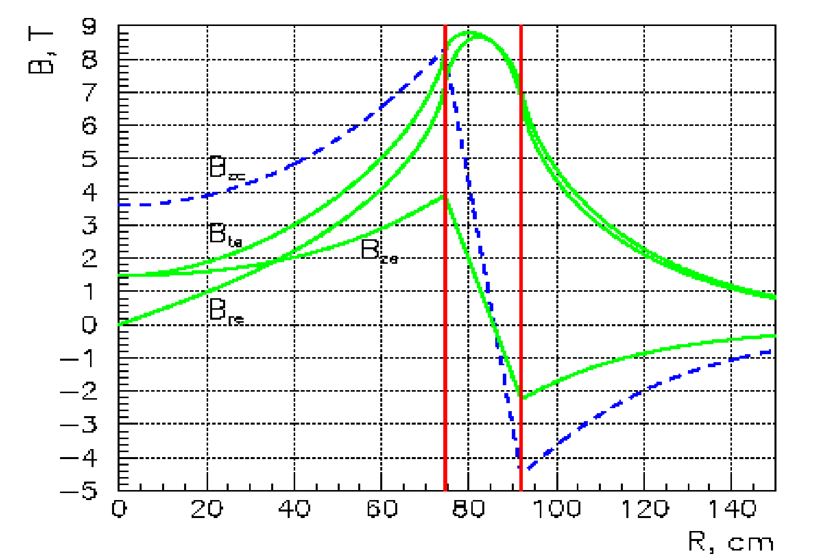

Figure 7: Radial distribution of magnetic field. Dotted line is the field in the center plane of solenoid; the other lines show end field components.

Significant repulsive forces between magnets in the channel can significantly complicate the channel design unless one takes special precautions. For magnets in the middle of the channel, the repulsive force can reach approximately 20 MN from each neighboring magnet. These forces are balanced for a magnet inside the channel, but the first and the last magnet must each have an adequate support to withstand the force. If one of the magnets inside the channel quenches, the balance of forces for neighboring magnets is broken, and this results in unacceptable longitudinal forces. This requires using rigid supports for each magnet in a channel, and this significantly complicates the mechanical design of the channel. To avoid this, it is possible to consider the removal of stored energy simultaneously from all magnets in the channel. For this purpose, a reliable and fast quench detection scheme is required. One possible solution can be a bridge-type quench detector. When the voltage on the resistive section of a coil exceeds a threshold value, the quench detector generates a signal to start protective actions.

Central field, T	3.6
Bore diameter, m	1.4
Total current, MA	9.64
Total number of turns	1600
Inductance, H	2.55
Operating current, kA	6
$I_{nominal}/I_c$ ratio	0.5
Cu/SC ratio	35:1
Coil length, m	0.80
Cryostat inner diameter, m	1.4
Cryostat outer diameter, m	2.18
Cryostat length, m	1.0
Coil thickness, mm	175
Coil inner radius, m	0.745
Cable length, km	8.5
Cable mass, kg	3600
Mass of magnet, ton	8.0
Stored energy, MJ	48.0

Table 4: Parameters of a magnet in the cooling channel.

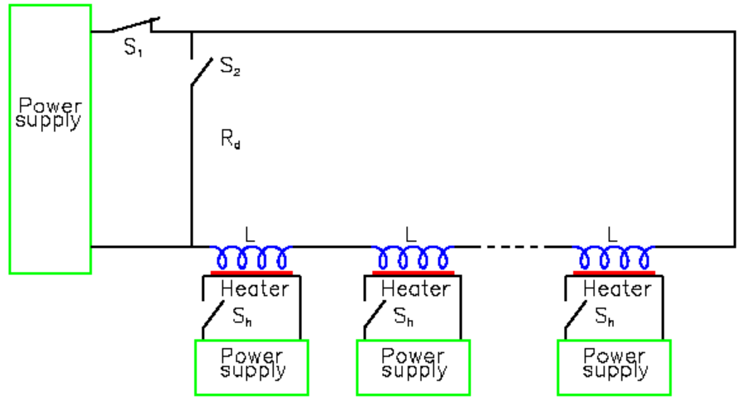

Figure 9: Quench protection sketch of magnets for the fourth channel.

There is a total of 90 magnets in the cooling channel. Each magnet is placed in its own cryostat. The cryostat inner diameter is 1.4 m and the outer diameter is 2.2 m. The gap between the neighboring cryostats is 10 cm. The magnet coil is wound using Nb_3Sn cable with a cross-section of 8.0 x 10.6 mm^2. For quench protection, the copper-to-superconductor ratio is 35:1 for this cable. The coil has 1600 turns in 16 layers. The total length of cable is 8.5 km, and its weight is about 3.6 ton, so several cable splices are to be done during winding. The main parameters of a magnet in the cooling channel are listed in Table 4.

The total energy stored in the channel is 4.3 GJ, and this makes development of a quench protection system for the channel a first priority issue. As was mentioned earlier, some protective precautions must be used like fast quench detection and fast removal of stored energy from the channel into the external dump resistor and/or "smearing" of this energy inside the magnets using heaters. A protection circuit for the cooling channel that takes these special features into account is discussed below. The quench protection scheme is presented in Figure 9. All magnets in the channel are connected in series into one string. A 3 MW power supply is used that allows reaching the nominal current level within 1 hour. There is no dump resistor in this scheme because it appears to be inefficient for the cooling channel. All magnets are equipped with heaters that are fired by switches S_h simultaneously. The stored energy of each magnet is dissipated inside its cryostat, in the magnet coil. The maximum temperature reaches about 230 K in the magnet where the quench has originated; for other magnets, the maximum temperature is below 190 K. Quench process diagrams for the magnets of the channel are shown in Figure 10.

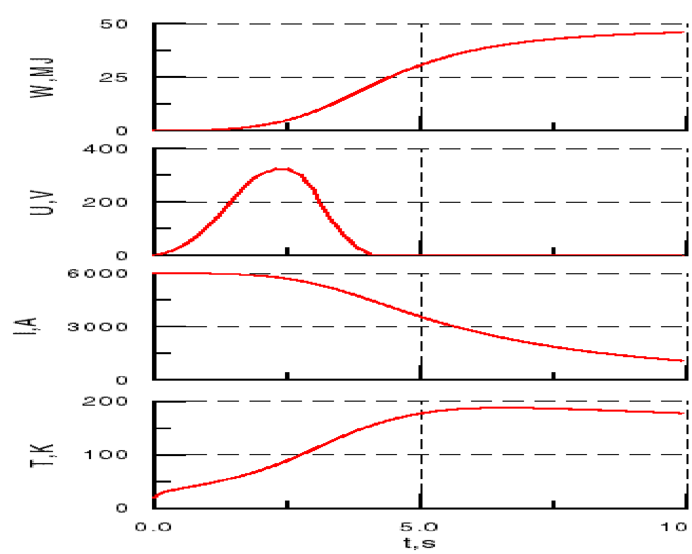

9.3 Power supply and cryogenic system requirements

Table 5 summarizes the requirements on the power supply for each channel described above. Table 6 presents the calculated budget of heat leaks in the cryogenic system which can be considered as the initial requirements for the cryogenic plant providing cooling agent to the channels.

The essential feature of the channel is the long time required to cool down the magnets. In the protection scheme that was described it may take several days to reach 4.5 K after a quench. A more efficient protection scheme that dissipates energy out of the cryostats is a subject for R&D.

Channel	Drift	RF	I.L.	Cooling
Operating current, kA	6	6	6	6
Voltage, V	30	30	30	500
Power, kW	180	180	180	3000
Current stability	10^{-3}	10^{-3}	10^{-3}	10^{-3}
Total inductance of magnets, H	0.61	4.0	1.1	230
Ramp rate, A/s	30	10	30	1.7
Number of power supply	1	2	2	1
Energizing time, s	200	600	200	3600

Table 5: Power supply parameters for the NF front-end magnet channels.

Channel	Drift		RF + Drift		Induction Linac		Cooling	
Temperature	4.5	80	4.5	80	4.5	80	4.5	80
1. Cryostats:	52	650	86	1480	187	1370	300	3400
Radiations, W	30	550	52	1300	45	1120	100	2500
Supports, W	10	80	20	160	83	160	137	800
Voltage taps, W	10	20	10	20	42	90	45	100
Seals between coils, W	2		4		17		18	
2. Transfer line, W	1	20	2	20	10	200	10	200
3. 30% margin, W	17	230	32	500	63	430	90	1000
4. Total, W	70	900	120	2000	260	2000	400	4600
5.Current leads, l/h	21		41		41		21	
Required power, kW	115	26	219	57	331	57	383	133

Table 6: Budget of heat leak in the cryogenic system.

9.4 Conclusion

As part of this Fermilab Neutrino Factory study, a preliminary analysis has been made to realize the feasibility and complexity of the magnetic systems for the drift channel, phase rotation channel, and cooling channel. For each channel, a simple optimization was done with the goal of reducing its cost. It was impossible during this short study to identify and to address all the problems that can arise during magnet development and design. Some of these problems can be resolved in a normal way. Others need an additional research stage.

A preliminary cost estimate for the magnetic system construction and operational expenditures can be made based on the data obtained during this study. This cost estimate can be updated after the R&D program is completed at the time of a technical proposal. For each channel, it was shown that the major portion of the cost is the cost of the superconducting magnets. The cost of the drift channel makes up the bulk of the cost of the entire magnetic system. Technical difficulties anticipated in building the cooling channel indicate that the future R&D program must be devoted mainly to analyzing and modeling this channel.

REFERENCES

[1] Neutrino factory technical study coordinator: N.Holtkamp and D.Finley. See http://www.fnal.gov/projects/muon_collider/nu-factory/nu-factory.html

[2] M.A.Green et al. Superconducting Solenoids for the Muon Collider. MT-16, 1999, Ponte Vedra Beach, Fl, USA. http:/www.matweb.com/SpecificMaterial.com/
[3] Handbook on physical and technical basis of cryogenic. Editor by M.P.Malkov. Moscow, Energoatomizdat, 1985, p.2.

10. The 200 and 400 MHz High Power RF Systems

10.1 Introduction

In the neutrino source the largest number of high power rf systems is required in the cooling channel itself. Ionization cooling of muons requires strong solenoidal magnetic fields and the cavities, which replenish the energy loss in the absorbers, have to be placed inside. Overall this leads to a complex technical layout which includes magnets, absorbers, cavities and diagnostics together with cryogenic feeds, high power rf couplers and water for cooling the structures. A typical layout under study for the cooling channel is shown in Figure 1 where superconducting coils surround the normal conducting cavities. This cooling channel is approximately 150 meters long and requires more than 75 klystrons. The total installed voltage is approximately 2 GigaVolts. The geometric layout of the klystron gallery for the cooling channel has been worked out in much greater detail than for the superconducting accelerator, because the high density of rf power sources makes the building, the installation, and the maintenance a challenge. The general facility requirements for the klystron gallery of the superconducting accelerators are scaled from the cooling channel gallery.

For the superconducting accelerators, 200 and 400 MHz power sources are required. While the pulse length here is much longer, the total number of klystrons required to accelerate the beam from 0.1GeV to 50 GeV is less than in the cooling channel. In this case many cavities are powered by a single klystron station. The pulse length of the klystron is much longer because the cavities are filled over a much longer period of time (compared to the Muon Accelerator Driver in chapter 7).

10.2 Considerations and Specifications for the Cooling Channel

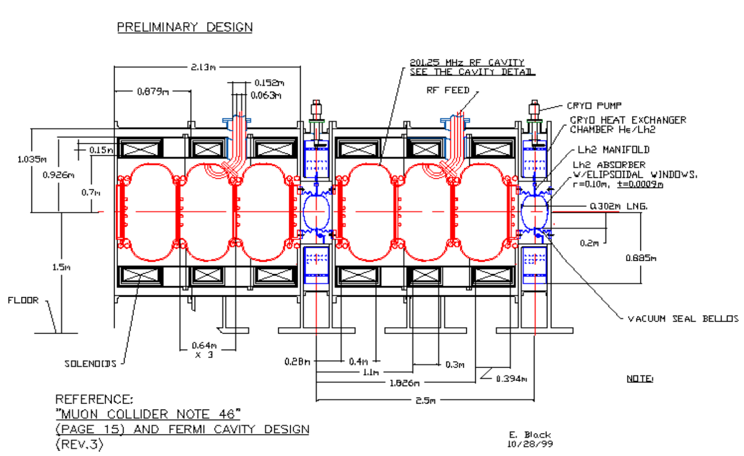

Figure 1: Conceptual layout of two cooling cells, taken as the basis for the design of the rf systems layout of the cooling channel. Changes of the cooling channel design during the study have not been implemented here for two reasons. The first one being that the peak power requirement per meter does not vary significantly for the different designs, and the second one being that we used the full 6 month study time to develop a consistent engineering design.

With the parameters in Table 1 to work with, a number of different rf devices have been investigated. Given the issues of either limited gain, limited experience, or geometric size of the devices, it was decided at this early stage to propose a klystron (even though the length is an issue, possibly as long as 7.75 meters down to maybe less than 4 meters for a Multibeam Klystron). A klystron in many ways seem less risky than other devices and should have a very good lifetime and performance. The MTBF (Mean time between failure) is an important consideration from the very early stage of the design, since there will be about 75 systems operating in the Cooling Channel alone. With no experience in building a pulsed 10 MW peak power klystron with klystron at 200 MHz, development time and significant R&D money is needed to implement such a design.

FREQUENCY:	201 MHZ
Rf Power:	5 MW /m
Rf Pulse width:	150 µsec
Duty Factor:	0.23%
Rep Rate:	15 Hz
Length of Channel:	~150 m

Table 1: Preliminary design parameters for the rf system in the cooling channel.

10.2.1 Proposed RF Station Blocks

The klystron specifications are shown in Table 2. The 10 MW rating is meant to achieve approximately 50% efficiency, but the klystron could most likely run at higher power levels with some reduction in efficiency. The final klystron's peak power requirements will depend on the specific cavity design for the cooling channel, which at this point in time is not finalized.

10.2.1.1 RF Power Source – Multi-Beam Klystrons

Table 2 lists a possible design envelope for a Multi-beam klystron operating at 10 MW. Special attention will be required to keep the cost per klystron to a reasonable level. This will most likely involve trade-offs in the following areas: rf versus mechanical design in the gun region, the output window, the rf cavities, and magnetic focusing. It may be that the total lengths shown in Table 3, for a multi-beam klystron are just not practical because of cavity coupling, geometry, or other mechanical constraints. The multi-beam option, nevertheless, has the potential of reducing the length considerably, which at least would allow the use of existing infrastructure in industry or other laboratories during the R&D phase. It should be mentioned that this technology has been demonstrated to a certain extent (see for example TESLA design report[2]). In the presently foreseen layout, one 10 MW klystron will drive two cavities similar to the ones shown in Figure 1. A total of 75 klystrons station would therefore be required with about one Klystron every 2 meters.

PEAK RF POWER OUTPUT:	10 MEGAWATT
Beam Voltage:	~ 65 Kvolts
Beam Current:	~ 310 amps.
Duty Factor	0.23%
Rep Rate:	15 Hz
Efficiency:	~ 50%
Gain:	~ 50 dB
Rf output connection:	14 inch diameter copper coax with EIA flange.

Table 2: Multi-beam klystron specification

Frequency, MHz	200			
RF Power, MW	10			
µPerveance , $A/V^{1.5}$	2			
Efficiency, %	44			
Item	Value	Value	Value	Units
Type	ring	3 pole	2 ring+1	-
Number of beams	6	12	19	-
Vb	81	62	51	kV
Itotal	279	368	442	A
Bz	233	251	264	G
Total anode dia	53.3	58.4	60.9	cm
l_q	6.201	5.279	4.759	m
Gun + collector len	1.05	0.87	0.77	m
Total length is from	2.6	2.18	1.96	m
to	4.15	3.51	3.15	m

Table 3: Design envelope for a Multi-beam klystron [1].

10.2.1.2 Modulator Specifications for the Proposed Multi-Beam Klystron

The Modulator specifications are given in Table 4. With recent advances in high power solid-state electronics, Insulated Gate Bipolar Transistors (IGBTs) are a very attractive (and cost effective) solution for delivering high voltage to the klystron. Similar modulators with much longer pulse length have been built for the TESLA test facility. Solid State Modulators have been built commercially for similar applications and are being considered for use in other high energy physics projects, currently planned [2]. (The HV power supply is included as part of the Modulator.) Each klystron will have its own Modulator.

VOLTAGE:	65 KVOLTS
Peak Power:	20 Megawatts
Current:	310 Amps
Average Power:	60 Kwatts
Pulse Width:	200 uSec.
Size:	1.2 x 1.2 x 2.4 Meter
Rep Rate:	15 Hz.
Droop:	~ 5%

Table 4: Solid State IGBT Modulator specifications.

10.2.1.3 14 inch Diameter Coaxial Transmission

A 14 inch diameter rigid coaxial transmission line with standard EIA flanges will be used to couple power from the klystron to the cavity. To preserve the coaxial line's interior surface and insulators, the line will be pressurized to 0.5 psig with dry air. There will be two rf windows in each system. The klystron window is an integral part of the klystron. The other window is located at the input to the rf cavity. The total electrical wavelength between the klystron and the cavity will be adjusted to be an integer number of half wavelengths long.

10.2.2 Water Skid – Temperature Regulation

Each water system will supply tempered water for each two meters of cavity. This local water skid will have its own heaters, pumps, de-ionized water loop, and heat exchangers with primary cooling to the heat exchanger supplied from a central chilled water loop. Approximately 22.5 Kwatts of heat will be dissipated in each two meters of cavity. Low conductivity water (LCW) of about 10 MΩ cm resistivity will regulate the temperature of the cavities. The water skids will be located as shown on the floor plan layout. This location was chosen to minimize both the piping to the tunnel and equipment gallery piping.

10.2.3 Station Relay Racks

Each rf station will have five racks for housing controls, power supplies, LLRF (Low Level RF), and a 250 W solid state driver amplifier. These racks are the standard 24 inches wide by 30 inches deep and 86.5 inches high. The different components installed in the rack are listed below.

Controls - Digital I/O & Analog monitor

The control system could be similar to the one used at Fermilab's Main Injector which uses a local VME based system for local station applications and communication with the main control room (ACNET).

Power Supplies

A number of ion pump power supplies will be required for the klystron and the accelerating cavity along with the klystron solenoid power supplies.

LLRF

Each station will have a local feedback loop for phase regulation. Spark detection will include circuits to protect the Klystron, rf windows, cavity surfaces, and transmission line. A commercially available 250 W solid state amplifier will be used to drive the klystron.

10.2.4 Water distribution

The water distribution system is a standard water system for this type of an installation (stainless steel piping). The requirements for the normal conducting cavities in the cooling channel have been included.

	Per station	75 stations
95 degree cooling LCW	75 gpm	5625 gpm
Industrial chilled water	20 gpm	1500 gpm

Table 5: List of requirements for the cooling water requirement.

10.2.5 Electrical Power

The AC power distribution will be done by using cable trenches as shown on the floor plan of the building (comp. Figure 3). Only signal cables will be located in overhead be cable trays.

480 Volt 3-phase		Per station	75 Stations
	Filament:	5 kW	375 kW
	Modulator:	60 kW	4500 kW
	Solenoid power supplies:	10 kW	750 kW
	Solid State rf Amp:	2.5 kW	188 kW
	Water Skid:	20 kW	1500 kW
	Misc:	10 kW	750 kW
	Pumproom:		750 kW
120/208 volts			
	Relay racks:	5 kW	375 kW
	Ion pump PS:	3 kW	225 kW
	Misc:	2 kW	150 kW
Total Power		117.5 kW	9,562.5 Kw

Table 6: Summary of electrical power requirements.

10.2.6 Installation

Since the rf systems will be installed in a new building, all of the supporting utilities for the high power rf will be installed as part of the building construction. The LCW piping, ICW piping, 480/208/120 AC power distribution, and cable trays will be an integral part of the construction. Two overhead cranes running the length of each equipment gallery are required for installation of the klystrons and solenoids. They will mainly be used if a klystron and/or a solenoid has to be replaced. The width of the building can probably be reduced to about 75 feet if the klystron R&D program determines that the fabrication of 200 MHz, 10 MW klystrons with a total length of fewer than 15 feet is feasible. The klystrons could be mounted vertically in this case.

10.2.7 Equipment Gallery Layout for the Cooling Channel

Figure 2 and Figure 3 show a portion of a typical rf gallery layout along with a cross section of the building. The building is approximately 150 meters long by 30 meters wide. Each single rf source can supply enough peak power for 2 meters of rf structure. Therefore, the klystrons are not only arranged side by side, but also on both sides of the gallery. The modulators are next to the klystrons with enough space reserved for maintenance.

10.3 Considerations and Specifications for the Superconducting Accelerator

The three superconducting accelerators consist of the preaccelerator, the first recirculating Linac (RLA1) and the second recirculating Linac (RLA2). With the use of superconducting cavities, the power loss in the cavities is negligible and because the energy extracted by the beam does not have to be replenished during the pulse, a very slow fill mode will be used (compare chapter 7 on the Muon Accelerator Driver). The peak power per unit length in order to charge up the cavities to the operating gradient can therefore be comparatively low. In order to minimize the number of active components, the peak power delivered per klystron station should be maximized. For the required pulse length of 2 milliseconds, a comparison was made to existing klystrons in terms of average rf power being achieved versus peak power. A 10 MW

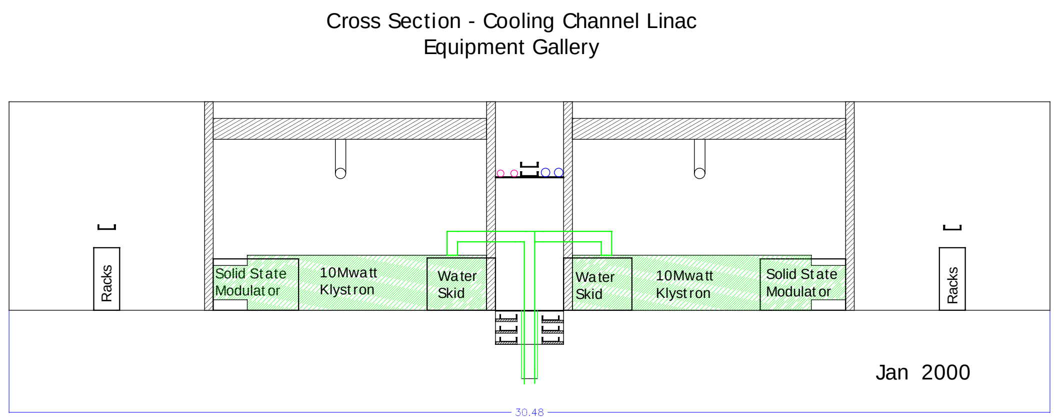

Figure 2: Cross section of equipment gallery

klystrons operating at a pulse length of 2 milliseconds, and a repetition rate of 15 Hz would clearly not be limited in terms of average power as compared to other high power devices. The length of such a klystron is similar to the ones proposed for the cooling channel, but a much larger collector is required because of the larger duty cycle.

10.3.1 Klystron Layouts for 200 and 400 MHz

The klystrons that have been considered for the superconducting accelerators are multi beam klystrons as well, and are very similar to the one described in Table 2 and Table 3. The basic advantage of more beams per klystron is a reduced voltage and therefore a reduced length of the rf circuit. At 400 MHz, the length reduces even more. For the 200 MHz klystron, beam parameters identical to the cooling channel klystron were assumed. For the 400 MHz klystron, the same arguments hold. At this frequency the current density goes up as well as the power dissipation in the collector. From a technical point of view this klystron is more challenging than the 200 MHz klystron.

Frequency, GHz	0.4			
Rf pwr, MW	10			
µPerveance , A/V$^{1.5}$	2			
Efficiency	44%			
Item	Value	Value	Value	Units
Type	ring	3 pole	2 ring+1	-
Number of beams	6	12	19	-
Vb	81	62	51	kV
I total	279	368	442	A
Bz	233	251	264	G
Total anode dia	53.3	58.4	61.0	cm
l_q	3.170	2.692	2.423	m
Gun + collector len	1.05	0.86	0.77	m
Total length is from	1.84	1.54	1.38	m
to	2.63	2.2	2.0	m

Table 7: Preliminary design parameters for a 400 MHz klystron operating at 10 MW output power [1].

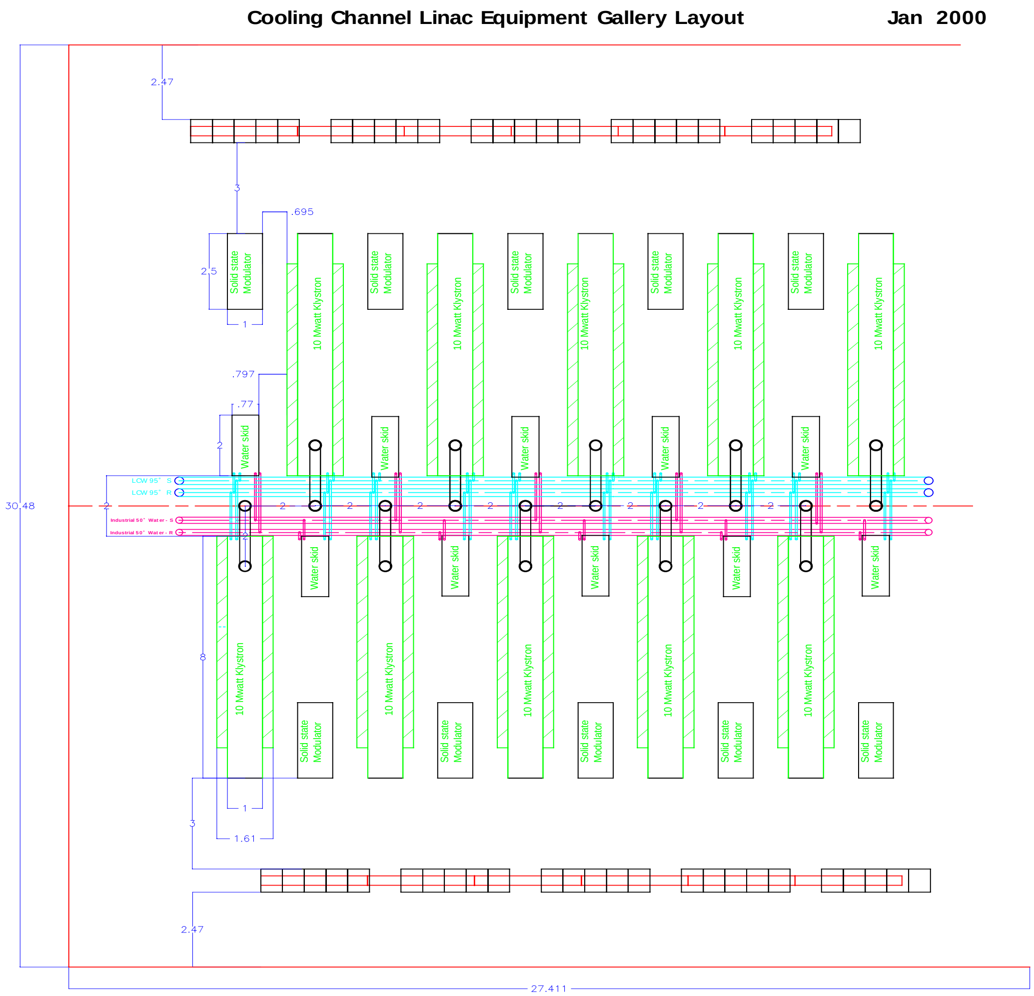

Figure 3: Partial floor plan of equipment gallery for the cooling channel.

10.3.2 Power Distribution into the Cavities

The power distribution into the superconducting cavities is described in this section. The 200 MHz cavities have a peak power of 820 kW/cell which is necessary to fill each cell within 2 msec. For 400 MHz cavities, only 200 kW/cell is required. The rf power distribution into the cells and the total number of klystrons are shown in Table 8. Similar to the Cooling Channel's 75 rf stations, a total of 80 klystrons and modulators are required for the three superconducting accelerators.

Name	Freq MHz	Pulse width msec	MW per Linear meter	Cells per klystron	Number cells	Total installed Votage/GeV
preaccel.	200	2	0.55	10	320	3.6
RLA1	200	2	0.55	10	231	2.6
RLA2	400	2	0.2	60	1,511	8.5
Total						14.7
Name	Peak MW	Ave Pwr kW per klystron	No. of klystrons	Linear meters per klystron	Linear meters	Average rf Power MW
Preaccel.	8.25	247.5	32	15	480	7.9
RLA1	8.25	247.5	23	15	347	5.7
RLA2	9	270	25	45	1133	6.8
Total			80		1960	20.4

Table 8: Description of the power distribution for the superconducting accelerators.

10.4 Conclusion

It became obvious very early in the study that the high power rf systems are one of the major cost drivers for the whole facility. In the cooling channel, the klystron density required to feed the normal conducting cavities represents an additional difficulty which leads to a comparatively large rf power installation with a large klystron gallery and a high density of klystrons. The average rf power required for each accelerator is almost identical for each accelerator and would be four times as high for RLA2, if RLA2 would operate with 200 MHz cavities. Therefore, there is a strong desire to go to 400 MHz at this point in the accelerator chain. The intrinsic efficiency for converting AC to rf power for both rf systems in the cooling channel and in the superconducting accelerators, is assumed to be very high. The long rf pulse length in combination with the use of Multi-beam klystrons will allow higher efficiencies than usually achieved in pulsed rf systems. For this report, a modulator efficiency of 85% will be assumed, which brings the system efficiency to approximately 35% and therefore the total average power consumption for the RLA's for the rf to 60 MW of ac power.

REFERENCES:

[1] courtesy of D. Sprehn, Stanford Linear Accelerator Center. Provided during working meeting on Feb.17th and 18th at Fermilab, Feb.2000, "Feasibility of Super-Conducting RF systems and Magnets for Muon Acceleration".

[2] (editor: R. Brinkmann, et al.) "Conceptual Design Of A 500-Gev E+ E- Linear Collider With Integrated X-Ray Laser Facility. VOL. 1+2", DESY-1997-048, May 1997. 1183pp.

11. Cryogenic Systems

11.1 Introduction

The proposed Neutrino Factory will require an extensive helium cryogenic installation to provide sufficient cooling for subsystems that are based on superconducting technology, e.g. the target solenoid, the solenoid channels, the various accelerating stages and the storage ring. The design of such a system is an iterative process of optimization of cost and performance with respect to the many requirements, both quantitative and qualitative. The starting point of the iteration is a system concept with point designs for the major processes. In the following paragraphs a first approximation to such a starting point is presented.

11.2 Refrigeration Plant and System Layout

An important feature of the cryogenic system of the Neutrino Source is the variety of components in the system, and the mixture of warm and cold components along the beam lines. It is inevitable in the Neutrino Factory that distribution of cryogens to a system of cryogenic modules is a major issue. It is reasonable to investigate a system that has one refrigeration plant first. A possible layout of this type is pictured in Figure 1. The refrigeration plant is centrally located, and five cryogen transfer lines distribute cooling to the cryogenic modules in five subsystems: one line serving the injector components and the pre-accelerator linac; one line for the linacs of RLA1; two lines (a loop) for the two linacs and the superconducting magnet systems of RLA2; and one line for the superconducting magnet systems of the storage ring. Figure 1 is schematic. The lengths of the lines given here are estimated from the site layout in chapter 13 on civil construction.

Figure 1: Layout of Transfer Lines

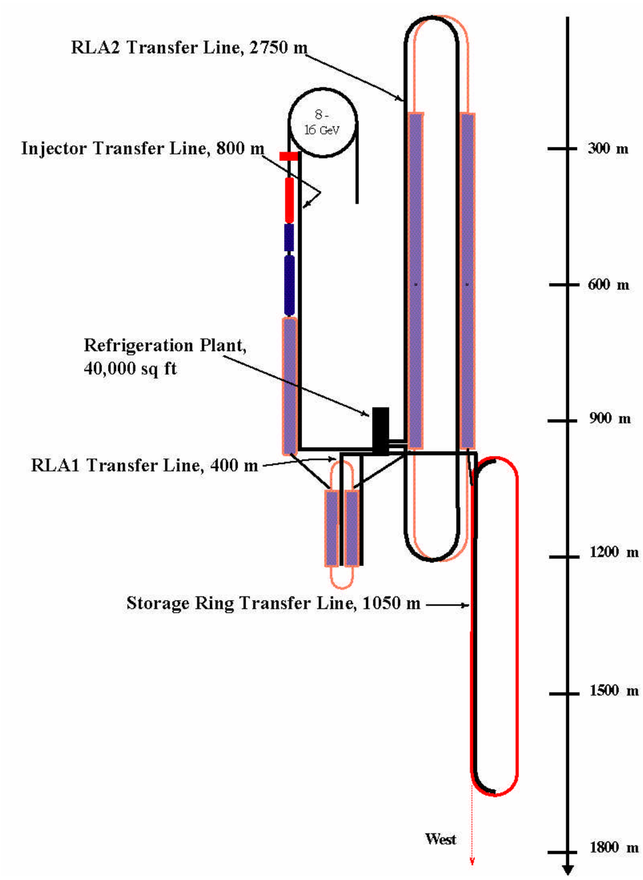

11.3 System Process

Refrigeration is provided by the plant in four forms. Table 1 lists the refrigeration plant streams and gives appropriate thermodynamic details.

1) 4.5 K refrigeration is provided by a flow of helium at 3 bar pressure and 4.5 K. This is expanded in a J-T process (Joule Thomson) to saturated helium at 4.5 K. The saturated gas is returned to the refrigeration plant.
2) 4.5 K liquefaction is provided from the 3 bar, 4.5 K stream returning at 1 bar and 300 K.
3) Shield cooling is provided by a stream delivered from the refrigeration plant at 19 bar and 40 K and returned at 16 bar and 60 K.
4) 40 K liquefaction is provided from the 19 bar, 40 K stream also returning at the standard state.

11.4 Cryogenic System Components

At the level of abstraction of this report, the cryogenic system of the Neutrino Factory consists of three kinds of components: Refrigeration plant; transfer line; and boxes. These will be described below.

11.4.1 Refrigeration Plant

Anticipating the results of the capacity requirement roll up and from the discussion below, the capacity required in this plant for the Neutrino Factory is 80 kW equivalent at 4.5 K. This is equal to two LHC-size refrigeration stations. LHC is installing four stations each with two cold boxes of 20 kW equivalent capacity at 4.5 K [1]. This experience makes the specification and procurement of a refrigeration plant for the Neutrino Factory a straightforward engineering task with low risk.

The Neutrino Factory plant will contain approximately twenty helium screw compressors, oil removal, and inventory management equipment. This system will require about 24,000 square feet of medium rise floor space isolated for noise control and ventilated for about 2 MW of heat dissipation. The cold boxes will require about 15,000 square feet of space. In addition 1,500 square feet of air-conditioned space would be needed for control system electronics and local control room.

The total installed power in this plant will be about 25 MW with a nominal operating power of about 18 MW. Heat rejection of 25 MW with redundancy will be needed.

11.4.2 Transfer Line

The transfer line system includes four cold lines and two warm lines. The cold lines carry the supply and return streams listed in Table 1. The sizes required for these lines will be different for the different transfer lines, but typical sizes are: 2 and 3.5 inch ips sch 5 for the 4.5 K supply and return: and 2.5 inch ips, sch 5 for the 40 - 60 K shield system supply and return. The transfer line will contain a shield thermally connected to the 60 K return line. The outside diameter of the vacuum jacket of the cold line assembly will approximately 18 inches.

Stream / Condition	Pressure	T	Enthalpy	Exergy	Ideal work	Watts/watt
	bar	K	J/g	J/g	J/g	
Standard State	1.0	300	1573.516	7910		
4.5 K Refrigeration - Carnot						65.667
4.5 K refrigeration - Supply	3.0	4.5	11.782	1075		71.825
4.5 K Refrigeration - Return	1.2	4.5	31.526	2493		
4.5 K Liquefaction					6835	
40-60 K Refrigeration Supply	19.0	40	223.611	4259		6.14
40-60 K Refrigeration Return	16.0	60	329.762	4911		
40 K Liquefaction					3651	

Table 1: Refrigeration Plant Streams and Thermodynamic Conditions

The two warm lines are warm helium gas supply and return - the supply for module purging and warm-up and the return for the liquefaction load and for module cool-down. The sizes of these lines might be 2 and 4 inch ips.

The transfer line system will include other components such as supports, periodic vacuum barriers in the cold line, and an insulating vacuum system with monitoring.

11.4.3 Boxes

The variety of requirements for modules that must operate in this cryogenic system can best be satisfied by providing a minimum set of components in each connection box. These components are needed for connecting an individual module to the transfer line. Each module will contain the special equipment required in addition to the minimum set. Examples of special situations are modules that have saturated helium baths or current leads. The saturated bath would need a liquid level gauge and the current leads would need flow control for the liquefaction flow.

In general the boxes will require four cold shut-off valves, two cold control valves, and valves for the warm gas lines. In addition there will be a vacuum barrier between the transfer line and the module and some means of disconnecting the module - U-tubes or field joints. Some instrumentation and some relief devices will be standard in the boxes as well.

11.5 Module and Component Heat Loads

Cryogenic system heat loads in each of the four categories for modules in the Neutrino Factory subsystems are given in Table 2 below with discussion following. These are divided into static and dynamic components. The static heat load is that which is present when the beam and all power supplies are not operating.

11.5.1 Current Leads

The Neutrino Factory is assumed to use HTC current leads throughout. The HTC bottom ends of the leads are to operate up to 60 K and are to be conduction cooled. The top ends are to be cooled by a flow of 40 K from the shield circuit returned to the refrigeration plant at 300 K. This is high-pressure gas regulated by a valve at room temperature, and the circuit will probably have to have a cold shut-off valve. In the heat load estimate the requirement is taken to be 0.1 g/s at 40 K and 1 Watt at 4.5 K both per kA-pair. The 40 K liquefaction load is divided equally into static and dynamic.

11.5.2 Target Solenoid and Channels

Heat load estimates for the target solenoid were made at the National High Magnetic Field Laboratory [1][2]. The heat load estimates for the solenoid channels appear in chapter 9. It is assumed that each channel will have one pair of 6 kA current leads.

Module	Number	Boxes						
			Static Heat Load				Dynamic Heat Load	
			40 - 60 K	4.5 K	4.5 K Liq.	Lead kA	40 - 60 K	4.5 K
			Watts	Watts	g/s	kA	Watts	Watts
Injector								
Target Solenoid, 20 T	1	1	42	420		10		
Decay Channel	1	1	900	70		6		
LIA Channel	1	1	2000	260		6		
Cooling Channel	1	1	4600	400		6		
3.4 GeV Linac								
200 MHz short module	16	16	200	33	0.1			27.5
200 MHz long module	30	30	300	50	0.2			55
Focusing Solenoid	46	46	200	33		1		
RLA I								
200 MHz long module	24	24	300	50	0.2			55
RLA II								
400 MHz Long Modules	91	91	200	33	0.2			132
East Arcs								
Splitter Magnets	8	8	200	33		5		
Half-Arc	10	20	540	90		25		80
West Arcs								
Splitter Magnets	6	6	200	33		5		
Half-Arc	8	16	540	90		25		80
Storage Ring								
Half-Arcs	4	8	540	90		50	3717	441
Total Modules	247							
Total Boxes		269	50	20				
Total Transfer Lines, m	5000		2.5	0.1				

Table 2: Heat Loads of Modules and Components

11.5.3 Superconducting Linac Modules

The average heat load of the 10 m cryomodules of the 350 MHz LEP SRF system is 80 watts at 4.5 K. This system does not have intermediate temperature shielding, but it does have a 4.5 K liquefaction load of 0.25 to 0.05 g/s per cavity from gas cooling on HOM cables, beam tubes, tuners and power couplers [4][5]. The KEKB coupler also uses gas cooling [6], and in the design of SNS 0.05 g/s static and 0.025 g/s dynamic is allowed for each coupler[7]. The cryomodules for both CEBAF and the TESLA TTF have heat loads of about 1 W/m average for the parts of the system at 4 K and below.

It is somewhat difficult to directly extrapolate values for the 200 MHz 10 m long modules from this disparate set of previous designs. However, it would probably safe but not extravagant to estimate 5 W/m for the 4.5 K refrigeration load for these modules. Also we can take the 80 W load mentioned above as the shield load for the long modules,

Subsystem	**Number**	**Loads**						
		Static				Dynamic		
		40 - 60 K	40 K Liq.	4.5 K	4.5 K Liq.	40 - 60 K	40 K Liq.	4.5 K
		Watts	g/s	Watts	g/s	Watts	g/s	Watts
Front End		8742	1.4	1298	0	0	1.4	0
Target Solenoid, 20 T	1	42	0.5	430	0	0	0.5	0
Decay Channel	1	900	0.3	76	0	0	0.3	0
Induction Linac Solenoid	1	2000	0.3	266	0	0	0.3	0
Cooling Channel	1	4600	0.3	406	0	0	0.3	0
Transfer Line, m	400	1000		40				
Boxes	4	200		80				
3.4 GeV preaccelerator		27000	2.3	5472	7.6	0	2.3	2090
200 MHz short module	16	3200	0	528	1.6	0	0	440
200 MHz long module	30	9000	0	1500	6	0	0	1650
Focusing Solenoid	46	9200	2.3	1564	0	0	2.3	0
Transfer Line, m	400	1000		40				
Boxes	92	4600		1840				
RLA I		9400	0	1720	4.8	0	0	1320
200 MHz long module	24	7200	0	1200	4.8	0	0	1320
Transfer Line	400	1000		40				
Boxes	24	1200		480				
RLA II		44645	26	8700	18.2	0	26	13452
400 MHz Long Modules	91	18200	0	3003	18.2	0	0	12012
East Arcs								
Splitter Magnets	8	1600	2	304	0	0	2	0
Half-Arc	10	5400	12.5	1150	0	0	12.5	800
West Arcs								
Splitter Magnets	6	1200	1.5	228	0	0	1.5	0
Half-Arc	8	4320	10	920	0	0	10	640
Transfer Line, m	2750	6875		275				
Boxes	141	7050		2820				
Storage Ring		5185	10	825	0	14868	10	1764
Half-Arcs	4	2160	10	560	0	14868	10	1764
Transfer Line, m	1050	2625		105				
Boxes	8	400		160				
Total Load by Category		94972	39.7	18015	30.6	14868	39.7	18626

Table 3: Cryogenic Load by Subsystem and Category

applying one factor of two for the larger size and a second factor of two rounded down to reflect the fact that we will not want the shield to be a critical item. Including 0.05 g/s of 4.5 K liquefaction for each cavity, the total static cryogenic load of the 200 MHz 10 m module is estimated to be 50 Watts at 4.5 K, 300 Watts at 40-60 K and 0.2 g/s liquefaction at 4.5 K.

To get a similar estimate for the static loads 200 MHz short module and the 400 MHz module we take 2/3 of the load for the 200 MHz long module. The dynamic loads of the linacs are discussed in Chapter 7 of this Report. The values taken in Table 2 are the baseline values chosen in the Superconducting Study Meeting [11][12]: these are for the Preaccelerator, 2090 W; for RLA1, 1337 W; and for RLA2, 12,034 W. This is approximately a factor of three more than what has been presented in chapter 7, which assumed an ideal case with all the cavities achieving the specified Q0 and no contributions to the dynamic load from other sources (field emission, higher order modes, couplers etc). The number presented here is certainly conservative in that sense and should become smaller as the R&D progresses.

11.5.4 Half-Arcs of the Storage Ring

The arcs of superconducting magnets in the muon storage ring are illustrated and discussed in Chapter 8 of this report. Each of the two arcs is divided into two half-arc cryogenic modules each about 86 m in length. For the purposes of estimation of the cryogenic performance, each of the half-arcs contains 9 cells: a total of 18 dipoles and 18 quadrupoles; and each operates as a magnet string with a feed box at one end and an end box at the other. The magnet string operates with a flow of 40 g/s of single-phase helium, which passes down the length of the string in alternating half-cells and recoolers, and returns down the string again in alternating half-cells and recoolers. After passing through all of the magnets in the string, the single phase flow is flashed into the shell side of the recoolers. The two-phase sides of the recoolers are connected in series.

The heat loads are estimated in Chapter 8: the static load is 5 W per half-cell at 4.5 K and 30 W at 40-60 K. The dynamic loads are due to particle heating of the magnet iron and of the tungsten liner inside the magnet bore which is cooled by a flow of 40-60 K helium. The total lead current is 50 kA for each arc of the storage ring. It has been assumed that the half-arcs will have a transfer line connection box at both ends.

Issues in the storage ring cryogenic system are first, the large tilt of the ring, and second, the deep location of the west arc of the ring. The tilt requires that the magnet strings of the arcs operate on a slope that varies from about 20 % at the end of the arc to level at the apex of the ring. This presents problems in controlling the flow of the two-phase helium in the recoolers mentioned above. Each of the 4 strings of magnets will have to be operated so that the two-phase flow is down hill, and the recoolers will have to be equipped with wiers to distribute the two-phase fluid on the heat exchange surfaces. CERN has had to take similar measures in the LHC which has a slope much smaller than here. The 200 meter depth of the west arc in the storage ring presents problems with head pressure in the distribution of cryogens. For example, a 200 m head of saturated liquid helium is a pressure of 2.3 bar and of saturated gas, 0.43 bar. These are significant pressures compared to the saturation pressure of 1.3 bar, at it is clear that the depth places requirements on the cryogenic system. At LHC this problem is dealt with by dividing the refrigeration plant cold boxes at the 20 K level, putting the cold end down in the tunnel. This would be appropriate for the storage ring if it proves to be cost effective to have a local plant rather than distributed refrigeration for the deep end. An alternative to this is to put a cold compressor at the deep end to provide the head pressure. This was the choice made in the SSC cryogenic system design and it will work here also.

11.5.5 Solenoids of the Pre-Accelerator and Splitters and Arcs of RLA2

At the time of the Superconducting Study Meeting [11][12] there was no engineering design for the magnetic elements in the Pre-accelerator or the arcs of RLA2. For the purposes of cryogenic load estimation we take the static loads in the arcs of RLA2 to be the same as those in the arcs of the storage ring. The dynamic load due to particle loss in the last arc of RLA2 is estimated to be 2 W/m [12]. We therefore choose half this peak value or 80 W per half-arc for the dynamic load. Likewise we use half of the magnet current of the storage ring for an average in the RLA2 arc.

Proceeding in the same way to choose static and loads for the pre accelerator solenoids and the splitters in RLA2 we take the same values as for the short 200 MHz module, recognizing that this may, at least in the case of the solenoids, be an over-estimate.

11.5.6 Transfer Lines and Boxes

The heat load of the transfer lines are taken be taken to be roughly the same as the LHC Cryogenic Distribution Line [1]. This includes functions of both the Neutrino Factory transfer lines and boxes and does not include shut-off valves for all circuits or disconnect devices such as u-tubes. The heat load values for the lines and boxes in Table 2 includes allowances for the valves, and for module connection piping.

11.6 Cryogenic Load of the Neutrino Factory Subsystems

In Table 3 the component and module heat loads are added up and displayed by category for each of the five cryogenic subsystems. The transfer line lengths and boxes have been distributed among the subsystems, so that the table gives the connected load for each subsystem.

11.7 4.5 K Equivalent Cryogenic Loads

In order to get a feeling for what is implied in terms of hardware by the cryogenic loads presented in Table 1, and to be able compare and combine loads in different categories to get an estimate of total refrigeration plant requirement, it is convenient to reduce all of the loads to a common basis in thermodynamic ideal power. The ideal power is familiar as the power required to reversibly move heat from a temperature T to a higher temperature T_o. According to Carnot's formula this is $(T_o - T)/T$. For refrigeration at 4.5 K with heat rejection at T_o = 300 K the ideal work is 65.7 Ideal watts per watt of refrigeration. This is given also in the second line of Table 1 above. Ideal work or power can be determined for all of the categories of refrigeration plant load, and these are given in Table 1 also. For example, refrigeration with a supply and return at 4.5 K as indicated in lines 3 and 4 of the table requires 71.8 w/w and refrigeration at 40-60 requires 6.14 w/w. The ideal power of a refrigeration process is given in terms of J/g, that is ideal power per g/s of flow.

The ideal power equivalents in Table 1 are used to express the loads in Table 3 in terms of equivalent power at 4.5 K. These are given in Table 4 below together with the percentage distribution of the equivalent power over the five cryogenic subsystems.

This table presents the start of a second law analysis of the Neutrino Factory cryogenic system. It is interesting to note that 70% of the equivalent load is in the static and dynamic loads at 4.5 K., about 20% in the shielding loads; and only 10% in liquefaction. This suggests that as the engineering design of the components gets started, trying to intercept more heat on the shields and in liquefaction streams could reduce the operating cost and the size of the cryogenic plant

The total equivalent load is approximately 60 kW. This gives an understanding of both the size and cost of cryogenic plant for the Neutrino Factory. The CERN cryogenics group gives scaling methods [2][3] by which plant equipment cost can be scaled from equivalent load. Also we can say that the equivalent load here requires a plant capacity approximately half that of LHC for high-availability operation.

	Equiv. Load	Percent	Percent by System				
	Watts at 4.5 K		Injector	Linac	RLA1	RLA2	Ring
Static			8	16	23	28	39
40 - 60 K	8880	15.3	1.41	4.36	1.52	7.20	0.84
40 K Liq.	2207	3.8	0.13	0.22	0.00	2.49	0.96
4.5 K	19704	34.0	2.45	10.33	3.25	16.42	1.56
4.5 K Liq.	3185	5.5	0.00	1.37	0.86	3.27	0.00
Total Static	33977	58.6	3.99	16.27	5.63	29.39	3.35
Dynamic							
40 - 60 K	1390	2.4	0.00	0.00	0.00	0.00	2.40
40 K Liq.	2207	3.8	0.13	0.22	0.00	2.49	0.96
4.5 K	20373	35.2	0.00	3.94	2.49	25.39	3.33
Total Dynamic	23970	41.4	0.13	4.17	2.49	27.89	6.69
Total Load	57947	100.0	4.13	20.44	8.12	57.28	10.04

Table 4: Load Equivalent at 4.5 K

REEFERENCES

[1] *The Large Hadron Collider* - Conceptual Design, (The Yellow Book) CERN/AC/95-05(LHC) October 1995

[1] Private communication from Mr. Soren Prestmon, NHMFL S. Claudet,

[2] S. Claudet, Ph. Gayet, Ph. LeBrun, L. Tavian, and U. Wagner, "Economics of Large Helium Cryogenic Systems: Experience from Recent Projects at CERN", Advances in Cryogenic Engineering, **V45,** Plenum Press, New York 2000 (also CERN LHC Project Report 317, Dec., 1999)

[3] L. Tavian and U. Wagner, "LHC Sector Heat Loads and Their Conversion to Refrigerator Capacities", CERN LHC Project Report 140, May, 1998

[4] G. Cavallari et. al., "Status Report on Sc.RF Cavities at CERN" in Proceedings of the 5th Workshop on RF Superconductivity, D. Proch, Editor, DESY August 19 - 23, 1991, DESY M-92-01, April 1992

[5] G. Cavallari et. al., "Status of the RF Superconductivity at CERN" in Proceedings of the 6th Workshop on RF Superconductivity, R. Sundelin, Editor, CEBAF October 4 - 8, 1993

[6] S. Mitsunobu et. al., "High Power Test of the Input Coupler for KEKB SC Cavity" in Proceedings of the 7th Workshop on RF Superconductivity, B. Bonin, Editor, Gif-Sur-Yvette, France, 1995, p735-739 CEA/Saclay/96 080/1

[7] Superconducting Radio Frequency Linac for the Spallation Neutron Source, Preliminary Design Report SNS-SRF-99-101 December 1999

[8] W. Schneider et. al., "Thermal Performance of the CEBAF Superconducting Linac Cryomodule", Advances in Cryogenic Engineering, **V39**, p589-596 Plenum Press, New York 1993

[9] F. Alessandria et. al., "Design, Manufacture and Test of the TESLA-TTF Cavity Cryostat", Advances in Cryogenic Engineering, **V41**, p855-861 Plenum Press, New York 1995

[10] G. Horlitz, T. Peterson, and D. Trines "The TESLA 500 Cryogenic System Layout", Advances in Cryogenic Engineering, **V41**, p911-920 Plenum Press, New York 1995

[11] Superconducting RF Study Meeting, Held at Fermilab February 17 - 18, 2000. Draft Summary by N.Holtkamp issued March 1, 2000.

[12] Private communication from M. Harrison, BNL

12. Power Supplies and Power Conversion for the Neutrino Factory

12.1 Introduction

The engineering design of the power supplies for the Neutrino Factory has just begun. It is recognized that these power supplies will determine about 40% of electrical power needs of the facility (which is considerable). This subject needs more detailed analysis.

12.2 Power Supplies for the Proton Driver

The power requirements for the power supply for the proton driver is approximately 12-15 MW.

12.3 Power Supplies for the Four Solenoid Channels

Different power supplies are required to provide a current of 6000 amps to the solenoids in each of the channels as shown in Table 1 an d is extracted from chapter 9. Due to the large stored energy in some of the solenoid channels the turn on time is significant. More critical though is the design of the quench protections systems which have to be an integral part of the power supply design

	# needed	Volts	Amps	Turn on time (secs)
Decay Channel	11	30	6000	122
Decay Channel Plus RF	2	30	6000	456
Induction Linac	2	30	6000	111
Cooling Channel	1	500	6000	2867

Table 1: Basic parameters for the solenoid power supplies.

12.4 Other Power Supplies

The power supplies for the other subsystems are somewhat described in the other chapters.

12.5 Total Power consumption

The overall power consumption of the facility according to the design presented in this report is in the range of 100-150 MW dependent on the details of the accelerator layout.

12.6 Summary

It is anticipated that the designs for the various power supplies needed for the Neutrino Factory will need engineering development, but not research. The power consumption for a 50 GeV accelerator is significant but within the capability of the laboratory network.

REFERENCE:

[1] D. Wolff, Fermilab, private communication.

13. Conventional Facilities for the Neutrino Factory

13.1 Introduction

The Conventional Facilities for the proposed Neutrino Factory include all necessary civil construction components required to house the beam facilities and on-site physics detectors including below grade enclosures, access shafts, halls, and surface support buildings. In addition, Conventional Facilities includes site improvements such as grading, roadways, utilities, heat rejection facilities such as cryogenic plants and cooling ponds, and high voltage electrical supply.

We have included the incorporation of some of the existing Fermilab infrastructure into the preliminary design of this study. The Collaboration has assumed that the existing Proton Physics program would most likely not be viable at that time in the future when the Neutrino Factory would be complete and ready for operation. This makes available the existing Fermilab infrastructure including; roadways, utilities, heat rejection facilities, high voltage electrical supply, office buildings, and mechanical support facilities for use in this proposed facility.

The following pages describe the preliminary conceptual design for the Conventional Facilities portion of the proposed Neutrino Factory and Muon Storage Ring at the Fermi National Accelerator Laboratory (Fermilab) site in northeastern Illinois. Conceptual Drawings and Sketches are presented in the following pages to reflect the design assumptions that were made and to represent the level of design development that was performed for this report.

13.2 Description of the Proposed Conventional Facilities

The technical components of the facility include the 16 GeV Booster, Target Hall, Decay Drift Channel, Induction Linac, Bunching, Cooling, 2 GeV Linac, Recirculating Linear Accelerators 1 and 2 (RLA 1 and RLA 2, and finally the Muon Storage Ring (MuSR) which houses beamline components to direct the neutrino beam to its final destination. Several layouts for the Fermilab site were derived. Constraints for these layouts included the size of the elements and their respective adjacencies, site radiation requirements, existing environmentally sensitive areas and existing developed areas. Existing developed areas and wetlands were avoided to minimize cost and environmental impact.

The layout shown in Figure 1 meets all the criteria mentioned above and is relatively close to existing cooling ponds and electrical distribution systems. This layout utilizes the existing 400 MeV H-minus Linac, includes a new 16 GeV Booster around the existing Antiproton Source, includes a beamline to carry 16 GeV protons to the existing Main Ring beam enclosure, and eventually to the infield of the Main Ring (currently undeveloped) where the remaining machine elements would be constructed. Figure 2 through Figure 8 show design sketches in plan and section.

We anticipate improving and expanding the existing Fermilab infrastructure as it relates to mechanical and electrical systems, grading, paving and parking. The following sections outline the current required improvements for each.

13.3 Mechanical Systems

We anticipate a total cooling load of approximately 150 MW for this proposed facility. We assume 80% (120MW) is technical component power and 20% (30MW) is conventional power for cooling, lights, etc. In addition, 75% of technical component cooling is chilled due to high klystron concentrations and cryogenic facilities and 25% is exchanged pond cooling (95LCW). At the 150MW level pond-water circuiting would not interfere with other current operations on site, if they were to remain. Pond-water cooling would be circuited through equipment in a Central Cooling Plant (CCP) and spray discharged into Lake Logo, on the eastside of RLA2. Following natural site topography pond-water would cascade from Lake Logo (20 acres remaining), through Main Ring Lake (42 acres), through Lake Law (45 acres), and through the AE Sea (49 acres), where a 100,000 gpm pump station would be located ahead of the outfall to the Sea of Evanescence and Ferry Creek. The pump station would return pond-water through dual 48" HDPE lines to the CCP and out to the Lake Logo spray headers. For additional cooling the Tevatron and Main Injector Ring ponds can be used for an additional 50MW if the physics program is not using this capacity. This involves additional chillers, pumps, piping, etc. in the same proportions as above.

13.4 Electrical Systems

The anticipated electrical load required for this facility is 150 MW. The existing Kautz Road substation has a capacity of between 160 and 200 MW. We anticipate using this substation with upgrades for the proposed study including rehabilitation of the existing transformers, installation of a new 50 MW transformer, concrete duct bank and feeder from the Kautz road substation to the Main Ring infield.

13.5 Grading

We anticipate utilizing earthen berms for radiation shielding above most cut and cover enclosures. Fermilab currently has over 7 miles of earthen shielded cut and cover enclosure of a similar type. General site grading for drainage and wetland mitigation would also be required. An attempt would be made to balance cut and fill volumes to minimize earth excavation and hauling costs.

13.6 Paving

Paving would be required to create access roadways on the Main Ring infield.

13.7 Parking Areas

New parking areas would be required at all new facilities. Existing parking at such areas as Wilson Hall and Industrial Center will remain. The above systems design and construction requirements are very familiar to the Fermilab Engineering and Operation Personnel.

13.8 Surface Buildings

The Collaboration does not anticipate requiring any additional office or manufacturing buildings. However, beamline support buildings and klystron galleries above the enclosures will be required. Figure 2 shows a site overview of these surface buildings, and Figure 3 through Figure 5 show the relationship of the surface buildings to the beam enclosures. We estimate as much as 300,000 sf of these low-rise industrial type buildings will be necessary. Below grade facilities for this study include cut and cover type enclosures and sloping enclosures constructed with tunneling technology.

The estimated 18,500 lineal feet of near surface enclosures constructed with the cut and cover construction would vary in width from 10 feet in the 16 GeV Booster beam enclosure to as much as 60 feet in the RLA arcs. Heights will range from 8 to 10 feet. These underground areas will be used to house beamline elements starting with the 400 MeV H-minus beam and ending with the extraction of the muon beam from the second recirculating linac. Earthen cover of between 15 and 25 feet will be typical for these enclosures. The majority of this accelerator complex would be constructed at or near the surface with cut and cover construction. The near surface enclosures are shown in Figure 3 through Figure 5. Sloping enclosures for the Muon Storage Ring (MuSR) will be constructed with methods including cut and cover at the shallow arc, soft tunneling in the glacial moraines and drill and blast methods in the lower shale and dolomite rock. Figure 6 shows cross sections of the MuSR tunnel in these two regions indicating the difference in construction techniques. The MuSR consists of 5800 lineal feet of enclosure sloping at 13% pointed nearly due West to deliver Neutrinos to a detector located somewhere on the West Coast of the United States. Tunnel enclosure cross sections for the proposed MuSR are expected to be approximately 10’ wide and 13’ high as shown in Figure 6. Fermilab is currently constructing a tunneled below grade enclosure for the Neutrinos at Main Injector (NuMI) project that is very similar to this proposed construction.

We believe the Fermilab Geology provides an excellent media for constructing such an enclosure. Based on our research the proposed 13 degree slope creates an acceptable environment for the required mucking of the drill and blast tunneling method. Figure 7 shows the Muon Storage Ring in an elevation view with the Fermilab Geology represented. Figure 8 shows the lower end of the Muon Storage Ring.

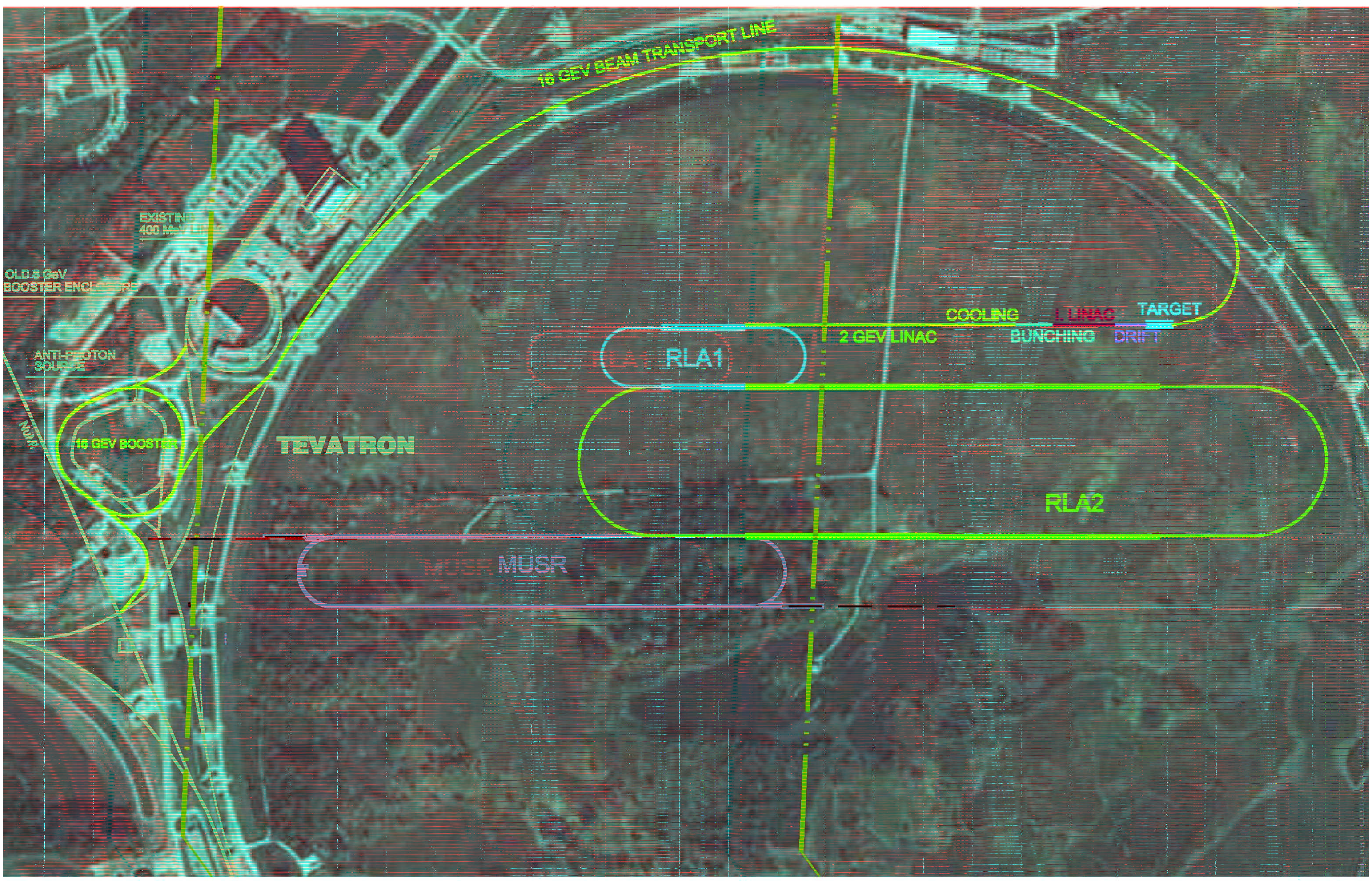

Figure 1: Layout of the Neutrino Factory on a photograph of the Fermilab site.

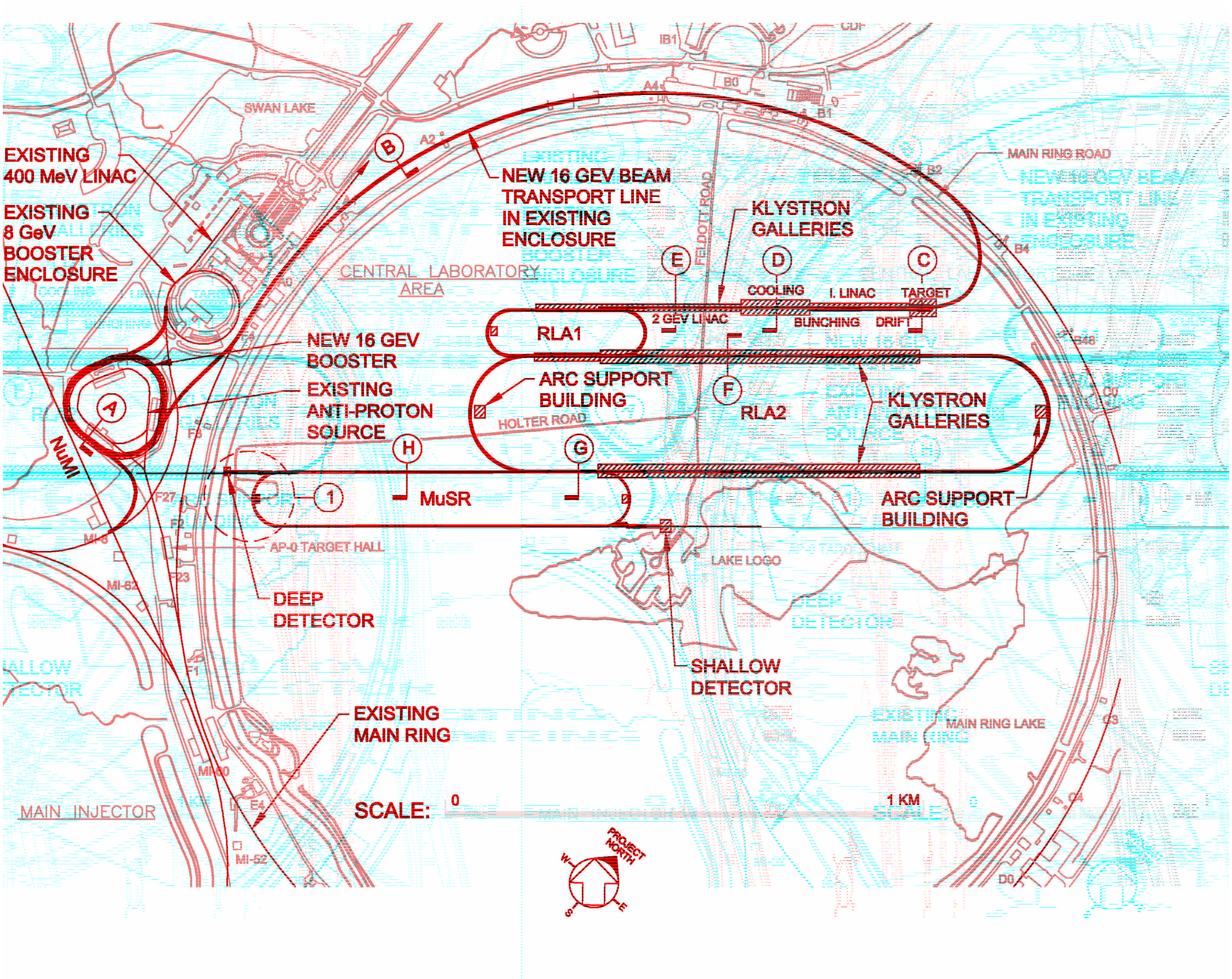

Figure 2: Sketch of the Neutrino Factory layout on the Fermilab site. The sections (A through F) and details (1 and 2) are shown in the Figures which follow. The hashed areas indicate new surface buildings.

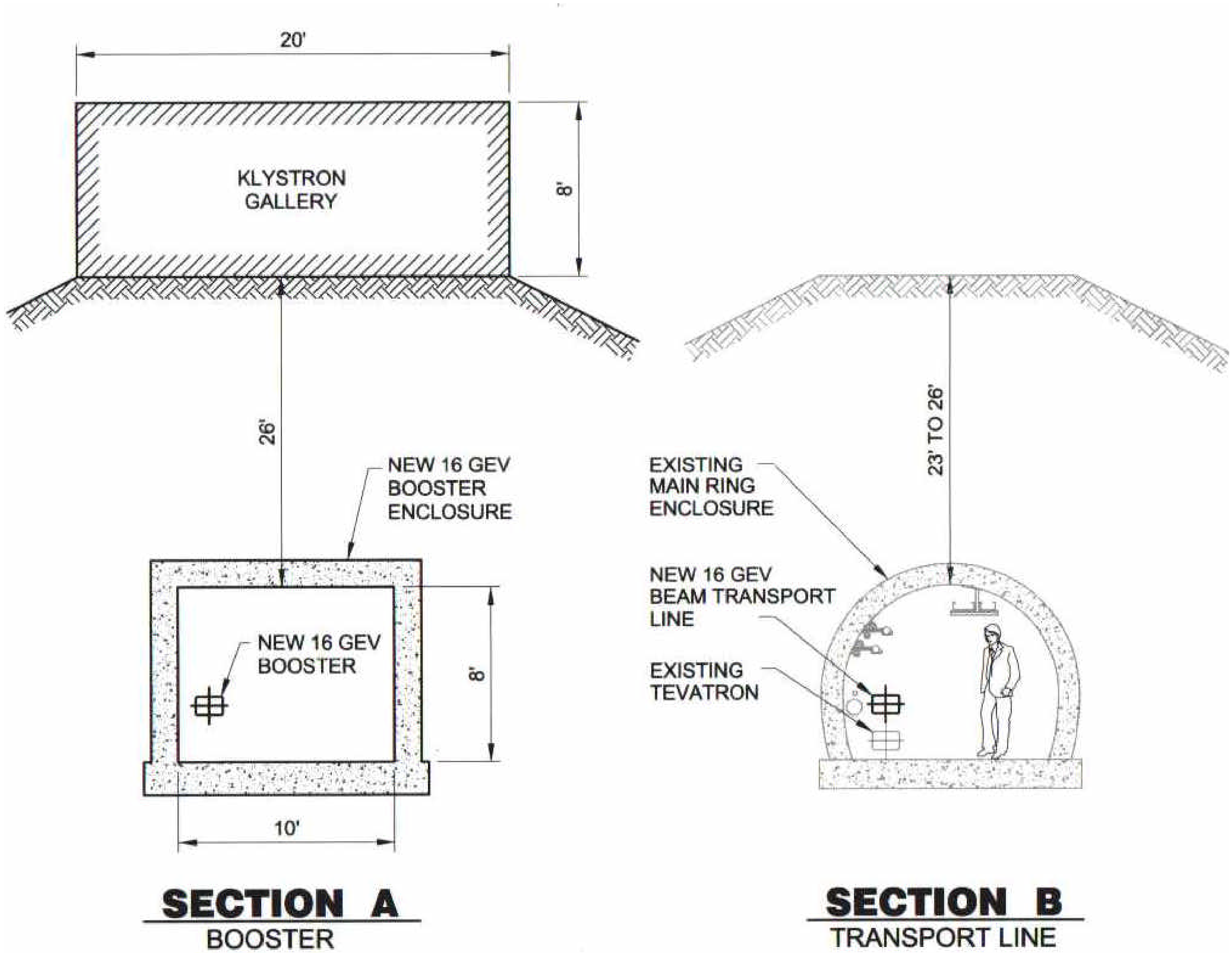

Figure 3: Section A shows the 16 GeV Booster klystron gallery over the beam enclosure with a sketch of a magnet cross section. Section B shows the existing Main Ring beam enclosure with a Tevatron magnet below the 16 GeV permanent magnet beam transport line.

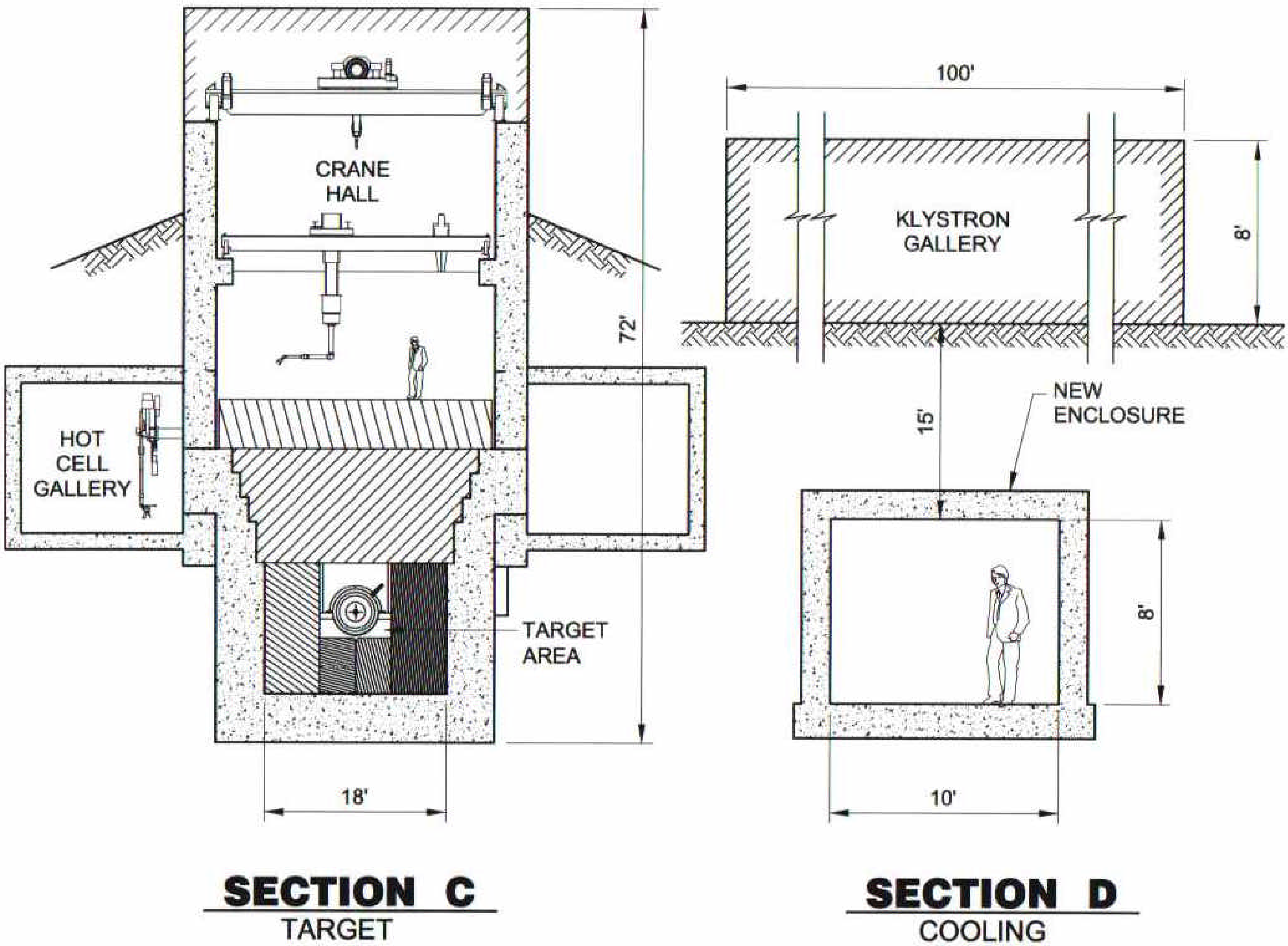

Figure 4: Section C shows a cross section of the Target facility building. Section D shows a cross section of the Cooling facility with the klystron gallery above the beamline enclosure.

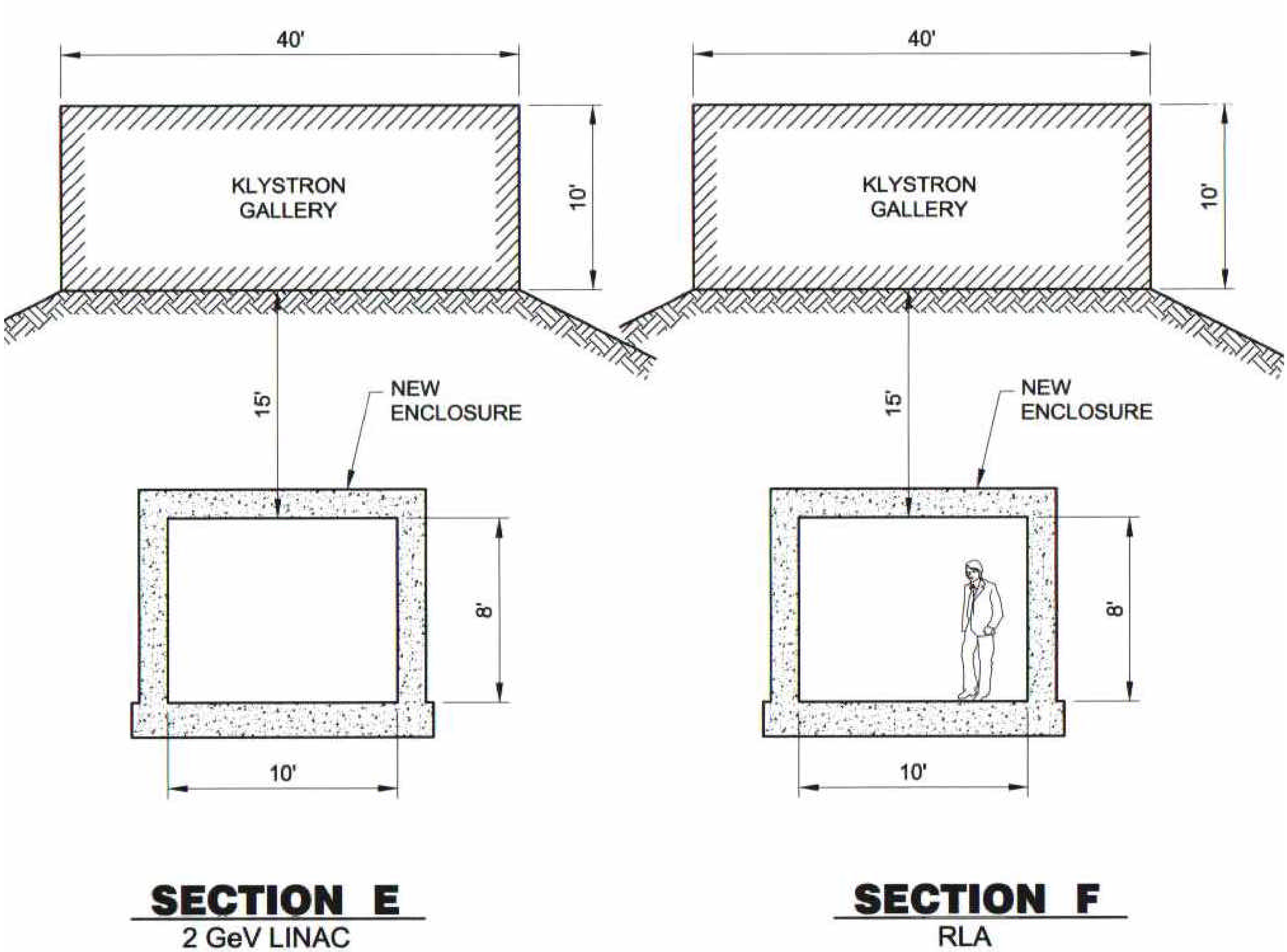

Figure 5: Section E shows the muon linac klystron gallery and beam enclosure. Section F shows the klystron gallery and beam enclosure for a Recirculating Linac.

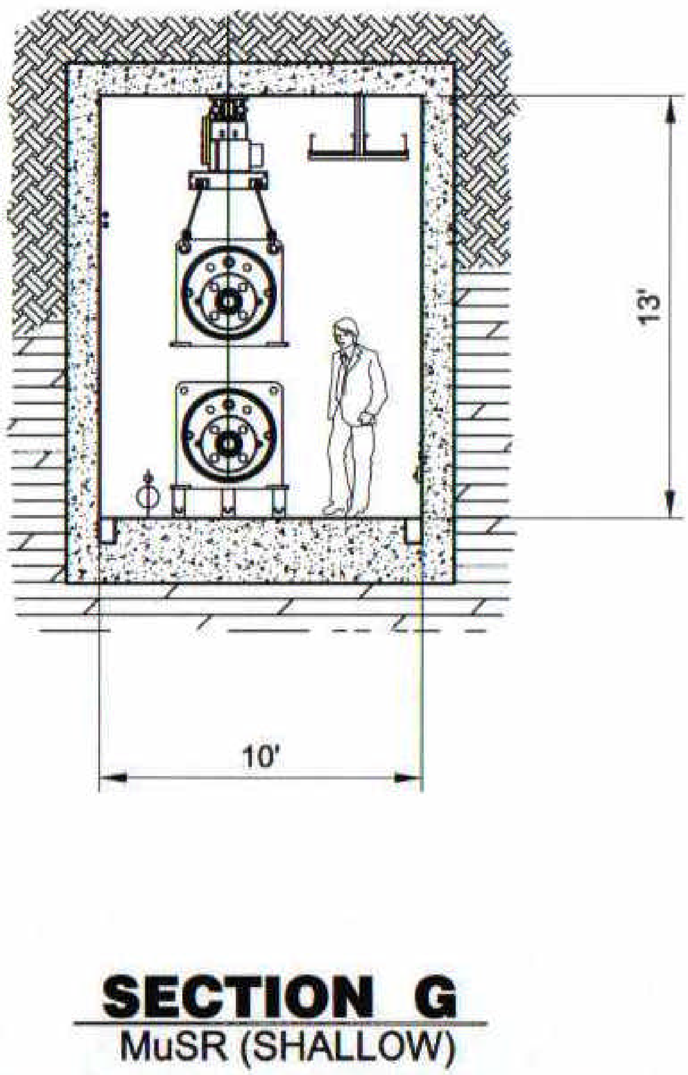

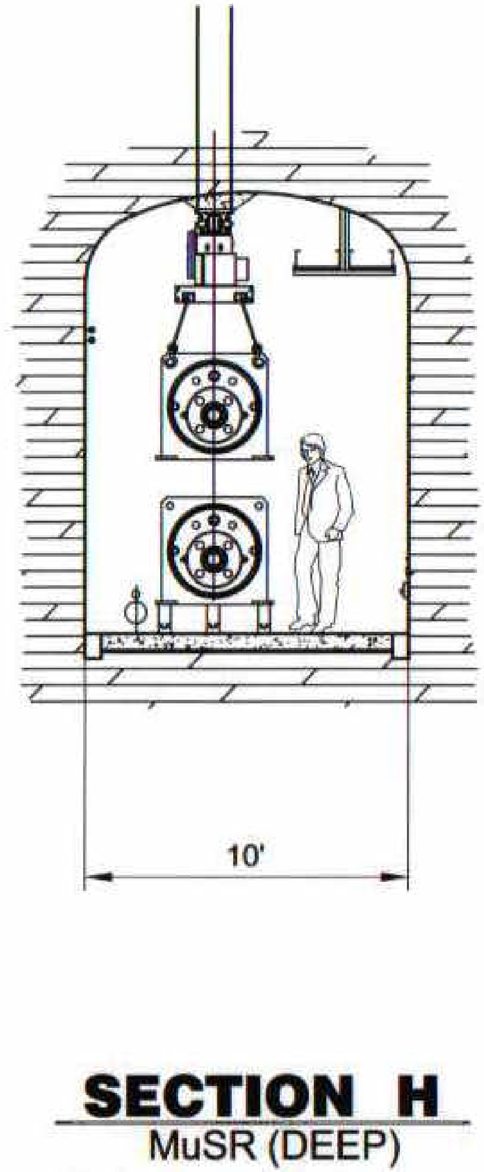

Figure 6: Section G shows the Muon Storage Ring in its beam enclosure near the top of the tunnel where soft tunneling or cut and cover will be used. Section H shows the beam enclosure where drill and blast through dolomite or shale will be used.

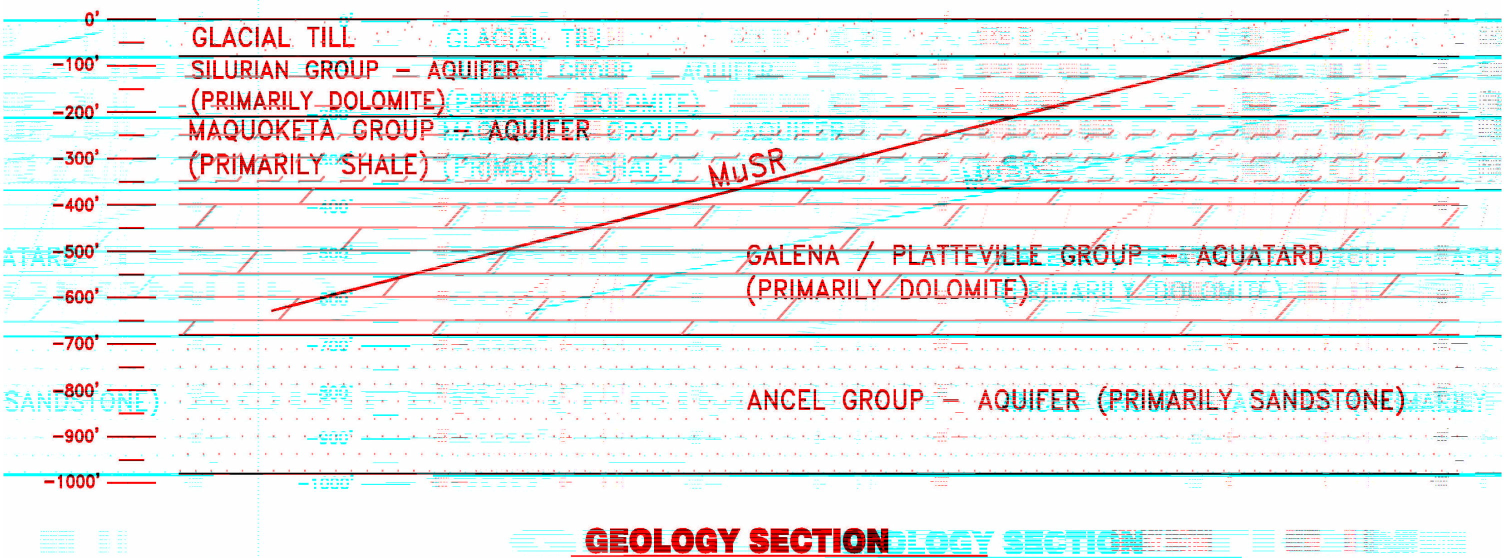

Figure 7: The above shows the geology beneath the Fermilab Site.

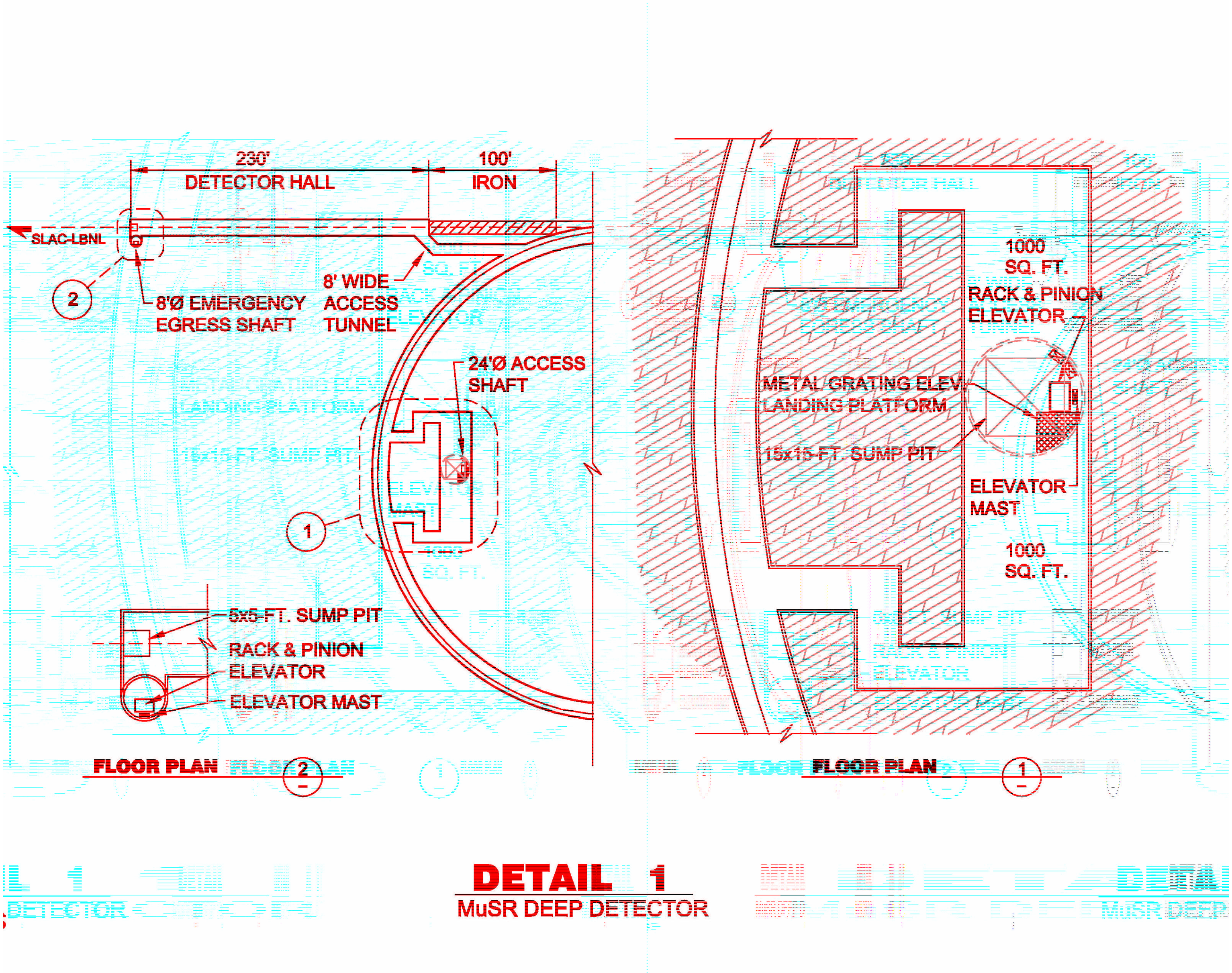

Figure 8: Detail 2 shows the lower end of the Muon Storage Ring and its relationship to the lower physics detector. The two 1000 sq.ft. areas indicated on the floor plan are for accelerator support equipment such as power supplies and cryogenic plant.

14. **Environment, Safety, and Health Considerations for the Neutrino Source**

14.1 Introduction

The Neutrino Source presents a number of challenges in the general area of environment, safety, and health. It is the intent of this chapter to identify these challenges and make a preliminary assessment of how they might be addressed and of their potential impact on the project. Many of these issues are very similar to those that have been encountered and solved during the construction and operation of other facilities at Fermilab and elsewhere while others are quite novel. The novel ones will require particular attention as the project proceeds to assure their timely resolution in a cost-effective manner that meets the approval of the Department of Energy and the public. It is concluded here that with adequate planning in the design stages, these problems can be adequately addressed in a manner that merits the support of the Laboratory, the Department of Energy, and the public.

14.2 Procedural/Regulatory Matters

The actual design, construction, and operation of the Neutrino Source will have to meet a number of procedural/regulatory milestones in the area of environment, safety, and health to assure its success. The devotion of early attention to these issues is likely the best way to enhance public support of the project. These requirements are currently provided in Fermilab's Work Smart Standards in Environment, Safety, and Health which is reviewed annually [1]**.**

14.2.1 Environmental Protection Procedural/Regulatory Matters

All new DOE projects are subject to the National Environmental Policy Act (NEPA). Initially, the project will be the subject of an Environmental Assessment (EA). The required analysis is broad in scope and includes societal impacts along with the standard environmental protection topics. DOE will choose the methods used to involve the public. The conclusion of the environmental assessment process is either a Finding of No Significant Impact (FONSI) or the need to prepare an Environmental Impact Statement (EIS), a likely result for this project due to its scope and cost. The completion of the EIS results in the issue of a formal notice called a Record of Decision (ROD). The NEPA process is generally considered to be arduous, but one that can be followed to a successful conclusion. This task must be completed, customarily by using external resources, prior to expenditure of project funds. Other procedural requirements apply in the arena of environmental protection in the form of environmental permits that will be needed. Some of these apply during the construction stages, others apply to operations, and some apply during to both stages. Topics covered by such permits include storm water discharges, discharges of cooling water, wetlands mitigation, releases of air pollutants for both non-radioactive pollutants and for radionuclides, and construction in any floodplains. The lead-time required for submittal of these permits is typically 180 days. Archaeological sites are also located on the Fermilab site which might need further investigation and study prior to the commencement of construction.

14.2.2 Safety and Health Procedural/Regulatory Matters

The Laboratory will be required to prepare an assessment of the environment, safety, and health issues associated with this project in the form of a Safety Assessment Document (SAD). Given the size, and scope of this project, the preparation of a Preliminary Safety Assessment Document (PSAD) will likely occur first. The purpose of the PSAD is to identify the relevant ES&H issues at an early stage and propose how they might be mitigated. The SAD, then, documents the resolution of them. It is nearly certain that DOE will review these safety documents by utilizing an external review team. Just prior to facility operation, a readiness review will be conducted in similar fashion. PSAD/SAD activities generally begin after funds are issued. Here, too, early planning will help this task. DOE is presently "self-regulating" in the areas of industrial safety and occupational radiation protection. This situation could change at some future time. Related developments are being monitored closely to identify new requirements or procedures that might apply to new projects such as the Neutrino Source.

14.3 Occupational Safety During Construction of the Facility

14.3.1 Proton Driver, Target Station, Cooling Region, and Muon Acceleration Linacs

These facilities all would be located within the glacial till strata at a distance below the surface of less than 30 ft (10 meters). At this level, the construction is likely to proceed by the standard "cut and fill" method. The Occupational Safety and Health Administration's (OSHA's) regulations on the construction activities will be followed. Industrial radiography operations and any other work conducted using radioactive sources must be performed in compliance with State of Illinois requirements. There are no new occupational safety issues identified with this work.

14.3.2 Muon Storage Ring (MuSR)

The MuSR will be excavated through several geologic units that are shown in Figure 1. The glacial till does not contain an aquifer. All of the bedrock units contain aquifers except for the Galena/Platteville, which is largely an aquatard. The 13.16-degree downhill slope poses some unique issues. While the eastern (uphill) end would be accessible by conventional means of egress, the western (downhill) end, would be located approximately 630 feet (192 meters) below the surface. Regulations pertaining to underground operations (i.e. "mining" activities) come into play. Concerns about tunneling safety, material movement, and provisions for emergency response including underground rescue must be addressed. The NuMI project should provide valuable experience in these matters.

Given the location within several major aquifers, and the downward slope, it is clear that stringent measures must be taken to prevent flooding both during the construction period and thereafter. Likewise, the downward slope, about four times that of the NuMI tunnel, requires careful planning to include provisions for adequate protection against uncontrolled, hazardous downward movements of equipment and materials. These protective measures need to be consistent with mitigation of environmental protection concerns (see below).

14.4 Environmental Protection During the Construction of the Facility

14.4.1 Proton Driver, Target Station, Cooling Region, and Muon Acceleration Linacs

Erosion control measures similar to those employed elsewhere will be employed in accordance with good engineering practice and Federal and State regulations. Dust from any spoil piles must be kept under control. Likewise, a stormwater management plan will need to be developed. Since more than 5 acres (2.0 hectares) of land surface are impacted by the construction, a National Pollutant Discharge Elimination System (NPDES) Stormwater Permit for construction will be needed which will include specific actions which must be followed during the construction period. The usual precautions to prevent pollution from spills of regulated chemicals from the construction equipment will need to be taken. Noise from construction activities is not expected to be significantly more intense than that associated with normal civil construction activities in the vicinity of Fermilab. If more than 3 acres (1.2 hectares) of wetlands are impacted, compensatory man-made wetlands will need to be created. It is important to demonstrate adequate care for floodplains due to significant local public concerns about flood prevention.

14.4.2 Muon Storage Ring (MuSR)

The tunneling in the bedrock units will result in the removal of a considerable volume of rock. The NuMI experience will be most useful in learning how to manage the rock spoil, dust, noise, vibration, and "aesthetic" issues. The storm water management plan will need to take into account any releases of groundwater generated in the course of "dewatering" the tunnel. Careful hydrogeologic studies need to be performed to understand the interplay of the construction of the project with the various aquifers. This must be done to establish with certainty that the construction activities will not cause significant perturbations of the local individual and municipal water supplies, either in quality or in quantity. The exact depth of the top of the aquatard of the Galena/Platteville unit is known to be non-uniform across the Fermilab site. Accurate measurements of it are needed to plan a strategy for preventing the tunnel from serving as a possible path of contamination from the upper aquifers, commonly used by individual wells and municipalities, to those below the aquatard, commonly used by the local municipalities. During construction, precautions are needed to guarantee that spills of chemicals, including lubricants and fuels from the construction equipment, are captured before they enter the groundwater. The downward slope presents special considerations in this regard.

14.5 Occupational Safety During the Operation of the Facility

14.5.1 "Ordinary" Occupational Safety Hazards

The occupational safety hazards encountered at all other large particle accelerator facilities will be found in this facility. These have been successfully addressed by well-known techniques and are simply listed below:

- The project will use high current electrical circuits in the magnets on a large scale.
- Radiofrequency (RF) generation and distribution equipment will be used extensively.
- Large amounts of cables in cable trays, with associated fire protection implications, will be installed.
- Long tunnels will be present with corresponding egress and fire protection issues that need to be addressed.
- There will be movements and alignment of large, heavy components.

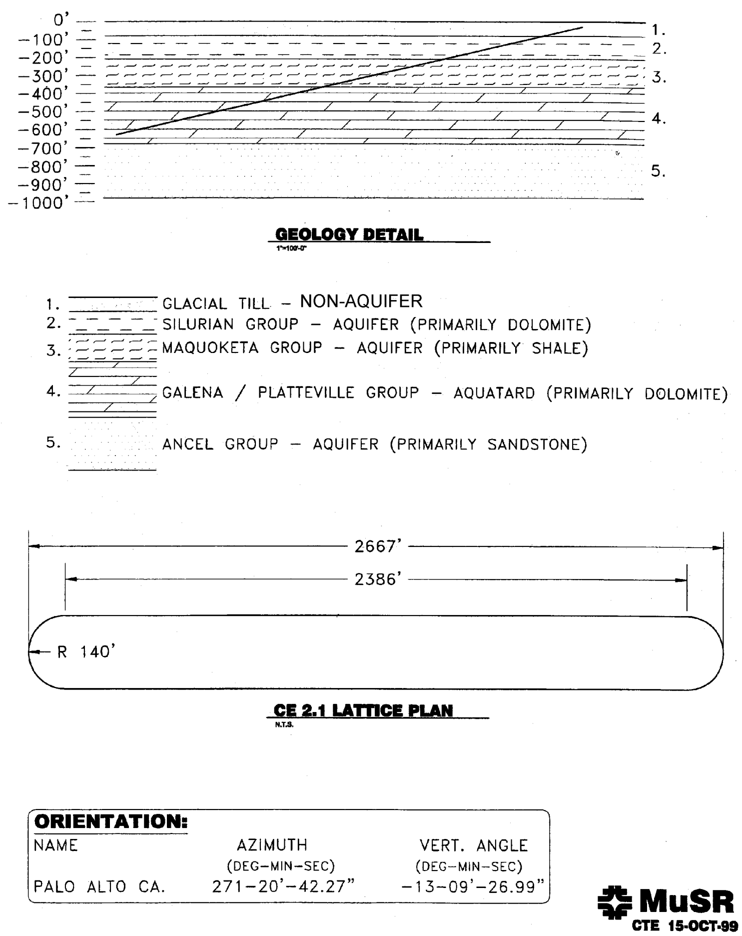

Figure 1: Conceptual layout of the Muon Storage Ring (MuSR) in the various geological units**.**

14.6 Novel Occupational Safety Hazards

14.6.1 Large Scale Use of Cryogens

The extensive use of cryogenics in both magnets and RF structures presents special problems, but similar in kind to those solved at present accelerators. Portions of these cryogenic systems will be deep underground, at the lower end of the Muon Storage Ring and on large slopes. Provisions will need to be made for the safe release of cryogens to the surface both during normal operations and in the event of quenches. Standard engineering practices developed to mitigate both direct cryogenic hazards and the accompanying oxygen deficiency hazards (ODH) should be used.

14.6.2 Utilization of Liquid Hydrogen (LH_2)

The use of ionization cooling in a LH_2 medium presents significant fire/explosion hazards. Also, the LH_2 cells will be interleaved with RF structures and magnets that handle a great deal of electrical energy. In the past, Fermilab has successfully used stringent review procedures involving internal and external review committees of experienced individuals to provide advice on the management of large scale usage of LH_2 in bubble chambers and targets. A recommended approach to address concerns related to this system is to convene a review committee of qualified individuals at the earliest reasonable state in the design.

14.6.3 Muon Storage Ring Life Safety (Egress) Considerations

The MuSR, as aligned for this study, constitutes a long tunnel with the western end rather deep in the ground. The fire protection/egress considerations of this configuration, including the adequacy of the access shaft and "safe room", will need to be reviewed by a qualified fire protection professional, and others, for adequacy. Plans will need to be made for the evacuation of any injured or ill personnel through the sloped arcs. Again, the NuMI experience should be helpful.

14.6.4 Muon Storage Ring Slope Hazards

The steep slope of the MuSR presents unique hazards during operation as well as during construction. The surface of the finished floor should be made sufficiently rough to provide good traction to individuals wearing ordinary shoes. Gutters should be provided to direct water flowing into the tunnel toward the large sump pits at the lower end. They might also be designed to retard the unwanted downhill movement of large items, particular that of any portable pieces of equipment on wheels. An idea that might address this, and other considerations, is to arrange the gutters in a spiral fashion, regularly crossing the tunnel to direct such items toward one of the walls. Regular tie-down points for heavy items of equipment could be provided. These problems can be solved if they are addressed early in the design process.

14.7 Ionizing Radiation Safety During Operation of the Facility

14.7.1 Proton Driver

14.7.1.1Prompt Radiation Shielding

The Proton Driver and the Neutrino Source Target Station will require massive amounts of hadron shielding similar in scale and type to that of other proton accelerators in this energy regime. Detailed calculations made using MARS have already been performed to determine the amount of shielding required [2]. It is clear that suitable combinations of steel, concrete, and earth shielding can meet the standard criteria for above ground shielding at Fermilab. At 16 GeV, the range of the muons of maximum energy is less than 30 meters of earth. Due the their forward-peaking, any muons produced by stray beam loss should be ranged-out and hence are of no consequence. Thus, the shielding against the prompt radiation hazards is well understood and can be addressed by conventional means. The transport of beam from the synchrotron to the Target Station poses no peculiar problems with respect to prompt radiation shielding. Provision for the shielding of "stray", large-angle muons, not captured into the muon beam, should be provided downstream of the target.

14.7.1.2Residual Radioactivity of Components

The Proton Driver, under maximal operation, will handle up to 40 times the beam power of the present Fermilab Booster. Many important radiation effects scale roughly with the beam power. The handling of this large beam power has already received, and merits, careful attention [3]. Efforts should continue to better control such losses of beam both from the standpoint of component activation and also with respect to soil and groundwater activation.

14.7.1.3Residual Radioactivity at the Target Station

Given the high beam power, the residual activation of the Target Station merits special attention. The residual absorbed dose rates to be found in the Target Station are not presently known in detail, but will be large, of the order of krads hr^{-1} (tens of Sv h^{-1}). There will also be significant activation of water used to cool the non-cryogenic components as well. Remote handling capabilities of the style used by other facilities such as the Los Alamos Meson Physics Facility (LAMPF) and being planned for the Spallation Neutron Source (SNS) at the Oak Ridge National Laboratory will be needed. The activation of the carbon target itself will be quite significant. ^{3}H (12.3 year half-life), ^{7}Be (53.6 day half-life) and ^{11}C (20.3 minute half-life), will be the dominant, long-lived radionuclides produced. Each 16 GeV proton produces about 1.5 nuclear interactions (i.e., "stars") in a carbon target. Using the standard values of the total inelastic cross section for high-energy interactions along with the production cross sections for the nuclides ^{3}H [4], ^{7}Be and ^{11}C [5], one can estimate the total activities in the target. The calculation has been done for 1.5 MW beam power, at saturation (i.e., after a run that is long in duration compared with any of the half-lives). The result is about 1540 Ci (57 TBq) of ^{3}H, 1020 Ci (3.8 TBq) of ^{7}Be, and 2055 Ci (76 TBq) of ^{11}C. The gamma-emitting ^{7}Be will be the major contributor to residual exposure rates. Taking its branching ratio of 10.4 % into account, and crudely assuming the target to be a "point" source, the absorbed dose rate at 1 meter would be about 21 rad hr^{-1} (0.21 Gy h^{-1}).

DOE has developed special requirements for nuclear facilities [6]. Such facilities are subject to levels of safety analysis, quality assurance, and training requirements that are significantly more stringent than those normally applied to accelerator facilities. The present DOE definition of nonreactor nuclear facility excludes accelerators. However, it is not clear that it excludes radioactive materials in excess of certain levels of activity as specified in the requirements [7]. While the values calculated above for the target itself do not exceed these thresholds, the total activity for the target station might. Questions about the status of the facility as a nuclear facility need to be resolved. If the target or target station ends up being classified as a nuclear facility, it would be advisable to segregate the operation of the target from that of the rest of the facility to the extent possible. The Laboratory continues to monitor the ongoing development of DOE requirements on this topic.

14.7.1.4Airborne Radioactivity

The production of airborne radioactivity in the vicinity of the Target Station will constitute the dominant source of airborne radioactivity emissions for the facility. At this early stage, a comparison with the work already done on the NuMI Target Station [7] may be useful since the beam powers of the two facilities are comparable. The NuMI Target Station will operate at a beam power of 0.404 MW. It will release a total of about 15 Ci (555 GBq) annually. This is dominated by 5 Ci (185 GBq) of ^{11}C (half-life = 20.3 min.) and 9.8 Ci (363 GBq) of ^{41}Ar (half-life = 1.83 hours). Such releases will result in an annual dose equivalent of about 0.009 mrem (0.09 microSv) at the site boundary. The NuMI Target Station was designed to assure that this level is well below a value of 0.1 mrem (1 microSv) in one year, which is a threshold for the sum of the emissions from all sources at Fermilab. Above 0.1 mrem in one year, a stringent continuous monitoring program and other requirements specified by U. S. Environmental Protection Agency Regulations [8] must be met to demonstrate that the regulatory limit of 10 mrem (100 microSv) in one year is not exceeded. The NuMI results were achieved by carefully designing the ventilation system to maximize the decay in transit from the point of production to the release stack. The helium volume immediately surrounding the target that is proposed elsewhere in this report should help to mitigate this problem. The Laboratory must also decide which other facilities might operate concurrently with the Neutrino Source since these emissions, effectively, represent a "zero sum game" for all of Fermilab.

14.7.1.5Radioactivity in Soil and Groundwater

The calculation of the radioactivity produced in the soil around the Proton Driver and Target Station can be accomplished in a straightforward manner using current versions of Monte-Carlo shielding codes. Recent studies have found that the glacial till generally provides for very small hydraulic conductivities. When the gradients are included, a very slow migration downward of radionuclides produced in the soil results, affording considerable time for decay in transit. However, before the exact location of the facility is irrevocably determined, detailed hydrogeologic studies should be conducted to determine the relevant parameters precisely, as they are known to vary over the Fermilab site. Documented methods for calculating groundwater concentrations of radionuclides exist [9].

14.7.2 Cooling Stages and Muon Acceleration Stages

In the Cooling Stages, the collected muons from pion decays will deposit considerable energy in the LH_2 cells in the course of being "cooled". This energy will end up largely in the form of heat transferred to the hydrogen and dispersed by the refrigeration equipment. Given the low energy of the muons at this stage only energy loss by ionization is important. It is straightforward to design shielding appropriate to ranging out "stray" muons that might miss the cooling apparatus as well as the electromagnetic cascades induced by the decay electrons. Present Monte-Carlo codes are adequate to provide accurate calculations of this effect. The forward-peaked nature of the muon field should minimize the lateral extent of the shielding necessary. The production of induced radioactivity in these stages is also severely limited by the energy, and the fact that leptons are the only particles present. At the higher energy stages, the scale of the muon shielding required will increase, but even the final muon energy is still relatively small since the mean range of a 50 GeV muon in soil is only about 109 meters. Likewise the size and importance of the electromagnetic cascades produced by the decay electrons will grow as the energy increases. Radioactivation could be expected, but at levels much smaller than those to be experienced in the Proton Driver and Target Station.

14.7.3 Muon Storage Ring

14.7.3.1Control of Radiation Dose Due to Neutrinos

The most unusual radiation consideration pertaining to the Muon Storage Ring is that due to the neutrinos produced by the decaying muons. Obviously, the design of the entire facility is optimized toward the production of a high fluence of neutrinos in the intended direction downward (westward). This also results, unavoidably, in a similar stream of neutrinos in the upward direction. The methods for calculating radiation dose equivalent from the neutrino fluence have been described elsewhere[10],[11]. The Department of Energy has specified the annual limits on the radiation dose equivalent that can be received by occupational workers and members of the public [1][12]. These limits rather clearly refer to the dose equivalent that could plausibly be delivered to actual people. For individual members of the public, the primary limit is 100 mrem (1mSv) in a year, not including man-made, medical, or enhanced natural radioactivity. Special reporting requirements apply when the annual dose equivalent received by an individual exceeds 10 mrem (0.1 mSv) in a year. For comparison, the average annual radiation dose equivalent received by individuals living in the United States from natural sources of radiation, including exposure to radon indoors, is about 300 mrem (3000 microSv) [13].

Figure 2 schematically shows the "lobe" of neutrino radiation due to neutrinos produced by muon decays in the downward (westward) production straight section of the MuSR. The parameters *L* and *R* describe the length and maximum radius of a chosen contour of equal annual dose equivalent. *L* is measured from the end of the MuSR straight section along the centerline of the neutrino trajectory, while *R* is measured perpendicular to the neutrino trajectory. Cylindrical symmetry should hold about this axis for this radiation field. Due the extreme forward peaking, the dose equivalent at the surface due to these neutrinos is zero. A similar radiation field will penetrate the surface due to muon decays in the upward (eastward) return straight section of the MuSR centered about the axis of the return straight section. Mokhov has calculated these radiation fields and has plotted the results for two different contours of annual dose equivalent, 1 mSv (100 mrem) and 0.1 mSv (10 mrem) [14]. These values are given in Figure 3. One might decide to place the MuSR so that a selected annual isodose contour, say either 10 or 100 mrem, lies entirely underneath the present Fermilab property. Also, performing a simple inverse-square scaling, a dose equivalent rate of about 4.8×10^{-5} mrem (0.48 nSv) per year is found at SLAC/LBNL, 2700 km downstream on the centerline axis, a value completely insignificant compared with local variations in natural background.

It is also desirable to also locate the MuSR so that there is no exposure to offsite areas near the surface of the ground from the upward lobe of neutrinos. Somewhat arbitrarily, one postulates that it is extremely unlikely that a tall building, say 600 ft (183 meters), will be built just outside of the eastern boundary of the Fermilab site during the projected lifetime of the Neutrino Source. If such a building were to be constructed, one would desire the annual dose equivalent due to the neutrinos at any level of the building to be less than 10 mrem (100 microSv). To do this, simple trigonometry requires that the center of upward lobe to emerge from the ground at least 2600 feet (792 meters) west of the eastern site boundary. The operational year of the Neutrino Source specified in this study of 2×10^{7} sec amounts to 5555 hours. Thus, following present practice of limiting prompt radiation levels in fenced outdoor levels to 100 mrem h^{-1}, the annual dose equivalent that could be delivered in such an outdoor, fenced area could be as high as 5.7×10^{5} mrem. Performing a simple scaling calculation, one finds that the annual dose equivalent due to the neutrinos is reduced to 5.7×10^{5} mrem at a distance of 24.2 meters (79.4 feet) from the end of the MuSR enclosure on the axis of the neutrino beam. If this end of the enclosure is located a distance of 5.5 meters (18 feet) below the surface, the highest annual dose equivalent accessible above the surface will not exceed this level, and thus the above-ground area could simply be fenced off. At these levels of neutrino fluence, given the small interaction cross sections involved, the radioactivation of soil and ground water is insignificant.

Figure 4 and Figure 5 show how the Neutrino Source could be placed on the Fermilab site and meet these criteria.

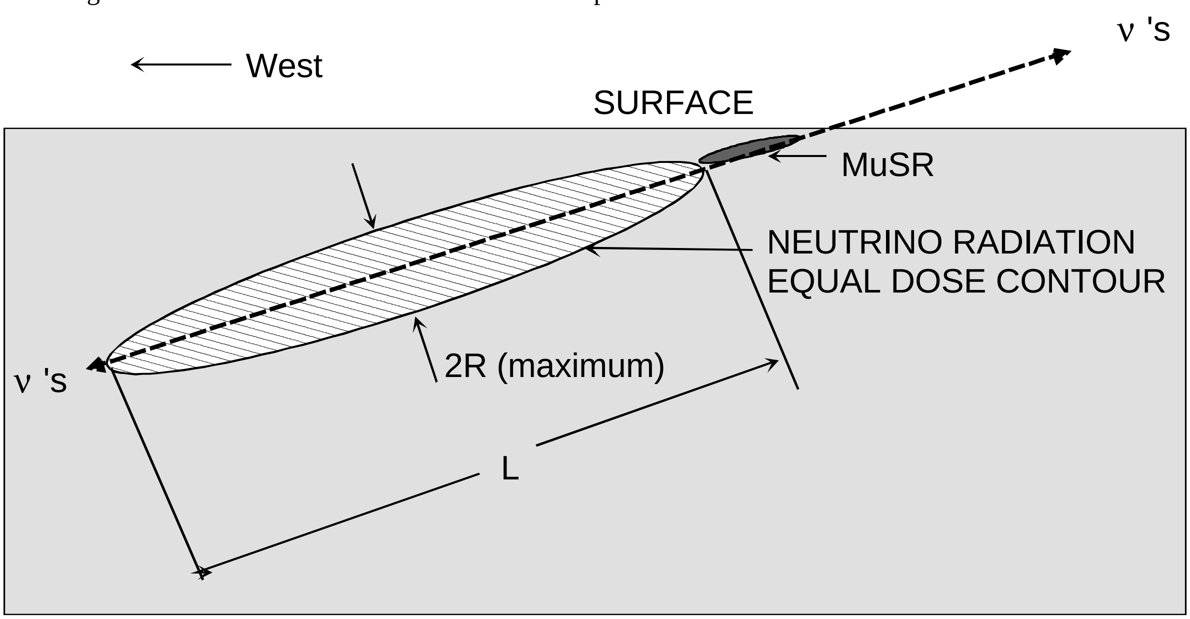

Figure 2: Schematic representation of the neutrino radiation fields due to muon decays in the MuSR. The gray region is the earth while the cross-hatched region is a schematic representation of the region inside of a selected contour of equal dose equivalent due to the neutrinos resulting from downward muon decays. A similar neutrino radiation lobe is to be found in the upward direction due to upward muon decays in the other straight section of the ring. The parameter L describes the intersection of this isodose contour with the centerline of the neutrino beam trajectory while R is its maximum radial extent. The actual contours are more forward-peaked, and narrower than this symbolic ellipse. Symmetry about the center line of the neutrino trajectories is expected.

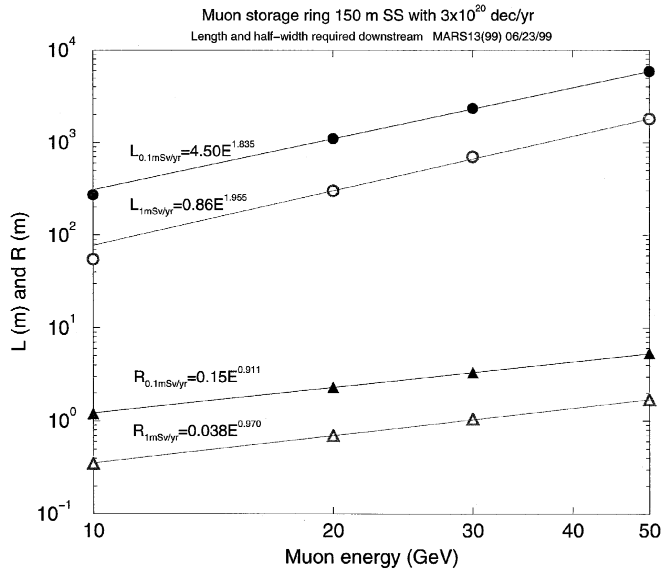

Figure 3: Results of calculations of the values of L and R (see Figure ESH.2) which describe the neutrino radiation field resulting from muon decays from one Muon Storage Ring straight section ("SS") as a function of muon energy[14]. Results are given for two different annual dose equivalents, 1 mSv y^{-1} and 0.1 mSv y^{-1}.

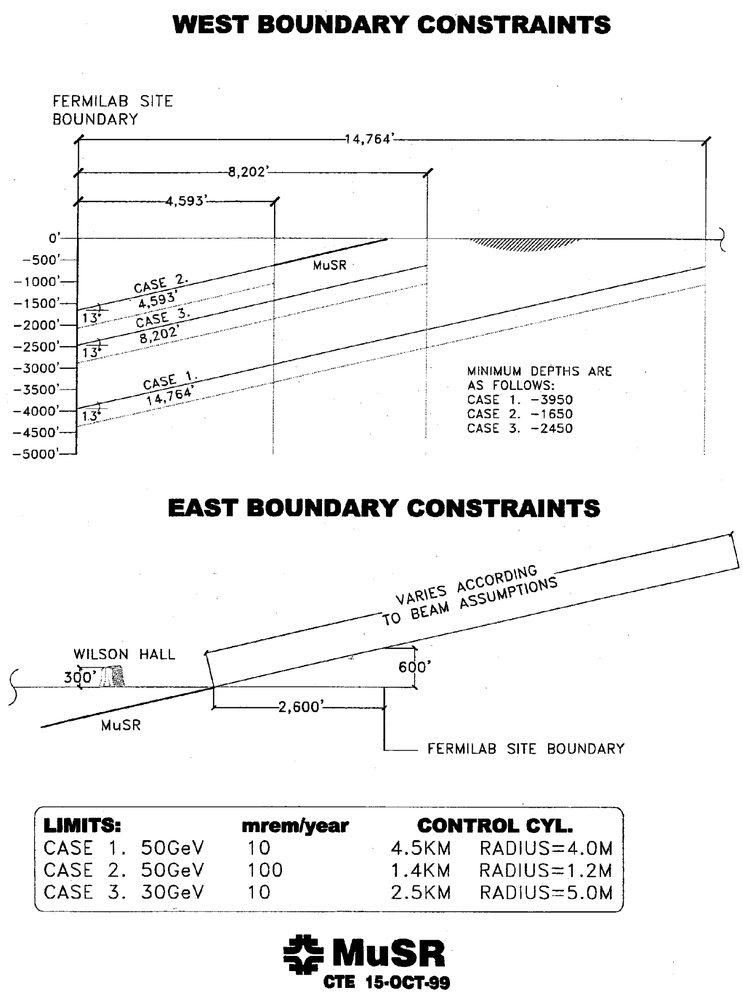

Figure 4: East-west vertical cross section through the Fermilab site showing the radiological constraints on siting the MuSR explained in the text for two different choices of annual dose equivalent and two different choices of muon energy.

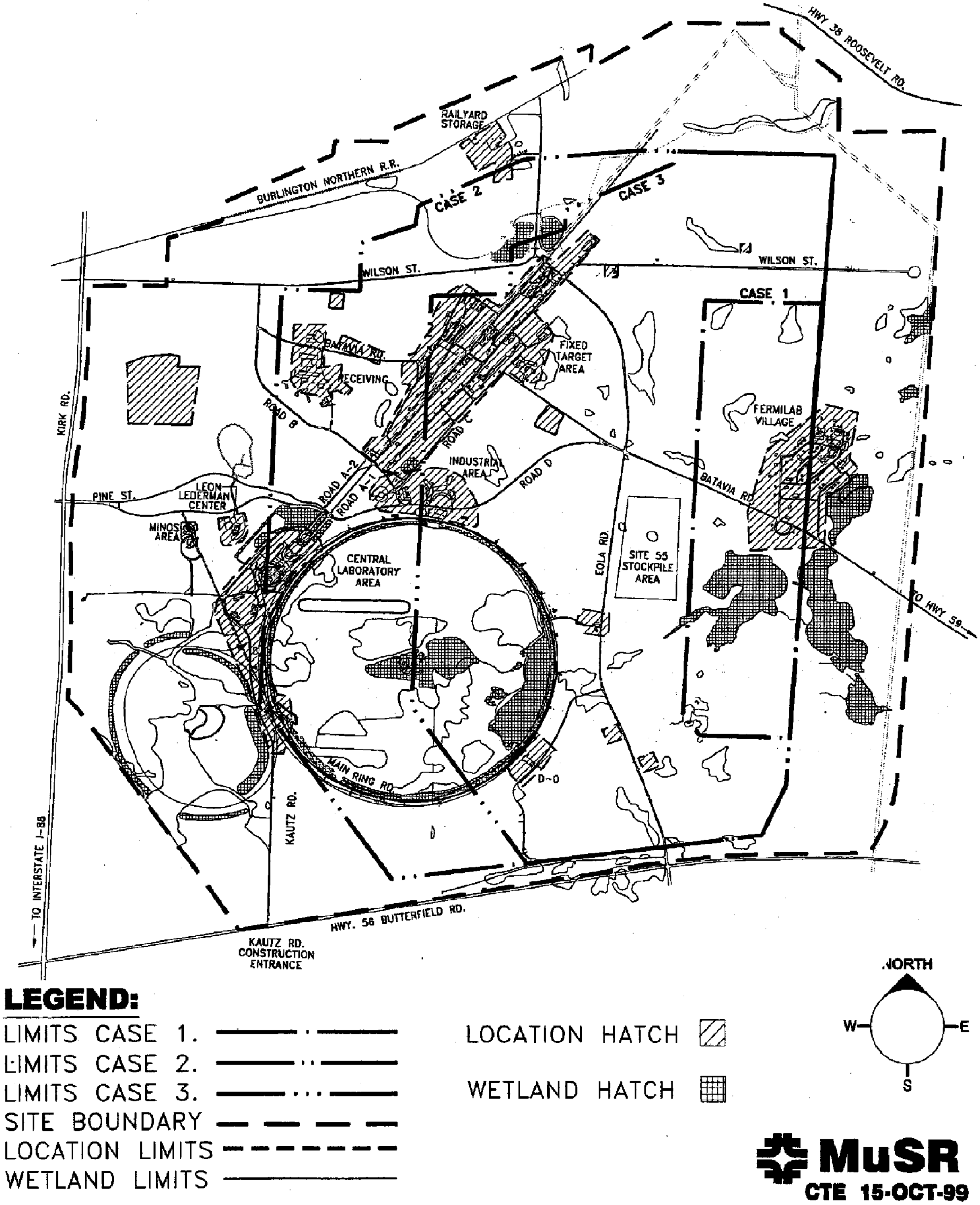

LIMITS:		**mrem/year**	**CONTROL CYL.**	
CASE 1.	50GeV	10	4.5KM	RADIUS=4.0M
CASE 2.	50GeV	100	1.4KM	RADIUS=1.2M
CASE 3.	30GeV	10	2.5KM	RADIUS=5.0M

Figure 5: Map of the Fermilab site that displays the siting constraints for locating the MuSR explained in the text for two different choices of annual dose equivalent and two different choices of muon energy.

14.7.3.2Other Radiation Sources

The bombardment of the walls of the MuSR components will involve a nearly uniform irradiation by electrons. Calculations of both the energy deposition in the superconducting magnets and the induced radioactivity due to these electromagnetic cascades were performed by Mokhov [15]. Residual dose equivalent rates due to these cascades will be small, less than about 1 mrem h^{-1} (10 microSv h^{-1}) after a 30 day irradiation and a 1 day cooldown. It is feasible for the muons stored in the MuSR to be catastrophically lost in the event of a sudden power outage or some other failure of the magnets. However, given the orbit time of 6 microseconds and the likely inductive time constants of the magnets, the loss of the muons during such an event would be distributed over many turns and large portions of the ring. Only a tiny fraction of them would be directed in a manner in which they penetrate the surface. Further calculations should be made to demonstrate this. It is certain that the near detector halls will be exclusion areas during operations due to neutrinos as well as the other background sources that are unavoidably present.

14.8 Non Radiological Environmental Protection Issues During Operation

14.8.1 Proton Driver, Target Station, Cooling Region, and Muon Acceleration Linacs

The issues are straightforward ones related to the control of non-radioactive wastes. Efforts should be made to prevent the creation of regulatory mixed wastes and to control spills. Surface water discharges should be managed in accordance with the current Laboratory policies and any State and Federal environmental permits that may be in place. These considerations are quite similar to those encountered at other Fermilab facilities located in the glacial till.

14.8.2 Muon Storage Ring

The location of the MuSR in aquifer units requires especially stringent protection against spills. It is also very important to continue to avoid the cross-connection of surface waters with the various aquifer layers and cross-connections between different aquifer layers. Efforts must be made to assure that any pumping necessary to keep the enclosure dry does not create perturbations of local community or individual drinking water supplies. Careful attention to these problems during the design and construction phases should lead to their successful solution.

14.9 Summary

The Neutrino Source provides a number of challenges in the area of environment, safety, and health. Many of these have been encountered, and effectively addressed, at Fermilab and other accelerators. Some of the problems are common to technological advancements in other accelerators worldwide. For these, collaborative efforts should continue to develop and improve the solutions that are needed. This project raises a few new issues that must be addressed. Continued attention to these issues is anticipated as the project proceeds.

References

[1] "Fermilab Work Smart Standards Set", Fermi National Accelerator Laboratory, http://www-lib.fnal.gov/library/protect/worksmart.html, November 15, 1999.

[2] N. V. Mokhov, MARS calculations, private communication, January 2000.

[3] W. Chou, "Proton Driver Study at Fermilab", Fermilab Report FERMILAB-Conf-99/277, October 1999.

[4] Yu. Konobeyev and Yu. A. Korovin, "Tritium Production in Materials from C to Bi Irradiated with Nucleons of Intermediate and High Energies", Nucl. Instrm. and Meth. in Phys. Res. B82 (1993) 103-115.

[5] M. Barbier, *Induced Radioactivity*, (North-Holland Publishing Company, Amsterdam and London, Wiley Interscience Division, John Wiley and Sons, Inc, New York, 1969).

[6] U. S. Department of Energy, "Nuclear Safety Analysis Reports", DOE Order 5480.23, April 30, 1992. The classification criteria specified in this Order are provided in a DOE Standard, "Hazard Categorization and Accident Analysis Techniques for Compliance with DOE Order 5480.23, Nuclear Safety Analysis Reports", DOE-STD-1027-92 Change Notice No. 1, September 1997. The criteria are augmented by additional radionuclides in LA-12981-MS, UC-940, "Table of DOE-STD-1027-92, Hazard 3 Threshold Quantities for the ICRP-30 List of 757 Radionuclides", Los Alamos National Laboratory Report, August 1995.

[7] N. L. Grossman, D. J. Boehnlein, and J. D. Cossairt, "Production and Release of Airborne Radionuclides Due to the Operation of NuMI", Fermilab Report TM-2089, August 1999.

[8] United States Code of Federal Regulations, Title 40, Part 61, Subpart H, "National Emissions Standard for Hazardous Air Pollutants (NESHAP) for the Emission of Radionuclides other than Radon from Department of Energy Facilities", 1989.

[9] J. D. Cossairt, "Use of a Concentration-Based Model for Calculating the Radioactivation of Soil and Groundwater at Fermilab", Fermilab Environmental Protection Note 8, December 1994 and J. D. Cossairt, A. J. Elwyn, P. Kesich, A. Malensek, N. Mokhov, and A. Wehmann, "The Concentration Model Revisited", Fermilab Environmental Protection Note 17, June 1999.

[10] J. D. Cossairt, N. L. Grossman, and E. T. Marshall, "Assessment of Dose Equivalent Due to Neutrinos", Health Physics 73 (1997) 894-898.

[11] N. V. Mokhov and A. Van Ginneken, "Neutrino Induced Radiation at Muon Colliders", presented at the 1999 Particle Accelerator Conference, New York, New York, March 19-April 2, 1999, FERMILAB-Conf-99/067.

[12] U. S. Department of Energy, "Radiation Protection of the Public and the Environment", DOE Order 5400.5, January 7, 1993.

[13] National Council on Radiation Protection and Measurements, Ionizing Radiation Exposure of the Population of the United State and Canada from Natural Background Radiation, NCRP Report No. 94, December 1987.

[14] N. Mokhov, private communication, January 2000.

[15] N. Mokhov, "Radiation Load on Muon Storage Ring Magnets", Presentation given at Fermilab, January 25, 2000.

15. R&D Plan

15.1 Introduction

In this section we summarize the key R&D activities required to validate the design concepts described in this Neutrino Source Feasibility Study. The items covered here fall into two categories: *i*) those required to validate or improve the components that drive the fabrication costs of the facility, and *ii*) those required to address the performance and/or feasibility of fabrication of particular components. In the first case, R&D will mainly involve hardware fabrication and testing without beam. In the second case, performance tests with beam will generally be required in addition to prototyping. Much of the hardware R&D of this second class must be guided by knowledge gleaned from simulation studies in which realistic errors on component performance are included.

What is presented here a long-term schedule for carrying out the R&D activities. A technology-limited schedule in which we assume that there is available staff to carry out the program is assumed, and available funding to support it. With these assumptions, we believe that, at the end of this period, the R&D program will have progressed to the stage where we could confidently begin developing a Conceptual Design Report for a Neutrino Factory. It is important to note that much of the hardware development effort envisioned should proceed in parallel on several fronts and at different laboratories. Indeed, it *must* proceed this way if we are to complete the R&D tasks in a reasonable time frame. Clearly, however, our progress on this time schedule requires funding commensurate with the program needs; this is the resource over which we have the least control.

15.2 Proton Driver

The main technical issue to address here is the production of high intensity, short proton bunches, with a beam power of the order of 1 MW or more and with very small beam loss during acceleration. We are fortunate that there are a number of existing proton synchrotrons and linacs available for testing some of the concepts and components needed. This program is already under way at several laboratories, not all of which are motivated by the need for an intense muon beam.

15.2.1 Hardware Development

Hardware that may be required for this purpose in the synchrotron includes high-gradient, low frequency RF cavities to produce short bunches, inductive inserts to compensate for space-charge blowup, a thin-walled chamber to minimize eddy current effects, and tracking circuitry to maintain the ratio between various magnet families during the ramp cycle. Development of effective collimator systems, feedback systems, fast full-aperture kickers, and efficient and reliable power supply technology are also important R&D topics. Hardware for the initial linac includes an RF chopper, a high-brightness proton source, and a high-current radio-frequency quadrupole (RFQ).

15.2.2 Experimental Program

Experiments to study intense short, bunches have started and will continue. These will involve using inductive inserts, testing the behavior of RF cavities with beam (beam loading compensation, impedance effects), and studies of the microwave instability below transition energy. Tests of a cavity loaded with Finemet will be carried out to study its behavior in a beam. These will initially be done with a CW system at a gradient of about 30 kV/m and a frequency of a few MHz. Studies of much higher cavities are underway. Bunch compression tests to study methods of reaching high peak current and nanosecond bunch lengths will be done at a number of laboratories (BNL, CERN, Fermilab, GSI, Indiana University, and KEK).

15.3 Target System

The primary technical issue to address in this area is the survivability of a target subjected to a proton beam power of about 1,5 MW. Both solid and liquid (mercury-jet) targets are candidates for the Neutrino Source. These pose different problems, but experimental validation of the available computer codes is needed in either case. In the context of this Study, R&D for target systems is a broad category that includes development work for the mechanical design of the target and beam dump, design of the remote handling hardware, and safety and environment issues that may impact the target system design. These are divided into near-term activities that should begin next fiscal year and long-term activities for the next two to five years. General issues related to target performance are mainly covered under the Targetry R&D program of the Muon Collaboration. Included in this broader category are: the calculational and experimental studies of the behavior of a mercury-jet target; yield measurements from the target (both pions, which determine the muon yield, and neutrons, which define the radiation environment near the target); lifetime and power deposition tests with a carbon target; materials studies for the superconducting 20-T target solenoid; studies of the proton beam dump; and exploration of solid-target geometry and cooling options, such as a band target configuration.

15.3.1 Near-Term R&D

The primary short-term goal is to determine the survivability of a passively cooled graphite target under the thermal and radiation conditions expected at a Neutrino Factory. A test of a strained graphite target is planned at the 1-MW Spallation Radiation Damage Facility at LANL very soon in collaboration with colleagues from ORNL. This will involve the following activities: *i*) evaluation of the properties of different grades of graphite, including carbon-carbon composites; *ii*) thermal tests to determine bending-creep and axial-creep effects on full-scale target rods for various support schemes; *iii*) investigation of non-uniform power distribution on full-scale rods to determine temperature and stress effects; *iv*) thermal shock tests on small scale samples; *v*) neutron irradiation tests to determine target survivability; *vi*) designing and testing of one or more water cooling schemes for the target support tube. Other activities will include investigation (by calculation and tests) of the pressure shock-wave effects due to the very short duration beam spill, development of a design for a water-cooled graphite target if tests on the passively cooled target are unsuccessful (i.e., fabrication of small-scale samples of graphite with cooling tubes and testing them for thermal and radiation survivability), and evaluation of safety and environmental requirements. Beam tests at the A3 line of the AGS at BNL will be carried out, beginning next year.

15.3.2 Long-Term R&D

After the initial tests, the next step will be to design and fabricate a full-scale prototype of a target and its support tube, complete with coolant interfaces. This target will be tested in a proton beam under realistic conditions. Another important task will be to develop design details for the high-power beam dump, which is integrated in the decay channel. It is envisioned that we will carry out small-scale tests to demonstrate feasibility. Work on the alternative of a mercury-jet target will also be pursued. This will include operation of a jet target in a high magnetic field at the NHMFL. Beam tests at the AGS will continue. Ultimately, yields will be measured.

The most challenging magnet is the capture solenoid in the target region, and clearly the most critical area in that subsystem is the resistive poly-Bitter magnet nearest the target. This magnet is critical primarily because the 20 T magnetic field cannot be achieved without it. Magnet lifetime is expected to be dominated by erosion associated with the extreme cooling requirements but, in addition, the device has an uncertain radiation tolerance. There is a large body of data on the radiation tolerance of a wide range of insulating materials and there is also very good experience with the poly-Bitter technology at the NHMFL. While there is every reason to expect that a good solution can be found, it is important that a careful study be undertaken to unify existing experience, to incorporate candidate materials into a systematic design process, and to demonstrate compatibility of candidate materials and components in a working poly-Bitter magnet model. This may require beam time at the 1-MW Spallation Radiation Damage Facility at LANL.

There are also “facility” design issues worthy of R&D effort. We will develop full-scale mock-ups (using simulated components and substitute materials where possible) to demonstrate remote handling of key components. A partial mock up of the target region, complete with utility interfaces (electrical, cooling, instrumentation) will be fabricated. This setup will be used to demonstrate replacement of the target module, replacement of the Bitter coil, and replacement of the proton beam window. Finally, consequences of possible failure modes, e.g., of the beam isolation window, will be investigated to make sure the design is robust against such occurrences. We expect to benefit in this area from close collaboration with groups at existing facilities (or those now under construction, for example the SNS at ORNL) that have similar requirements for beam power on target.

15.4 Decay, Capture, and Bunching

One of the more challenging areas of the front-end system is the phase rotation section, which makes use of an induction linac system to reduce the energy spread of the beam prior to bunching and cooling it. This device is intended to operate at an accelerating gradient of 2 MV/m (from –0.5 to +1.5 MV/m) with a pulse structure consisting of four ~150 ns pulses within a 2 μs interval. In addition, it must accommodate superconducting solenoid coils in the accelerating gaps to maintain the transverse focusing of the beam along the length of the linac. The design considered here is based on a device of similar size, but lower gradient and normal conducting coils for focusing, built for the DARHT project. Nonetheless, the combination of high gradient, internal magnetic field, and untested pulse structure mean that a prototype induction cell and pulser must be built and tested. The R&D program will determine whether the induction linac can provide the acceleration waveforms needed for the phase rotation. Important issues are the accuracy and reproducibility of the voltage waveform, determining limits on the gradient, and the lifetime and reliability of the modules. The integration of the internal superconducting solenoids with the accelerating structure must be tested.

As discussed in Chapter 5, the beam energy spread after phase-energy rotation and bunching is larger than desired, even in the induction linac phase rotation scenario. A smaller energy spread may be accomplished by better optimization of the decay section and induction linac, or it may make use of an initial phase rotation using RF cavities. This is an area that will benefit from more integrated simulation studies of the complete cooling system.

15.4.1 Hardware Development

The induction linac R&D effort will include the design, construction, and testing of a prototype module of the 200 MeV induction linac. This module will consist of a single induction cell (–0.5 to 1.5 MV), a vacuum chamber, a four-pulse generator module, and a superconducting magnet assembly with its associated cryogenic cooling system and power supply. Because the induction cores provide the dominant load for the four-pulse generator module, no beam test is necessary.

Initial activities will consist of conceptual design work and small-scale component tests. Design tradeoffs will be performed to establish a set of beam parameters, such as pulse width vs. pulse separation along the linac, that are consistent with pulse-generator constraints. Further study will be done to optimize the design of the pulse-train generator. Specifically, recent and anticipated advances in the technology of high voltage/high power switches will be explored and samples tested in an attempt to reduce or eliminate the magnetic compressor pulse charge stages. Alternate pulse generation topologies will be explored and a detailed circuit simulation model will be developed and exercised. Induction cell core tests will be performed to establish accurate loss current vs. time characteristics. A full-scale core using the most promising material will be built and tested. Engineering will be done on the superconducting magnet to bring it to the conceptual design level.

After defining the system, we will fully prototype such a cell and its pulser. First, hardware for a 1 m cell and a pulser capable of two-pulse operation will be procured. Initial testing will begin, first in a single-pulse mode and then in a two-pulse mode. Hardware will next be procured for an additional two pulses, after which testing of the full four-pulse prototype system will commence. This staged approach to testing and hardware procurement allows early identification of problems and permits their solutions to be incorporated into the design before committing to all the hardware. Parallel simulation efforts will finalize the voltage profile requirements that the pulser and induction linac must meet.

A number of different solenoid magnet designs are needed for the capture and decay channel region. Though most of these are straightforward, it will be prudent to develop prototypes of each type to ensure that there are no lurking fabrication issues. Throughout this region, it will be necessary to develop and optimize both cooling and quench protection schemes, with an eye toward enhancing system reliability.

The buncher requires cavities with lower gradient than those of the cooling channel, and it may be possible to enlarge their aperture. If simulation studies confirm this, development of a modified cavity will be needed. If a two-frequency buncher is adopted, a second-harmonic cavity will be needed. Ideally, this cavity would maintain the same aperture as the lower frequency cells, which makes its aperture relatively large.

15.5 Cooling Channel

15.5.1 Cooling Theory, Simulation, and Optimization

Although considerable progress has been made in understanding the issues involved in applying ionization cooling and in designing realistic cooling channels, more simulation work is clearly needed to optimize performance, to test error sensitivity, and to minimize cost. In particular, the present baseline design does not fully meet the requirements for intensity at the end of the cooling channel. Cooling the longitudinal phase space would ease the design requirements for all downstream components (acceleration and storage ring portions of the facility), thus reducing cost and permitting a more efficient implementation. The current strategy is to examine emittance exchange (longitudinal-to-transverse) because, based on our present simulations, we are confident that this would increase transmission in the cooling channel. An in-depth look at this question will occur in Fall ’00 when a planned Emittance Exchange Workshop takes place at BNL. A solenoid channel with only a single polarity change appears promising in initial simulations, and we will follow up on this concept. In addition, we wish to consider a configuration based on a helical magnetic channel. Once a scheme is developed, we need to understand the uncertainties in its expected performance with respect to various model assumptions (e.g., correlations between straggling and large-angle-scattering, the atomic form factor in models used in estimating the multiple scattering distribution and energy straggling, and the effect of intense magnetic fields on these processes). Work will continue to refine the figure of merit that characterizes the front-end performance. In addition, particle distributions at the end of the cooling channel will be transmitted through the acceleration and storage ring sections to ensure a self-consistent design for the entire complex.

In Section 6 we presented two ionization cooling schemes based on differing design principles. The objective of our study is to design an efficient transverse cooling channel with components that can be built at the present time, or could be developed with a well-defined R&D plan. Continued interaction and iteration with the engineers will be a key part of our work. Detailed simulation studies are required to obtain the optimal solution for each of the available cooling channels. These studies will be crucial in selecting the best design, based on performance, engineering constraints, and cost. For example, the engineering details of the RF-cavity grids or windows (see Section 6), and their corresponding electric fields, will be implemented in our simulations. This activity will require the use of full three-dimensional codes and diagnostics to estimate reliably both the effects of scattering from these complicated shapes and the effects of the field distortions on the longitudinal phase space. Evaluating the effect of alignment errors also requires three-dimensional codes. Another activity that requires code development is the study of cooling channels that can achieve longitudinal cooling, because these involve elliptical or wedge-shaped absorbers. In addition, the optimization of each design must respect the engineering constraints on coil current densities, coil placement, and forces on the coils. Successive iterations of our simulation studies with the engineering analysis of each of the design variants will achieve the best solution.

The performance of any cooling channel is tightly coupled to the performance of the machine components upstream of it and to the acceptance of the acceleration section that follows. For this reason, the optimization of the cooling channel must be iterated in the context of the designs of these other sections. Based on the present work, there are several places where additional effort is needed. The transverse matching between the buncher section and the downstream cooling channel needs to be improved, and the longitudinal bunching itself can be made somewhat more efficient. The combination of the induction linac and its upstream drift section needs to be optimized to reduce the energy spread of the beam going into the cooling channel. The cooling channel itself needs further optimization. The figure of merit used is the number of muons per incident proton within a specified transverse and longitudinal emittance. For now, we choose the transverse emittance cut to be 6000 mm-mrad, i.e., four times the rms emittance initially specified. This value can easily be accepted in the acceleration section to follow.

To provide a realistic experimental validation of the cooling concept we adopt, an experimental program (MUCOOL) has been initiated at Fermilab. This effort will design, fabricate, and test all of the components required for a cooling channel cell—absorber, RF cavity (both a beryllium foil and a gridded cavity will be built and tested), and superconducting solenoid. This program will focus initially on producing prototypes of all these components and bench testing them. (As noted in Section 15.5.2, the absorber will be tested in a beam of protons or electrons as part of its initial commissioning.) After all components are available, a complete cooling cell will be assembled and its performance tested cryogenically and electrically. Part of the MUCOOL task is to develop instrumentation capable of measuring the muon beam properties within the cooling channel. Access to a beam will be necessary for this work.

15.5.2 Absorbers

The liquid hydrogen (LH_2) cells that will serve as the cooling channel absorbers have a number of R&D topics that need study. The baseline (FOFO) cooling design requires liquid-hydrogen absorbers that are thin (~13 cm) relative to their diameter (20–30 cm). For a given pressure differential, hemispherical windows are thinnest but, with this oblate shape, thicker ellipsoidal or torispherical windows are required to provide a sufficiently short sagitta. A program of design studies backed up by carefully designed tests will be needed to establish safe design and operating parameters for the LH_2 containment windows. Because multiple scattering in the windows is a major source of "heating" of the muon beam, every effort must be made to minimize window thickness. Aluminum is our default material choice, but AlBeMet—a beryllium-aluminum alloy—is an attractive alternative if it is shown to be compatible with liquid hydrogen. With 40% greater strength than aluminum and 2.1 times the radiation length, AlBeMet has the potential to lower the total radiation-length fraction per absorber from ~2.4% to 1.8% or less, depending on the detailed optimization of absorber dimensions. (While beryllium windows may also be feasible, there appears to be little additional gain compared with AlBeMet.)

In all scenarios the specific power dissipation in the absorbers is large and represents a significant cryogenic load. Handling this heat load is a significant design challenge in terms of fluid dynamics and requires sophisticated thermal modeling of target heating. An R&D program is now under way at the Illinois Institute of Technology (IIT) to understand the thermal and fluid-flow aspects of maintaining a constant temperature within the absorber volume despite the large spatial and temporal variations in power density. This program is beginning with computational-fluid-dynamics studies and is planned to proceed to bench tests and high-power beam tests of an absorber prototype over the next year. The prototype absorber will be built and initially tested for safety and then with a proton or electron beam to explore pulsed heating effects. Ultimately, one or more absorbers of a selected design will be tested.

In some scenarios (especially those with emittance exchange), lithium hydride (LiH) absorbers may be called for. Since it is a solid, LiH can in principle be fabricated in arbitrary shapes. In emittance-exchange channels, dispersion in the lattice spatially separates muons according to their energies, whereupon specially shaped absorbers can be used to absorb more energy from muons of higher energy and less from those of low energy. Unfortunately, solid LiH shapes are not commercially available, and procedures for their fabrication need to be developed. Such an effort is challenging since LiH is very reactive.

15.5.3 Diagnostics

Techniques for optimizing the operation of a physical cooling channel must also be developed. The beam emittances and particle losses in these cooling channels must be measured in order to optimize running conditions. These beam measurements will be complicated by the large size of the beam, the limited space available for detectors, the high magnetic fields, and the need for low-temperature insulation. Although measurements of muon beams have been done for years, the issues associated with the cooling channel will make the required measurements difficult. For this reason, some R&D directed at beam diagnostics and beam measurements is clearly required for the design of the neutrino source.

Diagnostic information for the following is needed: *i*) initial matching of the cooling optics to the beam parameters, *ii*) accuracy of this match down the length of the cooling channel, *iii*) the accuracy of physical alignment of beam components, *iv*) identification of transverse and longitudinal loss mechanisms, and *v*) measurement of the emittance at various stages of cooling. Because the emittance will only change by only a few percent in each cooling cell, it will be desirable to have a few special diagnostic sections interspersed with cooling sections to make precise measurements.

This is an R&D area in which University groups can make significant contributions because new ideas are required in this area. Developing concepts as well prototypes perfectly fits infrastructures that are available in Universities while actual beam tests would be done in close collaboration with the participating laboratories.

15.6 Acceleration

There are a number of technical issues in this area that will require R&D effort. A very short section of linac that immediately follows the cooling channel might use normal conducting RF, i.e., it is basically a continuation of the cooling channel RF system, without the absorbers. However, it will be followed by a superconducting linac operating at the same frequency (201 MHz) to raise the beam energy to 3 GeV. The 201 MHz SCRF linac cavities must be designed and prototyped, and must be compatible with the attendant magnetic focusing system. Even weak stray magnetic fields from the focusing system would render the superconducting RF (SCRF) cavities inoperative, so effective magnetic shielding is a necessity. These cavities give rise to several challenges. Although we envision filling them with a low-power, long-pulse technique that reduces the number of klystrons and diminishes the power requirements on the input coupler, the Lorentz force detuning and microphonics remain significant issues. These effects are at least an order of magnitude more severe than in comparable installations at CERN, JLab, SNS, or CESR. Given the critical role played by the 201-MHz SCRF in our design, these issues merit special attention. Close collaboration with universities and institutes in the US as well as abroad is foreseen. We plan to encourage and support the technical development of the cavity structures as well as the testing. We have identified the acceleration as one of the major cost drivers and therefore have to have a strong program in this area very soon to reduce costs.

Optimization of the RLAs in terms of the number of passes in each must be done. This depends on the details of the splitter and recombiner magnet designs and also on the beam energy spread coming from the cooling channel. Designs for these magnets must be developed and—depending on how nonstandard they are—prototypes will be needed. Work on finalizing the optics design for the arcs must be done. Designs that avoid the use of strong sextupoles look promising but must be simulated based on the actual particle distribution provided from the front-end simulation effort. Optimization of the arcs in terms of magnetic fields and technology (room temperature or superconducting magnets) must be completed. With SC magnets, radiation heating becomes an issue and must be assessed and dealt with. Assessment of field error effects on the beam transport must be determined to define acceptance criteria for the magnets. This will require use of sophisticated tracking codes like COSY that permit rigorous treatment of field errors and fringe-field effects. Because the beam circulates in each RLA for only a few turns, the sensitivity to magnet errors should not be extreme, though the large energy spread will enhance the effects. Though it seems likely that the RF cavity frequency in RLA1 will be 201 MHz, the RLA2 frequency could be either 201 or 402 MHz. The choice of the higher frequency has been made provisionally but should be validated by performance simulations. In particular, we must develop a longitudinal matching strategy that manages the single-bunch phase space through the acceleration cycle and we must verify that the increased energy droop associated with the higher frequency cavities can be accommodated in the beam transport. While a preliminary estimate of the beam-breakup instability shows that it should not be a problem, a full assessment of collective effects is needed in each RLA to determine whether higher-order-mode dampers are needed for the RF cavities.

15.6.1 Hardware Development

A prototype RF cavity will be built and tested at gradients up to 15 MV/m with a Q of $\approx 5 \times 10^9$. This cavity must also operate in a channel having decaying muons. Though SCRF cavities at higher frequencies are by now becoming common, cavities sized for 201 MHz have never been built. The large size of the cavity makes it more sensitive to microphonics; a prototype cavity will permit us to assess this aspect. Even extending fabrication and cleaning techniques to this size range is an R&D topic in itself. Developing the proper facilities is a long lead-time item and will require significant up-front expenditures. At high gradients, the input power coupler design will need to be tested and validated, though the chosen slow-fill technique is expected to make this straightforward. Detuning issues associated with the pulsed RF system must be evaluated. Finally, because of the large stored energy in a 201 MHz SCRF cavity, a reliable quench protection system must be designed and tested.

Prototypes of the special magnets (splitters, recombiners, and kickers) will be designed. If curved SC dipoles are used, a prototype will be fully engineered. Effective magnetic shielding concepts must be developed to protect the SCRF cavities. Beam diagnostics that function properly in a beam pipe containing a decaying muon beam must be designed and prototypes built and tested.

15.7 Storage Ring

The most serious R&D issue for the storage ring operation is a more exact understanding and modeling of large-aperture, strong quadrupole fringe fields. Once the end fields are accurately described (which appears to require detailed magnet designs), they must be inserted into the tracking programs and carefully studied by themselves and in combination with field and alignment errors.

Also, the requirements on beam steering in the production straight section, intensity monitoring, collimation of electrons from the long straight section etc have to be specified to see if they can be achieved.

15.8 Solenoids for Decay, Phase Rotation, and Cooling Channels

Although design and implementation of every solenoid channel discussed above is a nonstandard technical task, one can expect to meet the most challenging problems working with the cooling channel. Both radial and axial ponderomotive forces in this channel are extremely large as well as the interacting forces acting on the first and the last magnets in the string. Because the mechanical behavior of a magnet in this channel is the main issue to study, thorough modeling of the system is a must in this case. Other objects of study are optimization of the quench protection system and analysis of stresses in coils during cooling down and warming up. Undoubtedly, modeling and prototyping of the channel magnets must accompany development of magnetic systems for the Neutrino Factory front end.

The R&D scenario suggested for the next step includes:

- Optimization of the magnet design for the cooling channel with the goal of reducing mechanical stress in coils;
- Mechanical stability analysis for the magnets of the cooling channel, development of the channel mechanical scheme, and design of a mechanical support for coils and magnets in the cooling channel;
- Development of Nb_3Sn cable to use in the cooling channel; development of coil fabrication technology;
- Development and optimization of the quench protection system and the cooling scheme for each channel with the goal of increasing system reliability and reducing the time for cooling down and warming up;
- Building full-scale prototypes of magnets in each channel.

15.9 Cryogenic Systems

The estimates presented above place the cryogenic system of the Neutrino Factory within current practice, and no R&D is required. The next step to take is to try to get concepts for all of the cryogenic modules of the Neutrino Factory and to assemble as much design detail as possible. It is important also to begin to think about operating scenarios. With this additional information a much better estimate of the scope of the cryogenic system can be made, some assessment of its operating requirements can be developed, and we can begin to provide support for the component design process.

15.10 High Power RF Sources and Normal Conducting Cavities

Operation of the cooling channel requires normal conducting (NC) RF cavities operating at a frequency in the range of 175–201 MHz and a high gradient of about 15 MV/m. Moreover, the cavities are immersed in a strong solenoidal magnetic field. To increase the cavity shunt impedance (lowering power requirements) two alternatives are being explored. In one option, each cavity aperture is covered with a thin beryllium foil (125 μm thick) that serves to enhance the on-axis accelerating gradient while giving rise to only a modest amount of multiple scattering. In the second approach, the cavity apertures have a grid of tubes to achieve the same benefits. Both techniques have significant fabrication issues, and it is planned to build prototypes of both cavity types to test them. Either of these approaches causes some increase in multiple scattering, and thus some degradation of the cooling effect of the channel. Simulations will be used to evaluate the acceptability of each approach from the scattering viewpoint. High-power cavities built with each of the two candidate techniques will be tested for voltage handling capability, first without, then with a superimposed solenoidal magnetic field. This will permit evaluation of breakdown and multipactor behavior. In the beryllium foil case, heating from RF fields in the cavity (which scales as r^4) defines an upper limit for the aperture radius. Low-power tests of foil deflection are under way to validate the dimensions chosen; these must be repeated for the high-power test cavity. Fabrication techniques must be developed for attaching the beryllium foils to the cavity in a mechanically reliable manner while maintaining good thermal and electrical contact. High-power tests of the gridded cavity will be carried out to verify thermal behavior and electrical breakdown at high gradients. Fabrication of the grid tubes from AlBeMet rather than aluminum is attractive from a multiple scattering viewpoint and will be tested.

Development of a reliable high power (≥ 10 MW) RF source is another important R&D activity for the cooling channel. Candidate technologies include multibeam klystrons, single-beam klystrons, eventually inductive output tubes (IOTs) or even lower-gain devices. We envision development of prototypes in close collaboration with the available expertise in other laboratories (e.g. SLAC) and industry. Multibeam klystrons seem to be the most promising approach at present because of their potential for efficiency and compactness. These devices at some point require industrial development, which in turn means long lead times and significant up-front costs. A compact solid-state modulator based in IGBT technology will also be build and tested. After coupling the RF power source to multicell superconducting RF cavities, we will assess the need to have individual frequency and phase control of each cell.

15.11 Summary

Future R&D on the different subsystems that have been described in this report will involve a strong and growing simulation effort as well as an accompanying hardware R&D program. In some places more patience is required to define the actual hardware R&D so that careful decisions can be used to drive the work in a direction that is useful. Bad decisions could delay progress on the hardware developments that are really required. For the cooling channel as a whole this is even more important than for its component parts. From this report and from R&D items described in this chapter the appropriate programs can be identified and launched as soon as possible with the funding presently available.

The R&D program which is described in this chapter does not have a schedule attached to it which would allow either an estimate of the time necessary to perform the work nor tracking the actual progress that is required. Although laboratories and universities which could perform the R&D work have been identified, the goals, the people to work on the R&D, the funding and many other critical issues have not been dealt with. These details will have to be negotiated and folded into a schedule before it is useful and can be presented.

This R&D chapter nevertheless circumscribes the cost drivers as well as the technically challenging problems. These cost drivers are not necessarily the performance limiting components in the Neutrino Factory and the performance limiting components do not always drive cost. Both nevertheless will have a strong influence on the time that is required to deal with these subjects thoroughly. Both will also drive the number of people that are required in order achieve these goals.

For a facility of the scale that is presented in this report the R&D program is very different from what we are used to in High Energy Physics. While the detailed development of single components that can be mass produced (one way or the other) for the final project is the usual goal, the R&D here spreads over a wider range of issues and technologies. It requires the detailed development of many single components and for this reason needs much more support than usually anticipated and which can be spread over a large community. This support is what we are asking for.

A. Appendix: Cost Estimate for the Facility

Determining the cost of a facility as complex as the neutrino source presented here is a very difficult task within the short time period of six months. Three factors contribute to the uncertainty significantly:

1. The number of subsystems in the facility, which are described throughout the report, is comparatively large. All of the subsystems contribute a considerable amount of complexity and cost that have to be addressed by specific expertise in order to find a technical solution and a reasonable cost estimate. The variety of technologies is large and many of them have to be pushed to the edge or beyond and therefore has to be addressed with an appropriate R&D program. Cost savings from mass production will not be major for any of the subsystems in the neutrino source.
2. For many of the subsystems specific R&D has not even started. Although we are confident that the R&D programs will be technically successful, we do not exactly know what the cost of the final device is going to be. For many things estimates were based on present experience and on educated guesses.
3. Many things that are fairly conventional, for example, vacuum systems, correction magnets, and some of the diagnostics, have not been worked on by specialists. Again, educated guesses and experience from other projects have been used in order to determine cost figures. The overall contribution to the total cost from these systems is not more than approximately 10%, but this number could easily be wrong by a factor of two.

It must be understood that the cost estimate for the facility is very preliminary and although it is our best effort, it has a large uncertainty. Some areas are more difficult to estimate than others and it will be pointed out chapter by chapter where this is the case. For the large systems either engineers or project leaders for comparable programs have determined the cost numbers to their best knowledge. For the large systems, like the superconducting rf-accelerators and the high field solenoidal channels, experts (sometimes from all over the world) were brought together; this certainly helped us arrive at a more realistic cost figure. Nonetheless, the outcome of the R&D program could have a significant impact (either favorable or unfavorable) on the estimated cost of some components.

The Overall Cost of the Facility

The cost of the Facility is presented in two bar charts. One shows the distribution according to the different subsystems, the other shows the distribution according to the components summed up over all subsystems (magnets, power supplies etc).

The study does not include any contingency, EDIA nor does it consider escalation. It only lists the basic investment costs that have been estimated. Under the column called "Others," typically ten percent of the facility cost was added to account for those items not included; this should not be construed as contingency. The numbers also do not include the R&D money necessary to develop the different systems.

The Power Consumption of the Facility

The power consumption of the facility is significant. Approximately two-thirds of the power goes into the accelerating rf systems (70–80) MW. The proton driver will require approximately 30 MW of average power and the rest of the power is roughly evenly distributed. A total of 170 MW will be required for a 50 GeV facility.

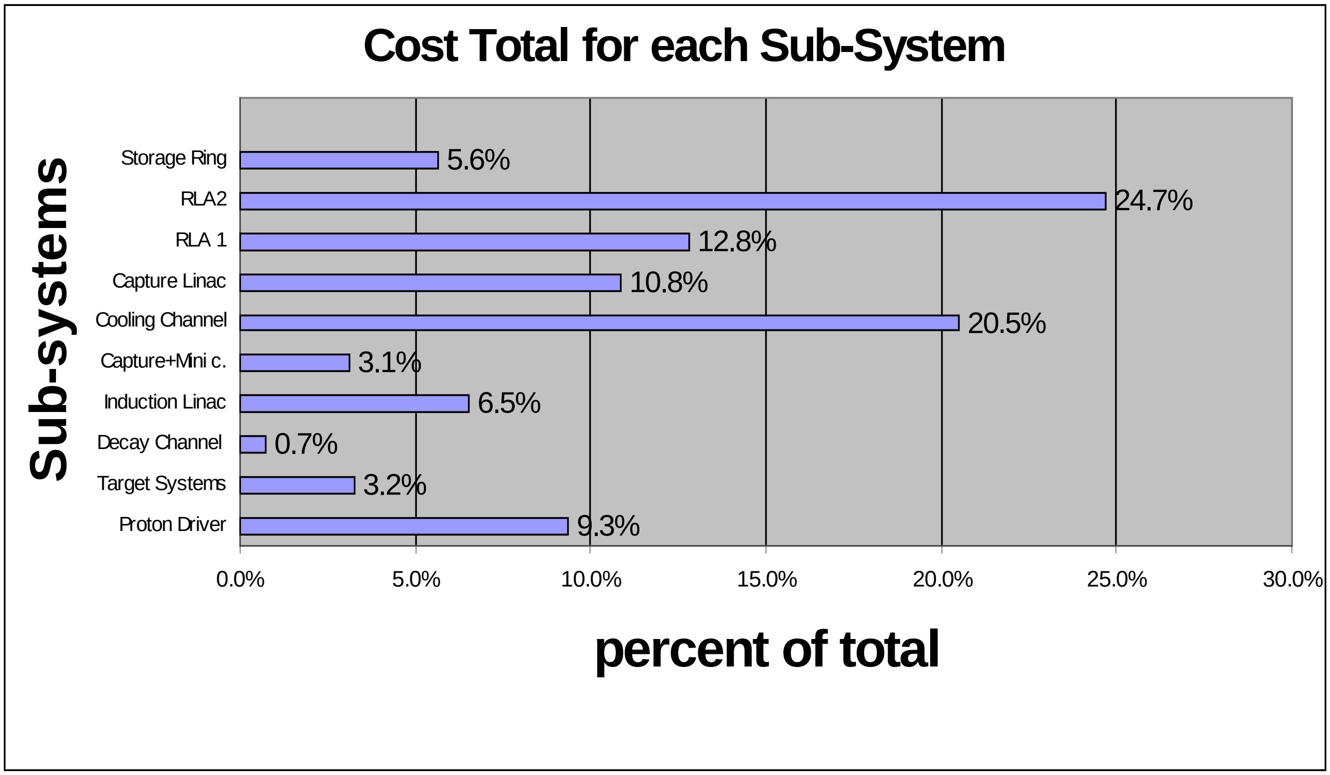

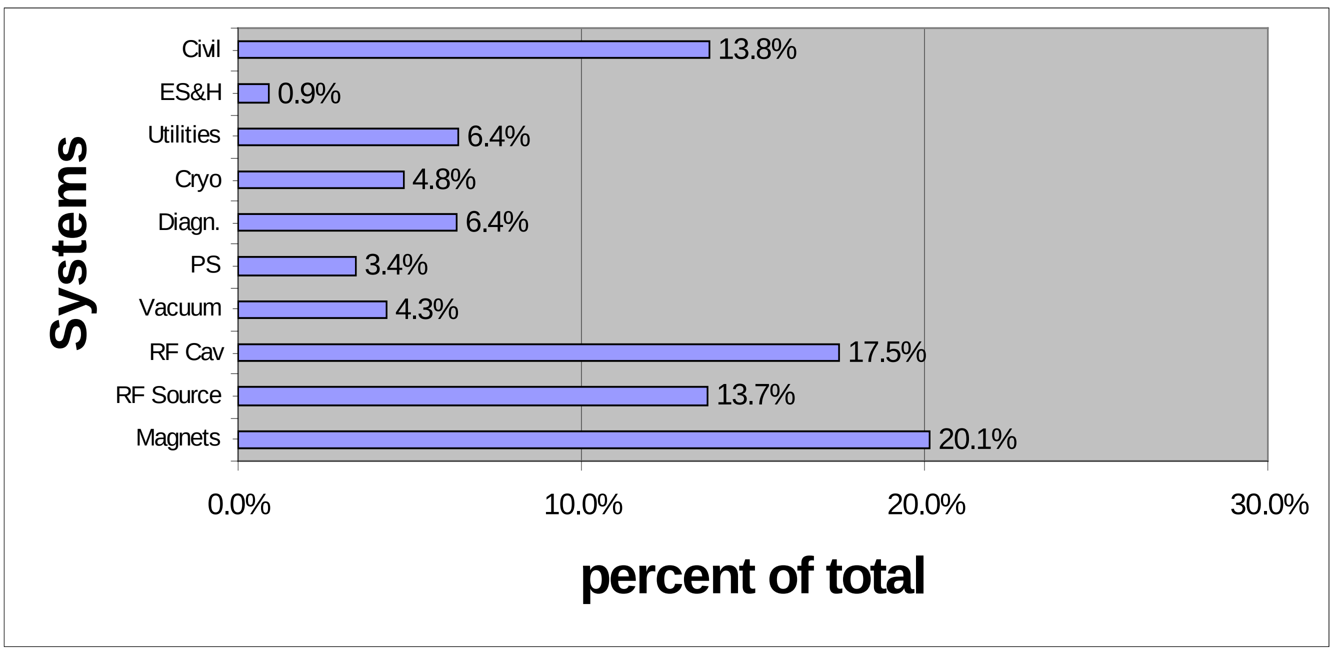

Distribution of cost in percent of the total for the different subsystems and for the components summed up over the subsystems.

Summary

The cost estimates presented here are the result of six month work of a group of approximately 20 FTEs at Fermilab, a large contribution from various other labs, probably another 50 FTEs in total and a number of external experts who were brought in for a couple of todays or for very specific topics. From the result it is obvious that for a complex of that size and complexity this is not enough to give precise estimates, but it is certainly enough to define the R&D programs and to get a first handle on how to stage and how to optimize such a facility. The number as well as the distribution of the cost will allow us to define a route towards such a facility with a minimum of risk and a maximum of physics for each step. It also gives us a clear idea on how to improve performance and on what technological improvements have to be made for each step.

REFERENCES

[1] Neutrino factory physics study coordinators: S. Geer and H. Schellman. See http://www.fnal.gov/projects/muon_collider/nu/study/study.html

[2] Neutrino factory technical study coordinators: N.Holtkamp and D. Finley. See http://www.fnal.gov/projects/muon_collider/nu-factory/nu-factory.html

B. Appendix: Scaling of Cost with Energy and Intensity

With the two ongoing studies, one for the physics program, [1] and one for the accelerator and facilities [2] on the "Neutrino Factory Based on a Muon Storage Ring", a number of interesting suggestions and ideas came up. Almost immediately the question of scaling cost with the storage ring energy and with intensity came up. Nevertheless, it was impossible to explore all those questions in great detail, either in the report or in the preliminary cost estimate that is presented in Appendix A. During the study it became more and more clear, that one of the unique features of a neutrino source, namely the possibility to balance the cost of the accelerator with the cost of the detector, would urge the accelerator people to find an answer to this question sooner rather than later. This appendix is an attempt to give this answer, very short and very preliminary.

Scaling with Energy

The assumption at the beginning of this study was that accelerating muons would be the only cost driving factor of the facility, given the experience from other actual projects for pulsed high energy accelerators. This is emphasized in our case by the fact that the acceleration has to be done at low frequency with relatively high gradient—a very unfortunate combination from the technical point of view. The prejudice turned out to be right, although compared to a very early guess the result presented in Appendix A is not as obvious as it was assumed to be. The superconducting solenoids, especially in the cooling channel, are equally challenging from the technical point of view and certainly very expensive.

In the Introduction (chapter 2) it is described that over a large range of parameters the product of: the energy of the muon beam times the mass of the detector times the intensity should be kept constant for a given physics reach. The physics study on the other hand defined a lower energy limit of 20 GeV for the stored muon beam in order to have good muon detection in the long baseline detector. Changing the scope from 50 GeV to 11 GeV or so would have an obvious solution in that the second recirculating linac (RLA 2) would be abandoned. With 20 GeV being the target energy for the accelerator, this is not so obvious. The fast answer nevertheless is that doubling the acceleration per turn in RLA 1 would bring the energy up to 20 GeV. Optimization of the number of turns versus purely doubling the installed voltage would have to be done in a more detailed study, and could lead to a cheaper solution. The cost saving by taking out RLA 2 (~25%) and doubling the voltage in RLA 1 (~5%) would reduce the total by approximately 20%.

For the storage ring, the tunnel circumference will be constant to achieve the same decay ratio in the straight section. The magnets, given the 50 GeV arc radius, could now be normal conducting, which will not automatically lead to any savings, because the aperture has to increase at least proportional to $\sqrt{(1/\gamma)}$. The aperture in the straight section will be constant, because, as the decay angle increases with $1/\gamma$, the emittance increases with γ but the divergence of the muon beam only increases with $\sqrt{\gamma}$. The divergence of the muon beam should be smaller than the $1/\gamma$, which makes the product constant if the β-function scales proportional to γ. An interesting result. Nevertheless, the ring would have to handle a larger energy spread because of the smaller adiabatic damping. The cost savings using normal conducting magnets could easily be eaten up by the increased power consumption and the more complicated chromatic corrections that will be necessary. For the rest of the front end nothing would be saved

Scaling with Intensity

In the summary bar chart in Appendix A one can see, that the total investment cost for the cooling channel is approximately as much as for RLA2. The obvious conclusion is that increasing the energy will approximately cost as much as increasing the cooling. Reduction in cooling will decrease the intensity and decrease the cost as the cooling channel gets shorter (or disappears). Because emittance cooling scales exponentially with the length of the cooling channel and given the fact that, with the study presented here, we are very close to the theoretical cooling limit (2-3 e-foldings) reducing the length is an obvious choice. If we would decrease the length to one half (1/2 the cost) the intensity within the given acceptance would only go down by 20% or so. Approximately 12% could be saved. A minimal solution where no cooling is applied, is under investigation right now and the achievable intensity could be of interest for an entry level machine with an intensity of order 10^{19} per year. The total would be reduced by 20%.

Cost savings that will scale with intensity are usually made by reducing the installed rf power. Especially in a superconducting accelerator, where usually most of the rf power is transferred to the beam, this scales almost linearly. Unfortunately this does not work in our case. Due to the low frequency and the high gradient the stored energy in the cavity is large enough to accelerate the beam over many turns without refilling. By the same argument, the extracted energy is only a small fraction of the total and the rf peak power is required purely to build up the stored energy. The transfer to the beam is of the order of a few percent only. A reduction in beam intensity will therefore not save any money in the rf systems. On the other hand no upgrade of the rf system is required up to the point where the power extraction from the cavity becomes significant. At twice the design intensity this starts to happen and a different filling scheme, where the rf power going into the cavity has to be matched to the power extracted, is required. At this point the installed rf power has to be upgraded significantly. The power transfer to the beam is more efficient and the average ac power will not necessarily go up. The number of klystrons will have to be approximately doubled, increasing the cost for each of the accelerating systems (sc-linac, RLA 1 and RLA 2) by about 1/3, which again is approximately 20%. The tungsten shielding in the storage ring magnets, now designed for 70 Watts of power loss per meter (2×10^{20}/year) in the arcs due to decay electrons, will have to be increased. The inner beam pipe of the superconducting dipoles has to be exchanged and a smaller emittance muon beam is required (because of the reduced aperture) or new magnets have to build. This will add another 2-3%. This cost might be prudently spent initially to provide design and operating margin and to avoid a subsequent shutdown as the intensity increases.

Summary

The reduction in scope for a neutrino source based on a muon storage ring can be twofold: Decreasing the energy or decreasing the intensity or both. Each of the steps will reduce the primary investment significantly (approximately 20% each, more than 40% for both). The physics goal of an entry level facility will define which way to go.

REFERENCES

[1] Neutrino factory physics study coordinators: S. Geer and H. Schellman. See http://www.fnal.gov/projects/muon_collider/nu/study/study.html

[2] Neutrino factory technical study coordinators: N.Holtkamp and D. Finley. See http://www.fnal.gov/projects/muon_collider/nu-factory/nu-factory.html